Studies on the Calibration and Optimisation of Detector Response in Liquid Argon Time Projection Chambers for Neutrino Experiments

Harry Scott

Supervisors: Prof. Neil Spooner, Prof. Vitaly Kudryavtsev

School of Mathematical and Physical Sciences
The University of Sheffield

A dissertation submitted in candidature for the degree of Doctor of Philosophy at the University of Sheffield

September 2025

Declaration

I, the author of this thesis, declare that, unless otherwise stated, the work presented is my own. No part of this thesis has been accepted or is currently being submitted for any other qualification at the University of Sheffield or elsewhere. Due to the collaborative nature of particle physics experiments, the work presented in this thesis builds upon the efforts made by collaborators on the Short-Baseline Near Detector (SBND), the Sheffield TEst-stand Experiment with Liquid argon (STEEL), and other experiments which are noted below.

Chapter 2, outlining the history and theory of the neutrino, and Chapter 3, providing an overview of liquid argon time projection chambers, contain work I have not contributed to. Credit to work outlined and figures presented in these chapters are sourced through references and citations. The overview of SBND in Chapter 4 represents the collective efforts of the SBND collaboration, that which I was a part of and contributed to throughout my PhD. Work outlined and figures presented that I was not directly involved in are referenced to their source through corresponding citations.

Contributions to the hardware and commissioning work on SBND from myself included the calibration and installation of Cosmic-Ray Taggers (CRTs) on the north wall of the detector. Chapter 5 presents work done on this calibration task, where assembly and cabling of the A-frames used to collect data for this task was performed by myself, Amy Filkins, Jiaoyang Li and Rohan Rajagopalan, led by Michelle Stancari and Chris Hilgenberg, with intellectual contributions from Henry Lay and Erin Yandel.

My contributions to SBND software involved developing code which simulates and reconstructs Monte Carlo (MC) event samples using the LArSoft package, as well as developing algorithms to decode SBND data files and reconstruct waveform information from the readout electronics system, under the guidance of Mike Mooney. These tasks were also performed to provide the inputs for the field response simulation validation task using MC event samples and SBND data, outlined in Chapters 6 and 7 respectively.

MC event samples were produced by Avinay Bhat using my workflow, and are used in the analysis presented in Chapter 6. Analysis scripts reconstructing the average wave-

form from SBND readout wires were adapted to SBND from a template written by Mike Mooney for the ICARUS collaboration. Detector response modelling and the field response validation analysis program were also adapted to SBND from scripts used for the ICARUS collaboration, which were written by Gray Putnam. For the purposes of demonstrating the signal processing concepts used to generate plots I made for SBND in Chapter 6, all plots shown in Section 6.1 are similar results from MicroBooNE, with appropriate citations.

Additional contributions to the SBND collaboration from myself include undertaking multiple shifts for the detector, both in-person at Fermilab and remote from the UK, for eight hours a day, three or four days in a row. I have also attended and presented my own work at most SBND collaboration meetings, held twice a year, as well as presenting my SBND work at a national conference, summer school and coding workshop.

Chapters 8 and 9 contain work done on STEEL, established by Neil Spooner, at the University of Sheffield. Detector construction, software development and early commissioning work, the results of which are outlined in Section 8.1, was undertaken by Dominic Barker, Nicola McConkey, Andrew Scarff and Ed Tyley. All commissioning work presented in Section 8.2 was undertaken by myself, Vu Chi Lan Nguyen and Ala Zglam, under the guidance of Anthony Ezeribe, with all presented plots generated by myself.

The 22-day data run used for the analysis in Chapter 9 was overseen by Ala Zglam and Praveen Kumar, based on earlier data runs which I was present for. STEEL data analysis tools used in Chapter 9 were developed by myself, with the following exceptions where these master's students made contributions: Jordan Carroll wrote the base of the analysis code used to track LAr purity through scintillation triplet lifetime measurements from PhotoMultiplier Tube (PMT) data, which I adapted to STEEL data; Hannah Burn developed the PMT afterpulse subtraction methodology and pixel track reconstruction script; and Wenqi Yao advanced these track reconstruction algorithms by matching tracks detected by the pixels with tracks tagged by the CRTs and internal PMT. The latter two students were supervised by Rhiannon Smith-Jones, who also provided intellectual contributions to STEEL. I led the efforts in analysing STEEL data in Chapter 9, organising weekly meetings with Anthony and Rhiannon to discuss results and set goals, as well as guiding Hannah and Wenqi on further developing STEEL analysis tools alongside myself.

I declare that at no point in my PhD were generative AI or large language models used while undertaking physics research presented in this thesis, nor during the writing process.

This thesis does not exceed the permitted word count of 80,000 words excluding footnotes, bibliography and appendices. An estimate of the word count is 69,442 words.

Acknowledgements

This PhD has truly been the most difficult and challenging experience of my entire life thus far, and I've completed the Pantheon of Hallownest in Hollow Knight. However, unlike beating Absolute Radiance after a 42 boss gauntlet in a single player game, I most certainly could not have got to this point, at the end of my PhD journey, without the support of the following many (many) people.

Firstly, I'd like to thank Neil and Vitaly for providing me the opportunity to undertake this life changing half-decade of my life, and for your overall supervision and helpful thesis feedback, I hope you're both making the best of your well-earned retirement. I'd also like to send an absolutely colossal thank you to Rhiannon, for not only being a great friend and coworker on both SBND and STEEL, but for swooping in and becoming my supervisor at the write-up stage. I seriously don't think I would have been able to submit this thesis without you and I truly cannot thank you enough.

It was a rocky start to the PhD journey during the COVID-19 pandemic, where I took an immediate 9-month leave of absence to wait for it all to blow over (it did not, in fact, blow over). But I was at least able to go back to the Sheffield office, where I'm thankful for the support Lan, Ali, Ed, Andrew and Ala provided me through the first year of my PhD. I'm also hugely thankful to Anna, Alex, Henry, and (again) Rhiannon for all the help you provided me on SBND during our weekly LAr meetings, and for being great friends throughout my PhD journey, we really did run a smashing SBND collaboration meeting.

On the subject of Sheffield, I'd like to thank to my fellow STEEL collaborators for making such a small experiment feel like such a large part of my life. Anthony, your excellent leadership on STEEL has been incredible, and I look forward to seeing how the experiment will turn out in the future. I'd also like to thank Ala for not only helping with my STEEL data analysis, but for working with me in the lab where I got to do some actual real experimental physics work when I was extremely disillusioned with fake physics coding. I promise Rhiannon this will be my last thanks to you, but your support on STEEL was truly needed when our little experiment had so few people. And thank you to STEEL's

master's students Hannah and Wenqi, you both did essential work on the experiment, and I hope you'll be using your time on STEEL to aid you in your future endeavours.

A significant part of my PhD journey was spending an entire year in the US at Fermilab where I met, befriended and worked with countless people outside (and sometimes within) my usual northern English bubble. First and foremost I'd like to thank Rob, my Fermilab partner in crime, and the cause of many domestic disputes at 12 Potawatomi. I'll never forget our road trips, late night viewings of British comedies and early YouTube videos and, of course, our Wendy's Wursdays. This thanks also extends to Beth 1, Holly, Beth 2 and Rachel for being such great friends during me LTA, your presence throughout was truly epic, and I thank you all for taking care of Rob and buying him Oreos in my absence. I'd also like to take this opportunity to thank Niam, Magnus, Joe, Abbey, Lucy and Karolina for being our awesome time together during my brief month-long stint in Fermilab, I promise we will have a glorious Caniac combo at Raising Cane's again one day.

I couldn't possibly talk about Fermilab without mentioning the absolute blast I had working on the CRT A-team. Michelle, Chris, Amy, Rohan, Jiaoyang, Erin and (again) Henry, thank you all for being such a great little working group and for providing me some much-needed hardware work on SBND. Additionally, I'd like to thank Mike, Linyan, Avinay and Gray for helping me with the field response validation project, and to Prabhjot for taking over and finishing my work when my time ran out, I'm greatly looking forward to our results being published in the SBND calibration paper. I also have to send a huge thank you to Ornella, Dave, Joseph and Andrzej. Not only have you kept SBND running so efficiently, but your boundless accommodation and support of new collaborators made me feel right at home in Fermilab. Outside of work, I certainly could not have survived the harsh winters, scorching summers and bountiful tornado warnings of Chicago without my Fermifriends. Amy, Lauren, Erin, Rohan, Afro, Flavia, Rodrigo, and the countless people who came and went over the course of my LTA, thank you so much for the experiences, journeys, arguments and Taco Tuesdays. Those were the wildest 9 months of my entire life, and I'll truly cherish every moment of them forever.

Everyone mentioned thus far was paramount in supporting me within my PhD, but that was only half the battle, since equal and essential support came from my friends and family outside the PhD world. Brad, my cheeky little goblin man, after a long days work in the coding mines, there was nothing I looked forward to more than our daily movies, so thank much for providing me some prime kino in my darkest hours. Now I couldn't possibly name every single one of my friends who was there for me in the last 5 years, so I will, in alphabetical order: Alex, Andrew, Blov, Charlie, Dan, Dixon, Flo, Hayley, Jono,

Joonas, Matt, Marv, Niam, Sam and in particular Emma Marshall. Your support, gaming bools in the discord, late night chats and respective PhD rants were essential in keeping me sane and happy in those tumultuous times, and I'm truly grateful for you bogarting fellas.

I'm incredibly thankful to have the most supportive family I could have possibly asked for throughout my PhD journey. To my mother and father, I really cannot thank you both enough for your loving emotional (and when needed, financial) support over the last 5 years and beyond, I seriously could not have started and finished this PhD without your incredible parenting. And to my siblings Eloise and Alex, and by extension Hebrown, Daisy and the scrimblo creature Bonnie, thank you all so much for all the chill hangouts, movie viewings, gaming bools and motivational talks helping me emotionally handle the toll this PhD journey has done on me, you really are the most fun people to be around.

And finally, to my partner Ceri, there aren't any combination words in the English language that exist (or that I know of due to my limited diction) that can possibly express how thankful I am for your unending and integral support. All the walks we've done, films we've watched, games we played and talks we've had during some of my lowest points have got me to this point, writing the last few words of this thesis, which I truly couldn't have done without you. So thank you, for everything.

Abstract

Neutrino physics has advanced to the point where all neutrino oscillation parameters have been determined, with current generation neutrino experiments probing new discoveries in the field such as the sterile neutrino. This is a fourth neutrino flavour that only couples to gravity, and is theorised to be the cause of previously measured anomalies in neutrino oscillation physics. The Short-Baseline Neutrino program will perform high resolution ν_μ and ν_e oscillation measurements from the Booster Neutrino Beam (BNB), utilising ICARUS and the Short-Baseline Near Detector (SBND). SBND is a Liquid Argon Time Projection Chamber (LArTPC), placed 110 m from the BNB target, allowing for high precision neutrino-argon cross-section measurements. This thesis presents a methodology characterising the timing drift and resolution of cosmic-ray taggers before their installation around the SBND cryostat, allowing for full cosmic-ray background mitigation. Also featured is a procedure for validating the detector response modelling algorithms used in SBND software, comparing the expected response to average waveforms reconstructed from Monte Carlo event samples and SBND data. SBND is expected to exhibit ambiguities in event reconstruction due to using planes of sense wires to read out charge, motivating a pixelated charge readout for future LArTPC experiments, such as the DUNE near detector. The University of Sheffield provides an R&D experiment for this technology, named STEEL. Scintillation data from a 22-day data run of STEEL is used to calculate singlet, triplet and intermediate decay constants as $\tau_1 = (12.4 \pm 0.8)$ ns, $\tau_3 = (0.715 \pm 0.009)$ µs and $\tau_i = (69.6 \pm 4.5)$ ns respectively, with pixel data used to determine the electron lifetime to be $\tau_e = (0.491 \pm 0.006)$ µs. Measurements of τ_3 and τ_e leads to average oxygen impurity density calculations of $[O_2]_\gamma = (1.48 \pm 0.04)$ ppm and $[O_2]_e = (1.42 \pm 0.01)$ ppm respectively.

Contents

1 Introduction **1**

2 Neutrino History and Theory **4**
2.1 Neutrino History . . . 5
2.2 The Standard Model Neutrino . . . 6
2.3 Neutrino Oscillations . . . 7
2.3.1 Historical Evidence . . . 8
2.3.2 The Neutrino Mixing Matrix . . . 10
2.3.3 Oscillation Probability Calculations . . . 12
2.3.4 CP Violation . . . 14
2.3.5 Best Fit of Oscillation Parameters . . . 15
2.4 The Sterile Neutrino . . . 18

3 Liquid Argon Time Projection Chamber Overview **20**
3.1 Motivation for Liquid Argon as a Neutrino Detector . . . 21
3.2 Technical Design of a LArTPC . . . 22
3.3 History of LArTPC Experiments . . . 24
3.4 Charged Particle Interactions with Argon . . . 26
3.5 Ionisation Electron and Photon Propagation in LAr . . . 28

4 The Short-Baseline Near Detector **30**
4.1 SBND and the SBN Program . . . 30
4.2 The Booster Neutrino Beam . . . 34
4.3 SBND Experimental Overview . . . 36
4.3.1 TPC and Cryostat . . . 37
4.3.2 Photon Detection System . . . 38
4.3.3 Cosmic Ray Tagger Array . . . 39
4.3.4 Readout Electronics . . . 43
4.3.5 Trigger and Data Acquisition . . . 44
4.4 SBND Simulation and Reconstruction Software . . . 45
4.4.1 Monte Carlo Event Generation . . . 45
4.4.2 PDS Simulation and Reconstruction . . . 47
4.4.3 CRT Simulation and Reconstruction . . . 48
4.4.4 SBND Data Decoding . . . 49

5 Calibrating the Internal Clock Drift of CRTs at SBND **50**
5.1 SBND Front-End Board Design and Operation . . . 50
5.2 The CRT Data Acquisition System . . . 52
5.3 FEB Calibration on A-frame Test Stands . . . 54
5.3.1 Experimental Setup . . . 55
5.3.2 Calibration of Event Rate . . . 57
5.3.3 T_0/T_1 Clock Reset Event Calibration . . . 59
5.3.4 FEB Timing Characterisation . . . 64
5.4 Conclusions . . . 71

6 Field Response Validation Using Monte Carlo Event Samples **72**
6.1 Signal Waveforms on SBND TPC Readout Wires . . . 72
6.1.1 Signal Processing in the SBND Readout Electronics Chain . . . 73
6.1.2 Electronics Response Function Modelling . . . 76
6.1.3 Field Response Function Modelling . . . 79
6.2 Reconstructed Monte Carlo Waveforms . . . 84
6.2.1 Validation Methodology and Event Selection . . . 85
6.2.2 Monte Carlo Event Sample Production . . . 86
6.2.3 Average Monte Carlo Waveforms on SBND TPC Wires . . . 88
6.3 Response Function Modelling on SBND TPC Wires . . . 93
6.4 Field Response Validation Results with Monte Carlo Event Samples . . . 100
6.5 Conclusions . . . 105

7 Field Response Validation Using SBND Data **106**
7.1 Reconstructed SBND Data Waveforms . . . 106
7.1.1 Average Data Waveforms on SBND TPC Wires . . . 107
7.1.2 Comparison Between East and West TPCs . . . 110
7.1.3 Comparison With Different Wire Bias Voltages . . . 114
7.2 Field Response Validation Results with SBND Data . . . 118
7.3 SBND Data vs Monte Carlo Waveforms . . . 124
7.4 Conclusions . . . 132

8 LArTPC Test Stand Commissioning at the University of Sheffield **133**
8.1 STEEL: Sheffield TEst stand Experiment with Liquid argon . . . 134
8.1.1 LAr Containment Vessel . . . 134
8.1.2 LArTPC and Pixelated Readout Plane . . . 138
8.1.3 Subsystems and Supplementary Detectors . . . 140
8.1.4 Operations and Data-collecting . . . 142
8.2 Commissioning of STEEL Subsystems . . . 145
8.2.1 Subsystem Voltage Calibrations . . . 145
8.2.2 CRT and PMT Coincidence Signal Triggering . . . 146
8.2.3 LAr/LN Circulation Tests . . . 149
8.2.4 Pixel Signal Timing Calibrations . . . 150
8.3 Conclusions . . . 152

9 Measurements of Electronegative Impurity Density in LAr at STEEL 154
9.1 Purity Tracking Through ENI Density Calculations 154
9.1.1 ENI Density Calculations Using Triplet Lifetime 155
9.1.2 ENI Density Calculations Using Electron Lifetime 156
9.2 Results From Triplet Lifetime Measurements 158
9.3 Results From Electron Lifetime Measurements 164
9.4 Conclusions 169

10 Conclusions 170

A Two Flavour Oscillation Probability Derivation 189

B Full Monte Carlo vs SBND Data Waveforms 191

C STEEL Uncertainty Propagation 195

D STEEL Full Lifetime and ENI Density Plots 196

Figures

2.1 Feynman diagrams showing the only two primary interaction vertices for neutrinos coupling via the weak interaction, where $l = e, \mu, \tau$. The left vertex shows a Charged Current (CC) interaction where a charged lepton turns into its corresponding neutrino by the emission/absorption of a $W^{\pm}$ boson. The right vertex shows a Neutral Current (NC) interaction where a neutrino scatters by emission/absorption of a Z^0 boson. 7

2.2 Number of observed electron-like (left) and muon-like (right) neutrinos in the multi-GeV energy range with respect to the cosine of the zenith angle, Θ, where cos(Θ) =-1 corresponds to upwards travelling and cos(Θ) = 1 to downward-travelling neutrinos. The shaded boxes indicate the Monte Carlo predictions with statistical errors for zero neutrino oscillations. Dotted lines show the Monte Carlo predictions for $\nu_\mu \rightarrow \nu_\tau$ oscillations assuming $\sin^2(2\theta) = 1$ and $|\Delta m^2_{13}| = 2.2 \times 10^{-3}$ eV^2. Graph sourced from [28]. 9

2.3 Neutrino mass eigenstate ordering: normal hierarchy (left) and inverted hierarchy (right). The atmospheric mass difference is defined as $\Delta m^2 \equiv \Delta m^2_{31}$ (NH) = Δm^2_{23}(IH) and the solar mass difference $\delta m^2 \equiv \Delta m^2_{21}$. Diagram sourced from [52]. 16

3.1 Experimental setup of a typical LArTPC. The U, V and Y sense wires represent the anode plane assemblies, where U and V are induction planes aligned $\pm 60°$ with respect to the vertical Y collection plane. Diagram adapted from [84]. 23

3.2 Schematic (left) and photo (right) of the two induction (U and V) and collection (Y) plane wires in a typical LArTPC APA. These depict the three wire planes for SBND, with 3 mm pitch and the induction plane wires angled $\pm 60°$ with respect to the vertical collection plane wires. Images sourced from [91]. 24

3.3 Diagram of the ICARUS T600 LArTPC (left) and annotated picture of the same LArTPC outlining its properties and components (right). Diagrams sourced from [96]. 24

3.4 Schematic (left) and cross-section (right) of the MicroBooNE LArTPC within its cylindrical cryostat. The beam is directed out of the page. Diagrams sourced from [98]. 25

4.1 The Short-Baseline Neutrino program at Fermilab, showing the three LArTPC experiments situated on the Booster Neutrino Beamline: SBND, the MicroBooNE detector and the ICARUS T600 detector. Image credit: Holabird and Root [84]. 31
4.2 Sensitivity to which the SBN program will determine Δm^2_{41} for ν_e appearance (left) and ν_μ disappearance (right). Allowed and excluded regions combines low energy $\nu_e/\bar{\nu}_e$ excess data from LSND [60], KARMEN [70] and MiniBooNE [63], with external contours calculate from SciBooNE/MiniBooNE [125], MINOS/MINOS+ [73] and IceCube [126]. Graphs sourced from [99] using global fit analyses provided by [76]. 33
4.3 Expected SBND CC ν_μ (left) and ν_e (right) event rates for an exposure of 10^{21} POT from the BNB from a continuous three-year data run. Graphs sourced from [99]. 34
4.4 Schematics of the experimental setup and operations of the BNB at Fermilab, USA. The left diagram shows an aerial view of the 8 GeV kinetic energy protons injected from the Booster accelerator into the target hall via the Main Injector; the right picture depicts a side-on view of the target hall and the decay pipe, showing how the magnetically focused hadrons resulting from the proton interactions with the beryllium target decay to result in a predominantly ν_μ beam, with few $\bar{\nu}_\mu$ and trace $\nu_e + \bar{\nu}_e$. Image sourced from [114]. 35
4.5 Simulated ν_μ beam flux from the BNB detected by SBND for off axis angles in increments of 0.2° from 0° to 1.6°. Left plot shows ν_μ flux with respect to neutrino energy, whereas the right plot shows the peak ν_μ CC interaction event rate with respect to the beam intersection with the east TPC of SBND. Plots sourced from [99]. 36
4.6 Schematic of the SBND cryostat with the TPC being lifted out by the top cap (left; image sourced from [84]). Drawing of the SBND TPC, the west, south and top-low CRT planes and the PDS array (right; image sourced from [139]). The north, east, bottom and top-high CRT walls, the cryostat and part of the north-side of the vertical drift cage have been removed for visual clarity. 37
4.7 Schematics of a PDS box (left) containing PhotoMultiplier Tubes (PMTs) and X-ARAPUCAs, and the full SBND PDS shown around the LArTPC (right). Both diagrams sourced from [139]. 39
4.8 Schematic showing the orientation of the seven CRT planes (grey) around the SBND cryostat (red), viewed from the north-west side of the cryostat. Image produced using the SBND GDML [146]. 40
4.9 Schematic showing the three sizes of CRT modules SBND utilises. The grey rectangles attached to each module are front-end boards which process, amplify and shape SiPM data into waveforms. 41

4.10 Scintillator strips (left) in a CRT module (middle) and four modules aligned orthogonally (right) to constrain x and y coordinates of cosmic-ray muon tracks. FEBs transfer information between modules through timing, logic and data cables. 42
4.11 Position of cold electronics readout boards around a pair of APAs [91] 43
4.12 Measured SER for PMTs (left; logarithmic scale) and X-ARAPUCAs (right; linear scale) in SBND. Simulated signal fluctuations of 22% for PMTs and 10% for X-ARAPUCA signals are also shown by grey shading. Image sourced from [139]. 48

5.1 Picture of a single FEB when plugged into a CRT panel with no input cables (left) and multiple FEBs daisy-chained together with labelled cables (right). 51
5.2 Picture (left) and schematic (right) of the CRT A-frame test stand. The numbers indicate the FEB number and the red and blue lines indicate the two separate T_{in}/T_{out} cable loops between the modules. 55
5.3 Three A-frame test stand setups used to commission the 18 north wall CRTs before their installation around the SBND cryostat. The four vertical modules, placed on A-frame 1 in the picture, would move to the A-frame that is being used to collect data. 56
5.4 Number of hits broken down by their flag type for an A-frame 0 data run. The right plot excludes flag 3 (data) events due to their high frequency compared to flag 7 (T_0 reset) and 11 (T_1 reset) events. The T_1 reset window was set to 4.72786501 Hz. 57
5.5 Number of flag 3 hits for each CRT on A-frames 0 (top left), 1 (top right) and 2 (bottom). Each DAQ run lasted for several hours and ran in 4-fold coincidence mode. For the A-frame 1 run, the event-rate for FEB 73 corresponds to the CRT module attributed to FEB 154, as FEB 154 needed to be swapped out for FEB 73 due to a malfunction. 58
5.6 Number of flag 3 hits on each SiPM channel, labelled 0–31, for a single CRT module. FEBs 72 (top left) and 75 (bottom left) are half-width vertical modules, and FEBs 157 (top right) and 134 (bottom right) are full size horizontal modules. 60
5.7 Number of flag 7 events (left) and flag 11 events (right) for each FEB connected to CRTs on A-frames 0 (top), 1 (middle) and 2 (bottom). 61
5.8 Flag 11 (left) and 7 (right) FEB occupancy plots for A-frames 0 (top), 1 (middle) and 2 (bottom). Shows the number of FEBs that have flag 11/7 TS0/TS1 values that deviate from the total average TS0/TS1 value by 20 ns. 63
5.9 TS0 (left) and TS1 (right) value frequency for flag 3 events collected from A-frames 0 (top), 1 (middle) and 2 (bottom). TS0 ranges from 0 to 1 second with 20 ms bin widths. The upper bound of TS1 values are 0.211512274 s for A-frame 0 and 0.909090909 s for A-frames 1 and 2 - equating to the inverse of their T_1 clock reset frequencies of 4.72785801 Hz and 1.1 Hz - with bin widths of around 4.23 ms and 18.2 ms respectively. 65

5.10 TS0 timestamp frequency of flag 7 events, subtracting the T_0 reset window of 1 s, for FEB 75 on A-frame 0 (top left), FEB 157 on A-frame 1 (top right) and FEB 71 on A-frame 2 (bottom). 66
5.11 TS1 value frequency of flag 11 events for FEB 75 on A-frame 0 (top left), FEB 157 on A-frame 1 (top right) and FEB 71 on A-frame 2. The T_1 reset window of 0.211512274 s for A-frame 0 and 0.909090909 s for A-frames 1 and 2 is subtracted. 67
5.12 Means (top) and standard deviations (bottom) of the flag 7 TS0 plots in figure 5.10 for each FEB on A-frames 1 (lighter blue) and 2 (darker blue). . . 69
5.13 Means (top) and standard deviations (bottom) of the flag 11 TS1 plots in figure 5.11 for each FEB on A-frames 1 (lighter blue) and 2 (darker blue). . . 70

6.1 Simulated signal waveform induced on the two induction planes and collection plane wires (labelled U, V and Y respectively) from an ideal MIP track using a 2D simulation of the MicroBooNE TPC. A 2D Garfield simulation was used to model the field response contribution to the waveform [154]. The electronics response takes the form of a parametric equation with a gain setting of 14 mV/fC and a 2 µs peaking time [162]. 74
6.2 MicroBooNE-simulated TPC signals for a MIP track travelling perpendicular to first induction plane (top left), second induction plane (top right) and collection plane (bottom) wires. Summing contributions from the central (0) wire with the highest signal amplitude, two and ten wires adjacent to the central wire. The MIP signal is convolved with the field response, simulated through Garfield [154], and the electronics response, taking the form of a parametric equation with a gain setting of 14 mV/fC a 2 µs peaking time [161]. 77
6.3 MicroBooNE pre-amplifier electronics response functions for a gain setting of 4.7 mV/fC and peaking times of 0.5 µs, 1.0 µs, 2.0 µs and 3.0 µs [161]. . . 79
6.4 Ionisation electron drift paths in the MicroBooNE TPC subject to a 273 V/cm electric field. The first induction, second induction and collection plane wires are voltage-biased at -110 V, 0 V and 230 V and are projected +60°, -60° and 0° with respect to the normal of the page respectively. The x-axis is in the electric field direction and the z-axis is in the beam direction [161]. Electron paths are calculated in 0.3 mm segments using the 2D Garfield software [154]. 81
6.5 Weighting potential field values for a single wire in the first induction (top left), second induction (top right) and collection (bottom) wire planes for the MicroBooNE TPC, with an electric field strength of 273 V/cm. The x-axis is in the electric field direction and the z-axis is in the beam direction. Weighting potential is dimensionless and is relative to the electric potential on the target wire, indicated as percentages on equipotential lines [161]. Weighting potential values are calculated using the 2D Garfield software [154]. 82

6.6 Total current induced over time from various paths of a single drifting ionisation electron for the closest wire on the first induction (U), second induction (V) and collection (Y) planes, each biased at -110 V, 0 V and 230 V respectively. Responses are also calculated for 1.5 mm boundaries between adjacent wires [161]. 83
6.7 MicroBooNE total wire response function on the closest wire to a single ionisation electron for the first induction, second induction and collection planes (labelled U, V and Y respectively). Calculated by convolving the field response, averaged over all electron drift paths and computed by Garfield [154], with the electronics response function from equation 6.7 using a gain of 14 mV/fC and a peaking time of 2 µs [161]. 84
6.8 Event display with ten MC cosmic-ray muons tracks within the SBND cryostat. The x (drift), y (vertical) and z (beam) directions are pointed down, towards the reader and to the right of the plot respectively, giving a top-down view of SBND with the east TPC on the top and west TPC on the bottom. The colour axis on the right shows the range of energies of each track element in ADCs. 87
6.9 Reconstructed MC waveforms on SBND TPC readout wires for the first induction (top left), second induction (top right) and the collection (bottom) planes, averaged over 200,000 simulated anode-cathode crossing muon tracks within an angle range of $20° \leq \theta_{xz} \leq 80°$. Track segments 2–5 cm from the APA were selected, exceeding amplitudes of 6 ADC and including contributions of ±5 wires adjacent to the central wire. 90
6.10 Total reconstructed MC waveforms on SBND TPC readout wires for the first induction plane (top left), second induction plane (top right) and the collection plane (bottom), broken down by $\Delta\theta_{xz} = 10°$ segments in the range $20° \leq \theta_{xz} \leq 80°$. Waveform plotting and selection criteria are the same as in Figure 6.9. 91
6.11 Total reconstructed MC waveforms on SBND TPC readout wires for the first induction plane (top left), second induction plane (top right) and the collection plane (bottom), broken down by $\Delta\theta_{xz} = 10°$ segments in the range $20° \leq \theta_{xz} \leq 80°$, with a narrower time axis range than Figure 6.10 of -25 µs $\leq t \leq$ 25 µs. 92
6.12 Induced current over time on SBND TPC readout wires for the first induction (top left), second induction (top right) and collection (bottom) wire planes. Currents are averaged over all electron paths, pitch angles and all wires in each wire plane. Field response functions are modelled using a 2D Garfield simulation [154]. 94
6.13 Induced current over time on SBND TPC readout wires with respect to electron path for the first induction (top left), second induction (top right) and collection (bottom) wire planes. Electron path deviation is measured in the transverse direction, parallel to the APA, at 0.3 mm segments, spanning -1.5 mm to 1.5 mm about the closest wire. Field response functions are modelled using a 2D Garfield simulation [154]. 95

6.14 Induced current on first induction (right), second induction (middle) and collection (left) plane wires for $\theta_{xz} = 24°$–$26°$ (top), $44°$–$46°$ (middle), $64°$–$66°$ (bottom). Currents are averaged over 0.3 mm path segments from -1.5 mm to 1.5 mm about the central wire. Field response functions are modelled using a 2D Garfield simulation [154]. 96
6.15 Electronics response function plotted from equation 6.7 using the parameters in equation 6.8, with a gain of 14 mV/fC and peaking time of 2.2 µs. 97
6.16 Convolved field and electronics response functions for the first induction (top left), second induction (top right) and collection (bottom) planes. Field response functions are modelled using Garfield [154] and electronics response from equation 6.7 using the parameters in equation 6.8, a gain of 14 mV/fC and a peaking time of 2.2 µs. 98
6.17 Convolved field and electronics response functions for the first induction (right), second induction (middle) and collection (left) planes, averaged over $\theta_{xz} = 20°$–$40°$ (top), $40°$–$60°$ (middle), $60°$–$80°$ (bottom). Field response functions are modelled using Garfield [154] and the electronics response is modelled from equation 6.7 using the parameters in equation 6.8 with a gain of 14 mV/fC and peaking time of 2.2 µs. 99
6.18 Comparisons of the average reconstructed MC waveform (calibrated response), the convolved field and electronics response functions (toy response) and the toy response convolved with a Gaussian (toy response $\circledast$ $\mathcal{G}$) on the first induction wire plane of the SBND APAs. Six $\delta\theta_{xz} = 2°$ segments of the track pitch angle were chosen between $26°$ and $80°$. Error bars on the calibrated response are calculated based on the standard error in the statistics of chosen tracks for that angle segment. 101
6.19 Comparisons of the average reconstructed MC waveform (calibrated response), the convolved field and electronics response functions (toy response) and toy response convolved with a Gaussian (toy response $\circledast$ $\mathcal{G}$) for the second induction wire plane of the SBND APAs. Six $\delta\theta_{xz} = 2°$ segments were chosen between $26°$ and $80°$. Error bars on the calibrated response are calculated based on the standard error in the statistics of chosen tracks for that angle segment. 103
6.20 Comparisons of the average reconstructed MC waveform (calibrated response), the convolved field and electronics response functions (toy response) and the toy response convolved with a Gaussian (toy response $\circledast$ $\mathcal{G}$) on the collection wire plane of the SBND APAs. Six $\delta\theta_{xz} = 2°$ segments of the track pitch angle were chosen between $30°$ and $80°$. Error bars on the calibrated response are calculated based on the standard error in the statistics of chosen tracks for that angle segment. 104

7.1 Average reconstructed waveforms on SBND TPC readout wires for the first induction (top left), second induction (top right) and the collection (bottom) planes using anode-cathode crossing cosmic-ray muon data. 108

7.2 Average reconstructed waveform on SBND TPC readout wires for the first induction (top left), second induction (top right) and collection (bottom) planes using anode-cathode crossing cosmic-ray muon data. Waveforms are averaged in track pitch angle segments of $\Delta\theta_{xz} = 10^\circ$ in the range $20^\circ < \theta_{xz} < 80^\circ$. 109
7.3 Average reconstructed waveforms on SBND TPC readout wires for the first induction (top left), second induction (top right) and the collection (bottom) planes using anode-cathode crossing cosmic-ray muon data from SBND, broken down based on which TPC the track spends the most time in. 112
7.4 Average reconstructed waveform on SBND TPC readout wires for the first induction (top left), second induction (top right) and the collection (bottom) planes using anode-cathode crossing cosmic-ray muon MC event samples produced by the SBND simulation, broken down based on which TPC the track spends the most time in. 113
7.5 Average reconstructed waveform on SBND TPC readout wires for the first induction (top left), second induction (top right) and collection (bottom) planes using anode-cathode crossing cosmic-ray muon data. Wire bias voltage for first induction plane wires was altered from the nominal value of -210 V, to -220 V and -180 V. 116
7.6 Average reconstructed waveform on SBND TPC readout wires for the first induction (top left), second induction (top right) and collection (bottom) planes using anode-cathode crossing cosmic-ray muon data. Wire bias voltage for collection plane wires was altered from the nominal value of 420 V to 460 V. 117
7.7 Comparisons of the average reconstructed waveform from first induction plane wires using a two-hour SBND data run (calibrated response), the convolved field and electronics response (toy response) and toy response convolved with a Gaussian (toy response $\circledast\ \mathcal{G}$) for six chosen $\delta\theta_{xz} = 2^\circ$ segments between 26° and 80°. Error bars on the calibrated response are calculated based on the standard error in the statistics of tracks. 120
7.8 Comparisons of the average reconstructed waveform on second induction plane wires using a two-hour SBND data run (calibrated response), the convolved field and electronics response (toy response) and toy response convolved with a Gaussian (toy response $\circledast\ \mathcal{G}$) for six chosen $\Delta\theta_{xz} = 2^\circ$ segments between 26° and 80°. Error bars on the calibrated response are calculated based on the standard error in the statistics of tracks. 121
7.9 Comparisons of the average reconstructed waveform on collection plane wires using a two-hour SBND data run (calibrated response), the convolved field and electronics response (toy response) and toy response convolved with a Gaussian (toy response $\circledast\ \mathcal{G}$) for six chosen $\Delta\theta_{xz} = 2^\circ$ segments between 26° and 80°. Error bars on the calibrated response are calculated based on the standard error in the statistics of tracks. 123

7.10 Average reconstructed waveforms on SBND TPC readout wires for the first induction (top left), second induction (top right) and the collection (bottom) planes using anode-cathode crossing cosmic-ray muons from MC event samples and SBND data. . . . 124
7.11 Average reconstructed waveforms on SBND TPC readout wires for the first induction (top left), second induction (top right) and the collection (bottom) planes using anode-cathode crossing cosmic-ray muons from MC event samples and SBND data, with a narrowed time axis of -25 μs $< t <$ 25 μs. . 126
7.12 Average reconstructed waveforms on SBND TPC first induction plane wires for anode-cathode crossing cosmic-ray muons from MC event samples and SBND data. Plots are broken down with respect to track pitch angle θ_{xz} in segments of $\Delta\theta_{xz} = 10°$ from 20° to 80°. Full ±100 μs plots are presented in Figure B.1 in Appendix B. . . . 128
7.13 Average reconstructed waveforms on SBND TPC second induction plane wires for anode-cathode crossing cosmic-ray muons from MC event samples and SBND data. Plots are broken down with respect to track pitch angle θ_{xz} in segments of $\Delta\theta_{xz} = 10°$ from 20° to 80°. Full ±100 μs are presented in Figure B.2 in Appendix B. . . . 129
7.14 Average reconstructed waveforms on SBND TPC collection plane wires for anode-cathode crossing cosmic-ray muons from MC event samples and SBND data. Plots are broken down with respect to track pitch angle θ_{xz} in segments of $\Delta\theta_{xz} = 10°$ from 20° to 80°. Full ±100 μs plots are presented in Figure B.3 in Appendix B. . . . 131

8.1 Picture of the STEEL experiment. . . . 135
8.2 Picture of the STEEL dewar containing the LArTPC, indicated by the black drawing on the face of the dewar. It is a stainless steel cylinder 60 cm in height and 24 cm in diameter capable of containing 27.6 L of argon. . . . 136
8.3 Schematic outlining the components and subsystems of STEEL, including the dewar, LArTPC, CRTs and purification/circulation system (sourced from [172]). . . . 137
8.4 STEEL LArTPC with labelled components. . . . 138
8.5 STEEL pixelated anode readout plane (pictured left), designed by the University of Bern [168], alongside its relative position in the STEEL LArTPC (pictured right). . . . 139
8.6 Schematic showing the relative position of the two side CRTs, top and bottom CRTs around the STEEL dewar with respect to the cold PMT and internal LArTPC. . . . 141
8.7 STEEL server rack showing the CAEN V1740 pixel DAQ processor, CAEN N417 logic discriminator unit and CAEN V6521 voltage supply units. . . . 143
8.8 Live tracking of thermal parameters such as LAr/LN temperatures and pressures, as well as the argon liquid level on a NI PXI-6229 slow DAQ live monitor system. Pictured displaying relevant parameters for a dewar filled with air. . . . 144

8.9 Time difference between side CRT hits from 1,000 cosmic-ray muon events with the STEEL dewar filled with room temperature GAr. 147
8.10 Two cosmic-ray muon events with one triggered in coincidence with the side CRTs and cold PMT (left) and the other triggering the top and bottom CRTs with the cold PMT (right). The logic trigger signal has a readout window set to 120 ns. 147
8.11 Frequency of PMT signal amplitude values fewer than or equal to -3 ADC, which contains 155 out of the 9,000 events in the dataset triggering only on the side CRTs. 148
8.12 Difference between pixel and Keysight DAQ event timestamps for the same muon track. Bin widths are 10 µs with 33,120 overlapping events. 151
8.13 Difference between pixel and Keysight DAQ events timestamps for the same cold PMT triggered muon track. Bin widths are 10 µs with 8,339 overlapping events. 152

9.1 Average cold PMT waveform aligning 200 scintillation pulses by their peak timestamp and averaging their ADC value bin by bin. Plots show the full 20 µs readout window (left) and a narrower time axis about the average scintillation pulse (right). 159
9.2 Average cold PMT waveform from Figure 9.1 inverted with a log scale. . . . 159
9.3 Inverted cold PMT waveform averaged over 200 events aligned by their signal peak, suppressing effects from PMT afterpulsing and with a log scale on the y-axis. The two and three component probability density functions in equations 9.2 and 9.3 respectively are fitted to the exponential decay to the right of the signal peak. 160
9.4 Daily average measured triplet lifetime τ_3' as a function of time since the start of the 22-day data run of STEEL. τ_3' was measured from fitting the two and three component exponential functions in equations 9.2 and 9.3 to averaged scintillation pulses from ∼200 events. The full unaveraged graph is in Figure D.1 in Appendix D. 162
9.5 Daily average oxygen impurity density ($[O_2]$) as a function of time since the start of the 22-day data run of STEEL. $[O_2]$ was calculated from equation 9.6 using $k_O = (0.86 \pm 0.03)$ ppm^{-1} [191] and $\tau_3 = (1.6 \pm 0.1)$ µs [159]. Uncertainty propagations are detailed in Appendix C. The full unaveraged graph is in Figure D.2 in Appendix D. 163
9.6 Pixel and ROI waveforms corresponding to the same ionisation electron signal on pixel 12 in ROI 14. Hits were matched by lining up the waveforms in time and finding the pixel waveform with the lowest χ^2 value compared to the ROI waveform. 165
9.7 Ratio of the measured charge over the expected charge $\Delta Q/\Delta Q_{\text{exp}}$ collected by all pixels of a single reconstructed muon track for 100 pixel events, plotted against track length l. An exponential decay is fitted with the decay constant equal to $1/(\tau_e v_e)$. 167

9.8 Daily average electron lifetime τ_e values as a function of time since the start of the 22-day data run of STEEL. τ_e was calculated from finding the exponential decay constant of the measured to expected charge ratio against track length from ∼100 pixel events each. The full unaveraged graph is in Figure D.3 in Appendix D. 168
9.9 Daily average oxygen impurity density $[O_2]_e$ as a function of time since the start of the 22-day data run of STEEL. $[O_2]$ was calculated from equation 9.14 using $k_e = 1.9$ ppm^{-1}μs^{-1} [192]. The full unaveraged graph is in Figure D.4 in Appendix D. 168

B.1 Average reconstructed waveforms on SBND TPC first induction plane wires for simulated MC cosmic-ray muon event samples and a two-hour run of SBND collecting cosmic-ray muon data. Plots are broken down with respect to track pitch angle θ_{xz} in segments of $\Delta\theta_{xz} = 10°$ from 20° to 80°. 192
B.2 Average reconstructed waveforms on SBND TPC second induction plane wires for simulated MC cosmic-ray muon event samples and a two-hour run of SBND collecting cosmic-ray muon data. Plots are broken down with respect to track pitch angle θ_{xz} in segments of $\Delta\theta_{xz} = 10°$ from 20° to 80°. . 193
B.3 Average reconstructed waveforms on SBND TPC second induction plane wires for simulated MC cosmic-ray muon event samples and a two-hour run of SBND collecting cosmic-ray muon data. Plots are broken down with respect to track pitch angle θ_{xz} in segments of $\Delta\theta_{xz} = 10°$ from 30° to 80°. . 194

D.1 Measured triplet lifetime τ_3 as a function of time since the start of the first day of the 22-day data run of STEEL for 243 Keysight DAQ data files. τ_3 was measured from fitting the two and three component exponential decay models in equations 9.2 and 9.3 to averaged scintillation pulses from ∼200 events. 196
D.2 Calculated Oxygen impurity density $[O_2]$ in LAr as a function of time since the start of the first day of the 22-day data run of STEEL for 243 Keysight DAQ data files. $[O_2]$ was calculated from equation 9.6 using a quenching rate of $k_O = (0.86 \pm 0.03)$ ppm^{-1} [191] and a maximum triplet lifetime value for zero ENI presence of $\tau_3 = (1.6 \pm 0.1)$ μs [159]. Uncertainty propagation calculations are detailed in Appendix C. 197
D.3 Measured electron lifetime τ_e as a function of time t since the start of the first day of the 22-day data run of STEEL for 808 pixel data files. τ_e was calculated from finding the exponential decay constant of the measured to expected charge ratio against track length from ∼100 pixel events. Data points with poor exponential fits or with greater measured charge than expected charge were discarded. 197
D.4 Calculated oxygen impurity density $[O_2]$ in LAr as a function of time since the start of the first day of the 22-day data run of STEEL for 808 pixel data files. $[O_2]$ was calculated from equation 9.14 using $k_e = 1.9$ ppm^{-1}μs^{-1} [192]. 198

Tables

2.1 Global Best Fit (BF) of neutrino oscillation parameters, including long-baseline data from T2K and NOvA; reactor data from Daya Bay, RENO and Double Chooz; atmospheric data from IceCube, DeepCore, ANTARES and Super-Kamiokande (SK), as well as additional solar data from SK. Inverted Hierarchy (IH) ranges refer to the local minimum, as opposed to Normal Hierarchy (NH). Global fit values taken from [54–57]. 17

3.1 Comparison of particle detecting properties of liquid noble elements. 21

4.1 Overview of each SBN program detector's distance downstream of the BNB target, total and active liquid argon mass [114]. 32
4.2 Predicted number of events detected by SBND based on interaction type and neutrino flavour, for 112 tons of active LAr mass and an exposure of 6.6×10^{20} POT [114]. 33

5.1 Possible flags assigned to each event outputted by the FEBs based on the presence and/or reset of the T_0/T_1 clocks, with the important flags highlighted in bold. 54

7.1 Number of waveforms selected by the average waveform analysis code applied to the two-hour data run. Waveforms are broken down based on wire plane and which TPC the track associated with the waveform spent the most time traversing, with percentages indicating the track selection yield of that given TPC. 111
7.2 Number of waveforms selected by the average waveform analysis code applied to the 200,000 cosmic-ray muon Monte Carlo (MC) event sample. Waveforms are broken down based on wire plane and which TPC the track associated with the waveform spent the most time traversing, with percentages indicating the track selection yield of that given TPC. 111
7.3 Number of waveforms selected by the average waveform analysis code applied to the SBND data runs altering the plane 0 wire bias voltage from the nominal of -210 V to -220 V and -180 V; and plane 2 from nominally 420 V to 460 V. 115

9.1 Total average excimer decay lifetime values τ_1, τ_3 and τ_i, oxygen impurity density [O_2] and χ^2/DOF values for the two and three component exponentials in equations 9.2 and 9.3 fitted to 243 scintillation data files containing ∼200 events each throughout the 22-day data run of STEEL. Uncertainties on the average χ^2/DOF values are the standard error of the statistical average of individual χ^2/DOF values. 163

Acronyms and Abbreviations

ADC Analogue-to-Digital Conversion

APA Anode Plane Assembly

ArgoNeuT Argon Neutrino Teststand

ASIC Application-Specific Integrated Circuit

BES Beam Extraction Signal

BNB Booster Neutrino Beam

BNL Brookhaven National Laboratory

CC Charged Current

CL Confidence Level

CPA Cathode Plane Assembly

CRT Cosmic-Ray Tagger

DAC Digital-to-Analogue Converter

DAQ Data AcQuisition

DOF Degrees Of Freedom

DP Dual-Phase

DUNE Deep Underground Neutrino Experiment

EM ElectroMagnetic

ENI ElectroNegative Impurities

FD Far Detector

FEB Front-End Board

FEMB Front-End Mother Boards

FFT Forward Fourier Transform

FPGA Field-Programmable Gate Array

GAr Gaseous Argon

GDML Geometry Description Markup Language

HK Hyper-Kamiokande

HLTs High Level Triggers

HV High Voltage

ICARUS Imaging Cosmics And Rare Underground Signals

IH Inverted Hierarchy

IMB Irvine-Michigan-Brookhaven

JSNS^2 J-PARC Sterile Neutrino Search

K2K KEK To Kamioka

LAr Liquid Argon

LArIAT Liquid Argon In A Testbeam

LArTPC Liquid Argon Time Projection Chamber

LEMs Large Electron Multipliers

LEP Large Electron-Positron collider

LHEP Laboratory for High Energy Physics

LLTs Low Level Triggers

LN Liquid Nitrogen

LSND Liquid Scintillator Neutrino Detector

MC Monte Carlo

MicroBooNE Micro Booster Neutrino Experiment

MiniBooNE Mini Booster Neutrino Experiment

MINOS Main Injector Neutrino Oscillation Search

MIP Minimum Ionising Particle

MSW Mikheyev–Smirnov–Wolfenstein

NC Neutral Current

ND Near Detector

NH Normal Hierarchy

NI National Instruments

NL NonLinearity

NTB Nevis Trigger Board

NuMI Neutrinos at the Main Injector

PCB Printed Circuit Board

PDG Particle Data Group

PDS Photon Detection System

PE PolyEthylene

PMT PhotoMultiplier Tube

POT Protons On Target

ppm part per million

PPS Pulse Per Second

ppt parts per trillion

PSI Pounds per Square Inch

PTB Penn Trigger Board

PTP ParaTerPhenyl

RMS Root Mean Square

ROI Region Of Interest

RTD Resistive Temperature Detector

SBN Short-Baseline Neutrino

SBND Short-Baseline Near Detector

SCE Space Charge Effects

SER Single Electron Response

SiPM Silicon PhotoMultipler

SK Super-Kamiokande

SLC SLAC Linear Collider

SLD SLAC Large Detector

SM Standard Model

SNO Sudbury Neutrino Observatory

SP Single-Phase

SPEC Simple PCIe Express FMC Carrier

STEEL Sheffield TEst stand Experiment with Liquid argon

T2K Tokai To Kamioka

TDC Time to Digit Converter

TPB TetraPhenyl Butadiene

TPC Time Projection Chamber

UV Ulta Violet

VCXO Voltage-Controlled Crystal Oscillator

VUV Vacuum Ulta Violet

WIB Warm Interface Boards

WR White Rabbit

Chapter 1

Introduction

Since its inception in the early 20th century, neutrino physics has been at the forefront of particle physics research, with every decade since then marking several discoveries and advancements in the field, utilising the most sophisticated experiments to detect and study the elusive particle. Chapter 2 outlines the history of neutrino physics, from its detection and integration into the Standard Model (SM), up to the discovery of neutrino oscillations; the most significant observation of physics beyond the SM. Also outlined is the theory behind neutrino oscillations, and how studying this phenomenon can probe CP violation measurements, related to whether disparities in neutrino oscillation probabilities between matter and antimatter are large enough to explain why the universe is matter-dominated.

Chapter 2 also outlines the history and theory behind the sterile neutrino, an additional neutrino flavour which only interacts with the force of gravity, making it impossible to detect with modern technology. Discovery of the sterile neutrino will elucidate previously measured anomalies in neutrino oscillation physics, and is the primary goal of the Short-Baseline Neutrino (SBN) program. Utilising the Imaging Cosmics And Rare Underground Signals (ICARUS) T600 detector and the Short-Baseline Near Detector (SBND), the SBN program measures ν_μ and ν_e oscillations from one of the highest intensity neutrino beams, the Booster Neutrino Beam (BNB), to perform the highest precision sterile neutrino searches yet. One of the focal experiments of this thesis is SBND, which utilises Liquid Argon Time Projection Chamber (LArTPC) technology to detect neutrinos. Chapter 3 contains the history and experimental applications of LArTPCs, alongside descriptions of how neutrinos are detected through propagation and collection of ionisation electrons and scintillation photons.

Chapter 4 states the primary goals of SBND and provides a brief description of the BNB, followed by an overview of the experimental setup of SBND and its various subsystems, such as the Photon Detection System (PDS) and Cosmic-Ray Tagger (CRT) array, its

sophisticated readout electronics chain and Data AcQuisition (DAQ) system. Additionally, the physics analysis software framework, from the generation of MC event samples using the SBND simulation to the algorithms used to decode and reconstruct data from the PDS, CRT and Time Projection Chamber (TPC), is described in this chapter.

Work done on calibrating the timing drift and resolution of CRTs before their installation on the north wall of SBND is presented in Chapter 5. This involved utilising a temporary setup of CRTs collecting cosmic-ray muon data in-situ on their A-shaped packaging apparatus, called the A-frames. This is to ensure that cosmic-rays are detected by the CRT array to the same timing resolution as neutrino interactions read out by the TPC, with $\mathcal{O}(2$ ns) precision, to fully mitigate cosmic-ray backgrounds in SBND.

Reconstructing neutrino interactions with argon and identifying initial neutrino flavour involves extracting TPC waveforms modelled from ionisation electrons inducing signals on anode readout wires. These waveforms are shaped and smeared by current inductions from the electric field of electrons and the signal amplification process, called the field and electronics responses respectively. In order to deconvolve the ionisation charge signal from these detector responses, accurate models of the field and electronics responses must be fully understood and integrated into SBND software. This is achieved through comparisons of the expected detector response to average waveforms reconstructed from readout wires using MC event samples generated by the SBND simulation, presented in Chapter 6, and from early SBND TPC data, presented in Chapter 7.

Also shown in Chapter 7 are studies on the variations in TPC waveform shape using early SBND data runs selecting tracks from either the east or west half of the LArTPC and altering the voltage bias applied to readout wires. Additionally, the first MC versus data comparisons of average reconstructed TPC waveforms on each wire plane, broken down by track pitch angle, using early SBND data runs, are presented in this chapter.

Most modern neutrino experiments utilising LArTPC technology use three planes of sense wires to read out ionisation charges. This mechanism has been shown to exhibit ambiguities in event reconstruction and ionisation charge pile-up near the anode for detectors with high event-rates, such as SBND. This motivates the need for an alternative charge readout mechanism, particularly for future LArTPC neutrino detectors expected to experience high neutrino interaction rates, such as the Deep Underground Neutrino Experiment (DUNE) Near Detector (ND). One such mechanism is the use of an array of pixels to read out charges, where a LArTPC test stand at the University of Sheffield has been established to provide an R&D ground for testing this new pixelated readout technology, called the Sheffield TEst stand Experiment with Liquid argon (STEEL).

Chapter 8 provides an overview of STEEL, its Liquid Argon (LAr) dewar, LArTPC setup, pixel readout plane, LAr purification and Liquid Nitrogen (LN) cooling systems, external CRTs and internal 'cold' PhotoMultiplier Tube (PMT). Then, essential commissioning work is presented, calibrating the operating voltage and trigger settings of the STEEL CRTs, cold PMT and pixels, as well as performing LAr and LN circulation tests in preparation for a continuous 22-day data run of STEEL collecting cosmic-ray muon data.

The first physics analysis of STEEL from this data run is shown in Chapter 9: determining the density of ElectroNegative Impurities (ENI) in LAr using scintillation triplet lifetime measurements from cold PMT data, and then using electron lifetime measurements from pixel data. The theory behind calculating ENI density in LAr from triplet lifetime or electron lifetime is also outlined, followed by the results from these respective studies, tracking LAr purity over each day of the 22-day data run of STEEL.

Finally, Chapter 10 summarises the work and key results presented in this thesis.

Chapter 2

Neutrino History and Theory

Major developments in the field of particle physics have been made over the past century, such that nearly all matter in the observable universe can be described as well-understood elementary particles interacting with each other through fundamental forces of nature. This encapsulates the SM of particle physics, which categorises particles by intrinsic quantities such as their electrical charge, spin, mass, and their interaction modes through three forces: strong, weak and ElectroMagnetic (EM). Understanding all SM particles and their mechanisms of interaction is essential in building a complete description of the components and dynamics of the universe, particularly in the short moments after its creation. This chapter focuses on the neutrino, one of the most abundant particles in the universe, which is notoriously difficult to detect. The SM assumes the neutrino to be massless, but this fact was overturned by the confirmation of neutrino oscillations, describing how neutrinos randomly and spontaneously change flavour over long distances, marking it one of the few confirmed observations of physics beyond the SM.

A detailed account of the history and current theoretical modelling of the neutrino is presented in this chapter. Section 2.1 outlines the history of the neutrino, with Section 2.2 describing how it is integrated into the SM. Section 2.3 states the history of neutrino oscillations, from its experimental observations to its mathematical modelling, and where the current state of neutrino oscillation physics stands. One such area of investigation for experiments such as SBND is the detection of the sterile neutrino, which could explain a number of observed anomalies in neutrino oscillation data, described Section 2.4.

2.1 Neutrino History

Neutrino history began in 1896 when Becquerel first observed nuclear β decay through studies of uranium radiation emission channels [1]. β decay involves the atomic nucleus emitting a β particle (later identified as an electron e^- or positron e^+), becoming an adjacent isobar (different atomic number but the same nucleon number). Later, in 1903, Rutherford would categorise β decay as one of the three main radioactive emission processes for atomic nuclei, with the other two being α decay (emission of a He-4 nucleus) and γ decay (emission of a high energy photon) [2]. These processes were well understood at the time to be two-body decays, where the parent nucleus emits a single particle to become the daughter nucleus, resulting in a narrow energy distribution for the emitted particle. To this day, α and γ decays retain their two-body nature. However, further studies of β decays undertaken by Meitner and Hahn in 1911 [3], further corroborated by Danysz in 1913 [4], revealed the energy distribution for the emitted e^- to be continuous, which is indicative of a three-body decay where a third emitted particle is taking some of the lost momentum.

In 1930, Pauli suggested an electronically neutral, low mass particle had to be emitted to account for the lost momenta, calling it the neutron [5]. It was later renamed to the neutrino ν (Italian for 'little neutral one') in 1932, which is what the particle would be known as henceforth, in order to distinguish it from the heavy nuclear baryon of the same name. By 1934, Fermi had developed a complete theory of β decay where he claimed that the e and ν were created as a result of a neutron n decaying into a proton p^+ [6]. Later developments in particle physics would make the distinction between β^- and β^+ decay, where the former involves a neutron n decaying into a proton p^+, emitting an electron e^- and the neutrino's antimatter counterpart, the antineutrino $\bar{\nu}$, proceeding via the reaction

$$n \rightarrow p^+ + e^- + \bar{\nu}. \tag{2.1}$$

β^+ decay is a rarer phenomenon, where a proton p^+ borrows binding energy from the atomic nucleus to transform into a neutron n, emitting a positron e^+ and neutrino ν through

$$p^+ \rightarrow n + e^+ + \nu. \tag{2.2}$$

Despite the solid theory by Fermi, no experimental evidence for the neutrino would be uncovered until 1956, when the Cowan-Reines neutrino experiment used a large tank of water doped with cadmium chloride $CdCl_2$ to image e^+ resulting from the high flux of $\bar{\nu}$ emitted from the Savannah River Nuclear Plant [7]. This marked the first observation of

an inverse β decay reaction, which is described by the process

$$\bar{\nu} \ + p^{+} \ \rightarrow \ n \ + \ e^{+}, \tag{2.3}$$

confirming the existence of the neutrino through indirect observation of the antineutrino $\bar{\nu}$. At the time, observation of a ν or $\bar{\nu}$ was often defined by the charge of the lepton they produced in the detection interaction. Introduction of lepton number L in 1953 by Konopinski and Mahmoud would quantify this distinction, where ν and e^{-} are assigned $L = 1$ and $\bar{\nu}$ and e^{+} have $L = -1$ [8]. In 1936, Anderson and Neddermeyer discovered evidence for an additional charged lepton called the muon μ, and later in 1975 the tau τ was discovered by Perl et al. [9], motivating the distinction between flavours of leptons. For example, the $\bar{\nu}/\nu$ observed in $\beta^{\pm}$ decays are actually electron (anti)neutrinos $\bar{\nu}_e/\nu_e$ and are produced alongside $e^{\pm}$. Similarly, muon (anti)neutrinos $\bar{\nu}_\mu/\nu_\mu$ and tau (anti)neutrinos $\bar{\nu}_\tau/\nu_\tau$ are defined as being produced alongside $\mu^{\pm}$ and $\tau^{\pm}$ respectively. This led to the law of conservation of lepton number, confirmed by Danby et al. at Brookhaven National Laboratory (BNL) in 1962 through confirmation of two distinct neutrino flavours [10], where the absolute and generational lepton numbers L_e, L_μ and L_τ were theorised to be conserved in every observed reaction. $L_\tau = 1$ is assigned to τ^{-} and its corresponding neutrino ν_τ, $L_\mu = 1$ is assigned to μ^{-} and ν_μ, and $L_e = 1$ to e^{-} and ν_e, with $L_{e,\mu,\tau} = -1$ given to their antimatter counterparts. Therefore, the ν and $\bar{\nu}$ depicted in Equations 2.1, 2.2 and 2.3 would actually be ν_e and $\bar{\nu}_e$ respectively.

2.2 The Standard Model Neutrino

In the SM of particle physics, every elementary particle is described by their electrical charge, spin, relative mass, and which fundamental force they couple to. The two main types of particles in the SM are fermions, with half-integer spin obeying Fermi-Dirac statistics; and bosons, with integer spin following Bose-Einstein statistics. In order of decreasing overall coupling strength, the three fundamental forces are the strong, EM and weak interactions (there is currently no theory of gravity in the standard model). Fermions interact with other fermions through these forces via the exchange of a force-dependent gauge boson with spin equal to one. Additionally, fermions with non-zero mass couple to the Higgs field through exchanging a spin-zero Higgs boson, which is responsible for particles having mass [11]. The neutrino was integrated into the SM by assuming it as a neutrally-charged massless lepton which only couples to matter through the Charged Current (CC) and Neutral Current (NC) weak interactions, depicted as primary Feynman diagram vertices in Figure 2.1.

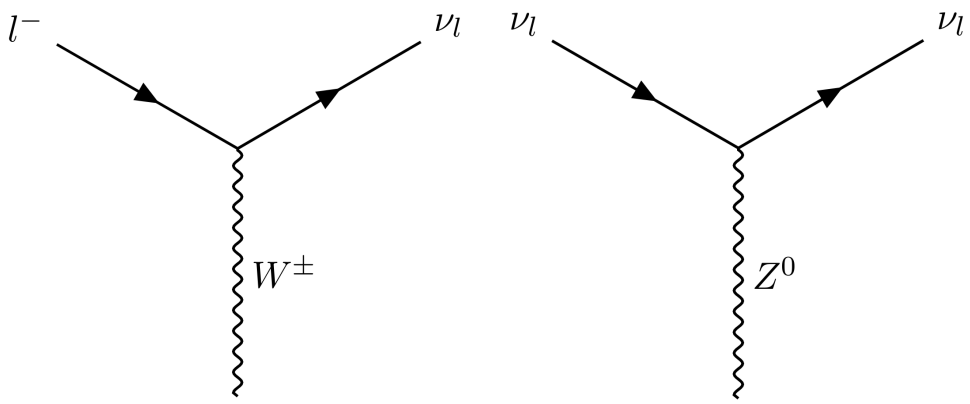

Figure 2.1: Feynman diagrams showing the only two primary interaction vertices for neutrinos coupling via the weak interaction, where $l = e, \mu, \tau$. The left vertex shows a Charged Current (CC) interaction where a charged lepton turns into its corresponding neutrino by the emission/absorption of a $W^\pm$ boson. The right vertex shows a Neutral Current (NC) interaction where a neutrino scatters by emission/absorption of a Z^0 boson.

CC weak interactions transform the neutrino into its corresponding charged lepton, and vice versa, through the absorption/emission of a $W^\pm$ boson, whereas NC weak interactions involve scattering through the absorption/emission a Z^0 boson. The SM assumes three neutrino flavours, which was confirmed from 17 million Z^0 resonance measurements by the four main Large Electron-Positron collider (LEP) experiments (ALEPH [12], DELPHI [13], L3 [14] and OPAL [15]) and 600 Z^0 decays by the SLAC Large Detector (SLD) experiment [16] using the SLAC Linear Collider (SLC) polarised beam, to be $N_\nu = 2.9840 \pm 0.0082$ [17]. This is consistent with experimental observations as indirect evidence of ν_e, ν_μ and later ν_τ by the DONUT collaboration in 2000 [18] have been confirmed.

2.3 Neutrino Oscillations

Neutrinos in the SM were assumed to be massless since no evidence for the contrary had been observed at that point in time. However, throughout the mid-20th century, multiple solar, atmospheric, beam and reactor neutrino detectors reported evidence of neutrinos randomly and spontaneously changing flavours from their source to the detection medium. This phenomenon would be known as neutrino oscillations, which can only occur if neutrinos have non-zero rest mass. The discovery of neutrinos having mass is regarded as physics beyond the SM, since integrating neutrino masses into the SM involves the addition of new coupling fields and exchange bosons to the SM Lagrangian.

2.3.1 Historical Evidence

Neutrino oscillations were first postulated by Pontecorvo in 1957 as ν transforming into their corresponding antiparticle $\bar{\nu}$, similar to neutral meson oscillations [19]. Then, after Lederman et al. discovered the muon neutrino in 1962 [10], a mathematical model for two-flavour neutrino oscillations was developed by Maki, Nakagawa and Sakata the same year, which stated that the neutrino flavours detected by experiments (ν_e and ν_μ) are actually a linear superposition of neutrino mass states (ν_1 and ν_2) [20]. Evidence for two flavour neutrino oscillations was first uncovered by Davis et al. in 1968 using a tank of liquid perchloroethylene to measure the total neutrino flux from the sun, deep underground in Homestake mine, South Dakota, to shield the tank from cosmic-ray backgrounds [21]. Solar ν_e are identified through their interactions with chlorine atoms to produce argon via

$$\nu_e \; + \; {}^{37}\mathrm{Cl} \; \rightarrow \; {}^{37}\mathrm{Ar}^{+} \; + \; e^{-}. \tag{2.4}$$

Results showed that the observed solar neutrino flux was approximately one third that of the most accurate theoretical prediction, calculated in 1968 by Bahcall using the standard solar model [22]. This would be known as the solar neutrino problem, and one of the leading solutions to this problem was published in 1969 by Pontecorvo and Gribov, using the model of two flavour oscillations proposed by Maki, Nakagawa and Saki in 1962, suggesting that solar ν_e can randomly and spontaneously change flavour over long distances [23].

Further evidence for neutrino oscillations was uncovered by the Kamiokande experiment, using 50,000 tons of ultrapure water in a large cylinder with a PMT array lining the walls to detect Cherenkov radiation emitted from high energy atmospheric neutrinos. These are neutrinos produced in the upper atmosphere as a result of cosmic-ray interactions with atmospheric nuclei, producing charged pions which decay into $\mu^- + \bar{\nu}_\mu$ or $\mu^+ + \nu_\mu$ depending on the charge of the initial pion. The μ^- subsequently decays into $e^- + \bar{\nu}_e + \nu_\mu$ and μ^+ into $e^+ + \nu_e + \bar{\nu}_\mu$, giving an expected ratio of the total observed muon neutrinos to electron neutrinos $(\nu_\mu + \bar{\nu}_\mu)/(\nu_e + \bar{\nu}_e)$ to be around 2. However, in 1992 the Kamiokande experiment observed this ratio to be approximately 1.2 with a 2.8σ statistical significance deviating from the expected value of 2 [24], suggesting that ν_μ were oscillating into ν_τ. Further confirmation of this deficit in observed ν_μ/ν_e came from two atmospheric neutrino experiments: firstly in 1992 from the Irvine-Michigan-Brookhaven (IMB) detector [25], and secondly in 1997 from Soudan-2 [26].

All anomalies observed thus far were indicative of the existence of neutrino oscillations, and therefore neutrinos having non-zero rest mass, but did not exceed the 5σ statistical

significance required for a particle physics result to be confirmed as a discovery. That was until 1996, when the Kamiokande experiment upgraded to Super-Kamiokande (SK), increasing its fiducial mass by 20 times, greatly improving neutrino event rates as well as making improvements to its data analysis techniques and MC simulations [27]. SK collected atmospheric ν_μ and ν_e flux data with respect to the zenith angle Θ, with the results of this study presented in Figure 2.2.

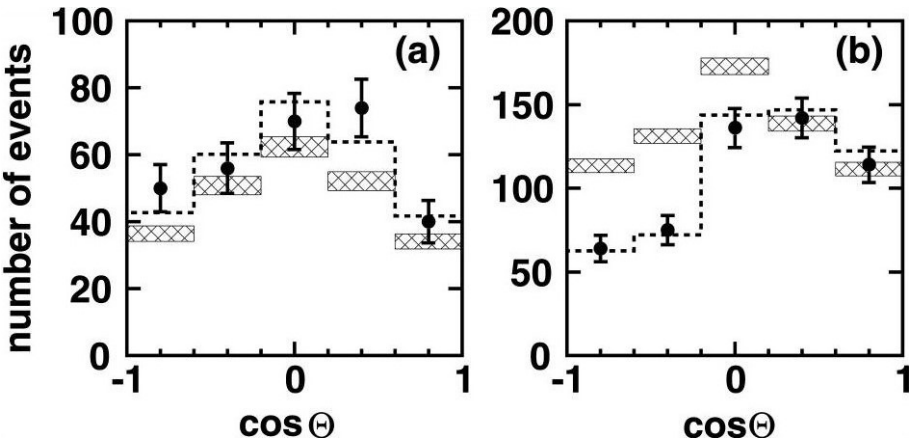

Figure 2.2: Number of observed electron-like (left) and muon-like (right) neutrinos in the multi-GeV energy range with respect to the cosine of the zenith angle, Θ, where cos(Θ) =-1 corresponds to upwards travelling and cos(Θ) = 1 to downward-travelling neutrinos. The shaded boxes indicate the Monte Carlo predictions with statistical errors for zero neutrino oscillations. Dotted lines show the Monte Carlo predictions for $\nu_\mu \rightarrow \nu_\tau$ oscillations assuming $\sin^2(2\theta) = 1$ and $|\Delta m^2_{13}| = 2.2 \times 10^{-3}$ eV^2. Graph sourced from [28].

Figure 2.2 shows a deficit in upward-directed ν_μ with a statistical significance of $> 6\sigma$ and almost no dependence on Θ for ν_e distance travelled, suggesting that ν_μ have transformed into ν_τ whilst travelling through the Earth. This 6σ significance of the atmospheric ν_μ deficit marked the first experimental confirmation of neutrino oscillations [29]. Further confirmation of neutrino oscillations came in 2001 from observations of solar neutrinos by the Sudbury Neutrino Observatory (SNO), which had a similar experimental setup to SK, using D_2O (heavy water, replacing hydrogen atoms in H_2O with deuterium) as the detection medium instead of H_2O. Heavy water allowed for a larger number of NC events and elastic scattering of ν_e against atomic electrons compared to H_2O. This allowed SNO to measure both the ν_e flux $\phi(\nu_e)$ and total neutrino flux $\phi(\nu)$ coming from the sun.

Using the standard solar model, only ν_e are emitted from the sun such that $\phi(\nu)_{\text{theo}} = \phi(\nu_e)_{\text{theo}} = (5.1 \pm 0.9) \times 10^{-6}$ cm^{-2}s^{-1}, so $\phi(\nu_\mu)_{\text{theo}} = \phi(\nu_\tau)_{\text{theo}} = 0$. However, results from SNO found $\phi(\nu_e)_{\text{exp}} = (1.76 \pm 0.1) \times 10^{-6}$ cm^{-2}s^{-1} with $\phi(\nu_\mu)_{\text{exp}} + \phi(\nu_\tau)_{\text{exp}} = (3.41 \pm 0.63) \times 10^{-6}$ cm^{-2}s^{-1} and $\phi(\nu)_{\text{exp}} = (5.17 \pm 0.64) \times 10^{-6}$ cm^{-2}s^{-1} [30]. These results showed that

the total solar neutrino flux matched the theoretical value calculated using the standard solar model, but with smaller ν_e and larger ν_μ and ν_τ contributions, confirming that ν_e have oscillated into ν_μ and ν_τ whilst travelling from the sun to the detector. This discovery, along with the confirmation of neutrino oscillations causing the atmospheric neutrino deficit by SK, led to the 2015 Nobel Prize in physics being awarded to Takaaki Kajita (leading the research team at SK) and Arthur McDonald (leading the research team at SNO) for "the discovery of neutrino oscillations, which shows that neutrinos have mass" [31].

2.3.2 The Neutrino Mixing Matrix

Neutrinos only couple to the weak force through CC interactions, exchanging a $W^\pm$ boson, and NC interactions, exchanging a Z^0 boson, described by the Feynman diagrams in Figure 2.1. Therefore, when a neutrino is detected through either of these interactions, only their flavour eigenstate is observed, where the flavour eigenstates ν_e, ν_μ, ν_τ are a linear superposition of mass eigenstates ν_1, ν_2, ν_3 with rest masses of m_1, m_2, m_3 respectively. Mixing of eigenstates can be mathematically described by a 3×3 complex, unitary matrix called the PMNS matrix U named after the four main contributors to neutrino oscillation theory: Pontecorvo, Maki, Nakagawa and Sakata [32]. To ensure that the total number of neutrinos is conserved (e.g. one neutrino does not oscillate into two), the unitarity condition

$$UU^\dagger = I \tag{2.5}$$

must hold in every oscillation. Mathematically, any 3×3 complex, unitary matrix can be described by three Euler angles and one complex phase. These angles are called the mixing angles θ_{12}, θ_{13}, θ_{23}, and are related to the probability that any one neutrino flavour oscillates into another. The complex phase δ_{CP} is called the CP-violating phase, and drives how the oscillation probability varies with respect to charge-conjugation and parity transformations acting on the system, which is further outlined in Section 2.3.4. Putting all this together, the three-flavour PMNS matrix is stated as

$$U = \begin{pmatrix} 1 & 0 & 0 \\ 0 & c_{23} & s_{23} \\ 0 & -s_{23} & c_{23} \end{pmatrix} \begin{pmatrix} c_{13} & 0 & s_{13}e^{-i\delta_{\text{CP}}} \\ 0 & 1 & 0 \\ -s_{13}e^{i\delta_{\text{CP}}} & 0 & c_{13} \end{pmatrix} \begin{pmatrix} c_{12} & s_{12} & 0 \\ -s_{12} & c_{12} & 0 \\ 0 & 0 & 1 \end{pmatrix} \begin{pmatrix} e^{i\eta_1} & 0 & 0 \\ 0 & e^{i\eta_2} & 0 \\ 0 & 0 & 1 \end{pmatrix}, \tag{2.6}$$

where the convention $s_{ab} = \sin(\theta_{ab})$ and $c_{ab} = \cos(\theta_{ab})$ is used for brevity. The matrix on the right side of equation 2.6 is only applicable if neutrinos are Majorana particles (i.e.

particles identical to their corresponding antiparticles, so $\nu = \bar{\nu}$). The Majorana phases do not affect oscillation probabilities and are only relevant in experiments concerned with neutrinoless double beta decay, and in some CP-violating interactions [33]. These Majorana phases are neglected for the remainder of this section, where neutrinos are assumed to be Dirac particles (i.e. particles distinct from their corresponding antiparticles, so $\nu \neq \bar{\nu}$).

After being created, each neutrino flavour $|\nu_\alpha\rangle$ exists as a linear, orthogonal superposition of mass eigenstates $|\nu_i\rangle$, and will collapse to the same or a different flavour eigenstate when a CC weak interaction is detected by a neutrino experiment, identifying the neutrino flavour based on the charged lepton it produces. Each $|\nu_i\rangle$ is weighted with an element of the PMNS matrix $U_{\alpha i}$ such that each $|\nu_\alpha\rangle$ can be expressed by

$$|\nu_\alpha\rangle = \sum_i U_{\alpha i}|\nu_i\rangle, \tag{2.7}$$

where $\alpha = e, \mu, \tau$ and $i = 1, 2, 3$ for the three neutrino paradigm [34]. This can be generalised in the form of the matrix equation

$$\begin{pmatrix} \nu_e \\ \nu_\mu \\ \nu_\tau \end{pmatrix} = \begin{pmatrix} U_{e1} & U_{e2} & U_{e3} \\ U_{\mu 1} & U_{\mu 2} & U_{\mu 3} \\ U_{\tau 1} & U_{\tau 2} & U_{\tau 3} \end{pmatrix} \begin{pmatrix} \nu_1 \\ \nu_2 \\ \nu_3 \end{pmatrix}. \tag{2.8}$$

Simplifying equation 2.8 into the two-flavour paradigm, assuming neutrino mixing to be primarily between the weak eigenstates ν_e and ν_μ and the mass eigenstates ν_1 and ν_2, which is mathematically equivalent to θ_{23}, $\theta_{13} \ll \frac{\pi}{2}$, gives

$$\begin{pmatrix} \nu_e \\ \nu_\mu \end{pmatrix} = \begin{pmatrix} \cos(\theta) & \sin(\theta) \\ -\sin(\theta) & \cos(\theta) \end{pmatrix} \begin{pmatrix} \nu_1 \\ \nu_2 \end{pmatrix}, \tag{2.9}$$

where the mixing angles have gone from three to one θ, which is analogous to θ_{12} in the three-flavour paradigm. Knowing the exact values of the mixing matrix elements is equivalent to precision measurements of the mixing angles; which was the main goal of many neutrino oscillation experiments over the past decade.

2.3.3 Oscillation Probability Calculations

Assuming a neutrino is created in its weak eigenstate $|\nu_\alpha\rangle$ at time $t = 0$ and 1-dimensional coordinate $x = 0$, the probability of observing that neutrino flavour as $|\nu_\beta\rangle$ after $t > 0$ and $x > 0$ is given by performing the inner product of these eigenstates from equation 2.7

$$P(\nu_\alpha \to \nu_\beta) = |\langle \nu_\beta | \nu_\alpha(x,t)\rangle|^2, \tag{2.10}$$

where $\langle \nu_\alpha| = (|\nu_\alpha\rangle)^*$ in Dirac notation. Since each neutrino mass eigenstate is a plane wave solution to the time-dependent Schrödinger equation, they can be expressed in terms of the neutrino energy E and momentum p such that their propagation is described as

$$|\nu_j(x,t)\rangle = e^{-i(E_j t - p_j x)}|\nu_j(0,0)\rangle. \tag{2.11}$$

Using the ultrarelativistic approximation $m_j \ll E_j$, and assuming each neutrino mass eigenstate has around the same energy $E_1 \approx E_2 \equiv E$, this simplifies equation 2.11 to

$$|\nu_j(x,t)\rangle = e^{-i\frac{m_j^2 x}{2E}}|\nu_j(0,0)\rangle, \tag{2.12}$$

where m_j is the rest mass of the $|\nu_j\rangle$ eigenstate. In the context of accelerator neutrino experiments with the neutrino source and detector separated by a baseline L, the position coordinate x can be relabelled to L, typically measured in km. For two-detector neutrino oscillation experiments, such as the SBN program, this is applicable if the ND is much closer to the neutrino source than the Far Detector (FD), neglecting oscillations between the neutrino source and ND. Substituting equation 2.12 into equation 2.7 expresses each flavour eigenstate in terms of the propagating mass eigenstates. Thus, the general probability of observing $|\nu_\beta\rangle$ in a pure $|\nu_\alpha\rangle$ neutrino beam with beamline L is given by the inner product of these two eigenfunctions, substituting them into equation 2.10, giving:

$$P(\nu_\alpha \to \nu_\beta) = |\langle \nu_\beta | \nu_\alpha(L,t)\rangle|^2 = \left| \sum_j U^*_{\alpha j} U_{\beta j} e^{-i\frac{m_j^2 L}{2E}} \right|^2. \tag{2.13}$$

Equation 2.13 is applicable to any number of neutrino mass eigenstates $j = 1, 2, ..., N_\nu$ for N_ν neutrino flavours. Separating the sum into its real and imaginary components of the PMNS matrix elements gives the general expression for the oscillation probability only in

terms of the neutrino beamline length L and beam energy E as

$$P(\nu_\alpha \to \nu_\beta) = \delta_{\alpha\beta} \; - \; 4\sum_{i>j} \Re\mathrm{e}(U^*_{\alpha i}U_{\beta i}U_{\alpha j}U^*_{\beta j}) \sin^2\left(\Delta m^2_{ij}\frac{L}{4E}\right) + 2\sum_{i>j} \Im\mathrm{m}(U^*_{\alpha i}U_{\beta i}U_{\alpha j}U^*_{\beta j}) \sin\left(\Delta m^2_{ij}\frac{L}{2E}\right), \tag{2.14}$$

where $\delta_{\alpha\beta}$ is the Kronecker delta which equals 1 for appearance probabilities (i.e. $\alpha = \beta$) and 0 for disappearance probabilities ($\alpha \neq \beta$) [34] and Δm^2_{ij} is the difference between the square of the ν_i and ν_j neutrino rest masses, defined with the convention

$$\Delta m^2_{ij} \equiv m^2_j - m^2_i, \tag{2.15}$$

for $i = 1, 2, 3$ in the three-neutrino paradigm. Equation 2.14 shows that in the context of neutrino accelerator experiments, oscillation probability only depends on the ratio of the length of the beamline and energy of the beam L/E. Considering the two-flavour oscillation paradigm, where ν_e and ν_μ flavour eigenstates are a linear superposition of ν_1 and ν_2 mass eigenstates, expressed by the matrix in equation 2.9, the two-flavour ν_μ disappearance probability $\mathrm{P}(\nu_\mu \to \nu_e)$ probability is calculated using

$$P(\nu_\mu \to \nu_e) = \sin^2(2\theta_{12}) \sin^2\left(1.27\frac{\Delta m^2_{12}[\mathrm{eV}^2]L[\mathrm{km}]}{E[\mathrm{GeV}]}\right), \tag{2.16}$$

derived in Appendix A. The corresponding $\mathrm{P}(\nu_\mu \to \nu_\mu)$ can be calculated using the fact that $\mathrm{P}(\nu_\mu \to \nu_\mu) + \mathrm{P}(\nu_\mu \to \nu_e) = 1$, since in the two-flavour paradigm, in a pure ν_μ beam only ν_μ or ν_e will be detected. As such, the probability of observing ν_μ in a ν_μ beam is

$$P(\nu_\mu \to \nu_\mu) = 1 - \sin^2(2\theta) \sin^2\left(1.27\frac{\Delta m^2_{12}[\mathrm{eV}^2]L[\mathrm{km}]}{E[\mathrm{GeV}]}\right). \tag{2.17}$$

Thus far only neutrino oscillations have been considered as opposed to antineutrino oscillations, where $\bar{\nu}$ oscillation probabilities can be derived from equations 2.14 by replacing the PMNS matrix elements with their complex conjugation. The only complex terms in the PMNS matrix in equation 2.6 involve the CP-violating phase δ_{CP} (ignoring the Majorana phases), which drives oscillation probability differences between matter and antimatter. This is also coupled with the Mikheyev–Smirnov–Wolfenstein (MSW) effect, describing disparities in ν and $\bar{\nu}$ oscillation probabilities through interactions with matter [35].

2.3.4 CP Violation

CP is a consecutive quantum operation composed of a parity transformation P followed by a charge conjugation operation C, which are both discrete symmetries in nature. A parity transformation operation reverses the spatial coordinates of a particle, relating to the conservation law that physical laws remain invariant if the system is mirrored. Reversing the spatial coordinates of a particle is also equivalent to swapping its helicity (alignment of momentum and spin vectors of a particle) from right-handed (parallel) to left-handed (antiparallel) and vice versa. A charge conjugation operation reverses the electrical charge of the applied fermion, relating to the conservation law of the Lorentz force acting on all charges in a system remaining invariant under all electrical charges in the system being reversed. This operation is also equivalent to transforming a particle into its corresponding antiparticle, reversing quantum numbers intrinsic to the particle such as baryon number, lepton number, strangeness etc. leaving only mass, energy, momentum and spin unchanged.

By 1956, parity was proven to be conserved in all strong and EM interactions, but not for weak interactions, motivating an experiment led by Wu in the same year to probe parity violations in the weak sector. A uniform magnetic field was applied to low temperature cobalt-60, aligning their spin vectors, before undergoing nuclear β decay through

$$^{60}_{27}\mathrm{Co} \rightarrow {}^{60}_{28}\mathrm{Ni} + e^- + \bar{\nu}_e + 2\gamma, \tag{2.18}$$

where the angular distribution of emitted e^- was studied with the magnetic field both aligned and anti-aligned with the direction of nuclear spin. γ ray emissions were verified to be equally distributed with and against the direction of nuclear spin to ensure that all cobalt-60 atoms had aligned spin vectors, since parity symmetry was already confirmed to be conserved in all EM interactions.

The results showed that the rate of e^- emission in the direction of atomic spin differed greatly in both magnetic field orientations, suggesting parity was violated in the weak sector. Emitted e^- were far more frequently directed against the nuclear spin vector, giving them left-handed helicity, and therefore the emitted $\bar{\nu}_e$ right-handed helicity. Further testing led to the confirmation that the weak sector violated parity symmetry, and the conclusion that only left-handed neutrinos and right-handed antineutrinos exist in nature [36]. In order to remedy this parity violation, it was proposed that the collective charge and parity operations, CP, are conserved in all particle interactions. While remaining true for all strong and EM interactions, evidence for violations of CP symmetry in the weak sector was observed in 1964 through observations of neutral kaon oscillations by Fitch and Cronin [37],

and then by LHCb through studies of B and D meson decays [38, 39].

CP-violating interactions in nature implies that the universe has an intrinsic favouring towards particle decays and transformations into matter over antimatter, supported by the fact that the observable universe is matter-dominated. Therefore, studying CP-violating interactions in the weak sector could lead to an explanation as to why the observable universe is composed of matter, as opposed to the universe always having equal amounts of matter and antimatter, eventually annihilating into zero mass, with the disparity most likely occurring during leptogenesis and/or baryogenesis, moments after the big bang.

Analyses of neutral meson oscillations have shown that there is insufficient CP-violating interactions in the quark sector to account for the matter domination present in the observable universe [40]. However, neutrino oscillations have been hypothesised to produce significant CP-violating interactions during leptogenesis, which is quantified by the CP-violating complex phase of the PMNS matrix, δ_{CP} [41]. As such, experiments such as DUNE and Hyper-Kamiokande (HK) aim to quantify the degree in which neutrino oscillations violate CP through high precision measurements of δ_{CP}.

2.3.5 Best Fit of Oscillation Parameters

The three-flavour neutrino oscillations model is governed by seven parameters which determine oscillation probabilities: the three mixing angles θ_{12}, θ_{13}, θ_{23}; three squared mass differences between neutrino mass states Δm^2_{12}, Δm^2_{13}, Δm^2_{23}; and the CP-violating complex phase δ_{CP}. Solar neutrino experiments typically measure θ_{12} and Δm^2_{12}, where SNO was the first experiment to report said measurements in 2001 by probing ν_e disappearance [42], further constrained by KamLAND in 2003 through $\bar{\nu}_e$ disappearance searches [43].

Atmospheric neutrino experiments usually measure θ_{23}, Δm^2_{23} and Δm^2_{13}, with SK measuring the former two in 1998 through ν_μ disappearance studies [29]. Further measurements of these parameters were carried out by accelerator experiments including KEK To Kamioka (K2K) in 2006 measuring ν_μ disappearance [44], Tokai To Kamioka (T2K) in 2011 measuring ν_e appearance in a ν_μ beam [45] and Main Injector Neutrino Oscillation Search (MINOS) in 2014 measuring ν_μ disappearance and ν_e appearance [46]. The most difficult mixing angle to determine is θ_{13}, which was finally measured by T2K in 2011 through observations of ν_μ and $\bar{\nu}_\mu$ disappearance [45], further constrained in 2012 by the reactor experiments Double Chooz [47], Daya Bay [48] and RENO [49] by studying $\bar{\nu}_e$ disappearance.

δ_{CP} is the most difficult oscillation parameter to determine, though significances can still be attributed to constraints and boundaries set, such as using the fact that $\delta_{\text{CP}} = 0, \pi$ corresponds to no CP violation, experiments can determine the likelihood of δ_{CP} being

these values in a given neutrino oscillation dataset. This was first undertaken by MINOS in 2013 through extraction of $\nu_\mu \rightarrow \nu_e$ and $\bar{\nu}_\mu \rightarrow \bar{\nu}_e$ probabilities from the full MINOS dataset [50]. Furthermore, in 2017, T2K excluded $\delta_{\text{CP}} = 0, \pi$ by a $> 2\sigma$ Confidence Level (CL), equivalent to a 95% chance of the true value of δ_{CP} being not equal to 0 or π.

Though the exact determination of neutrino rest masses is considered to be impossible with current generation neutrino detector technology, the squared difference between masses and the relative order of neutrino masses is feasible to determine and integral for oscillation probability calculations. What is currently known about the relative size of neutrino masses is that $m_2 > m_1$ ($\Delta m^2_{12} > 0$) and $|\Delta m^2_{13}| \approx |\Delta m^2_{23}|$ ($|\Delta m^2_{12}| \ll |\Delta m^2_{23}|$), but the sign of Δm^2_{23} is still unknown [51]. This gives two possibilities for the ordering of neutrino masses: either it follows Normal Hierarchy (NH) where $m_3 > m_2 > m_1$; or Inverted Hierarchy (IH) where $m_2 > m_1 > m_3$. Additionally, only two of the squared mass differences are independent since the sum of all three must equal zero such that

$$\Delta m^2_{12} + \Delta m^2_{23} + \Delta m^2_{31} = 0, \tag{2.19}$$

meaning that one square mass splitting can always be expressed by the other two. Historical convention dictates that the two independent squared mass differences are the solar mass difference $\delta m^2 \equiv \Delta m^2_{12}$ and atmospheric mass difference $\Delta m^2 \equiv \Delta m^2_{13}(\text{NH}) = \Delta m^2_{23}(\text{IH})$, which are both visualised in the diagram in Figure 2.3.

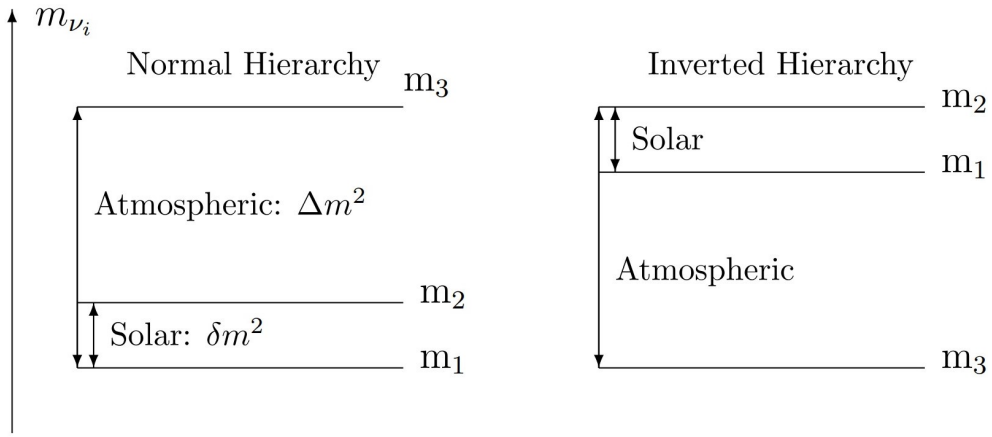

Figure 2.3: Neutrino mass eigenstate ordering: normal hierarchy (left) and inverted hierarchy (right). The atmospheric mass difference is defined as $\Delta m^2 \equiv \Delta m^2_{31}$ (NH) $= \Delta m^2_{23}$(IH) and the solar mass difference $\delta m^2 \equiv \Delta m^2_{21}$. Diagram sourced from [52].

In 2017, NOvA was able to determine the two best fits for δ_{CP} and θ_{23} in NH through ν_e appearance and ν_μ disappearance searches [53]. Table 2.1 shows the global best fit of all neutrino oscillation parameters as of 2018, derived by de Salas et al. [54].

Table 2.1: Global Best Fit (BF) of neutrino oscillation parameters, including long-baseline data from T2K and NOvA; reactor data from Daya Bay, RENO and Double Chooz; atmospheric data from IceCube, DeepCore, ANTARES and Super-Kamiokande (SK), as well as additional solar data from SK. Inverted Hierarchy (IH) ranges refer to the local minimum, as opposed to Normal Hierarchy (NH). Global fit values taken from [54–57].

Parameter	BF$\pm1\sigma$ (68% CL)	2σ range (95% CL)	3σ range (99% CL)
Δm^2_{21} [10^{-5}eV^2]	$7.55^{+0.20}_{-0.16}$	$7.20 - 7.94$	$7.05 - 8.14$
$\lvert\Delta m^2_{31}\rvert$ [10^{-3}eV^2] (NH)	2.50 ± 0.03	$2.44 - 2.57$	$2.41 - 2.60$
$\lvert\Delta m^2_{31}\rvert$ [10^{-3}eV^2] (IH)	$2.42^{+0.03}_{-0.04}$	$2.34 - 2.47$	$2.31 - 2.51$
θ_{12} [°]	$34.5^{+1.2}_{-1.0}$	$32.5 - 36.8$	$31.5 - 38.0$
θ_{23} [°] (NH)	$47.7^{+1.2}_{-1.7}$	$43.1 - 49.8$	$41.8 - 50.7$
θ_{23} [°] (IH)	$47.9^{+1.0}_{-1.7}$	$44.5 - 48.9$	$42.3 - 50.7$
θ_{13} [°] (NH)	$8.45^{+0.16}_{-0.14}$	$8.2 - 8.8$	$8.0 - 8.9$
θ_{13} [°] (IH)	$8.53^{+0.14}_{-0.15}$	$8.3 - 8.8$	$8.1 - 9.0$
δ/π (NH)	$1.32^{+0.21}_{-0.15}$	$1.01 - 1.75$	$0.87 - 1.94$
δ/π (IH)	$1.56^{+0.13}_{-0.15}$	$1.27 - 1.82$	$1.12 - 1.94$

Combining T2K, NOvA, SK and reactor neutrino experiment data, the global fit finds that $\delta_{\text{CP}} = \pi/2$ is strongly disfavoured, more for IH than NH. The best fit value for NH predicts $\delta_{\text{CP}} = 1.32\pi^{+0.21\pi}_{-0.15\pi}$ and for IH $\delta_{\text{CP}} = 1.56\pi^{+0.13\pi}_{-0.15\pi}$ [54, 55]. A global fit of data from NOvA, T2K, SK, various reactor neutrino experiments and neutrino telescopes leads to IH being disfavoured over NH at a significance of 3.4σ [54–57], though this does not exceed the 5σ threshold for a discovery in particle physics, and as such more experimental probing of the neutrino mass hierarchy is required to fully resolve this dichotomy in neutrino physics.

Calculating these seven oscillation parameters to higher accuracies and precisions, determining whether the neutrino mass hierarchy follows normal or inverted ordering and making constraints on δ_{CP} are but a few of the main goals of current generation neutrino oscillation experiments. Though larger scale and more sophisticated experiments are currently being built which are probing beyond these aforementioned aims. This includes determination of the octant of θ_{23}, resolving whether neutrinos are Majorana or Dirac particles and performing searches for particles beyond the SM, which could resolve previously measured anomalies in neutrino oscillation experiments [58]. One such particle is the sterile neutrino, a fourth neutrino flavour which only interacts through gravity, not just the weak interaction, the discovery of which is the primary goal of the SBN program.

2.4 The Sterile Neutrino

In 1968, Pontecorvo proposed that if lepton number is not a conserved quantity - where each neutrino flavour has a distinct non-zero mass - then processes such as $\nu \leftrightarrows \bar{\nu}$ and $\nu_e \leftrightarrows \nu_\mu$ are possible, as an analogue to previously observed neutral kaon oscillations [59]. Since the Wu experiment in 1956 concluded that only (massless) neutrinos with left-handed helicity and antineutrinos with right-handed helicity participate in weak interactions, these oscillations would transform active left-handed neutrinos into sterile right-handed neutrinos (vice versa for antineutrinos). These sterile neutrinos were named by Pontecorvo to indicate that they do not couple to the weak force and only interact through the force of gravity. However, the discovery of neutrino oscillations confirmed that neutrinos do have mass, opening up the possibility of the existence of sterile neutrinos as a potential fourth neutrino flavour [59]. This is consistent with the LEP and SLC results confirming three neutrino flavours through measurements of the number of neutrino flavours that participate in Z^0 decays, since the sterile neutrino does not couple to the weak force and thus are not present in Z^0 decay channels, so the result remains $N_\nu \approx 3$ [17] in the sterile neutrino mixing regime.

The first hints of a fourth neutrino flavour was observed by the Liquid Scintillator Neutrino Detector (LSND), a short-baseline neutrino detector that studied $\nu_e/\bar{\nu}_e$ appearance in a $\nu_\mu/\bar{\nu}_\mu$ beam. In 1996, results showed 40 ν_e events, in the $60 < E < 200$ MeV energy range, over the expected background of 21.9 ± 2.1 ν_e events given the known ν_e presence in the ν_μ beam, corresponding to an oscillation probability of $(2.6 \pm 1.0 \pm 0.5) \times 10^{-3}$ at a 3.8σ CL [60]. Furthermore, searches for $\bar{\nu}_\mu \to \bar{\nu}_e$ oscillations in 2001 found an excess of $87.9 \pm 22.4 \pm 6.0$ $\bar{\nu}_e$ events (with uncertainties corresponding to statistical and systematic respectively) over the expected background, with an oscillation probability of $(2.64 \pm 0.067 \pm 0.045) \times 10^{-3}$ [61].

This became known as the LSND anomaly and resolving it quickly became the primary focus of most neutrino experiments at the time. One such experiment built to probe this anomaly was the Mini Booster Neutrino Experiment (MiniBooNE): a large spherical tank of mineral oil detecting Cherenkov light emitted from neutrino interactions originating from the predominantly ν_μ BNB. It was situated 541 m from the beryllium beam target, increasing the baseline but also increasing the beam energy at the same rate to match the same L/E of LSND [62]. Combining all MiniBooNE data runs, amassing 18.75×10^{20} Protons On Target (POT) with the BNB in neutrino mode and 11.27×10^{20} POT in antineutrino mode, a total excess of $630.0 \pm 52.1 \pm 122.2$ $\nu_e + \bar{\nu}_e$ events in the energy range of $200 < E < 1250$ MeV were observed, at a statistical significance of 4.8σ [63–67]. This result aligned with the expected excess observed at LSND, thus confirming the $\nu_e/\bar{\nu}_e$ excess to be an anomaly in neutrino oscillation physics that needed to be resolved.

The leading explanation for these excesses in observed $\nu_e/\bar{\nu}_e$ events is the possibility of well-understood oscillation probabilities being modified from the three-flavour model due to the presence of a fourth neutrino flavour, the sterile neutrino. Though the sterile neutrino is currently deemed undetectable due to not coupling to any measurable interaction mode, its presence within the neutrino mixing matrix (changing from a 3×3 to a 4×4 matrix with a fourth mass state ν_4 and additional matrix elements $U_{\alpha 4}$ for $\alpha = e,\ \mu,\ \tau,\ s$) modifies oscillation probabilities between ν_e, ν_μ and ν_τ such that their existence can be indirectly inferred based on discrepancies found in measured oscillation parameters [68, 69]. Detecting sterile neutrinos is also important because their mixing with other neutrino (and antineutrino) flavours affects the measured value of δ_{CP}, sensitivity to neutrino mass hierarchy determination and neutrinoless double beta decay discovery.

Since the MiniBooNE result, multiple experiments have been contributing to further probing excesses in $\nu_e/\bar{\nu}_e$ appearance probabilities, as well as how sterile neutrinos can affect ν_e/ν_μ disappearance probabilities. This includes the reactor neutrino experiments KARMEN and OPERA, combining their analyses with the MiniBooNE dataset to impose boundaries on Δm^2 and $\sin^2(2\theta_{12})$ [66, 70, 71]. Global fits of data from accelerator experiments such as the MINOS detector [72, 73] and atmospheric experiments such as SK, IceCube and DeepCore [74, 75] were combined to set limits on the mass square difference between the ν_1 and ν_4 mass states Δm^2_{14} and the mixing matrix elements U_{e4} and $U_{\mu 4}$. These global fits also revealed great discrepancies in ν_e/ν_μ oscillation probabilities, motivating the need for more experiments to collect this kind of data to resolve this discrepancy [76].

Experiments are also currently being built, or are already collecting data, with the aim of setting limits on the sterile neutrino model of neutrino oscillations. These include the J-PARC Sterile Neutrino Search (JSNS^2) experiment at J-PARC Spallation Neutron Source, performing $\bar{\nu}_e$ appearance measurements using a $\bar{\nu}_\mu$ beam firing at a Gd-doped liquid scintillator detector [77]. Long-baseline experiments such as NOvA and T2K are also using their vast ν_μ disappearance datasets to probe the oscillation probability discrepancies and set limits on Δm^2_{24} and $U_{\mu 4}$ [78, 79]. Reactor neutrino experiments such as STEREO, DANSS, Neutrino-4 and PROSPECT are contributing to measurements of $\nu_e/\bar{\nu}_e$ appearance, setting boundaries on Δm^2_{41} and U_{e4} [80–83]. The most ambitious out of all these experiments in searching for the sterile neutrino is the SBN program at Fermilab, which will detect ν_μ disappearance and ν_e appearance from the BNB at short baselines, with the primary detectors being SBND and ICARUS. The SBN program aims to confirm or disprove the LSND/MiniBooNE anomaly with unprecedented precision, and will determine whether the anomaly can be explained by sterile neutrino mixing [84].

Chapter 3

Liquid Argon Time Projection Chamber Overview

The LArTPC is the principal technology used in many world-leading neutrino experiments such as SBND, ICARUS and the future neutrino oscillation experiment DUNE. It involves a large volume of LAr subject to a uniform electric field, such that all ionisation electrons resulting from charged particle interactions with argon drift towards an array of sense wires, where signals are read out. This setup allows for full 3D imaging of particle interactions by utilising the 2D coordinates of the ionisation electron signal inductions on the wire planes (x, y), and the time taken for electrons to drift from the charged particle tracks to the wire planes t, aided by the detection time of de-excitation photons. LArTPC technology has progressed to the point where it is now at the forefront of neutrino oscillation experiments, with high resolution particle detection and reconstruction capabilities.

This chapter outlines the technical setup and operations of a LArTPC, and how it is utilised in neutrino detectors to read out signals from ionisation charges and scintillation light. Section 3.1 motivates LAr as the most suitable neutrino detection medium over other liquid noble elements and water. Section 3.2 outlines the general design of a LArTPC, describing how neutrino signals are read out. Section 3.3 recounts the history of LArTPC technological development and integration into neutrino experiments. Sections 3.4 and 3.5 contain descriptions of how ionisation charges and scintillation photons, respectively, are produced and propagated through the LAr medium and read out as data.

3.1 Motivation for Liquid Argon as a Neutrino Detector

First proposed by Carlo Rubbia in 1977 in response to the need for higher resolution particle trackers in neutrino physics at the time, the LArTPC functions as a particle imaging apparatus that uses LAr to produce and read out ionisation charges and scintillation photons [85]. Theoretically, any noble liquid (i.e. He, Ne, Ar, Kr, Xe) could have been used as the neutrino detection medium, as they all have high scintillation and ionisation efficiencies and are also transparent to light, aiding in photon propagation. Additionally, ENI present in the active volume (such as O_2, H_2O and N_2) can be conveniently frozen out by the cryogenics process, minimising quenching of electron lifetime and scintillation light yield [86]. Different noble liquids are useful for different applications in particle physics; table 3.1 compares their relative particle detecting properties.

Table 3.1: Comparison of particle detecting properties of liquid noble elements.

	Helium	**Neon**	**Argon**	**Krypton**	**Xenon**
Boiling Point at 1 atm (K)	4.2	27.1	87.3	120.0	165.0
Density (g/cm^3)	0.125	1.2	1.4	2.4	3.0
Radiation Length (cm)	755.2	24.0	14.0	4.9	2.8
dE/dx (MeV/cm)	0.24	1.4	2.1	3.0	3.8
No. of Scintillation Photons (MeV^{-1})	19,000	30,000	40,000	25,000	42,000
Scintillation Photon Wavelength (nm)	80	78	128	150	175

In the context of using liquid noble elements to detect neutrinos, Table 3.1 shows LAr to be the most apt detection medium for neutrino experiments due to its higher density than helium and neon, as well as longer radiation length and scintillation light yield than krypton and xenon. This high yield of scintillation photons are also produced in a wavelength which is easily shiftable to be detected by most conventional photon detector devices. Argon is also relatively abundant compared to the heavier noble elements, making it cheaper and easier to obtain than neon, krypton or xenon [87].

The other most prolific neutrino detection medium is water, used in water Cherenkov neutrino experiments. High energy neutrinos interact with H_2O (or other molecules if the water has been doped) in large tanks, transforming into their corresponding charged lepton, which typically travel faster than the speed of light in water, producing an EM shower in

the form of a Cherenkov ring. The spatial and energy distribution of the photon cascade produced by this EM shower is detected by an array of photon detectors, and the flavour and energy of the initial neutrino is reconstructed based on these distributions.

Water is cheaper and easier to obtain in ultrapure form than argon without the need to expend energy to constantly cool to 87 K during operations. Furthermore, ν_μ and ν_e signals in water Cherenkov detectors are easier to distinguish based on their distinctive ring structures left by Cherenkov radiation on the photon detector arrays, where LArTPCs require a detailed reconstruction of the neutrino energy spectrum to determine the initial neutrino flavour. On the other hand, water Cherenkov neutrino experiments can only detect muons surpassing a 0.8 GeV energy threshold (1.4 GeV for nucleons) for producing Cherenkov radiation [88]. This was an issue with T2K where the J-PARC ν_μ beam had a peak energy of 0.6 GeV, losing most of its muon signals [89], whereas LArTPCs detect almost any charges passing through, making energy reconstruction much more accurate. As such, LAr continues to be utilised in neutrino detectors for particle physics research.

3.2 Technical Design of a LArTPC

Figure 3.1 shows the general setup of a LArTPC. Gaseous Argon (GAr) gradually fills the chamber, circulating through insulated transfer lines and centrifugal cryogenic pumps to a condenser system filled with liquid nitrogen at 78 K, cryogenically cooling the argon to liquid form at 87 K via thermal conduction and convection. This circulation process also contains purification systems such as activated copper material, to oxidise O_2 impurities, and molecular sieves, to filter out H_2O molecules from the argon volume [90]. When an incoming high energy neutrino interacts via the CC weak interaction with argon atoms in the ultrapure liquid argon, they transform into their corresponding charged lepton (typically e or μ), which in turn excites and ionises argon atoms, releasing ionisation electrons and de-excitation photons. The applied uniform electric field drifts ionisation electrons towards the anode planes at speeds of 1.66 mm/µs for an electric field strength of 500 V/cm.

The specific LArTPC depicted in Figure 3.1 utilises three wire planes in an Anode Plane Assembly (APA) to read out ionisation charges: two induction planes (U and V) angled at ±60° from the vertical collection plane (Y), shown in Figure 3.2. The Cathode Plane Assembly (CPA) consists of a wire mesh, where applying a negative High Voltage (HV) of around -100 kV over the wires implements an electric field across the detector, directing electrons towards the APA to have their signals read out. Though the entire APA frame is grounded to the detector building, the U plane wires are negatively voltage-biased,

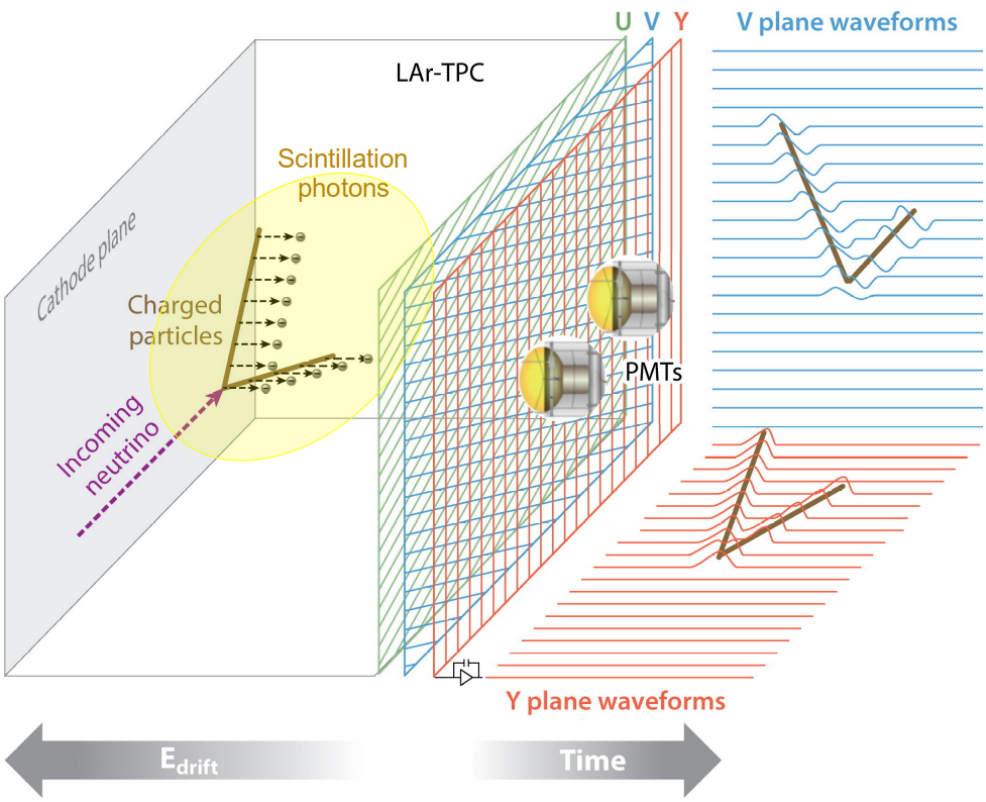

Figure 3.1: Experimental setup of a typical LArTPC. The U, V and Y sense wires represent the anode plane assemblies, where U and V are induction planes aligned ±60° with respect to the vertical Y collection plane. Diagram adapted from [84].

typically at around -200 V, with the V plane having no voltage bias, allowing drifting electrons to pass by the U and V plane wires, leaving bipolar differential current induction signals on them. The Y plane has a positive voltage bias of around 400 V applied to it, attracting electrons to terminate on its wires, resulting in a unipolar signal with amplitude proportional to the number of collected electrons [91].

Scintillation de-excitation photons also traverse the transparent LAr medium and are converted into a measurable electrical signal by an array of photon detectors, typically situated behind the APA as shown in Figure 3.1, primarily used to aid in determination of the initial neutrino-argon interaction time t_0. A combination of ionisation electron signals from APA wires with timing information derived from scintillation pulses outputted by the photon detectors can lead to full 3D imaging of charged particle tracks and high accuracy identification of initial neutrino flavour [84].

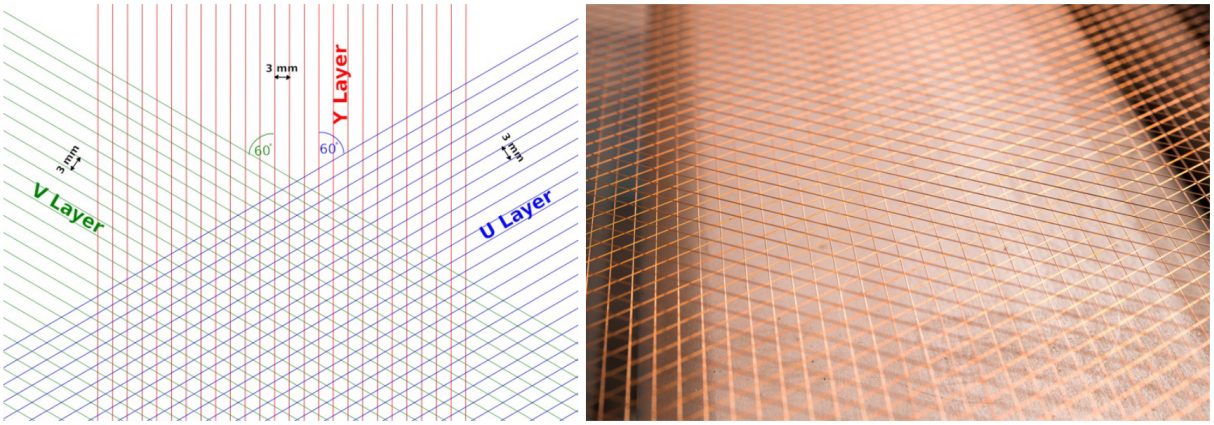

Figure 3.2: Schematic (left) and photo (right) of the two induction (U and V) and collection (Y) plane wires in a typical LArTPC APA. These depict the three wire planes for SBND, with 3 mm pitch and the induction plane wires angled ±60° with respect to the vertical collection plane wires. Images sourced from [91].

3.3 History of LArTPC Experiments

The first major implementation of LArTPC technology in a neutrino detector was with the ICARUS T600 detector, initially situated 1.4 km underground at Grand Sasso National Laboratory in Italy to collect solar and atmospheric ν_μ and ν_e data, as well as ν_μ beam data from the CNGS neutrino beam situated 730 km away at CERN, from 2004 to 2013 [92,93]. It was then moved to Fermilab, USA, in 2017 to be part of the SBN program to collect ν_μ beam data from the BNB [94]. ICARUS pioneered the LArTPC design featured in Figure 3.1, utilising two LArTPCs split between two cryostats, with a combined fiducial LAr mass of 476 tons [95], with the full experimental setup shown in Figure 3.3.

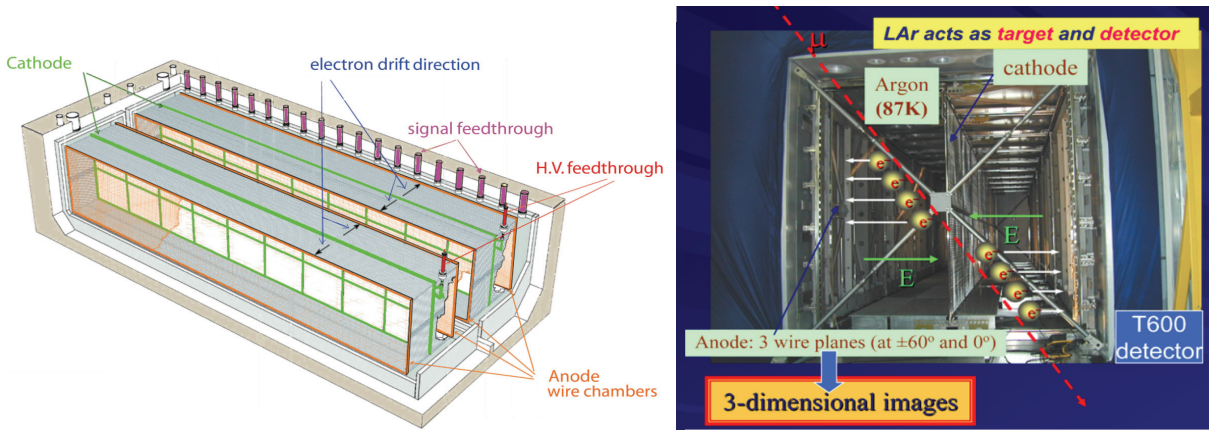

Figure 3.3: Diagram of the ICARUS T600 LArTPC (left) and annotated picture of the same LArTPC outlining its properties and components (right). Diagrams sourced from [96].

Another significant implementation of LArTPC technology was present in the Micro Booster Neutrino Experiment (MicroBooNE), a follow-up to MiniBooNE, built to further probe the LSND anomaly [60], which was confirmed by MiniBooNE in 2007 [63]. Also operating at Fermilab from 2015 to 2020, detecting ν_μ and ν_e from the BNB, MicroBooNE had a similar LArTPC design to the ICARUS T600 detector, but instead utilising a single LArTPC inside a cylindrical cryostat, housing 170 tons of fiducial LAr, shown in the diagrams in Figure 3.4. Whilst ICARUS opted to keep its readout electronics mounted to flanges outside the cryostat [97], MicroBooNE had readout modules directly attached to the APA support frames, paving the way for cold electronics systems used in future LArTPC experiments, greatly decreasing electronic noise and power consumption [98].

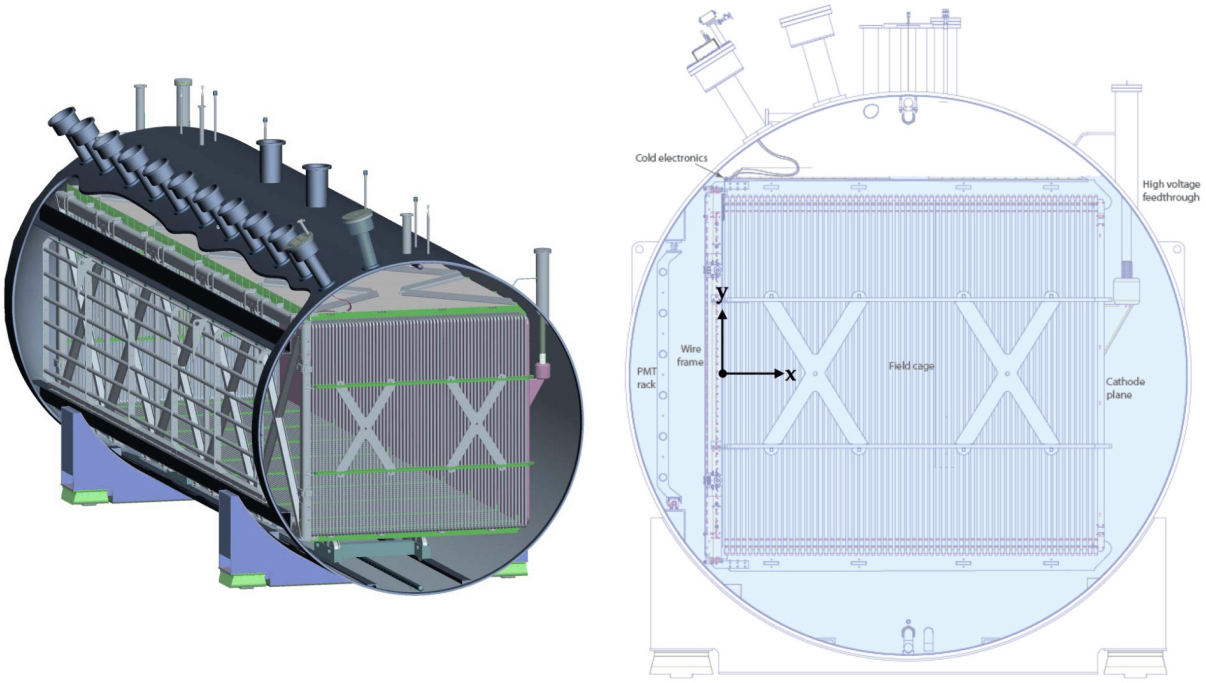

Figure 3.4: Schematic (left) and cross-section (right) of the MicroBooNE LArTPC within its cylindrical cryostat. The beam is directed out of the page. Diagrams sourced from [98].

The near detector of the SBN program is SBND: a single cryostat housing 112 tons of LAr covering two LArTPC volumes. SBND has a baseline of 110 m such that it receives the highest number of ν_μ and ν_e interactions of any neutrino detector in history, paving the way for the highest precision ν_μ-Ar cross-section measurements [99]. Whilst ICARUS and MicroBooNE perfected the design of LArTPCs, SBND made great innovations in how external detector subsystems, such as the PDS and CRT array, are integrated into the data readout chain to aid in track reconstruction and neutrino flavour identification. Information on the experimental setup and operations of SBND will be detailed in Chapter 4.

Two supplementary LArTPC-based neutrino detectors include the Argon Neutrino Teststand (ArgoNeuT) and Liquid Argon In A Testbeam (LArIAT) experiments. ArgoNeuT used a cylindrical cryostat containing 170 L of active LAr volume inside a cuboidal LArTPC to detect ν_e appearance in the Neutrinos at the Main Injector (NuMI) beam at Fermilab between 2009 and 2010, greatly advancing neutrino beam background rejection capabilities of LArTPC neutrino detector experiments [100]. LArIAT inherited the ArgoNeuT cryostat, aiming to further characterise neutrino beam backgrounds for rejection in energy ranges relevant to subsequent neutrino detector experiments such as SBND and DUNE, this time with higher statistics and a more advanced LAr purification system [90].

LArTPCs can either operate as Single-Phase (SP), where the entire argon volume is in liquid form (or gas for GArTPCs), or Dual-Phase (DP), containing a mix of LAr and GAr. Most modern LArTPCs are SP due to the simplicity of charge propagation in a homogenous medium, but other LArTPC experiments opt to use mostly LAr with a GAr layer at the top of the chamber. This was employed by the ProtoDUNE-DP detector, where the overlying GAr layer propagates charges towards an array of Large Electron Multipliers (LEMs), amplifying charges before being read out by the anode plane [101].

Most large scale neutrino detectors utilise the three wire plane setup, as depicted in Figure 3.2, over other anode readout mechanisms due to the fact that sense wires can cover entire breadths of the detector volume, minimising readout channels. However, projective wire plane readouts can exhibit ambiguities in event reconstruction due to high intensity beam spills causing detector pile-up near the anode [102]. For this reason, an alternative charge readout technology is being developed for future LArTPC neutrino detectors using an array of pixels, where a pixelated anode plane has been designed at the University of Bern called LArPix [103]. The University of Sheffield has a test stand using this LArPix technology named STEEL, which aims to provide the groundworks for the implementation of pixelated charge readout technology into the DUNE ND-GAr module [104]. Work done on commissioning of the STEEL subsystems and the first key results analysing pixel data at STEEL are presented in Chapters 8 and 9 respectively.

3.4 Charged Particle Interactions with Argon

In order for LArTPC experiments to accurately reconstruct charged particle energies and identify initial neutrino flavour, the energy lost per distance travelled of tracks, dE/dx, must be well understood. This can be well estimated using the Bethe-Bloch formula, which calculates the mean rate of energy loss for a Minimum Ionising Particle (MIP) travelling

through matter, with the only dependent variables being the electron density of the medium, the charge and energy of the MIP [105]. Using the known density of LAr at 87 K $\rho_{\text{LAr}} = 1.4$ g/cm^3, a minimum ionising muon has an average energy loss per unit distance of $dE/dx = 2.1$ MeV/cm. This parameter remains relatively constant for the duration of the particle traversing the detector until the Bragg peak is reached, when the muon rapidly loses all of its kinetic energy and terminates in the detector medium. Fluctuations in energy loss are described by a skewed Landau or Landau-Vavilov distribution, where the most probable energy loss is calculated depending on the thickness (g/cm^2) of the medium [106].

LArTPCs typically measure the number of ionisation electrons released from argon atoms per unit length, dQ/dx, which is then converted into dE/dx for neutrino flavour identification and energy reconstruction. However, this is not a one-to-one conversion, since there is a chance that drifting electrons recombine with argon ions, quantified by the recombination factor R_B; analogous to the inverse of the probability that an ionisation electron recombines with an argon ion. Conversion between dQ/dx and dE/dx is given by

$$\frac{dQ}{dx} = \frac{R_B}{W_{\text{LAr}}} \frac{dE}{dx}, \tag{3.1}$$

where W_{LAr} is the minimum energy required for a MIP to ionise an argon atom, essentially acting as a unit conversion between MIP energy loss and number of electrons ionised [107], with LAr at 87 K having $W_{\text{LAr}} = (23.6 \pm 0.3)$ eV [108, 109]. R_B is a dimensionless quantity, dependent only on the density of the medium and the applied electric field strength. There are two main models predicting how R_B varies with these parameters, the first being the Birks model which assumes electrons re-attach to the parent ion due to the pair's combined Coulomb field [110, 111]; the second is the modified box model predicting recombination occurs due to multiple ionisations happening with electron-ion charge densities in a cylindrical volume [112, 113]. Both models are more accurate in different contexts, but for the range of electric field strengths used by most LArTPC experiments (~ 500 V/cm), the Birks model is preferred, expressing the recombination factor as

$$R_B = \frac{A_B}{1 + \frac{k_B}{\epsilon \rho} \cdot \frac{dE}{dx}}, \tag{3.2}$$

where $A_B = 0.800 \pm 0.003$ and $k_B = 0.0486 \pm 0.0006$ (kV/cm)(g/cm^2) are both constants for LAr determined through data fitting, ϵ is the electric field strength (kV/cm) and $\rho_{\text{lar}} = 1.3973$ g/cm^3 is the density of LAr at 87 K.

3.5 Ionisation Electron and Photon Propagation in LAr

When a high energy neutrino interacts with argon atoms in ultrapure liquid argon, the CC weak interaction goes as

$$\nu_l \ + \ \mathrm{Ar} \ \rightarrow \ l^- \ + \ \mathrm{Ar}^* \ + \ N, \tag{3.3}$$

where ν_l (for $l = e, \mu, \tau$) is transformed into its corresponding charged lepton l^-, exciting the argon nucleus Ar^*, potentially resulting in the emission of one or more daughter particles N. The NC neutrino-argon scattering interaction occurs through

$$\nu_l \ + \ \mathrm{Ar} \ \rightarrow \ \nu_l \ + \ \mathrm{Ar}^* \ + \ N. \tag{3.4}$$

Depending on the energy of the ν_l, N could be one or more $\pi^{\pm}$, π^0 or other energetically allowed hadrons [114]. ν_μ are also detected through the same CC interaction in equation 3.3, whereas LArTPCs were not designed to detect ν_τ, so most modern LArTPC experiments are not concerned with ν_τ detection and just study ν_e and ν_μ oscillations. LArTPCs are particularly proficient at identifying the type of CC interaction through analysis of the final state lepton. Ionisation electrons drift towards the LArTPC APA at speeds dependent on the applied electric field. For a typical LArTPC with an electric field strength of 500 V/cm, the electron drift speed is calculated to be approximately 0.16 cm/µs [115]. However, ionisation electron drift path is influenced by detector systematics such as diffusion, Space Charge Effects (SCE) or absorption by ENI.

Diffusion is the deviation of electron drift paths caused by clusters of ionisation electrons electrostatically repelling one another, causing inaccuracies in MIP path reconstruction. Since diffusion is a result of Coulomb repulsion, the magnitude of it varies based on the applied electric field, differentiating between longitudinal (parallel to the electric field) and transverse (orthogonal to the electric field) diffusion. Characterising the effects of both longitudinal and transverse diffusion on electron drift path is essential in precisely reconstructing MIP tracks for accurate neutrino flavour identification [115]. SCE are the result of residual argon ions drifting towards the CPA at speeds of approximately 4 mm/s [116], altering the distribution of the applied electric field and causing deviations in electron drift paths, particularly at the edges of the LArTPC field cage [117]. Presence of SCE also causes inaccuracies in MIP track reconstruction and calorimetric determination, so determining the approximate distribution of SCE in surface LArTPC experiments such as SBND is integral in accounting for these inaccuracies.

Presence of ENI in the LArTPC field cage can quench measured electron lifetime and scintillation light yield through absorption of ionisation electrons and scintillation photons

respectively [92]. This results in charge and light signals becoming subdued or even completely lost, causing gaps in track reconstruction and deficits in calorimetric information. This motivates the importance of ensuring the LAr purification system in any LArTPC sufficiently removes ENI from the LAr volume, resulting in a long enough electron lifetime such that electrons can reach the APA, which is typically around 3 ms. ENI absorption of particles is not a problem for large scale LArTPCs such as ICARUS or MicroBooNE, as their LAr purification systems have advanced to the point of having measured electron lifetimes of 15 ms and 18 ms - equating to O_2 concentrations of 20 and 17 parts per trillion (ppt) respectively - far exceeding the minimum electron lifetime threshold of 3 ms for sufficient signals being read out by their APAs [118, 119].

High energy charged particles, resulting from CC neutrino interactions with argon atoms through equation 3.3, excites surrounding argon atoms, which subsequently de-excite to release scintillation photons, occurring via three main channels:

$$\mathrm{Ar}^* \rightarrow \mathrm{Ar} + \gamma\ (128\ \mathrm{nm}), \tag{3.5}$$

$$\mathrm{Ar}^* + \mathrm{Ar} \rightarrow \mathrm{Ar}_2^* \rightarrow 2\mathrm{Ar} + \gamma\ (128\ \mathrm{nm}), \tag{3.6}$$

$$\mathrm{Ar}^+ + \mathrm{Ar} \rightarrow \mathrm{Ar}_2^+ + e^- \rightarrow \mathrm{Ar}_2^* \rightarrow 2\mathrm{Ar} + \gamma\ (128\ \mathrm{nm}). \tag{3.7}$$

Direct de-excitation of an excited argon atom Ar^* results in the emission of a photon γ with wavelength (128 ± 10) nm in the Vacuum Ulta Violet (VUV) range [120], shown in Equation 3.5. Equation 3.6 depicts excited and ground state argon atoms forming an excimer Ar_2^* before de-exciting and emitting a photon of wavelength 128 nm. Equation 3.7 describes an ionised argon atom Ar^+ bonding with a ground state argon atom to form the bound state Ar_2^+, emitting an electron e^-. This electron then recombines with two argon atoms to form an excimer Ar_2^*, which then de-excites to emit a photon with a wavelength of 128 nm, but is time delayed with respect to the other decay channels [121].

Most conventional photon detectors - typically PMTs - used in LArTPC experiments cannot detect photons with wavelengths in the VUV range, so wavelength-shifting compounds such as TetraPhenyl Butadiene (TPB) are used to shift the photon wavelength to the Ulta Violet (UV) range so they are detectable [84]. Additionally, scintillation photons can undergo Rayleigh scattering off of argon nuclei, decreasing overall scintillation light collection yield by the photon detectors, the probability of which depends on their wavelength [122]. To mitigate this, TPB is also applied to the foils covering the CPA, shifting photon wavelengths and decreasing the probability of Rayleigh scattering [123], reflecting them back to the photon detectors behind the APA.

Chapter 4

The Short-Baseline Near Detector

SBND is a neutrino experiment utilising LArTPC technology, operating as the near detector of the SBN program, based in Fermilab, USA. SBND has its own intrinsic goals related to probing previously measured anomalies in neutrino physics and performing the highest precision neutrino-argon cross-section measurements at the GeV-scale. SBND will be joining its analysis framework and large neutrino dataset with another LArTPC based neutrino detector on the SBN program, the ICARUS T600 detector, to perform the most significant search for eV-scale sterile neutrinos from short-baseline neutrino oscillation measurements [84]. Utilising one of the world's most powerful neutrino beams, the BNB, the SBN program aims to resolve the low energy $\nu_e/\bar{\nu}_e$ event excess over expected background rates observed by LSND in 1996 [60] and MiniBooNE in 2007 [62], determining whether it is due to sterile neutrino mixing [114].

This chapter provides a detailed overview of the operations and status of SBND as an experiment in isolation and in the context of the SBN program. Section 4.1 outlines the motivation and setup of the SBN program. A breakdown of the BNB is provided in Section 4.2. Section 4.3 contains an experimental description of SBND, its various subsystems, and the data readout mechanisms. Details on the SBND simulation is outlined in Section 4.4, including MC event production and raw SBND data decoding.

4.1 SBND and the SBN Program

The SBN program was first proposed in 2014, utilising three LArTPC detectors along the BNB beamline, to perform the most sensitive search for eV-scale sterile neutrinos through short-baseline appearance and disappearance searches at a $\sim 5\sigma$ significance [99]. Figure 4.1 shows a schematic of the SBN program and its three principal detectors on the BNB

beamline. These three detectors are the ICARUS T600 detector as the FD, repurposed from its operations at Gran Sasso and moved to Fermilab for this goal; the MicroBooNE detector as the middle detector, which was the longest continually running LArTPC in history, placed where MiniBooNE stood to replicate the conditions for the low energy $\nu_e/\bar{\nu}_e$ excess; and a new ND, known as LAr1-ND at the time, which would utilise similar LArTPC technology as the other two detectors and expertise from ArgoNeuT [114]. LAr1-ND would later be called SBND, where the main results of the SBN program consists of a joint oscillation analysis between ICARUS as the FD and SBND as the ND.

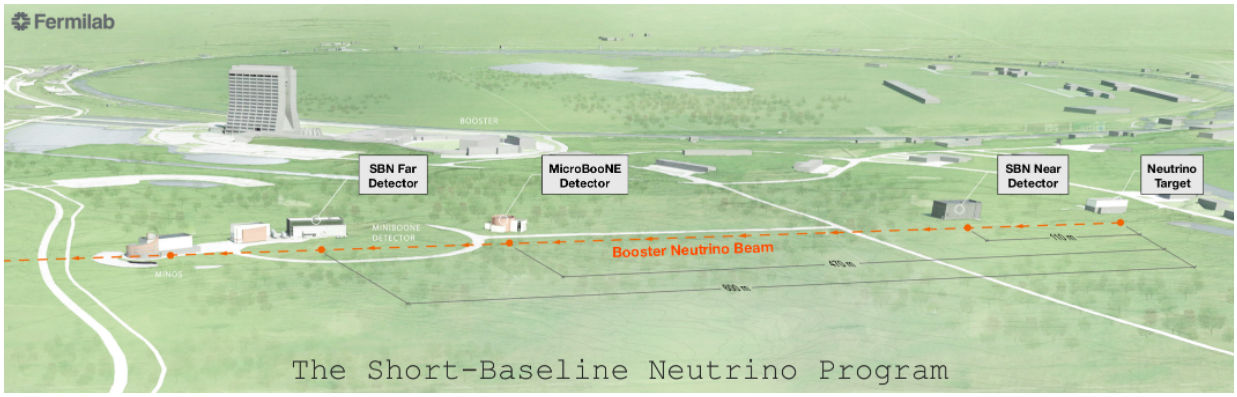

Figure 4.1: The Short-Baseline Neutrino program at Fermilab, showing the three LArTPC experiments situated on the Booster Neutrino Beamline: SBND, the MicroBooNE detector and the ICARUS T600 detector. Image credit: Holabird and Root [84].

Table 4.1 shows the distance each SBN program detector is placed on the BNB beamline, along with their total (in the cryostats) and active (in the field cages) LAr masses. SBND is placed 110 m from the BNB target, and the repurposed ICARUS T600 detector at 600 m from the beam target, allowing for high precision neutrino oscillation data taking. SBND determines the unoscillated flavour composition of the beam, before short-baseline oscillations occur over 490 m to ICARUS, where the oscillated flavour composition is determined. SBND has an active LAr mass of 112 tons, which is sufficient for observing high-statistics neutrino events with long particle tracks for event reconstruction, whereas the ICARUS T600 detector has a total active LAr mass of 476 tons. Comparing neutrino event distributions between detectors is made easier by both detectors employing functionally identical LArTPC technology, minimising systematic uncertainties [84].

MicroBooNE is situated at 470 m from the BNB target with an active LAr mass of 89 tons, and took on-axis BNB and off-axis NuMI beam data from 2015 to 2021 before ending its physics program and decommissioning, leaving SBND and ICARUS as the ND and FD of the SBN program. ICARUS collected on-axis BNB and off-axis NuMI beam data starting

Table 4.1: Overview of each SBN program detector's distance downstream of the BNB target, total and active liquid argon mass [114].

	Distance From BNB Target (m)	Total LAr Mass (tons)	Active LAr Mass (tons)
SBND	110	220	112
MicroBooNE	470	170	89
ICARUS-T600	600	760	476

in June 2022, and will continue to collect BNB data in conjunction with SBND to achieve the goals of the SBN program [94]. SBND officially began operations in July 2024, and started collecting stable BNB data in December 2024, where it has already collected the world's largest neutrino-argon interaction dataset, amassing $\sim 7,000$ neutrino events every day until its first major run is expected to finish in 2027/2028, where it will accumulate 10 million total neutrino interactions with LAr over an exposure of 10^{21} POT [99].

Figure 4.2 shows the sensitivity of the SBN program to measurements of Δm^2_{41} for ν_e appearance and ν_μ disappearance channel searches from the BNB, in pursuit of sterile neutrino searches. Sterile neutrino detection requires multiple channel searches in order to confirm or deny any given oscillation signal. In the $3+1$ sterile neutrino mixing model, the $\nu_\mu \to \nu_e$ mixing angle is driven by $\sin^2 2\theta_{\mu e} = 4|U_{\mu 4}|^2|U_{e4}|^2$, with the corresponding $\nu_\mu \to \nu_\mu$ mixing angle being driven by $\sin^2 2\theta_{\mu\mu} = 4|U_{\mu 4}|^2(1 - |U_{\mu 4}|^2)$. Additionally, the SBN program has the potential to observe spectral distortions as a result of sterile neutrino mixing in the NC scattering dominant energy spectrum (~ 100 MeV), inclusive of neutrino flavour and dependent on the BNB baseline [124].

Due to its proximity to the BNB target, SBND will record the highest number of sub-GeV/GeV ν_e and ν_μ events from a single data run of a neutrino experiment, resulting in the highest precision ν_e-Ar and ν_μ-Ar cross-section measurements to date. Simulations of the BNB neutrino flux predict that SBND will observe an excess of 803 oscillated ν_e events due to sterile neutrino mixing, compared to a background of $3,177$ for an exposure of 2.2×10^{20} POT, with a statistical significance of 5.4σ [114]. Table 4.2 shows the number of ν_μ and ν_e events SBND is expected to detect for an exposure of 6.6×10^{20} POT.

In total, SBND is expected to detect $\sim 2,000,000$ CC ν_μ and $\sim 15,000$ CC ν_e events every year. This is possible due to the placement of SBND at 110 m from the beam target, utilising the BNB with its well understood flavour composition and energy distribution. High resolution LArTPC technology also allows for the reconstruction of rare final state topologies in ν_μ/ν_e interactions with argon atoms, such as the production of hyperons Λ^0

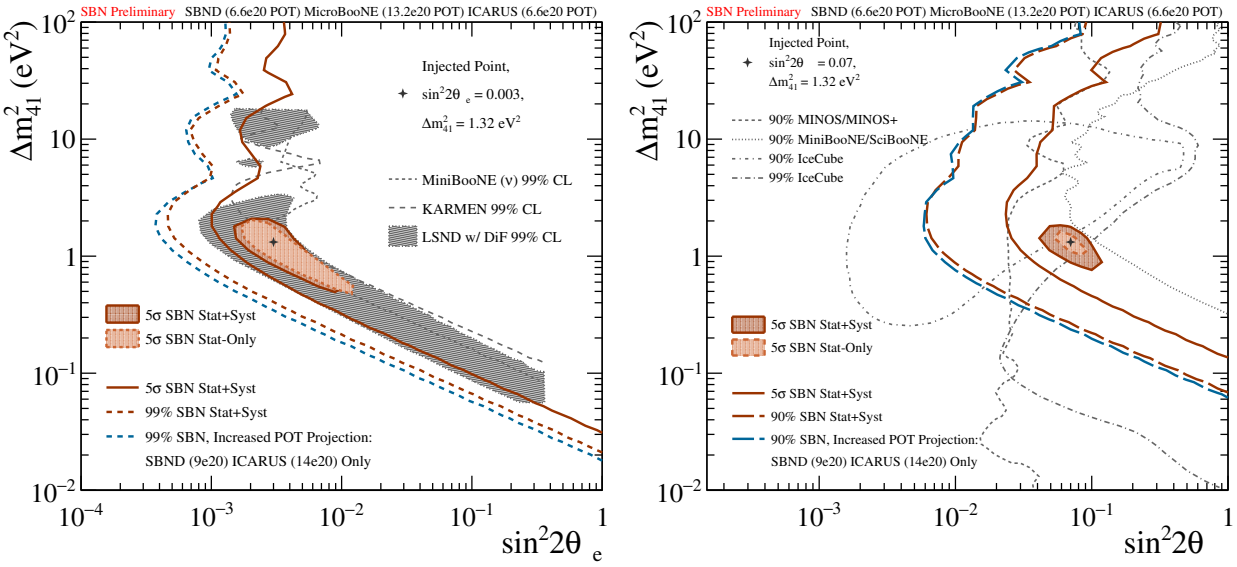

Figure 4.2: Sensitivity to which the SBN program will determine Δm^2_{41} for ν_e appearance (left) and ν_μ disappearance (right). Allowed and excluded regions combines low energy $\nu_e/\bar{\nu}_e$ excess data from LSND [60], KARMEN [70] and MiniBooNE [63], with external contours calculate from SciBooNE/MiniBooNE [125], MINOS/MINOS+ [73] and IceCube [126]. Graphs sourced from [99] using global fit analyses provided by [76].

Table 4.2: Predicted number of events detected by SBND based on interaction type and neutrino flavour, for 112 tons of active LAr mass and an exposure of 6.6×10^{20} POT [114].

	CC Inclusive	NC Inclusive
ν_μ Events	5, 212, 690	1, 988, 119
ν_e Events	36, 798	14, 351
Total Events	7, 251, 948	

and Σ^+. Figure 4.3 depicts the expected SBND energy spectra for CC ν_μ and ν_e interactions with the active LAr volume for an exposure of 10^{21} POT.

Furthermore, the high intensity BNB, SBND's close placement to the beam target and its large active LAr mass allows for the experiment to perform searches for physics beyond the SM. This includes various particles produced in neutral meson decays and the potential for detection of sub-100 MeV dark matter [114]. SBND will also have one of the leading sensitivities to searches of heavy neutral leptons decaying into neutral pions in the 140-260 MeV energy range, which is the subject of Lan Nguyen's PhD thesis [127]. Other dark sector particles that SBND has a sensitivity to detecting are Higgs portal scalars [128]; heavy axion-like particles decaying to photons or hadrons [129], resulting from kaon decays [130]; searches for light dark matter coupling to hadronic states via the exchange of a dark

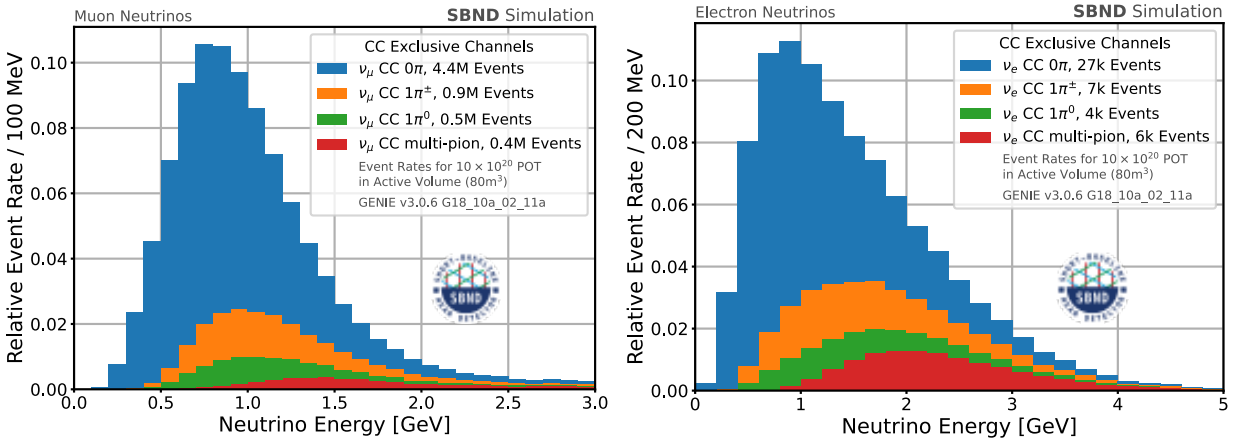

Figure 4.3: Expected SBND CC ν_μ (left) and ν_e (right) event rates for an exposure of 10^{21} POT from the BNB from a continuous three-year data run. Graphs sourced from [99].

photon [131]; and elastic/inelastic scattering off of argon atoms [132, 133]. From 2029, Fermilab plans to implement an accelerator restart program, allowing for the BNB to be operated in antineutrino mode, paving the way for the highest precision $\bar{\nu}_\mu$-Ar cross-section measurements to date, and increasing sensitivity to searches for new physics [99].

4.2 The Booster Neutrino Beam

Experiments on the SBN program beamline source their detected neutrinos from the BNB, which is shown in Figure 4.4 as top-down and side-on schematics. Protons from the Booster accelerator are injected as pulses into the BNB beamline via the Main Injector with an average kinetic energy of 8 GeV, directed towards a beryllium target. The protons then interact with the beryllium nuclei to produce a hadronic shower, primarily composed of pions and kaons, where magnetic toroidal aluminium alloy horns focus the positively charged hadrons into a concentrated beam. This beam of majority π^+ and K^+ traverses an air-filled 0.91 m radius tunnel for over 50 m where most of the hadrons decay into 92.5% ν_μ, 6.9% $\bar{\nu}_\mu$ and 0.6% $\nu_e + \bar{\nu}_e$. All other products from hadronic decays such as muons, electrons and residual hadrons are absorbed by concrete and steel muon absorbers at the end of the decay tunnel. ν_μ flux primarily results from the decay $\pi^+ \to \mu^+ + \nu_\mu$ for below 2 GeV, where $K^+ \to \mu^+ + \nu_\mu$ dominates above 2 GeV; the intrinsic ν_e contamination originates from the residual antimuons decaying via $\mu^+ \to e^+ + \nu_e + \bar{\nu}_\mu$ [99].

This describes the BNB in neutrino mode, where changing its operation to antineutrino mode is achieved by reversing the polarity of the magnetic horns, focusing negative hadrons into a concentrated beam instead of positive hadrons, eventually resulting in a concentrated

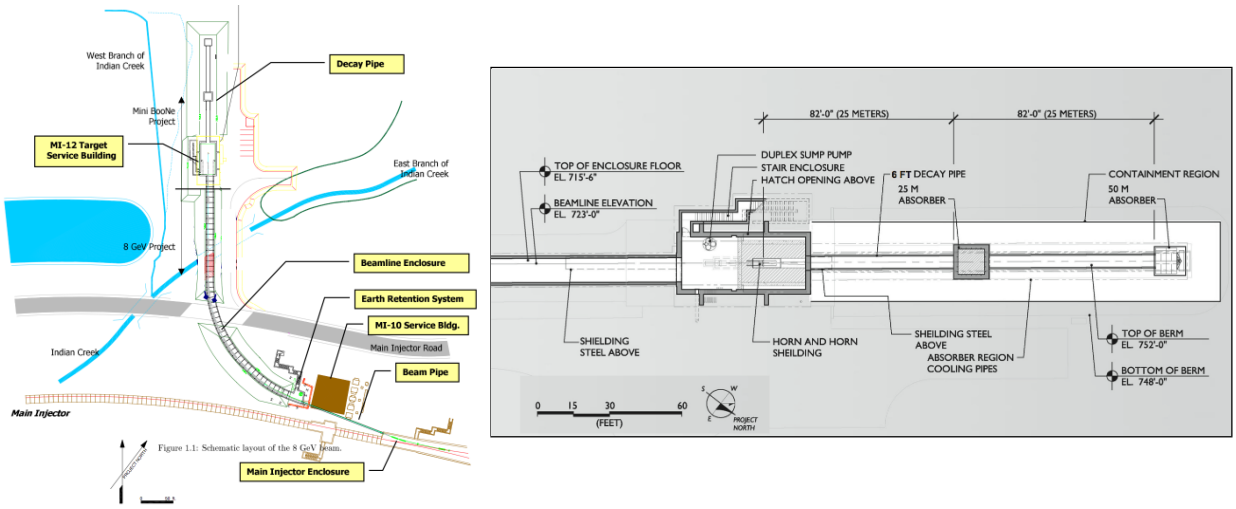

Figure 4.4: Schematics of the experimental setup and operations of the BNB at Fermilab, USA. The left diagram shows an aerial view of the 8 GeV kinetic energy protons injected from the Booster accelerator into the target hall via the Main Injector; the right picture depicts a side-on view of the target hall and the decay pipe, showing how the magnetically focused hadrons resulting from the proton interactions with the beryllium target decay to result in a predominantly ν_μ beam, with few $\bar{\nu}_\mu$ and trace $\nu_e + \bar{\nu}_e$. Image sourced from [114].

beam of majority $\bar{\nu}_\mu$, few ν_μ (but a greater proportion than $\bar{\nu}_\mu$ in neutrino mode) and an intrinsic contamination of $\nu_e + \bar{\nu}_e$ [114].

Nominally, the BNB produces beam spill pulses of $\sim 5 \times 10^{12}$ POT for 1.6 µs. Thanks to its operation as a stable neutrino beam since 2002, the flavour composition and energy spectrum of the BNB is extremely well understood and is emulated in a detailed simulation developed by the MiniBooNE collaboration [134], using proton-beryllium interaction data from the HARP experiment at CERN [135]. Detailed systematic errors have also been characterised with a total error of 8% at peak ν_μ flux and slightly larger in the high and low energy regions [136]. Contemporary data from the NA61/SHINE experiment at CERN will be invaluable at reducing systematic uncertainties and better constraining flux estimations for these low and high energy regions by providing a wider phase space of beam energy [137].

SBND is positioned close enough to the BNB target such that it will detect neutrinos emitted at angles up to 2° deviations from the central beamline direction. However, the BNB beamline intersects SBND 0.74 m east of its CPA to not only avoid concentrating neutrino events around the cathode, but also to take advantage of the PRISM effect, where the ν_μ energy spectrum becomes narrower and more concentrated the greater the angle neutrinos deviate from the central beamline. This is seen in Figure 4.5, showing the estimated ν_μ flux on SBND as a function of neutrino energy for different off-axis angles.

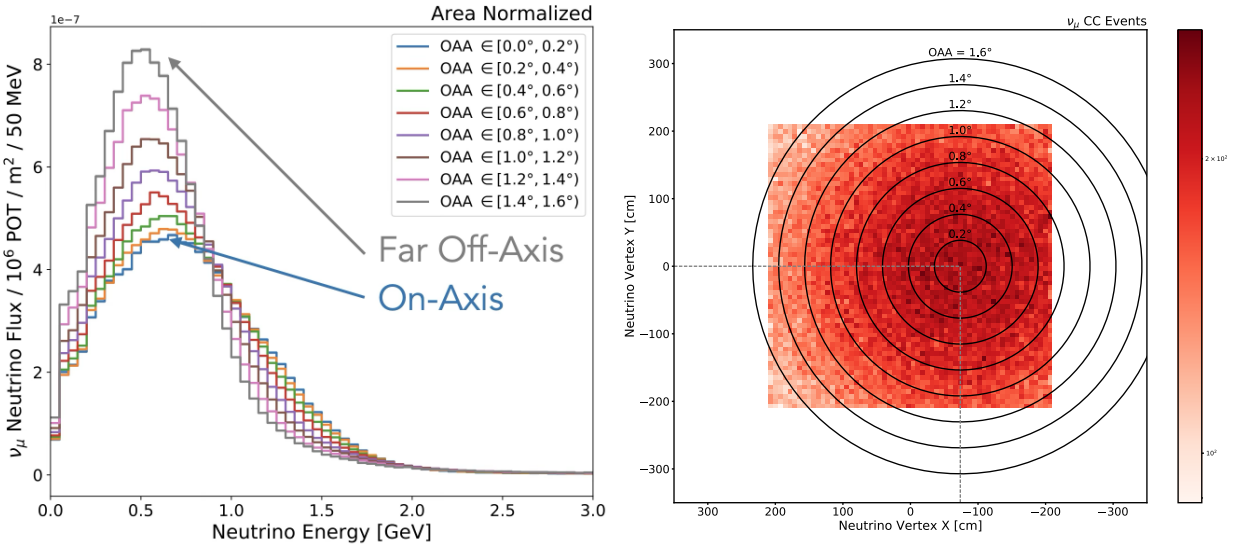

Figure 4.5: Simulated ν_μ beam flux from the BNB detected by SBND for off axis angles in increments of 0.2° from 0° to 1.6°. Left plot shows ν_μ flux with respect to neutrino energy, whereas the right plot shows the peak ν_μ CC interaction event rate with respect to the beam intersection with the east TPC of SBND. Plots sourced from [99].

Figure 4.5 shows how the peak ν_μ energy decreases the greater the lateral deviation neutrinos are directed from the central beamline, with a narrower ν_μ energy distribution. This PRISM effect results in an overall energy shift up to around 200 MeV in the most off-axis angle for SBND, leading to the potential for interaction model energy dependence and neutrino-argon cross-section measurements segmented by off-axis angle. SBND-PRISM allows for unique constraints on systematic uncertainties based on selecting neutrino flux spectra at different off-axis angles, which also helps remove background events with different angular distributions, as well as expanding the physics potential of SBND [99].

4.3 SBND Experimental Overview

SBND and ICARUS employ the same LArTPC technology outlined in Section 3.2, with differences arising in detector geometry, various experimental parameters and the implementation of detector subsystems. Where SBND proves itself as a world-leading neutrino detector is the efficacy to which its LArTPC technology interfaces with other detector subsystems, such as the PDS and CRT arrays, as well as utilising an advanced DAQ and electronics readout system to turn raw ionisation signals into readable physics data.

4.3.1 TPC and Cryostat

SBND sports a membrane-style stainless steel cryostat, similar to the ProtoDUNE Horizontal Drift (NP04) at the CERN Neutrino Platform [138]. The entire LArTPC is affixed to a cryostat top cap, suspending it in 220 tons of LAr volume. Figure 4.6 shows schematics of the SBND field cage and cryostat, as well as the various sub-detectors and LArTPC components. The field cage contained within the detector has a total volume of 5.0 m × 4.0 m × 4.0 m, with a central CPA splitting the detector into two LArTPC drift volumes with an APA on the east and west walls of the LArTPC. This gives SBND two conjoined TPC regions, each with 2 m of drift distance equating to a maximum electron drift time of 1.3 ms for a nominal electric field of 500 V/cm, where each field cage is surrounded by roll formed aluminium profiles and PolyEthylene (PE) end caps for insulation.

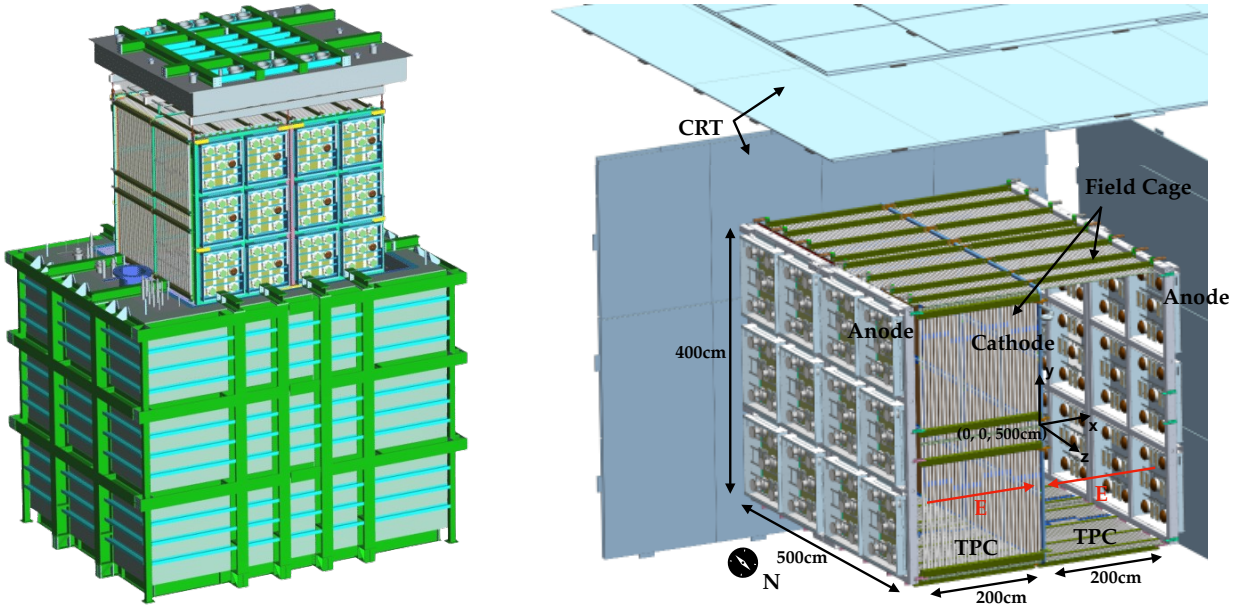

Figure 4.6: Schematic of the SBND cryostat with the TPC being lifted out by the top cap (left; image sourced from [84]). Drawing of the SBND TPC, the west, south and top-low CRT planes and the PDS array (right; image sourced from [139]). The north, east, bottom and top-high CRT walls, the cryostat and part of the north-side of the vertical drift cage have been removed for visual clarity.

Behind each APA is a composite PDS outfitted with photon detectors, some coated with wavelength-shifting compounds, TPB or ParaTerPhenyl (PTP). Additionally, the large active LAr volume of SBND and its placement above ground makes cosmic-ray interactions the largest background source, which is why all six sides of the detector is outfitted with full planes of CRT panels (with two planes on the top). These are designed to mitigate cosmic-ray backgrounds such that they are not conflated with neutrino interaction signals. A

detailed breakdown of the experimental setup and operations of the PDS and CRT systems are outlined in Sections 4.3.2 and 4.3.3 respectively.

The CPA is composed of two adjacent welded stainless steel mesh panel arrays, with a thin layer of reflective polymeric foil lined with TPB sitting between them, enhancing the total light yield by reflecting emitted photons back towards the PDS located behind both APAs. Each APA consists of a 4.0 m × 5.0 m steel frame supporting three planes of 150 µm diameter copper-beryllium wires, with pitch and plane spacing of 3 mm, tensioned at 7 N to prevent wire sagging in the cool LAr volume. SBND utilises the same three-plane projective wire readout setup outlined in Section 3.2, with two induction planes aligned at ±60° from the vertical collection plane.

Negatively voltage-biasing first induction plane wires allows ionisation electrons to induce signals on the induction plane wires as they drift past, then terminate on the positively voltage-biased collection plane wires. Attached to the edges of each APA is the cold electronics system, composed of custom-made pre-amplifiers, commercial Analogue-to-Digital Conversion (ADC) units and Field-Programmable Gate Array (FPGA) mounted motherboards reading out signals. These signals are sent to the warm electronics systems, external to the cryostat, where they are shaped and built into readable event packets for data analysis [84]. The SBND readout electronics chain is further elaborated upon in Section 4.3.4.

4.3.2 Photon Detection System

Sufficient collection of scintillation light is essential in determining the initial neutrino interaction time t_0, since photons traverse the entire drift volume within nanoseconds, where ionisation electrons typically take around a few milliseconds. Scintillation information can also be used to aid in calorimetric reconstruction of the initial interaction in conjunction with using the ionisation electron signals on collection plane wires, previously demonstrated by the LArIAT experiment [90]. As such, SBND utilises the PDS, located behind both APAs, to capture scintillation photons released from argon atoms, providing an R&D ground for light propagation and detection in LAr for large-scale LArTPC experiments. Figure 4.7 shows a schematic of the PDS implemented around the SBND field cage.

The SBND PDS consists of 24 planes of 1.25 m × 1.33 m boxes installed in the two optically-isolated TPC volumes behind the east and west APAs, each containing 13 photon detectors that collect scintillation light. Five of the photon detectors in each PDS box are circular 8 inch diameter Hamamatsu R5912-MOD model PMT devices [140], and the remaining eight are purpose-built X-ARAPUCAs [141], which trap photons inside a highly reflective box, using a wavelength-shifting slab to increase photon collection probability

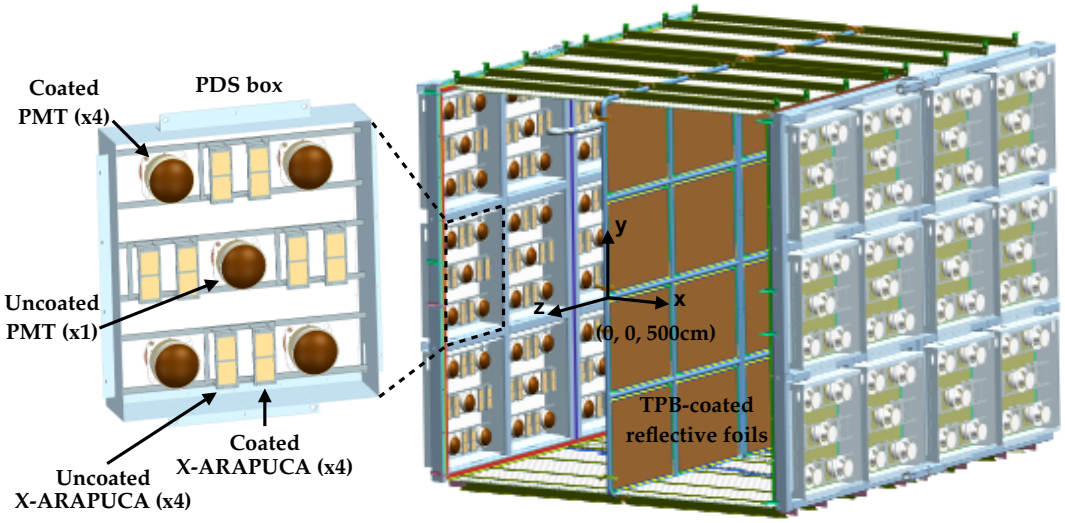

Figure 4.7: Schematics of a PDS box (left) containing PhotoMultiplier Tubes (PMTs) and X-ARAPUCAs, and the full SBND PDS shown around the LArTPC (right). Both diagrams sourced from [139].

by the internal Silicon PhotoMultipler (SiPM) readout. A total of 120 PMTs and 192 X-ARAPUCA devices make up the entire SBND PDS.

The PMTs have their scintillation signals read out using 500 MHz sampling CAEN VX1730SB digitiser modules [142], whereas the X-ARAPUCA devices are read out by front-end amplifiers similar to the DUNE FD1-HD PDS readout system [143], but instead located inside the cryostat using CAEN V1740B modules [144]. Further down the electronics readout chain, only the PMTs are used to build triggers, making them the primary photon collection devices. Four out of the five PMTs and four out of the eight X-ARAPUCA devices on each PDS box are coated with wavelength-shifting compounds (TPB for the PMTs and PTP for the X-ARAPUCAs) to shift the 128 nm photon wavelengths to the UV range. The remainder of the PMTs and X-ARAPUCAs are left uncoated to collect photons reflected off of the TPB-coated foil lining the CPA that have already been wavelength-shifted. This combination of coated and uncoated photon collection devices allows SBND to increase light yield and also make the distinction between photons directly emitted from argon de-excitation and secondary photons reflected/re-emitted in the UV range [139].

4.3.3 Cosmic Ray Tagger Array

Cosmic-rays consist primarily of high energy protons and alpha particles, originating from outside the solar system, which interact with air molecules in the Earth's atmosphere to create kaons and pions, decaying to atmospheric muons. When these high energy cosmic-

ray muons pass through the active LAr volume, they release high energy ionisation electrons from argon atoms (δ-rays), leading to EM showers due to further ionisation electron releases and photon emissions from bremsstrahlung radiation. Said photon signals can be conflated with ν_e signals by subsequent pair production or Compton scattering with argon atoms, producing further cascades of ν_e, π^0 or $\mu^{\pm}$ in the final state.

To mitigate these cosmic-ray backgrounds, the SBND cryostat is surrounded with aluminium panels consisting of scintillator strips and SiPM readouts, each acting as a cosmic-ray muon tracker, or CRT, shown in Figure 4.8. Each CRT detects incoming/outgoing cosmic-ray muons, measuring their interaction time and flight path outside the cryostat, identifying signals in the TPC readout that match the position of the detected cosmic-ray muon interaction and removing them from the data stream. SBND is surrounded by seven planes of CRTs, consisting of 146 total CRT modules: one plane on all sides of the cryostat, with two planes on the top, providing full 4π solid angle coverage [145].

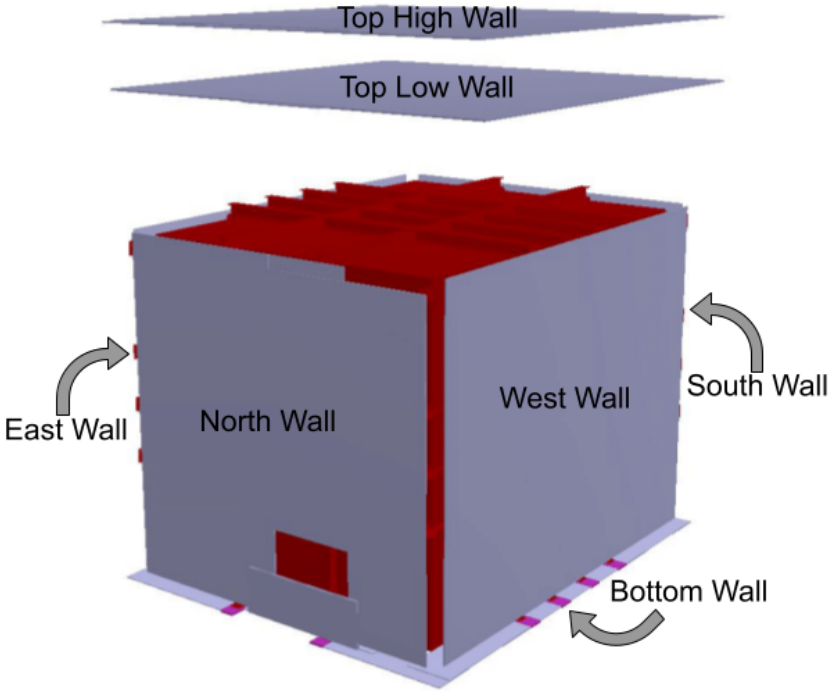

Figure 4.8: Schematic showing the orientation of the seven CRT planes (grey) around the SBND cryostat (red), viewed from the north-west side of the cryostat. Image produced using the SBND GDML [146].

Incoming cosmic-ray muons pass through the SBND TPC volume, interacting with CRTs on one side of the cryostat, leaving a track in the TPC(s), then interacting with CRTs on the outgoing side. The TPCs and CRTs are different subsystems, so matching the timing information of the same track detected by the TPCs and CRTs requires full

reconstruction of the muon. Once this is achieved, cosmic-ray muon backgrounds can be distinguished from muons resulting from ν_μ-Ar interactions. There are three main sizes of CRT panel, as shown in Figure 4.9. These include the full size 3.6 m × 1.8 m modules, which comprise the vast majority of CRT modules around SBND; the half-length 1.8 m × 1.8 m square modules, and the half-width 2.72 m × 0.96 m modules. The latter two module sizes are utilised to work around protrusions in the SBND cryostat such as the LAr inlet pipe, as seen on the north wall plane of CRTs in Figure 4.8.

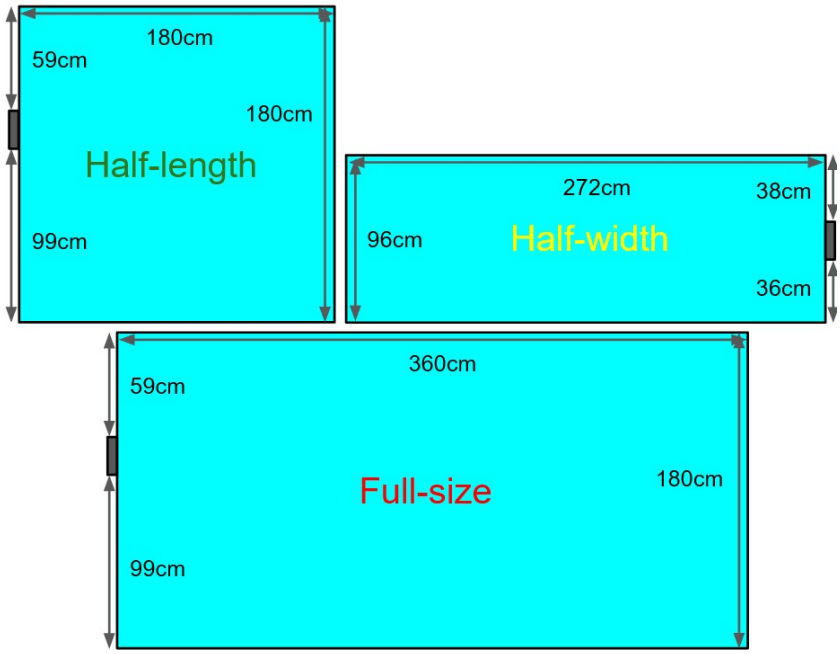

Figure 4.9: Schematic showing the three sizes of CRT modules SBND utilises. The grey rectangles attached to each module are front-end boards which process, amplify and shape SiPM data into waveforms.

All CRT walls around the SBND cryostat have the same size modules within their own wall, except the north wall which utilises 14 full-size, 2 half-width and 2 half-length modules. The east and west walls are composed of 18 full-size modules each, with the south wall sporting 16 full-size modules. The bottom plane is composed entirely of 26 half-width modules, with the top-low plane having 5 half-length and 20 full-size modules and the top-high plane having 25 full-size modules.

The CRT panels made for SBND were constructed at the Laboratory for High Energy Physics (LHEP) in Bern, with some repurposed from other Fermilab experiments such as MicroBooNE and MINOS. Each full size CRT panel consists of 16 BC-440 plastic scintillating strips - with dimensions 1 cm × 10 cm × 400 cm - shielded from external light by an aluminium casing. Figure 4.10 shows the simplified innards of a CRT panel and how

they tag cosmic-ray muon tracks. Photons emitted from muon interactions with scintillator strips are collected at one of two ends of the CRT panel, where the light is wavelength-shifted by two fibres and collected by two SiPMs, turning their signals into a measurable current. This current is then amplified and shaped by a data processing unit connected to the end of the CRT called a Front-End Board (FEB), which outputs data directly to the DAQ. Since a single CRT module's output data can only indicate which individual scintillator strip has been hit, x and y spatial coordinates of the tracks can only be reconstructed when the CRT panels are orthogonal to each other, shown in the right plot of Figure 4.10.

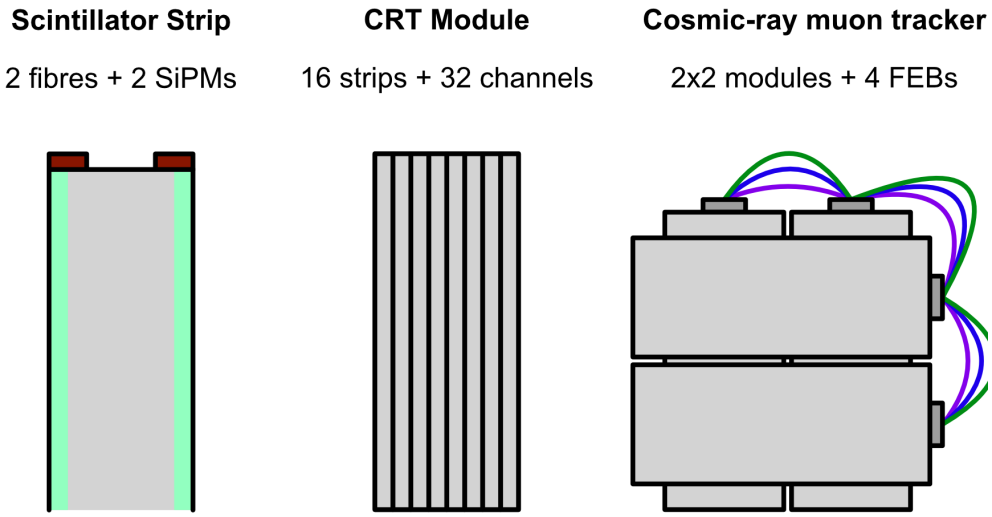

Figure 4.10: Scintillator strips (left) in a CRT module (middle) and four modules aligned orthogonally (right) to constrain x and y coordinates of cosmic-ray muon tracks. FEBs transfer information between modules through timing, logic and data cables.

The addition of a second CRT plane on top of the detector, the plane experiencing the highest muon flux, form a cosmic-ray muon telescope with a coordinate resolution of ∼3 cm and an angular resolution of ∼0.03 rad. Full rejection of cosmic-ray muon backgrounds is achieved by matching the time distribution and path extrapolation of muons tagged by CRTs with muon-like signals reconstructed from APA wires and the PDS. All seven CRT planes are required for this process, as well as utilising neural networks to recognise cosmic-ray muon-like tracks detected by the TPC wires to be rejected [145]. Every CRT panel has been tested and calibrated for their light yield, cosmic-ray muon detection efficiency and spatial/timing coordinate resolution at LHEP. Work only needed to be done calibrating the FEBs instead of the CRT modules, where the work done characterising the internal FEB clocks used to timestamp each cosmic-ray muon hit is outlined in Chapter 5.

4.3.4 Readout Electronics

In order for the ionisation electron signals from particle interactions with argon atoms within the SBND TPC to be read out for data analysis, a complex and sophisticated chain of readout electronics is utilised to amplify signals, form triggers with other subsystems and build events. This is split between the cold and warm electronics systems, with the former being submerged in the cryogenic LAr attached to the APA frames, minimising thermal noise and cable lengths, and the latter stationed across multiple server racks adjacent to the cryostat. Figure 4.11 shows how the cold electronics boards are directly connected to the APAs at the top and sides of the assembly.

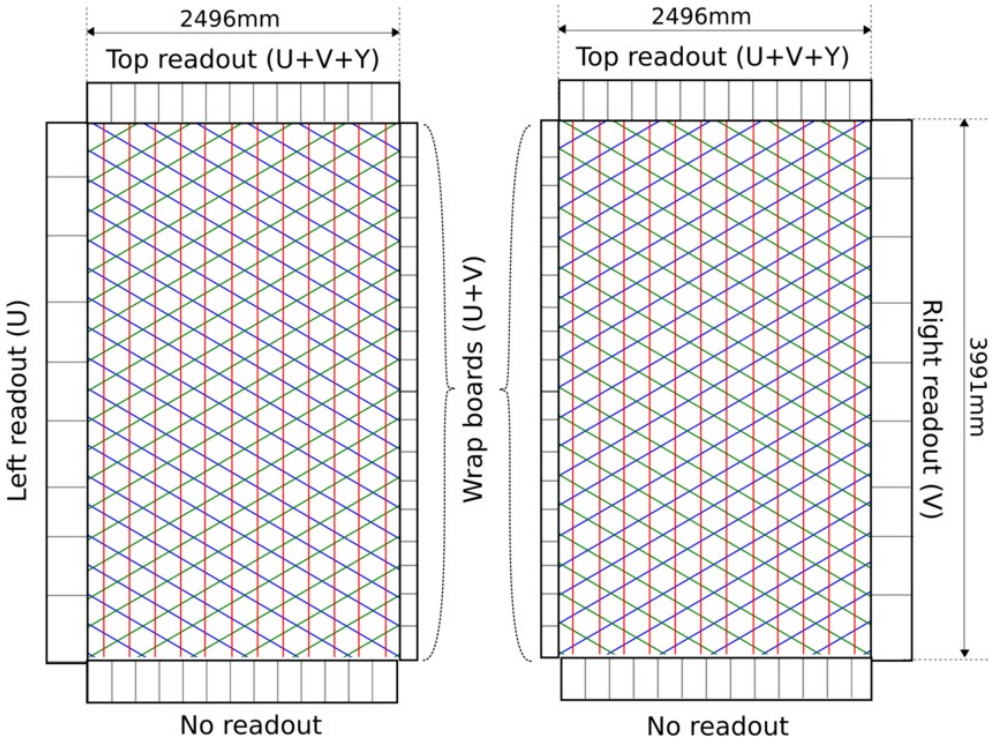

Figure 4.11: Position of cold electronics readout boards around a pair of APAs [91]

There are a total of 11,264 TPC readout wires across both APAs collecting ionisation electron signal information in SBND, which are amplified and digitised by the cold electronics readout boards connected to the APA. The cold electronics chain consists of 88 Front-End Mother Boards (FEMB), each fitted with 128 readout channels; one readout channel for each APA wire, with the signal amplification driven by a set of eight Application-Specific Integrated Circuit (ASIC) chips per FEMB, and linear ADC by 16 digitisers per ASIC chip. 128 readout channels of digitised TPC wire readout for each FEMB, and 88 total FEMBs gives a total of 11,264 readout channels; one for each TPC wire.

Digitised and amplified signals are processed through 24 Warm Interface Boards (WIB), which act as the buffer between the front-end (cold) and back-end (warm) electronics, sending data to 11 TPC crates. Each TPC crate consists of a Nevis Trigger Board (NTB) and 16 more FEMBs, where the NTB receives trigger information from the Penn Trigger Board (PTB), which builds a trigger based on the other subsystems (i.e. PDS, CRT, etc.), sending the resultant signal to a series of board readers to produce data fragments and build events in the SBND DAQ system. These events are then sent to server racks and/or hard disk for storage, allowing for offline data analysis to occur. This TPC readout electronics chain turns ionisation electron signals on APA wires into digitised events with a signal waveform for each wire plane.

4.3.5 Trigger and Data Acquisition

The SBND trigger builds events and controls the data readout stream window based on certain conditions from various subsystems being met, synchronising the data from all readout components and timing from the beam and GPS. Data is synchronised from the PDS, TPC, CRT, beam and the DAQ system, which provide inputs into the PTB to create triggers and synchronise data from all these subsystems. The PTB employs hierarchical logic by forming Low Level Triggers (LLTs) from different subsystem inputs into a number of High Level Triggers (HLTs), outputting a given signal in a certain data stream when selected HLTs are outputted within a chosen timeframe.

Timing of all SBND subsystems is synchronised to a White Rabbit (WR) Simple PCIe Express FMC Carrier (SPEC) Time to Digit Converter (TDC) unit, providing sub-nanosecond timing precision by phase-locking internal subsystem clocks to a GPS-locked global clock. WR is an Ethernet-based network, making use of a SPEC unit with multiple TDC modules to provide all subsystems a 10 MHz timing signal to all events [147]. The TDC of the timestamp generator within each CRT FEB is composed of a coarse counter - operating at a frequency of 250 MHz - and a delay-chain interpolator, allowing for $\sim$1 ns precision for each timestamp. Additionally, there is a 20 MHz Voltage-Controlled Crystal Oscillator (VCXO) used as a source for the reference clock of the timing circuit.

The readout window for the SBND trigger is 1.75 ms, starting 0.25 ms before the BNB beam spill, preceded by a Beam Extraction Signal (BES) sent to the PTB which initiates the readout window, encompassing the 1.3 ms maximum ionisation electron drift time within each TPC. The CRT and PMT readout windows start 1.5 ms before the beam spill, giving them a full readout window of 3 ms. PTB triggers are sent to the NTB, which distributes this trigger to the TPC crates whilst also providing additional triggers and conditions to

the other subsystems. This data stream has two settings: either continuous lossy data is sent to the TPC crates containing only TPC data, or lossless data built from the PTB trigger containing data from all other subsystems.

The SBND DAQ is composed of a chain of multiple board-readers and servers which converts signals from all the detector subsystems into readable physics data. The DAQ uses the Artdaq framework, capable of configuring readout electronics, interfacing between different systems, event-building and permanently storing physics data. Outputs from the SBND trigger are fed into the DAQ system along with data from the TPC, PDS and CRT subsystems, synchronising their timing to the WR SPEC-TDC, aggregating them into ROOT files with the LArSoft data format, used for offline physics analysis.

4.4 SBND Simulation and Reconstruction Software

The SBND simulation underpins the experiment's rich measurement program with high statistics MC event samples and models the signals generated by ionisation electrons on the detector readout wires. Section 4.4.1 provides a description of how the SBND simulation and MC event samples are generated. Details of the mechanisms in which MC particles are created, transported and detected by the PDS and CRTs are outlined in Sections 4.4.2 and 4.4.3 respectively. The SBND software framework contains workflows that decode and reconstruct raw data from SBND data runs, turning them into readable files which can be used in offline physics analyses, described in Section 4.4.4.

4.4.1 Monte Carlo Event Generation

The SBND simulation utilises the LArSoft coding package [148], developed from the Art event processing framework [149], to create MC particles and model signals outputted by TPC readout wires, emulating output data in the form of ROOT files [150]. There are multiple stages to LArSoft simulations, starting from modelling the SBND detector geometry using the Geometry Description Markup Language (GDML), distinguishing the outside world, detector enclosure, cryostat, TPC, PDS and CRTs. MC particles are then created using event generator programs in LArSoft, such as GENIE, which generates beam neutrinos [151]; and CORSIKA, used to simulate cosmic-ray interactions with the Earth's atmosphere, producing atmospheric muons contributing to SBND backgrounds [152].

Each generated particle is produced with a Particle Data Group (PDG) code (defining what type of SM particle it is), momentum 4-vector and coordinates of the track origin within (or outside) the detector. The GENIE event generator package also models dif-

ferential cross-sections on individual nuclei, and computes their possible final states and most likely interaction type. GENIE also provides re-weighting coefficients for calculating systematic uncertainties based on theoretical and empirical models of neutrino interactions with argon [151]. These MC truth particles are then fed through GEANT4 simulations, propagating them through liquid argon, simulating particle interactions with argon atoms, producing scintillation light and ionisation electrons [153]. This outputs ionisation electron signals induced on APA readout wires as a function of time, including LArTPC systematic effects such as the smearing of ionisation electron spatial distributions due to diffusion and SCE, the effects of which are outlined in Section 3.4.

The next stage of the LArSoft simulation involves simulating the detector systematics of a raw TPC ionisation signal. Signals are shaped and smeared through convolution with the field response, modelled by Garfield [154], and a parametrised electronics response function. Wire-Cell is a coding package utilised by SBND to extract ionisation signals from deconvolved raw ADC waveforms using 2D signal processing, but is used in this workflow to model the 2D response to induced and collected charge on TPC readout wires [155]. A typical 2D simulated ADC waveform is generated through GEANT4 via a signal convolution of the ionisation electron signals induced on TPC wires and signal broadening effects on the drifting ionisation electrons such as diffusion and SCE. This waveform is then convolved with the total wire response, modelled by Wire-Cell through a signal convolution of the field and electronics response functions. Then, the wire noise is simulated and added to the waveform, which is characterised through a data-driven analytical method. Finally, the waveform is broadened through simulation of the digitisation process, equivalent to transforming voltage waveforms into ADC waveforms.

Finally, after the MC truth information has been fully simulated, the reconstruction stage of the LArSoft workflow is executed, which is split into two stages. The first stage runs all the quick, less computationally intensive processes such that it can be instantly applied to SBND data. This includes deconvolving the scintillation light waveforms from the PDS and matching their signals with the TPC (and optionally CRT) signals, then employing clustering and hit-finding algorithms to reconstruct tracks and build events. The second reconstruction stage performs higher level tasks for more sophisticated data analysis, such as running Pandora's pattern recognition algorithms to identify particles from tracks and showers, or extracting calorimetric (dE/dx) information of the initial particle [156].

4.4.2 PDS Simulation and Reconstruction

As well as simulating and reconstructing ionisation electron signals on APA wires, the SBND simulation also has to emulate signals outputted from other detector subsystems, such as the PDS. GEANT4 generates scintillation photons based on the kinematics of the original interaction: $\sim 20,000$ γ/MeV in LAr subject to an electric field of 500 V/cm [157, 158]. Scintillation photon propagation through LAr is then modelled using a semi-analytical algorithm simulating the transport effects until they are detected by the simulated PDS system [123]. Throughout this propagation, photons can undergo processes such as Rayleigh scattering, reflections and refractions at detector boundaries, absorptions and re-emissions from argon atoms, and wavelength shifting.

Next, the arrival time distribution of photons detected by the PDS is simulated. This implements a double exponential decay structure characterised by fast and slow components relating to the singlet and triplet de-excitation channels of argon, holding values of 6 ns and 1.6 µs respectively [159]. Dedicated measurements of light signals without wavelength shifting showed the slow decay constant to be closer to 1.3 µs, so this value is used in SBND simulations. Rayleigh scattering and boundary reflections also broaden the arrival time of photons to the PDS, where semi-analytical models are used to simulate this broadening [123], as well as time delays occurring due to the process of wavelength shifting photons using TPB or PTP. Photon detection efficiencies are simulated as global factors in the estimation of number of photons collected by the PDS.

Each digitised and shaped photon waveform is converted to an output signal known as a Single Electron Response (SER), shown in Figure 4.12 for the PMTs and X-ARAPUCAs. Photon detectors have their outputs AC-coupled into a single cable, minimising readout times, making SER signals bipolar. Simulated optical waveforms are generated through scaling the number of photoelectrons outputted by the photon detectors by their previously calculated efficiencies, then convolving the arrival time distribution with the SER signal, applying Gaussian smearing to account for noise variations.

SER signals can vary significantly based on the photon detector, with responses spanning approximately 50 ns for the PMTs and 500 ns for the X-ARAPUCAs, as shown in Figure 4.12, and as such both subsystems require different reconstruction algorithms. Extracting the number of photoelectrons from PDS waveforms involves integrating the area under each waveform, subtracting the ADC baseline which can be shifted by multiple photons arriving at the same time. After deconvolving the waveform and applying a Gaussian filter to eliminate low/high frequency noise, optical hits are identified as photon signal pulses with amplitudes greater than 1/4 the SER height and 3 times the standard deviation of

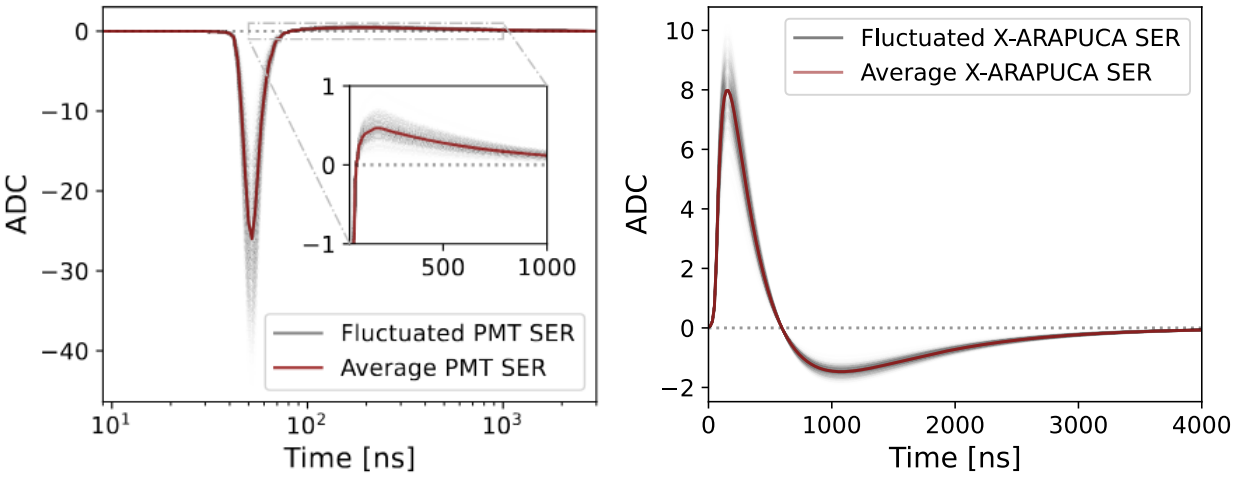

Figure 4.12: Measured SER for PMTs (left; logarithmic scale) and X-ARAPUCAs (right; linear scale) in SBND. Simulated signal fluctuations of 22% for PMTs and 10% for X-ARAPUCA signals are also shown by grey shading. Image sourced from [139].

the baseline Root Mean Square (RMS). Then the number of photoelectrons, and therefore initial photon signal, is reconstructed by integrating the area under the optical pulse signal, where the sum of optical hits is used to define the distribution of scintillation photons released by a given TPC interaction.

4.4.3 CRT Simulation and Reconstruction

CRT data can only be fully understood when validated by a simulation of cosmic-ray muon tracks traversing multiple CRT planes. Firstly, the geometry of the CRTs around the SBND cryostat is modelled using a GDML, pictured in Figure 4.8. In the SBND simulation, LArSoft is used to generate cosmic-ray induced atmospheric muons using CORSIKA, then GEANT4 simulates energy depositions of muons on scintillator strips within individual CRTs. An interface program matches these hits with x, y and z coordinates and a timestamp based on the scintillator strip channel and FEB number of the CRT panel at a specific time. Finally, detector effects such as SBND triggering, ADC thresholds and timing emulations are implemented to have the simulation mimic CRT data.

The results of reconstructing simulated CRT data is then directly compared to reconstruction of real CRT data from SBND data runs in order to validate the reconstruction methodology. After decoding real CRT data, the CRT reconstruction workflow starts by identifying which scintillator strip channels exceed the set ADC amplitude threshold constituting a muon hit, then groups coincidences between overlapping orthogonal modules in the same plane. 3D positions of muon hits are then created from these hit clusters, before

matching these hits in time between hits on other CRT walls, creating cosmic-ray muon tracks crossing the detector volume. Finally, algorithms are run matching muon tracks reconstructed by the CRTs with those reconstructed within the TPC, which is currently performed using Pandora [156].

4.4.4 SBND Data Decoding

SBND software contains algorithms that use LArSoft to decode and reconstruct SBND data into readable event files for physics analysis. SBND data is fed directly into a decoder program, which differs depending on the subsystem outputting said data. Each SBND subsystem has its own dedicated data decoder, which converts raw data from the DAQ system into data products which are readable by LArSoft and maps the detected subsystem to its corresponding channel number in the readout electronics chain. The outputs of the decoder are propagated directly into the reconstruction stages of LArSoft.

The first LArSoft reconstruction stage removes coherent noise from TPC wire channels, performs 2D signal deconvolution extracting the ionisation charge from the wire response, executes hit finding algorithms and implements space points along each reconstructed track to identify individual hits in the track at each time tick $t_s = 0.5$ µs. The second stage reconstructs tracks or particle showers, extracting calorimetric information and identifying particles within said track, as well as matching hits detected in the TPC with the PDS and CRT subsystems, along with other machine learning processes.

These reconstruction stages in the SBND data workflow are largely the same as their MC counterparts, with a few changes related to the different format SBND data has to MC events, as well as correcting any TPC-related issues in the post-readout electronics stage. A list of dead or missing TPC channels is included in this stage, containing information on dead FEMBs, shorted or noisy wires which are not included in the SBND reconstruction workflow. These dead components of the detector need to be accounted for in the reconstruction workflow as they cannot be replaced due to them being sealed inside the SBND cryostat. Other differences in the data workflow include coherent noise removal on bulk waveforms based on data-driven calibrations (single channel noise removal is applied in both MC and data), and signal processing now occurring in the first reconstruction stage instead of having a dedicated standalone stage in MC. Additionally, there are significant reductions in what modules and reconstruction algorithms are run compared to the MC workflow, along with a number of additional configuration changes.

Chapter 5

Calibrating the Internal Clock Drift of CRTs at SBND

Previously outlined in Section 4.3.3, in order for SBND to fully mitigate background signals from cosmic-ray muon tracks, 146 extruded scintillator strip panels are implemented around the detector, each with SiPM readouts to detect the timing and flight path of cosmic-ray muons, so they can be effectively removed from the process of reconstructing BNB neutrino events in the TPC [145]. Full removal of cosmic-ray muon backgrounds from the dataset requires the timing and spatial precision to which muons are detected by the SBND CRT system to be of $\mathcal{O}(2$ ns). Muon event timestamps are processed by a hardware unit attached to the edge of each CRT, called a FEB, where this internal timestamp has an intrinsic drift and distribution that needs to be calibrated for optimal cosmic-ray background mitigation.

This chapter outlines the work done on characterising the timing drift and resolution of each FEB attached to every CRT on the north wall of SBND, eventually applying the methodology to the other six CRT planes [160]. Section 5.1 describes the design and operation of a FEB unit. Section 5.2 outlines the experimental setup and functionality of the SBND DAQ system when used to collect SBND CRT commissioning data. Section 5.3 contains the timing calibration methodology and result applied to CRT modules collecting cosmic-ray data in-situ, before their installation on the north wall of the SBND cryostat. Section 5.4 contains conclusions to the work.

5.1 SBND Front-End Board Design and Operation

Transfer of timing and logic triggers between CRT modules, and sending SiPM data to the DAQ, are driven by cables extruding from each FEB attached to their respective CRT,

pictured in Figure 5.1. Logic triggers between modules are transferred through the T_{in} and T_{out} inputs, timing information is transferred through the T_0 and T_1 inputs, and SiPM data is sent to the DAQ through Ethernet data ports. FEBs also provide an adjustable bias voltage to each of the SiPMs within the module, which affects the number of photoelectrons outputted by the SiPM from a muon interaction with the scintillator strips [160].

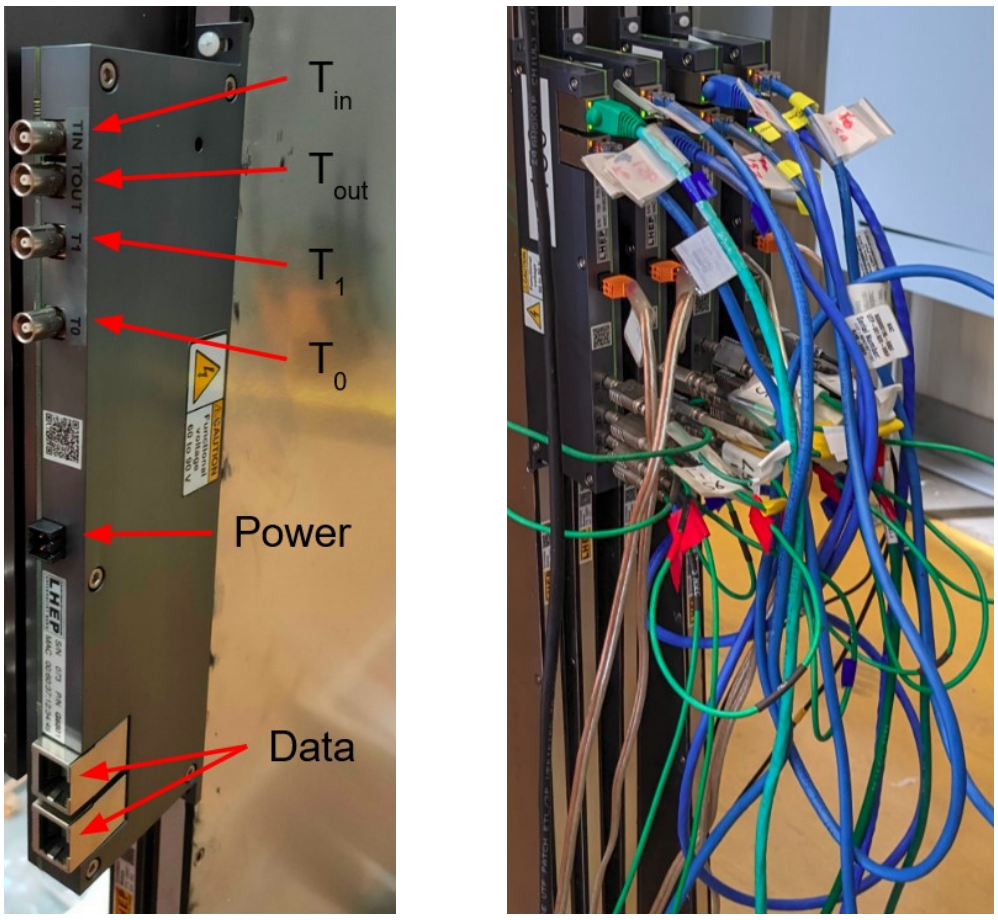

Figure 5.1: Picture of a single FEB when plugged into a CRT panel with no input cables (left) and multiple FEBs daisy-chained together with labelled cables (right).

Each FEB has internal trigger and logic capabilities to build events when multiple channels output a signal within a 150 ns window. There are 32 SiPM channels outputting scintillation signals within each CRT module; two for each scintillator strip for 16 strips. Single-hit events from each SiPM are disregarded due to contamination from gamma rays resulting from radiological decays in the aluminium casing and the surrounding concrete. This is enforced by employing a coincidence trigger on pairs of SiPMs on each scintillator strip, known as 2-fold coincidence; corresponding to a single muon event within a CRT.

To implement a 4-fold coincidence trigger, two CRT modules need to be aligned ortho-

gonally, with coaxial cables connecting the T_{in} port on one module to the T_{out} port on the other, and vice versa. In 4-fold coincidence mode, when a scintillator strip is hit on one CRT module and both SiPMs connected to that strip output coincidence signals, the FEB opens a 150 ns trigger window. When a similar 2-fold coincidence signal from an orthogonally aligned CRT module connected via alternating T_{in}/T_{out} connectors falls inside this trigger window, a 4-fold coincidence muon event is constructed by the FEB and outputted to the DAQ. A single CRT plane around SBND consists of two layers of orthogonally aligned CRT modules, so 4-fold coincidence is used to trigger on a single CRT plane and is the chosen coincidence mode for most SBND data runs. This can also be extended to 8-fold coincidence mode, implementing a trigger window between two horizontal and two vertical CRT modules connected via alternating T_{in}/T_{out} connectors.

Within each FEB is two internal clocks: T_0 and T_1, providing each event with a TS0 and TS1 timestamp value respectively, relative to the last interval in which these two clocks reset to zero seconds. More information on the exact functionality of the T_0 and T_1 clocks will be expanded upon in Section 5.2. Every module in each CRT plane is daisy-chained together with these T_0 and T_1 cables, so all timing information can be sent to the DAQ for additional data processing. Each FEB is also equipped with two Ethernet ports to daisy-chain the CRT modules together, sending SiPM data to the DAQ.

5.2 The CRT Data Acquisition System

A detailed breakdown of the SBND DAQ is outlined in Section 4.3.5, but this section describes how the DAQ is used to specifically collect CRT data. Most of the signal processing occurs within the FEBs, but event-building and timing synchronisation happens after the FEB sends these signals to the DAQ. Timing of the internal T_0 and T_1 clocks of the FEBs is synchronised to a WR SPEC-TDC unit, providing sub-nanosecond timing precision.

The WR SPEC-TDC unit is able to synchronise the internal clocks of all FEBs using a GPS-locked global clock (characterised by a UNIX timestamp) by sending Pulse Per Second (PPS) signals to all FEBs, measuring the time relative to the last PPS signal received. In the CRT subsystem, these PPS timestamps are transferred between FEBs through the T_0 cables. Events processed by the FEBs have a TS0 value relative to when the last PPS signal was received, resetting the T_0 clock to zero until the FEB receives the next PPS signal.

The T_1 clock operates similarly to the T_0 clock, but has a reset window based on when the DAQ receives a BES. When the BNB is running, the T_1 clock will reset shortly after a beam spill event, which occurs at a frequency of $\sim$5 Hz, arriving 333 μs before the beam

spill event. However, since the work presented in this chapter involved in-situ cosmic-ray muon calibrations, the T_1 clock reset window differed depending on the experimental setup. Put simply, the T_0 clock is for DAQ timing stabilisation, and the T_1 clock is to confine packets of muon beam interactions within the beam spill window.

The DAQ configuration for collecting cosmic-ray muon data with CRT modules in-situ involves integrating the PTB, TDC and a CAEN 1730 for PMT signal digitisation. The DAQ takes SiPM signals processed by the FEBs and reconstructs them into events with a timestamp and ADC waveform. Running the CRT DAQ involves writing configuration files containing the list of FEBs in the data chain, setting the T_1 reset window, and keeping track of any errors appearing on the DAQ message viewer. Every event outputted by the FEBs has a parameter assigned to it, called a flag, based on the corresponding TS0 and TS1 values, which is a combination of four binary fields resulting in a 16-bit value:

- Bit 0: presence of T_0 signal - if the T_0 signal is missing for > 1.2 s then this bit is set to 0, indicating problems with the GPS.
- Bit 1: presence of T_1 signal - if the T_1 signal is missing for > 1.2 s then this bit is set to 0, indicating an absent beam signal, or the T_1 reset window being too narrow.
- Bit 2: reset of T_0 clock - set to 1 if the FEB receives a PPS signal from the WR TDC. Absence means there is an issue with the PPS.
- Bit 3: reset of T_1 clock - set to 1 when the T_1 reset window elapses and a T_1 reset signal is sent to the FEB.

The flag assigned to each event signifies the quality of the data that the setup is outputting and the stability of the internal FEB clocks. Table 5.1 shows the possible flag values assigned to each event based on the combination of these four binary bits.

If the T_0 and T_1 clocks are functioning properly, every event read out by the DAQ should have T_0 and T_1 presence. Ergo, a good data run should only consist of flag 3, 7 and 11 events. A flag 3 event constitutes a typical data event, where the TS0 and TS1 values are within the T_0 and T_1 reset windows respectively. Flag 7 is a T_0 clock reset event, where a signal is sent to the DAQ every second to keep the internal T_1 clock stable and synchronised by the WR SPEC-TDC. Flag 11 indicates a T_1 clock reset event, which is similar to a T_0 reset event but with a reset frequency set based on the BES readout window.

If any DAQ run shows flag values other than 3, 7 and 11, then there is something wrong with either the CRT cabling, the FEB clocks, or the DAQ itself. There is no flag 0 because in the instance of no T_0/T_1 presence and reset signal, no event is read out. Events labelled

Table 5.1: Possible flags assigned to each event outputted by the FEBs based on the presence and/or reset of the T_0/T_1 clocks, with the important flags highlighted in bold.

Flag	T_1 Reset	T_0 Reset	T_1 Presence	T_0 Presence
1	0	0	0	1
2	0	0	1	0
3 (data)	**0**	**0**	**1**	**1**
4	0	1	0	0
5	0	1	0	1
6	0	1	1	0
7 (T_0 reset)	**0**	**1**	**1**	**1**
8	1	0	0	0
9	1	0	0	1
10	1	0	1	0
11 (T_1 reset)	**1**	**0**	**1**	**1**
12	1	1	0	0
13	1	1	0	1
14	1	1	1	0
15	1	1	1	1

with an even-numbered flag may signify that the T_1 clock is turned off. Even though flag 15 events indicate presence of both T_0 and T_1 signals, events flagged with this value correspond to T_0 and T_1 clocks simultaneously sending reset signals to the DAQ. Therefore, the T_1 reset window should be set to be out of sync with the T_0 reset window.

5.3 FEB Calibration on A-frame Test Stands

The CRT A-frame was a temporary setup used to commission at least six CRTs whilst they were positioned in their delivery packaging: a wooden frame shaped like an 'A' (hence the name 'A-frame'). The first A-frame is shown in Figure 5.2, where all following A-frames would follow the general setup of four vertical, half-width CRT modules and at least two horizontal modules. The four vertical CRTs and their corresponding FEBs had been previously calibrated for their optimal channel-level SiPM voltage, readout electronics waveform amplitude thresholds and pre-amplification gain settings.

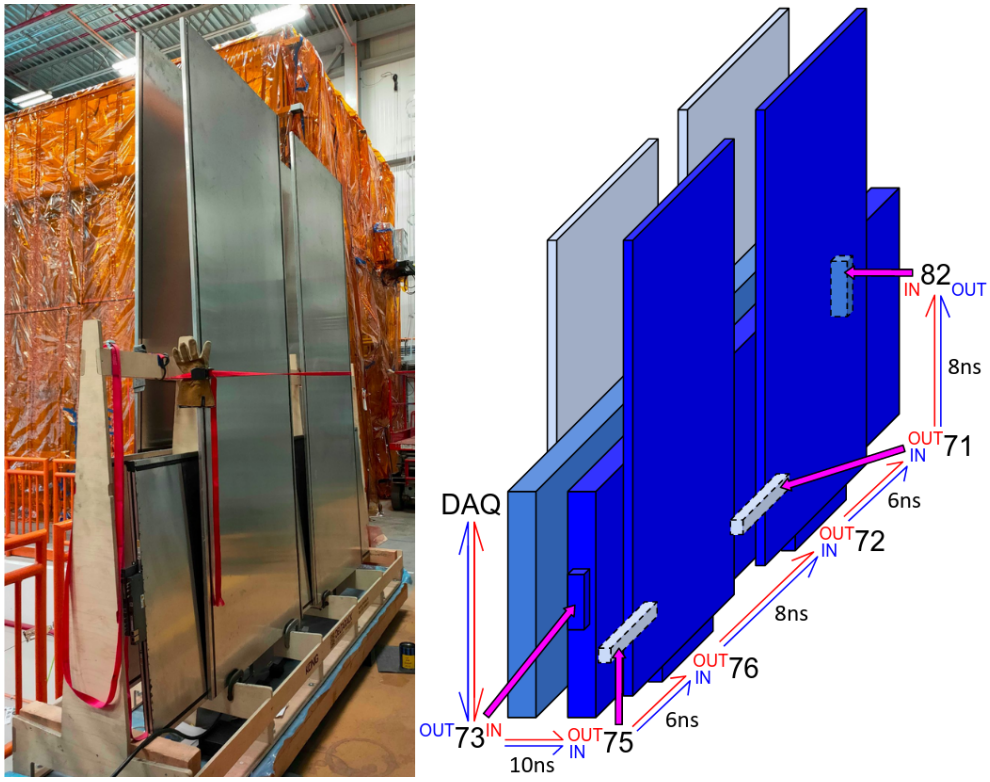

Figure 5.2: Picture (left) and schematic (right) of the CRT A-frame test stand. The numbers indicate the FEB number and the red and blue lines indicate the two separate T_{in}/T_{out} cable loops between the modules.

5.3.1 Experimental Setup

Commissioning of all 18 north wall CRT modules before their installation around SBND involved three separate A-frames, shown in Figure 5.3. The 18 uncalibrated modules were placed horizontally, split between the three A-frames, moving the four calibrated modules and placing them vertically on the A-frame that is being used to collect data to implement 4-fold or 8-fold coincidence between modules.

Every FEB has an identification number relating to the order in which they were manufactured, which is a parameter used by the DAQ to identify individual CRTs in the dataset. Each A-frame contains the following CRT modules with their corresponding FEB numbers:

- A-frame 0: half-width modules 73 and 82.
- A-frame 1: full size modules 153–159; half-length modules 181 and 182.
- A-frame 2: full size modules 134–136 and 149–152.
- Calibrated vertical modules: half-width modules 71, 72, 75 and 76.

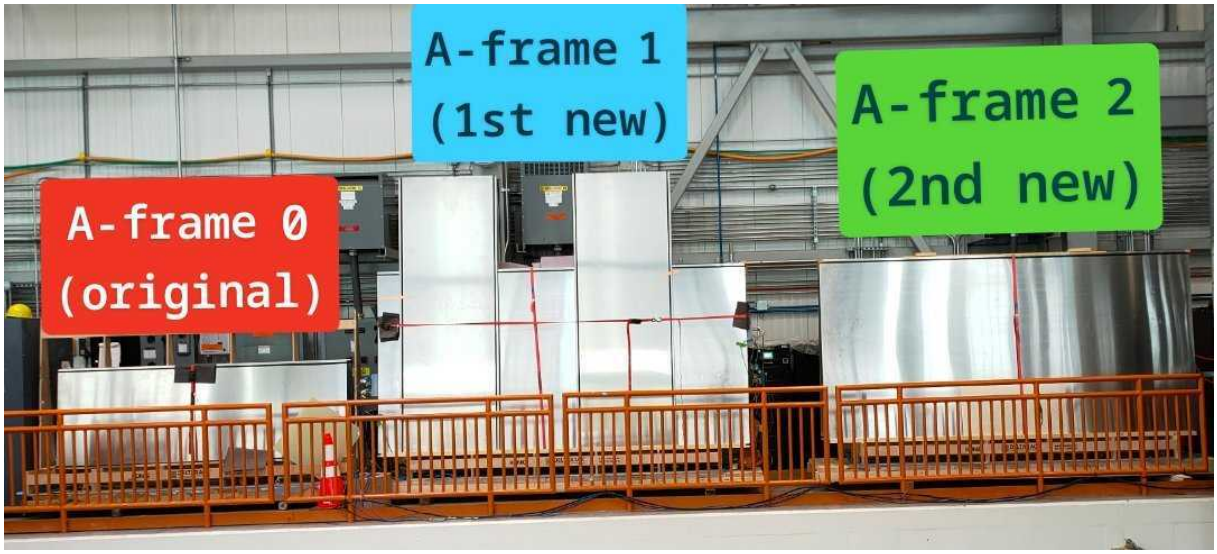

Figure 5.3: Three A-frame test stand setups used to commission the 18 north wall CRTs before their installation around the SBND cryostat. The four vertical modules, placed on A-frame 1 in the picture, would move to the A-frame that is being used to collect data.

Since the four calibrated vertical modules are moved between A-frames, the total number of CRTs on each A-frame are 6 for A-frame 0, 13 for A-frame 1 and 11 for A-frame 2.

Every CRT on each A-frame is connected through a chain of T_{in}/T_{out}, T_0/T_1, power and data cables plugged into the FEBs, shown in Figure 5.1. The right schematic in Figure 5.2, depicting A-frame 0, shows two separate T_{in}/T_{out} cable loops (red and blue). Starting from the DAQ crate, parallel modules are connected T_{in} to T_{in} and T_{out} to T_{out}; orthogonal modules are connected T_{in} to T_{out} and T_{out} to T_{in} with an additional long cable connecting the first and last module in the chain. The T_0/T_1 and data cables simply connects all the FEBs in a daisy-chain, starting from the DAQ and terminating at the last FEB in the chain. Finally, the power box has a long cable running underneath the middle of the A-frame from end-to-end, with additional cables connecting and powering all FEBs.

The calibrated vertical modules were used to commission the uncalibrated horizontal modules, optimising the SiPM voltage, readout electronics waveform amplitude thresholds, pre-amplification gain and clock drift of each FEB. Calibrating the SiPM voltage involves taking ADC distribution measurements between multiple modules in coincidence and adjusting the SiPM voltages to achieve a uniform signal between modules. Readout electronics waveform amplitude thresholds determine the distinction between data signals (cosmic-ray muon interactions with scintillator strips) and background noise (e.g. radioisotope decays of heavy metal contaminants within the aluminium casing). Preamplification gain determines how much the SiPM signal is amplified by the FEB before being processed by the DAQ.

The focus of the work presented in this chapter is calibrating the clock drift and timing resolution of each FEB for every CRT. Though the internal T_0 and T_1 clocks of the FEBs are GPS-locked to the WR timing system, this phase-locking is not exact and $\mathcal{O}$(ns) drift occurs for each FEB attached to every CRT.

5.3.2 Calibration of Event Rate

After setting up an A-frame, it must be verified such that each of the CRTs and SiPM channels are outputting good quality data and have uniform event rates. Firstly, a long data run of the setup is undertaken, making sure only flag 3, 7 and 11 events are present. Figure 5.4 shows plots of the number of events labelled with each flag variable for a typical run with good quality data on A-frame 0.

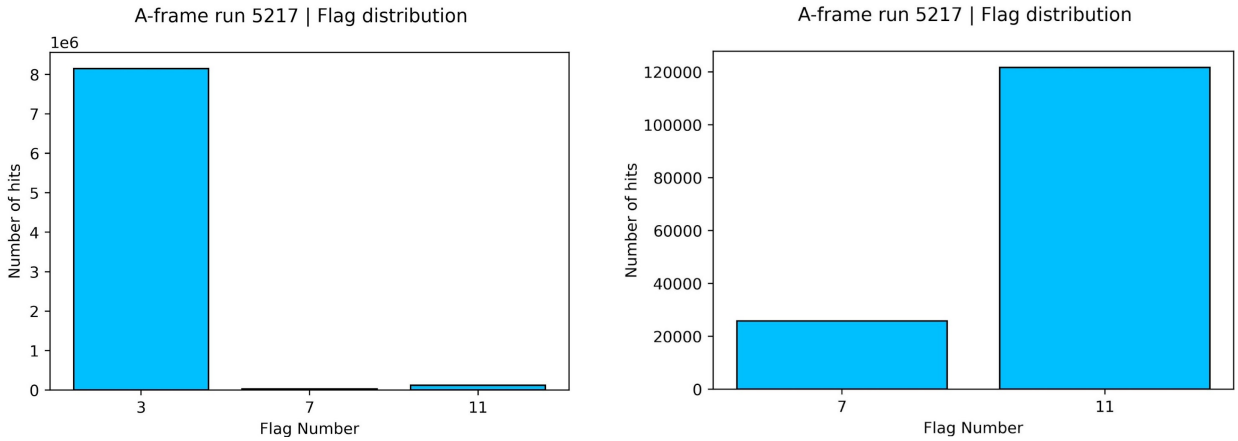

Figure 5.4: Number of hits broken down by their flag type for an A-frame 0 data run. The right plot excludes flag 3 (data) events due to their high frequency compared to flag 7 (T_0 reset) and 11 (T_1 reset) events. The T_1 reset window was set to 4.72786501 Hz.

If the flag distribution looks something akin to Figure 5.4 - predominantly flag 3 events with the expected number of flag 7 and 11 events based on the T_0/T_1 reset windows - then the data is deemed good quality enough to proceed with calibrations. A 'hit' is defined as a muon interaction with a scintillator strip, outputting a signal on the SiPM(s); whereas an 'event' is the processed data packet outputted by the FEBs after triggering SiPM hits between coincident strips/modules. To calibrate the event-rate of every CRT module on each A-frame, only flag 3 (data) events are selected from the dataset, followed by plotting the number of flag 3 events against FEB number. Three several-hour long runs were taken for each A-frame, moving the vertical modules between each A-frame to take 4-fold coincidence data, with the data event frequency histograms presented in Figure 5.5.

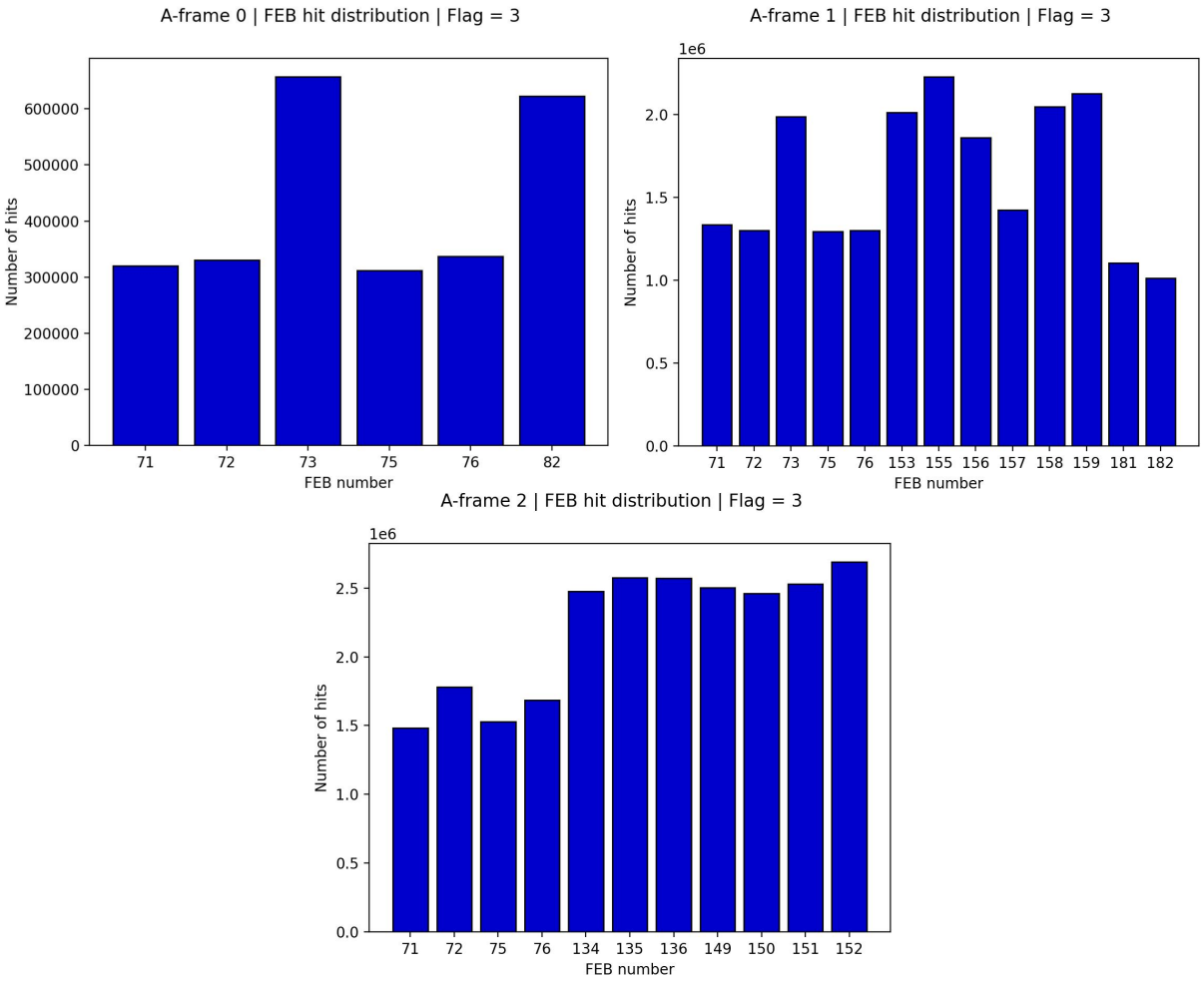

Figure 5.5: Number of flag 3 hits for each CRT on A-frames 0 (top left), 1 (top right) and 2 (bottom). Each DAQ run lasted for several hours and ran in 4-fold coincidence mode. For the A-frame 1 run, the event-rate for FEB 73 corresponds to the CRT module attributed to FEB 154, as FEB 154 needed to be swapped out for FEB 73 due to a malfunction.

Each FEB should output approximately the same number of flag 3 events per area of overlap between horizontal and vertical modules, assuming that SiPM voltage thresholds are optimised. The event distribution for A-frames 0 and 1 in Figure 5.5 show vertical modules (FEBs 71, 72, 75 and 76) outputting half the data events than horizontal modules (all other FEB numbers), which is expected as horizontal modules have two areas of overlap with vertical modules, which only have one each, as seen in Figure 5.2.

A-frame 1 shows same-size modules exhibiting similar event rates, with vertical modules outputting event rates slightly higher than half the horizontal due to the half-length modules being placed next to each other longways on the A-frame, slightly increasing the area of overlap with the vertical modules. Despite FEB 157 being attached to a full-size horizontal

module, it outputted the same event rate as modules with double the area of overlap. This was possibly due to it being placed at the end of the data chain, dropping events due to long cable delays exceeding the DAQ readout window. Anomalously low event rates could also indicate unoptimised SiPM voltages or ADC thresholds for that module.

Deficits in the total event rate, such as for FEB 157 on A-frame 2 in Figure 5.5, could also be an indication of SiPM channels exhibiting unoptimised voltage settings, or channels that have shorted altogether. Each CRT module has 32 SiPM channels: two per scintillator strip with 16 strips per module. It is possible to plot the number of hits detected by each CRT module, in order to see the event rate of each module broken down by its individual SiPM channels. Figure 5.6 shows the SiPM channel hit breakdown for FEBs 72 and 157 on A-frame 1 and FEBs 75 and 134 on A-frame 2. Muon interactions with scintillator strips will often trigger multiple SiPMs, typically two associated with the same strip. Therefore, the SiPM channel number associated with each event is decided based on the SiPM channel that outputs a waveform with the greatest ADC amplitude.

Theoretically, the hit rate distributions for vertical modules should be uniform. However, the plots for FEBs 72 and 75 in Figure 5.6 show great variation, with alternating high and low hit rates for adjacent SiPM channels. This is because, at the time of each data run, the SiPM voltages were uncalibrated, meaning that one SiPM on each strip would disproportionately amplify scintillation light signals to output more charge than the other SiPM on the same strip. Horizontal modules show a decreasing hit rate at higher channel numbers for FEB 157 and the lower channel numbers for FEB 134. This is because when horizontal CRTs are laid down on their side on the A-frame, the scintillator strips closer to the base of the A-frame have a smaller area of overlap with the vertical modules, and as such have a smaller angular acceptance of coincident hits between horizontal and vertical modules, and therefore a lower overall hit rate. These plots are essential to make for every FEB in order to adjust and optimise the individual SiPM voltage of each CRT module, until the hit rate across all SiPM channels is uniform.

5.3.3 T_0/T_1 Clock Reset Event Calibration

It is important to verify that every FEB on each A-frame is receiving the same number of T_0 and T_1 clock reset events. This involves plotting the number of flag 7 and flag 11 events against FEB number for T_0 and T_1 reset events respectively. Several hour long runs of A-frames 0, 1 and 2 were collected, ensuring only flag 3, 7 and 11 events were present in the dataset. Selecting only flag 7 and 11 events, T_0 and T_1 clock reset event frequency graphs for FEBs on A-frames 0, 1 and 2 were plotted and are shown in Figure 5.7.

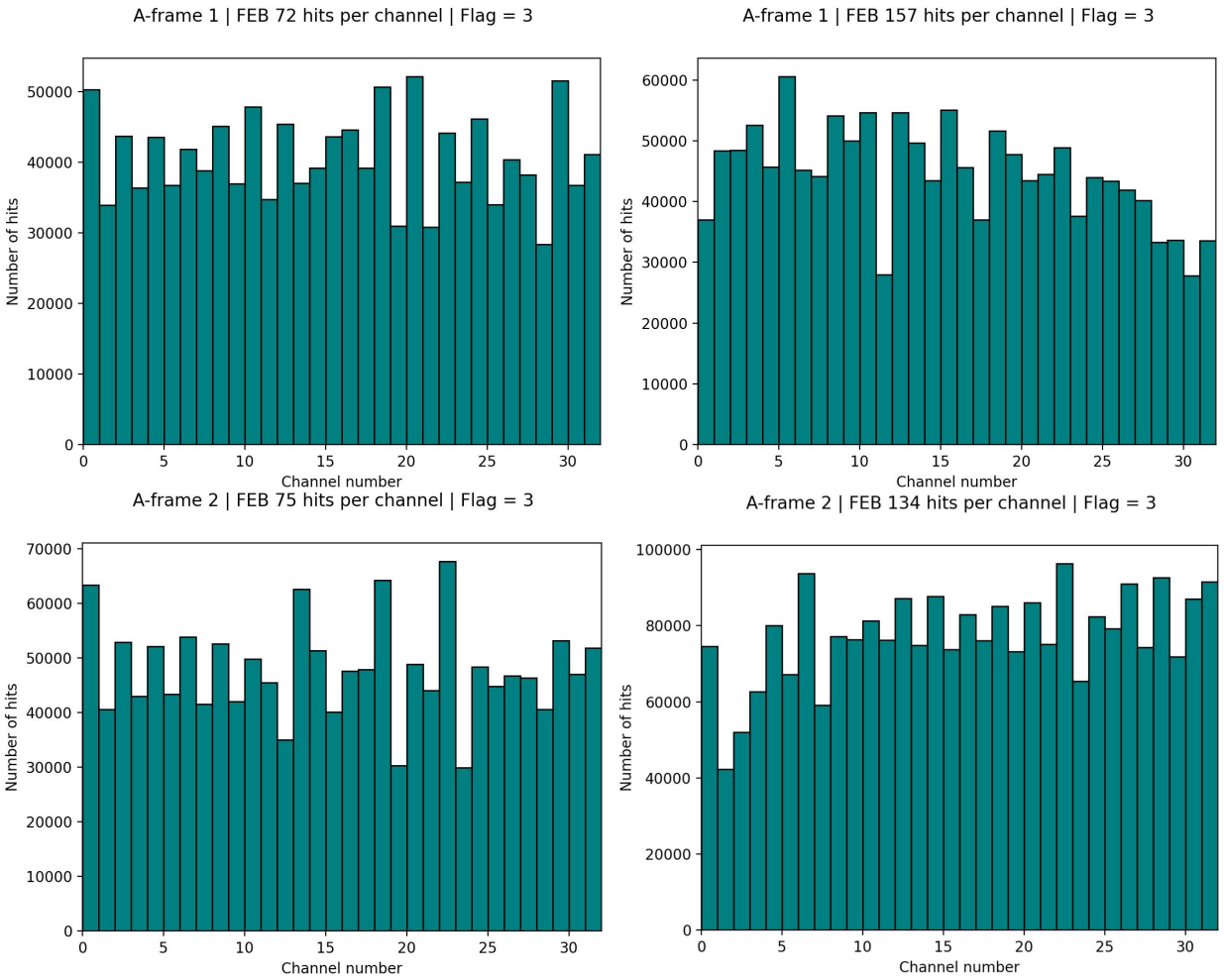

Figure 5.6: Number of flag 3 hits on each SiPM channel, labelled 0–31, for a single CRT module. FEBs 72 (top left) and 75 (bottom left) are half-width vertical modules, and FEBs 157 (top right) and 134 (bottom right) are full size horizontal modules.

Ideally, all plots in Figure 5.7 should be uniform, as each FEB should be receiving a T_0 reset signal every second and a T_1 reset signal at the set T_1 reset frequency. This uniform structure is predominantly seen in A-frame 0, unlike A-frames 1 and 2 which show more variation. Particularly, FEB 157 is shown to be missing T_0 reset events, and registering approximately half as many T_1 reset events than the rest of the FEBs in A-frame 1. Similar issues with FEB 157 regarding its anomalously low event rates were noted in the flag 3 event distributions in Figure 5.5, further suggesting that FEB 157 is not sending flag 3, 7 and 11 events to the DAQ due to it being at the end of the cabling chain, with events often falling outside the DAQ deadtime limit of 20 µs. This was remedied in the north wall CRT installation by having fewer than 13 CRTs in each of the two cable chains, with sufficiently short cables connecting them such that no FEB loses hits to deadtime.

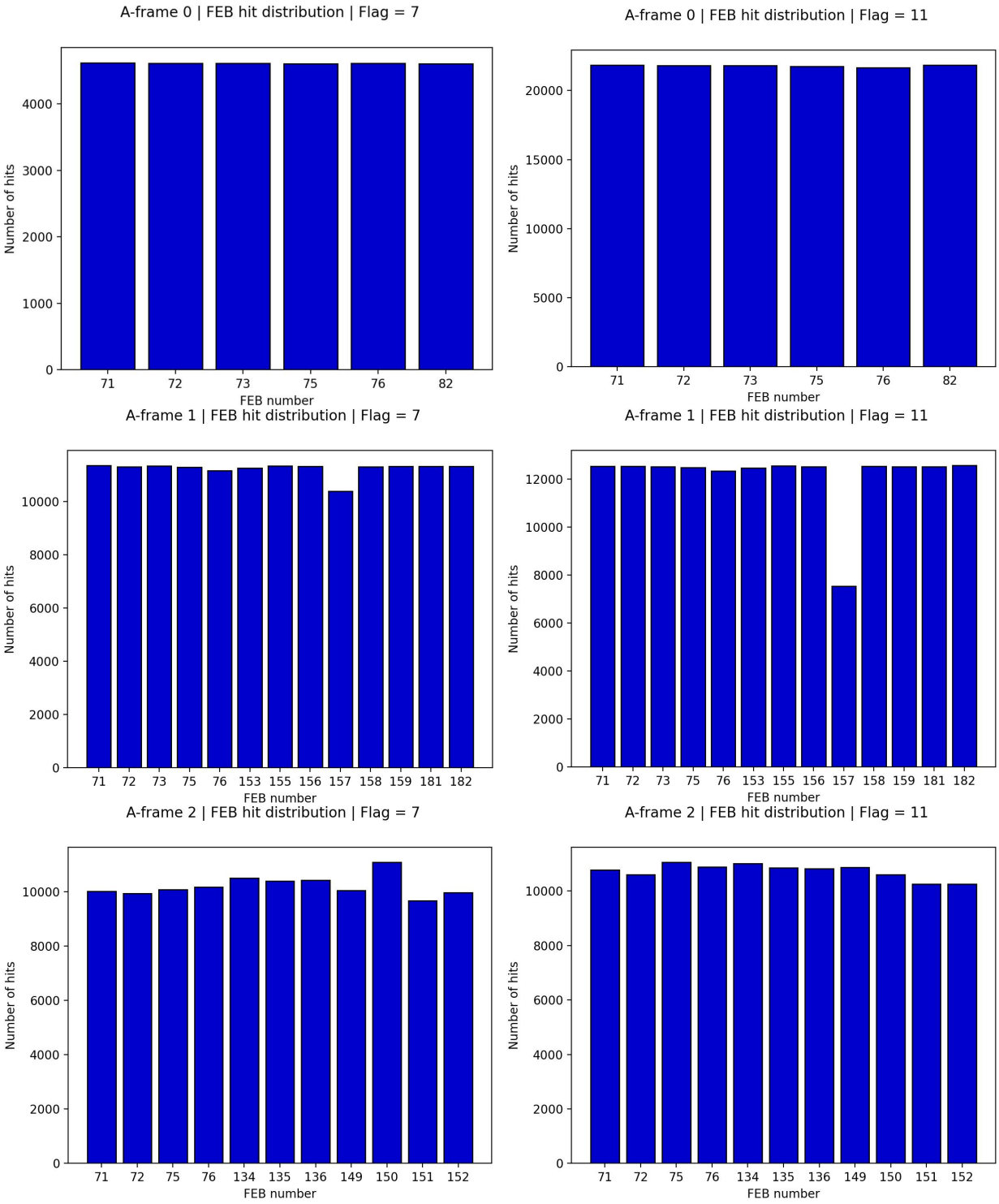

Figure 5.7: Number of flag 7 events (left) and flag 11 events (right) for each FEB connected to CRTs on A-frames 0 (top), 1 (middle) and 2 (bottom).

One way of tracking how many FEBs in the A-frame are missing T_0 and T_1 reset events is to plot a graph of FEB 'occupancy' for flag 7 and 11 events, shown in Figure 5.8 for A-frames 0, 1 and 2. When the T_0/T_1 clocks reset, a T_0/T_1 reset signal is sent to every FEB, where they all output a flag 7/11 event simultaneously within a precision of approximately 5 ns. The FEB occupancy is plotted by calculating the average TS0/TS1 value associated with each T_0/T_1 reset event for all the FEBs, then finding the number of FEBs that have a TS0/TS1 value within 20 ns of this average. Any FEBs outputting a flag 7/11 event outside this range is undoubtably a mislabelled flag 3 event. Due to TS0/TS1 timestamps resetting to zero seconds after every T_0/T_1 reset event, and that FEB occupancy plots require finding a 20 ns range around an average timestamp value, flag 11 events were selected for TS0 values and flag 7 events for TS1 values as they are uncorrelated.

The A-frame 0 FEB occupancy plots in Figure 5.8 show that all six FEBs are receiving the vast majority of T_0/T_1 reset events, marking A-frame 0 as ready for timing characterisation. A-frame 1 shows a relatively stable T_0 clock with 12 out of the 13 CRT modules receiving simultaneous T_0 reset events, the outlier most likely being FEB number 157 due to its deficit in flag 7 events featured in Figure 5.7. However, the T_1 reset plot having a modal peak of one FEB shows that there is a significant drift in the T_1 reset signal. Despite the T_0 clock being synchronised to a GPS-locked global clock by the WR, the T_1 clock is pushed by a function generator with an intrinsically drifting pulse rate of approximately 40 ns, so many T_1 reset events are either lost due to falling outside the DAQ deadtime window or are mislabelled as flag 3 events. A-frame 2 exhibits a wide deviation in number of T_0/T_1 reset events missed, but still shows all 11 FEBs are receiving T_0/T_1 reset events. This differs from A-frame 1 most likely due to the fewer CRTs in the data chain stopping flagged events from falling outside the DAQ pull window with longer cable delays.

Plotting the flag 7 and 11 event rates between CRT modules and the FEB occupancy plots for T_0 and T_1 reset events being missed are paramount in understanding the quality of data being outputted from each FEB. Before each CRT was affixed to the north wall of SBND, these plots were made to show how many T_0/T_1 clock reset events would be missed for the current A-frame setup. The setup was then altered - such as swapping out cables, altering the T_1 clock reset rate or modifying the DAQ readout window - until all FEBs received the same number, distribution and rate of clock reset events. The next step in the calibration process was to characterise the timing drift of the internal FEB clocks.

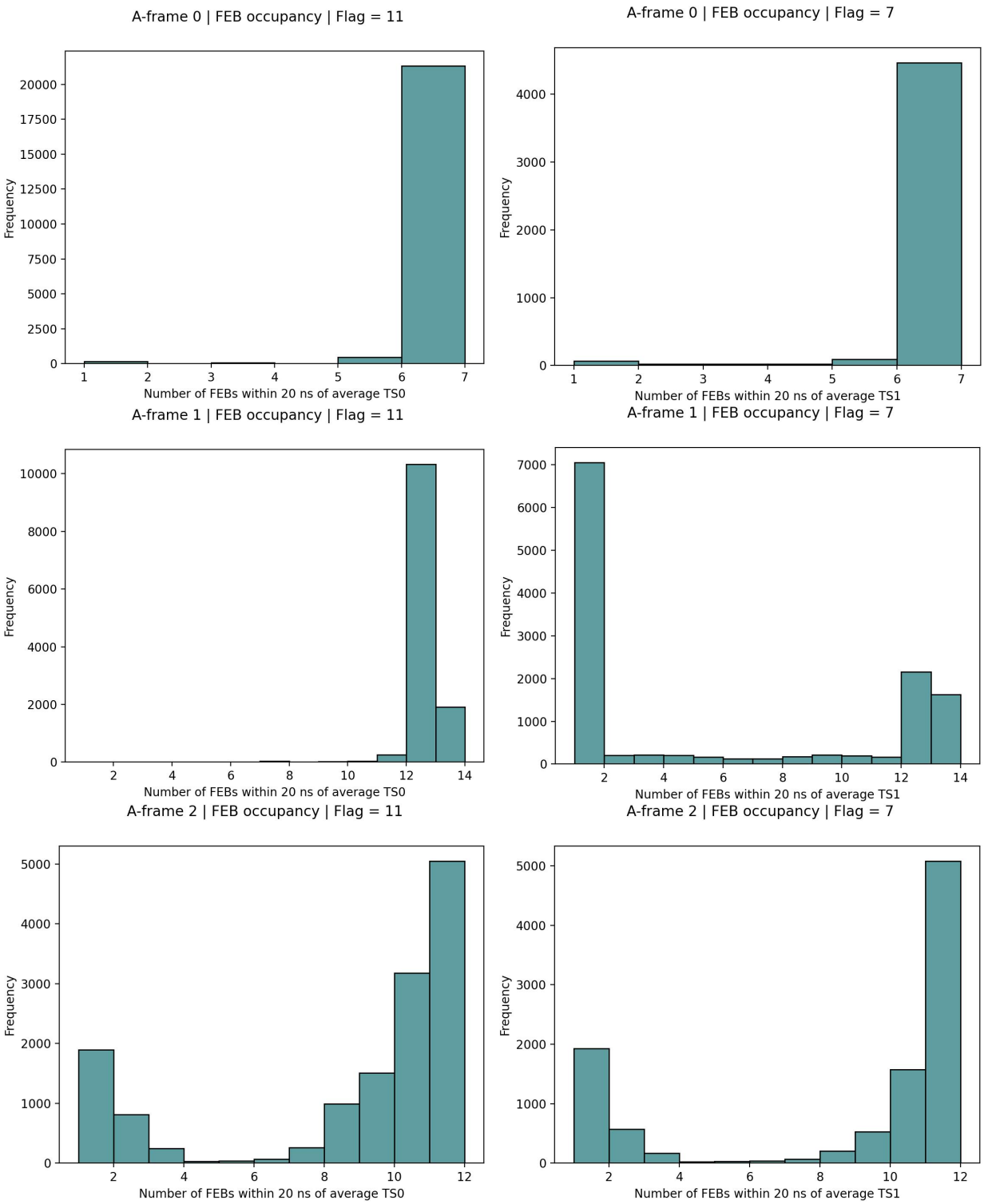

Figure 5.8: Flag 11 (left) and 7 (right) FEB occupancy plots for A-frames 0 (top), 1 (middle) and 2 (bottom). Shows the number of FEBs that have flag 11/7 TS0/TS1 values that deviate from the total average TS0/TS1 value by 20 ns.

5.3.4 FEB Timing Characterisation

Once it has been verified that every FEB on each A-frame is outputting only flag 3, 7 and 11 events, with each CRT registering approximately the same rate of these events, without missing a significant number of flag 7 and 11 events, then the FEB timing drift characterisation methodology can be executed. Firstly, the general stability of data event timestamps need to be verified by plotting the distribution of TS0 and TS1 values for flag 3 events, making sure they are uniform as there should be no correlation between flag 3 events and timestamp value. Long data runs of A-frames 0, 1 and 2 were taken, using 4-fold coincidence mode, plotting the TS0 and TS1 values for flag 3 events in the graphs presented in Figure 5.9. After this, the FEB clock drift is characterised by plotting the distribution of flag 7 TS0 and flag 11 TS1 values, subtracting the reset window (inverse of reset frequency). Calculating the mean and standard deviation of the distributions for each FEB is analogous to identifying the clock drift and timing resolution.

The A-frame 0 timestamp plots in Figure 5.9 show approximately uniform TS0 and TS1 distributions, with no biases in data events or anomalies in timestamp value, which is the ideal outcome. However, A-frame 1 shows clear anomalous peaks around the time when their respective clocks would reset. This is an indication of T_0 and T_1 reset events being mistakenly labelled as flag 3 events instead of 7 and 11 respectively, which is in line with Figure 5.8 showing that most FEBs on A-frame 1 are missing flag 7/11 events. One method of getting around the issue of flag 7 and 11 events being mislabelled as flag 3 is to implement a higher ADC amplitude cut, particularly around the T_0/T_1 reset time.

Though the TS1 distribution for A-frame 2 looks uniform, the TS0 distribution exhibits oscillating peaks occurring at a frequency of around 4 ms. This is most likely due to the DAQ reading out events using a CAEN 1730 with a function generator sending pulses to indicate when a readout should occur. The pull frequency of said function generator was set to 4 ms, the same as the frequency of dips in the TS0 distribution. The dips occur because some fraction of the events at those times fall outside the readout window. This was avoided in future runs by increasing the DAQ readout window to 200 ms.

Once the TS0 and TS1 distributions appear stable and uniform across all FEBs on each A-frame, the timing calibration plots can be generated. Starting with the T_0 clock, the plots in Figure 5.10 were produced by selecting flag 7 events and plotting a histogram of the frequency of TS0 values. Since a T_0 reset event is registered by the FEB every second before resetting the TS0 value to zero, one second is subtracted from every TS0 value to centre the distributions around zero. Then, the mean and standard deviation of each plot is calculated, corresponding to the timing drift and resolution of that FEB respectively.

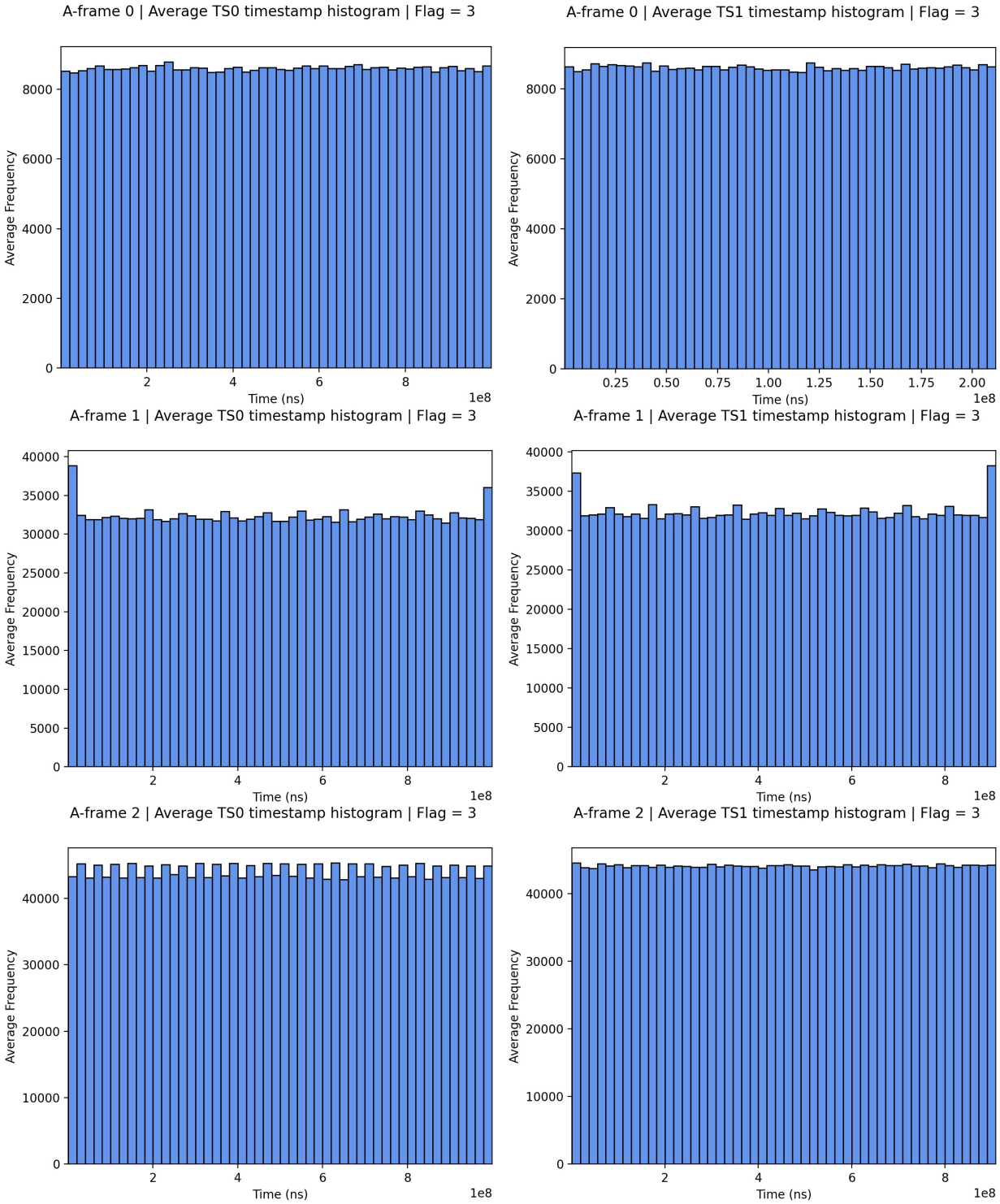

Figure 5.9: TS0 (left) and TS1 (right) value frequency for flag 3 events collected from A-frames 0 (top), 1 (middle) and 2 (bottom). TS0 ranges from 0 to 1 second with 20 ms bin widths. The upper bound of TS1 values are 0.211512274 s for A-frame 0 and 0.909090909 s for A-frames 1 and 2 - equating to the inverse of their T_1 clock reset frequencies of 4.72785801 Hz and 1.1 Hz - with bin widths of around 4.23 ms and 18.2 ms respectively.

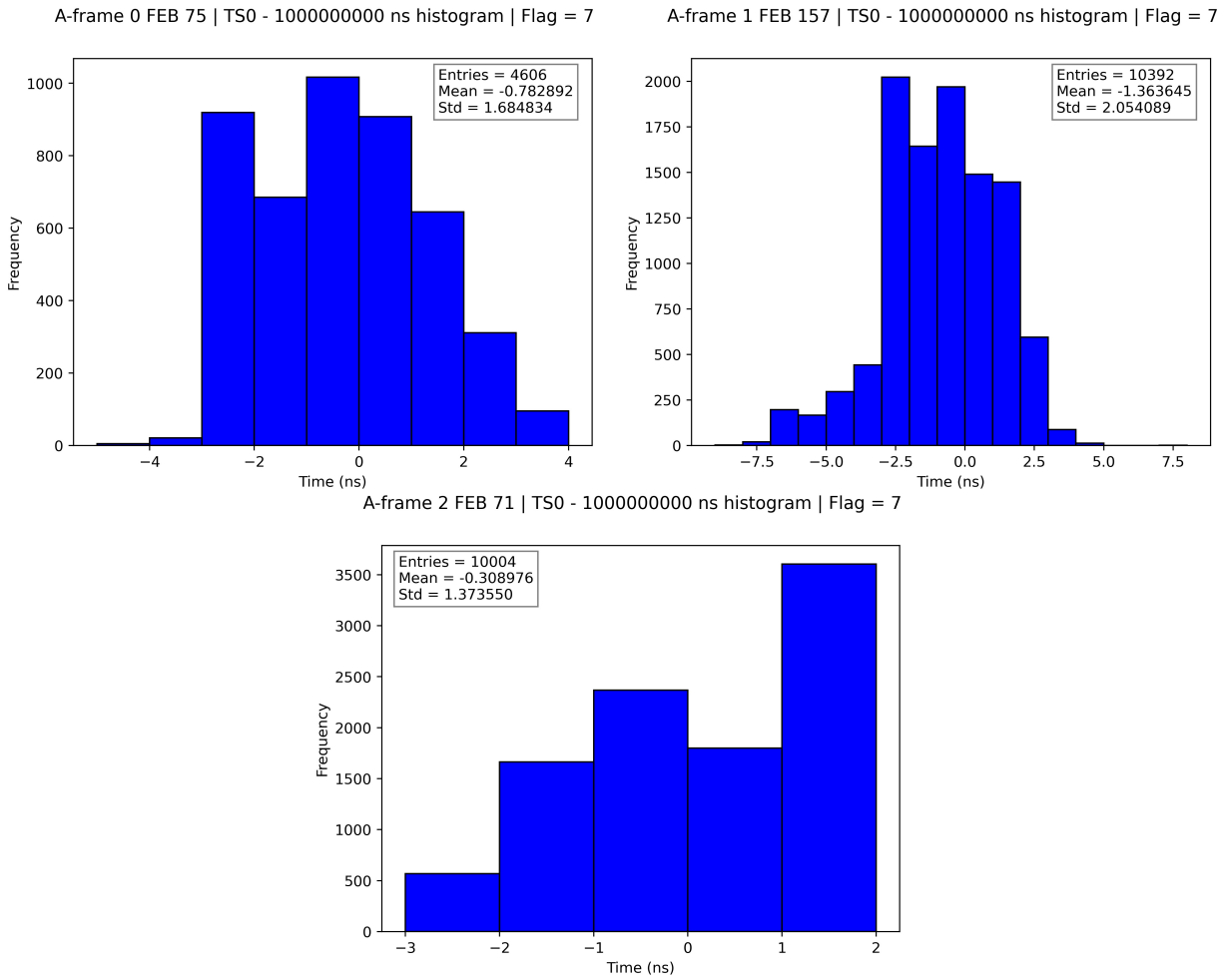

Figure 5.10: TS0 timestamp frequency of flag 7 events, subtracting the T_0 reset window of 1 s, for FEB 75 on A-frame 0 (top left), FEB 157 on A-frame 1 (top right) and FEB 71 on A-frame 2 (bottom).

The flag 7 TS0 distributions in Figure 5.10 are the main method in characterising the intrinsic T_0 clock drift and timing resolution in each FEB. One of these plots is generated for every FEB, with the mean TS0 value and standard deviation about the mean calculated and stored. Mean TS0 values indicate the drift of the T_0 clock, with the standard deviation relating to the timing resolution, which should be ≤ 1 ns and ≤ 2 ns respectively. A 4 ns total standard deviation is expected due to the 250 MHz clock frequency of the WR SPEC-TDC GPS-locking the T_0 clock. The plots in Figure 5.10 for FEBs 75 and 71 on A-frames 0 and 2 show minimal timing drift and resolution, with means and standard deviations both within the ≤ 1 ns and ≤ 2 ns ranges, so no additional timing corrections are necessary.

However, FEB 157 on A-frame 1 shows a much wider distribution and greater drift, meaning the FEB requires correcting at the hardware level. If there is still a drift observed,

then the mean TS0 value is subtracted at the post-data processing level to correct for this drift. The flag 11 TS1 distribution plots are presented in Figure 5.11, where the T_1 reset window of 0.211512274 s for A-frame 0 and 0.909090909 s for A-frames 1 and 2 are subtracted to centre the distributions around zero.

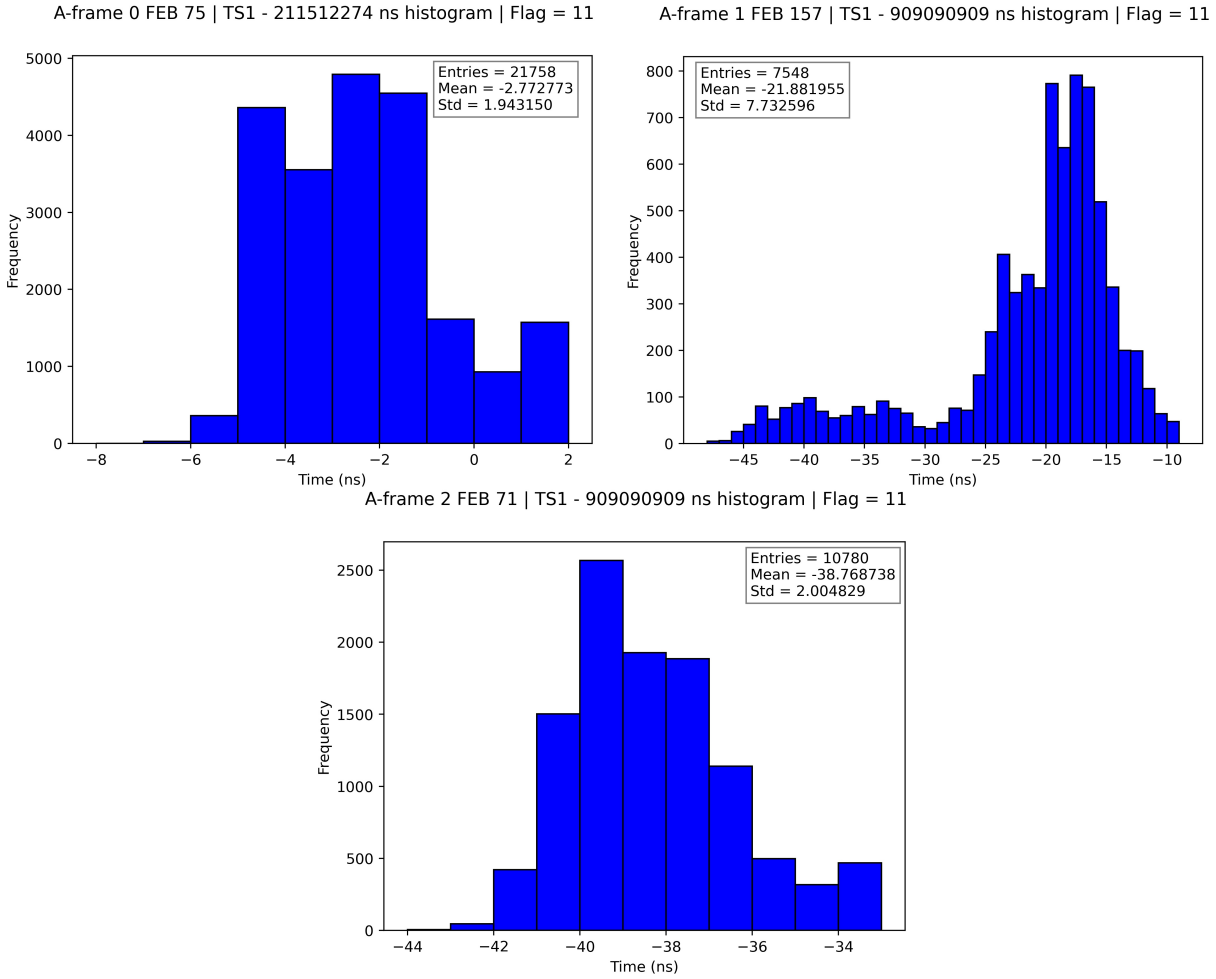

Figure 5.11: TS1 value frequency of flag 11 events for FEB 75 on A-frame 0 (top left), FEB 157 on A-frame 1 (top right) and FEB 71 on A-frame 2. The T_1 reset window of 0.211512274 s for A-frame 0 and 0.909090909 s for A-frames 1 and 2 is subtracted.

The T_1 clock within each FEB exhibits a much greater drift than the T_0 clock, as well as a generally wider distribution. This is due to the fact that the T_0 clock is synchronised to the global clock by the WR, whereas the T_1 clock is being pushed by a function generator with a drifting pulse rate. The expected level of drift of the function generator is approximately 20 ns, compared to the 1 ns drift of the TDC. The flag 11 TS1 distribution plot for FEB 75 on A-frame 0 shows minimal T_1 clock drift, with a mean and standard deviation of (-2.72 ± 1.94) ns. FEB 157 on A-frame 1 and FEB 71 on A-frame 2, however, demonstrates

a much larger drifting T_1 clock, with the TS1 mean having values of (-21.9 ± 7.7) ns and (-38.8 ± 2.0) ns respectively. Great drifts in the timestamp value can be corrected within the DAQ by subtracting the mean flag 11 TS1 value for each FEB.

The purpose of the timing plots in Figures 5.10 and 5.11 is to understand and calibrate the timing drift and resolution on each FEB, indicating whether they need additional hardware corrections or through post-data processing in the DAQ. All the mean and standard deviation values of the flag 7 TS0 and flag 11 TS1 timing correction plots have been collated and put into bar graphs in Figures 5.12 and 5.13.

Mean values are often negative because, even though it is possible to have timestamps exceeding the clock reset window, the intrinsic drift of internal FEB clocks are always ahead of the global clock it is synchronised to. Flag 7 TS0 mean values in Figure 5.12 show a variation of up to 4 ns for A-frame 1 and 3 ns for A-frame 2, which are expected due to the 250 MHz TDC frequency. The standard deviations show optimal calibration, with only a few FEBs exceeding 2 ns deviations, and only FEB 153 exceeding a 3 ns deviation. The flag 11 TS1 results in Figure 5.13 are far more sporadic, with the means and standard deviations of A-frame 1 being around -40 ns and 2 ns respectively, and A-frame 2 showing means and standard deviations of around -22 ns and 6 ns respectively.

Dependence on A-frame seems to be only apparent for the flag 11 TS1 values, which makes sense as the T_1 clock is pushed by a function generator with an intrinsic drift of around 20 ns, and is more affected by cable delays due to not being synchronised to the global clock like the T_0. The fact that the flag 11 TS1 mean and standard deviation values do not differ largely from each FEB on the same A-frame indicate healthy T_1 clocks, and any large discrepancies between A-frames can be accounted for in post-data processing.

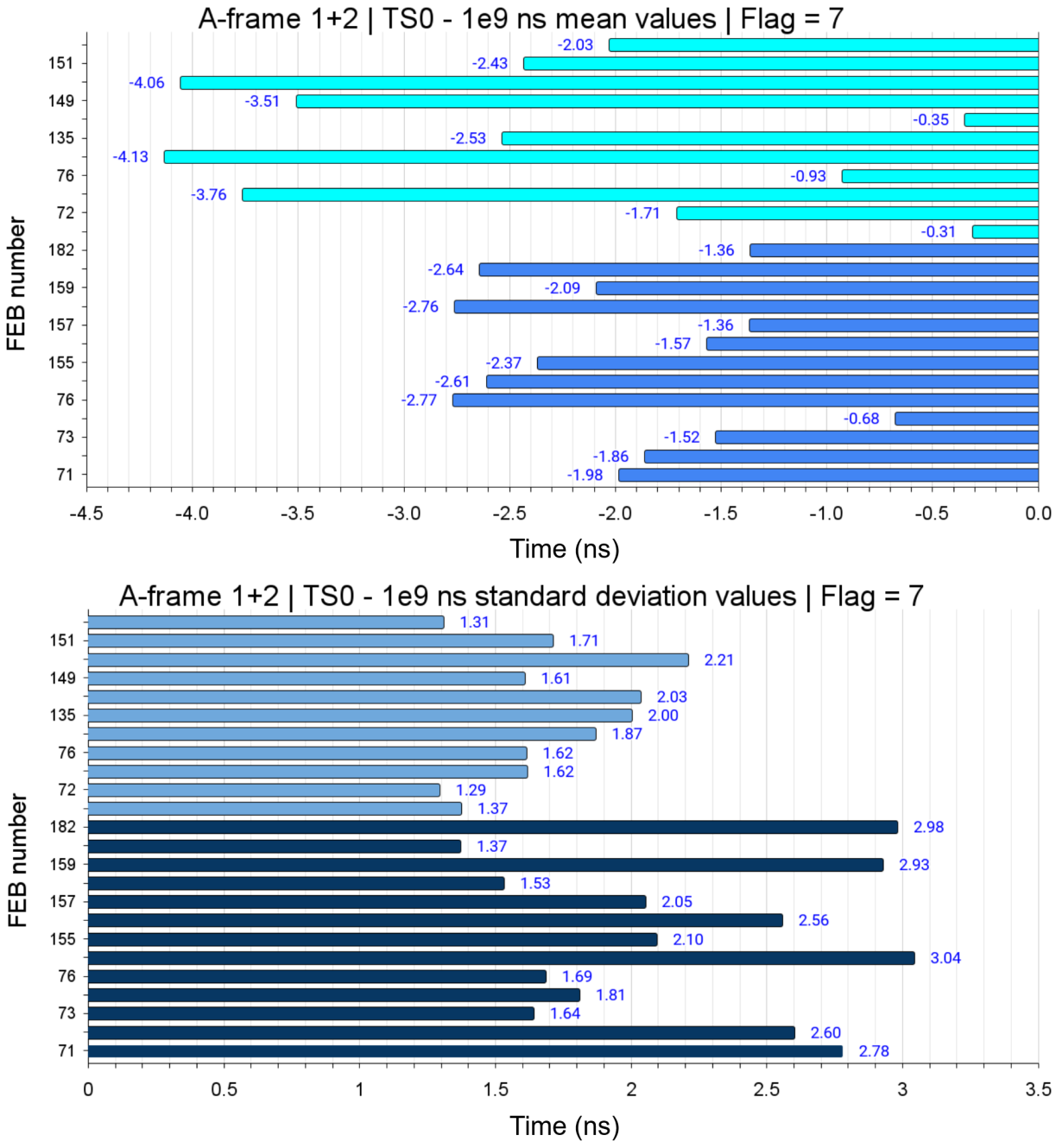

Figure 5.12: Means (top) and standard deviations (bottom) of the flag 7 TS0 plots in figure 5.10 for each FEB on A-frames 1 (lighter blue) and 2 (darker blue).

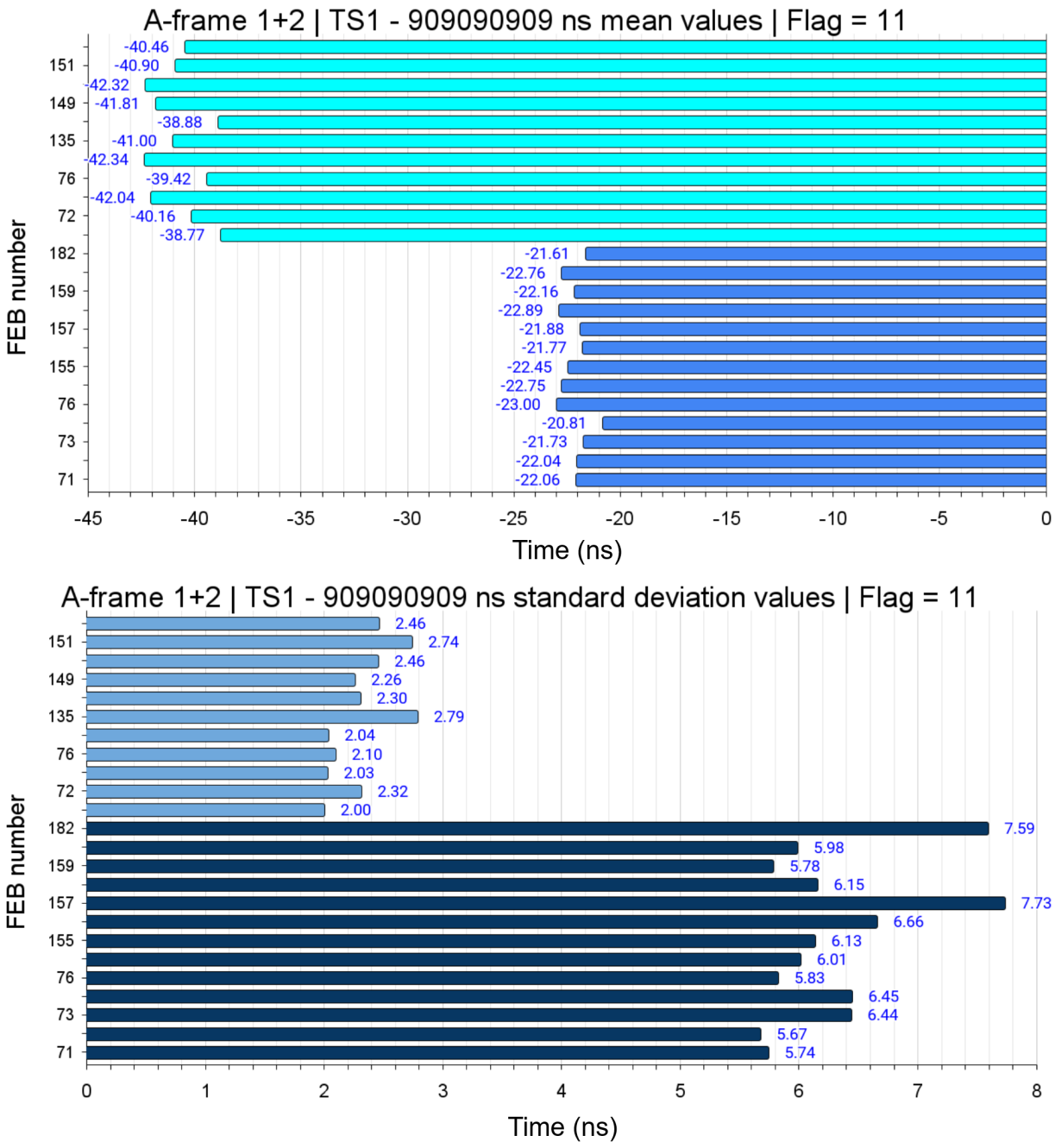

Figure 5.13: Means (top) and standard deviations (bottom) of the flag 11 TS1 plots in figure 5.11 for each FEB on A-frames 1 (lighter blue) and 2 (darker blue).

5.4 Conclusions

This chapter has demonstrated the development of a methodology calibrating the event rate distribution and clock timing drift/resolution of every FEB attached to the CRTs to be installed around SBND, and its application to the 18 CRT modules before their installation on the north wall. Since then, these methodologies have been applied to every subsequent A-frame housing the remaining 128 CRTs that have been installed on the rest of the CRT walls around SBND. After verifying that any clock drifts are purely intrinsic to the FEB and not the A-frame setup, any FEBs exhibiting a mean T_0 timing drift of > 1 ns or a timing resolution of > 2 ns would be corrected until the drift and resolution fall within these ranges. If the drift persisted after correction, the mean drift value would be subtracted from the data for that FEB after being processed by the DAQ.

Chapter 6

Field Response Validation Using Monte Carlo Event Samples

Reconstructing neutrino interactions in SBND requires a full understanding of the physical mechanisms underpinning the modelling of waveforms outputted by TPC readout wires. The shape of this waveform is smeared by current induction on readout wires from the electric field of electrons, and signal amplification from the front-end electronics, called the field response and electronics response respectively. Extracting the bulk ionisation electron signal induction on readout wires from the full output TPC waveform is integral to accurately reconstructing the calorimetric and spatial information of the particle track. This chapter presents the work done to validate the algorithms used in the SBND simulation to model how the field response shapes the output TPC waveform.

Section 6.1 contains a description of the signal processing chain in SBND and how it is used to generate waveforms from ionisation electrons inducing signals on TPC readout wires. Section 6.2 outlines the methodology for validating the field response modelling algorithms and presents the work done reconstructing waveforms from MC samples generated using the SBND simulation. Simulating the effect on TPC waveform shape from the field and electronics response is presented in Section 6.3. Then, the results of the field response validation study using MC samples is shown in Section 6.4. Finally, general conclusions to the work are presented in Section 6.5.

6.1 Signal Waveforms on SBND TPC Readout Wires

Before presenting the work done on validating the field response in SBND, important signal processing concepts and the mathematical groundworks underpinning the modelling of the

signal formation and response function calculations for SBND need to be outlined. This also includes descriptions of how MicroBooNE models the electronics and field response effects on the total waveform outputted from TPC readout wires, which is analogous to SBND as they have near-identical LArTPC designs and simulation frameworks.

6.1.1 Signal Processing in the SBND Readout Electronics Chain

The SBND APA is composed of three wire planes: two induction planes with wires angled at $\pm 60°$ from the vertical and one collection plane with vertical wires, with the wire planes denoted as U, V and Y (or 0, 1 and 2) respectively. Shaping and smearing of the ionisation signal due to the field and electronics response can be mathematically understood as the output TPC waveform being composed of a signal convolution between the ionisation signal, electronics response and the field response. The ionisation signal waveform is the distribution of the ionisation charge cloud deposited by ionisation electrons drifting past induction plane wires and terminating on collection plane wires, undergoing diffusion and absorption through SCE as they drift, resulting in broadening of the waveform.

The electronics response smears the ionisation signal waveform due to ASIC chips within the SBND cold electronics system, amplifying TPC readout currents. The field response shapes the ionisation signal as a result of current inductions on APA readout wires from the electric field of drifting ionisation electrons [161]. An example of a typical signal waveform outputted from a similar LArTPC-based wire plane neutrino detector experiment is presented in Figure 6.1, which shows a simulated signal waveform from an ideal MIP track inducing a signal on all three wire planes of the MicroBooNE TPC [162].

Due to the fact that both MicroBooNE and SBND are LArTPC-based neutrino experiments utilising the same three wire plane configuration for signal readout, the waveforms outputted by the SBND TPC will be modelled through the same signal formation mechanisms as the MicroBooNE waveform in Figure 6.1, and as such will look very similar. Any differences will be driven by their distinct detector geometry and physics parameters such as electric field strength and wire bias voltage settings. The first induction plane waveform shows the expected front-porch effect on the left-hand side of the waveform due to gradual current induction in readout wires as the ionisation electrons approach the APA. This results in a bipolar signal with a large negative peak due to negatively charged electrons inducing a signal on the negatively voltage-biased wires. Zero voltage bias is applied to the second induction plane wires leading to an approximately symmetrical bipolar signal: an initially positive peak, a median zero-point corresponding to when the electron crosses the wire plane, and a secondary negative peak of similar amplitude to the positive peak.

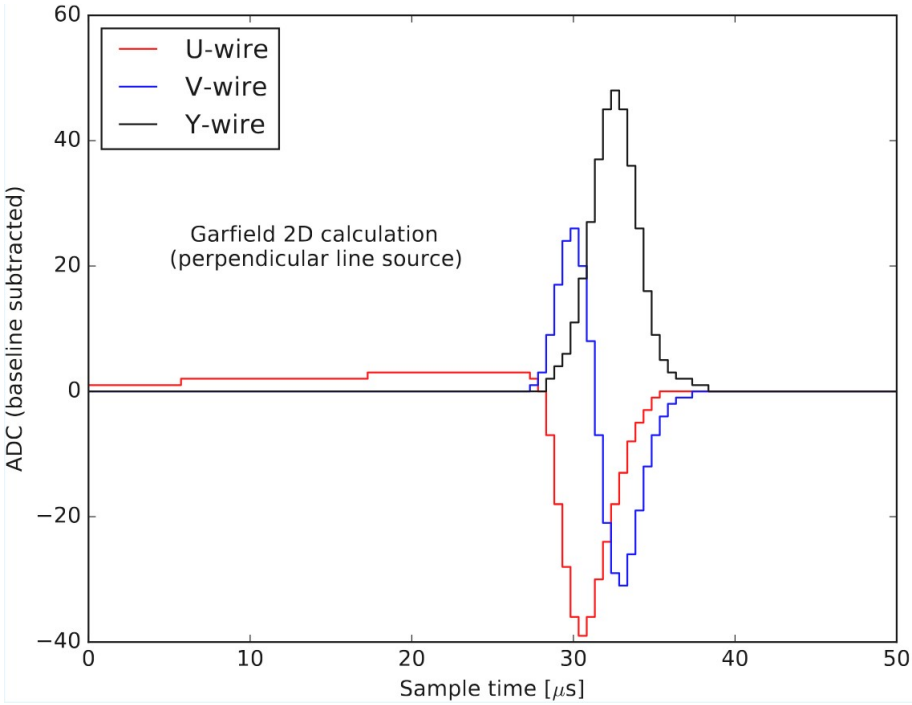

Figure 6.1: Simulated signal waveform induced on the two induction planes and collection plane wires (labelled U, V and Y respectively) from an ideal MIP track using a 2D simulation of the MicroBooNE TPC. A 2D Garfield simulation was used to model the field response contribution to the waveform [154]. The electronics response takes the form of a parametric equation with a gain setting of 14 mV/fC and a 2 μs peaking time [162].

The unipolar collection plane signal exhibits a larger pseudo-Gaussian positive peak, due to its positive bias voltage, as it is the result of ionisation charges terminating on the wires. Unipolar collection plane waveforms are easier to model in the SBND simulation compared to the intrinsically complex nature of bipolar induction plane waveforms. This is due to the fact that the resultant signal waveform on a single TPC wire channel is composed of many overlapping bipolar induction plane signals as thousands of ionisation electrons drift past the induction plane wires [161].

As stated previously, the resulting signal waveform from SBND TPC readout wires can be mathematically understood as a convolution of the ionisation signal, electronics response and field response. Signal convolution refers to the mathematical overlapping of two time-dependent functions to form a third function. In a typical LArTPC experiment, the measured signal $M(t')$ is a convolution of the ionisation signal $S(t)$ and the detector response function $R(t'-t)$, which is represented by the integral

$$M(t') = (R * S)(t') = \int_{-\infty}^{\infty} R(t'-t) \cdot S(t) dt, \tag{6.1}$$

where $R(t'-t)$ encapsulates the total wire response: a convolution of the field and electronics response functions. Since the charge information required for physics analysis is encapsulated in $S(t)$, the deconvolution technique must be employed to extract $S(t)$ from equation 6.1. This involves transforming equation 6.1 into the frequency domain using a Forward Fourier Transform (FFT), yielding: $M(\omega) = R(\omega) \cdot S(\omega)$, where ω is the angular frequency. During signal deconvolution, high frequency noises are disproportionately amplified compared to lower frequencies, motivating the need for a low-pass filter $F(\omega)$ in the equation. Rearranging this equation and implementing $F(\omega)$ gives

$$S(\omega) = \frac{M(\omega)}{R(\omega)} \cdot F(\omega). \tag{6.2}$$

Equation 6.2 describes the 1D deconvolution procedure where functions are only transformed in the time dimension. It assumes that the charge induced is uniform across all readout wires, and that the measured signal is contributed from only the primary induced wire. This is an approximation of the true case where signals induced on readout wires are topology-dependent and have contributions from ionisation charges inducing signals on adjacent wires. Assuming an approximately constant field response induced on all wires, the 2D deconvolution procedure approximating the measured signal from wire i, $M_i(t)$, can be adapted from equation 6.1 to give

$$M_i(t') = \int_{-\infty}^{\infty} (... + R_1(t'-t) \cdot S_{i-1}(t) + R_0(t'-t) \cdot S_i(t) + R_1(t'-t) \cdot S_{i+1}(t) + ...)dt, \tag{6.3}$$

where $S_{i-1}(t)$, $S_i(t)$ and $S_{i+1}(t)$ are the ionisation signal functions for wire i and those adjacent to it, extending to all wires around wire i on the same wire plane. Equation 6.3 assumes symmetrical response functions about wire i, so $R_1(t'-t)$ is the same for wires $i-1$ and $i+1$. Performing a FFT on equation 6.3 results in

$$M_i(\omega) = ... + R_1(\omega) \cdot S_{i-1}(\omega) + R_0(\omega) \cdot S_i(\omega) + R_1(\omega) \cdot S_{i+1}(\omega) + ..., \tag{6.4}$$

with the corresponding matrix representation

$$\begin{bmatrix} M_1(\omega) \\ M_2(\omega) \\ \vdots \\ M_{n-1}(\omega) \\ M_n(\omega) \end{bmatrix} = \begin{bmatrix} R_0(\omega) & R_1(\omega) & \cdots & R_{n-2}(\omega) & R_{n-1}(\omega) \\ R_1(\omega) & R_0(\omega) & \cdots & R_{n-3}(\omega) & R_{n-2}(\omega) \\ \vdots & \vdots & \ddots & \vdots & \vdots \\ R_{n-2}(\omega) & R_{n-3}(\omega) & \cdots & R_0(\omega) & R_1(\omega) \\ R_{n-1}(\omega) & R_{n-2}(\omega) & \cdots & R_1(\omega) & R_0(\omega) \end{bmatrix} \cdot \begin{bmatrix} S_1(\omega) \\ S_2(\omega) \\ \vdots \\ S_{n-1}(\omega) \\ S_n(\omega) \end{bmatrix}. \tag{6.5}$$

The ionisation signal for each wire $S(\omega)$ is extracted from the measured signal $M(\omega)$ using the known detector response from each wire $R(\omega)$ by rearranging equation 6.5 to $S(\omega) = R^{-1}(\omega)M(\omega)$ [163]. This 2D deconvolution method is far more accurate than the 1D case, while still remaining computationally efficient, despite the addition of the wire dimension. In order to visualise the effect on the measured waveform including contributions from adjacent wires, Figure 6.2 shows a simulated waveform outputted by a single MicroBooNE TPC wire for a MIP track, as well as the waveforms including signal contributions from ± 2 and ± 10 wires adjacent to the central peak wire, for each wire plane.

SBND signal processing typically includes waveform contributions from ± 5 wires adjacent to the central peak wire, which is sufficient in accurately deconvolving the ionisation signal from the measured signal whilst not being too computationally demanding. Every element of the R matrix in equation 6.5 is a convolution of the electronics and field response contributions for each TPC wire, and can be estimated or simulated through data-driven methods or mathematical modelling. This is expanded upon in Sections 6.1.2 and 6.1.3 for the modelling of the electronics and the field response functions respectively.

6.1.2 Electronics Response Function Modelling

At the front-end stage of the SBND readout electronics chain, currents induced on APA wires are inputted into FEMBs, which are amplified by ASIC chips and shaped by the ADC digitisation process. This turns raw TPC signals from ionisation electrons into a waveform with an ADC amplitude and time profile. ASIC amplification generates a pre-amplifier impulse response, converting the current units into a voltage waveform, which is then converted into an ADC waveform by the ADC digitisation process. This amplification process results in broadening of the TPC waveform, which is mathematically equivalent to signal convolution with an electronics response function [161].

Each ASIC chip has two configurable parameters affecting the shape of the output TPC

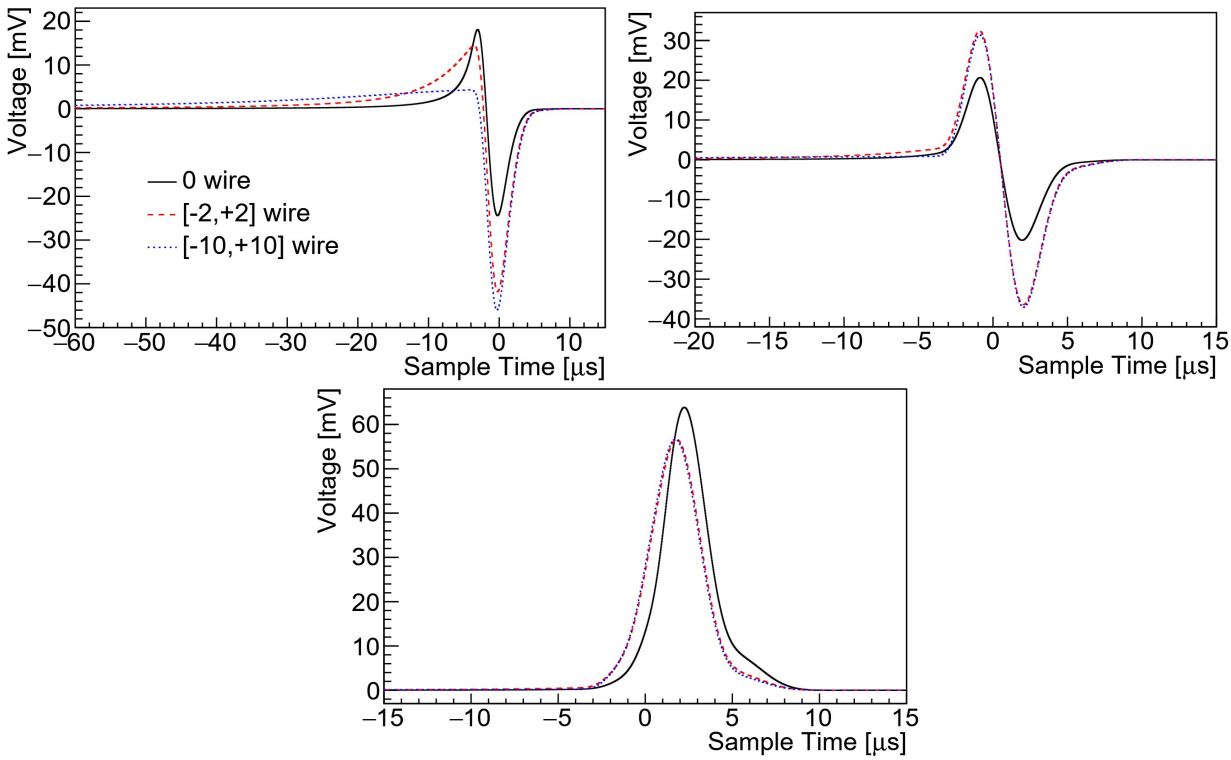

Figure 6.2: MicroBooNE-simulated TPC signals for a MIP track travelling perpendicular to first induction plane (top left), second induction plane (top right) and collection plane (bottom) wires. Summing contributions from the central (0) wire with the highest signal amplitude, two and ten wires adjacent to the central wire. The MIP signal is convolved with the field response, simulated through Garfield [154], and the electronics response, taking the form of a parametric equation with a gain setting of 14 mV/fC a 2 µs peaking time [161].

waveform. First is the gain, defining the magnitude of voltage amplification per unit of charge collected on the wires, with possible values of 4.7, 7.8, 14 and 25 mV/fC. The Second is the peaking time, defined as the time difference between the gain and the value deviating 5% from it in the electronics response function. The peaking time can be set to certain values in the range of 0.5 µs and 3.0 µs in the ASIC chip hardware configuration [163].

ASIC amplification and ADC digitisation can be understood as a series of unit conversions, where the overall goal is to understand how many electrons inducing a signal or collected on APA wires corresponds to 1 ADC unit. The magnitude of this unit conversion is driven by the gain setting, where for 14 mV/fC of gain, with each FEMB operating at 1800 mV having 4096 possible ADC channels, and a single unit of impulse response set to 1 fC, the number of ADCs per e^- induction/collection signal on APA wires is

$$N_{\mathrm{ADC}/e^-} = \frac{14\ \mathrm{mV}}{1\ \mathrm{fC}} \cdot \frac{4096\ \mathrm{ADC}}{1800\ \mathrm{mV}} \cdot \frac{1.602 \times 10^{-4}\ \mathrm{fC}}{1\ e^-} = 0.005104\ \mathrm{ADC}/e^-, \qquad (6.6)$$

which gives the number of electrons per unit of ADC (the reciprocal of N_{ADC/e^-}) to be $N_{e^-/\mathrm{ADC}} \approx 196\ e^-/\mathrm{ADC}$. The parametric form of the pre-amplification impulse response function (i.e. the electronics response) is described by

$$\begin{aligned} R(t, A_0, tp) = {} & A_1 E_1 - A_2 E_2(\cos\lambda_1 + \cos\lambda_1 \cos\lambda_2 + \sin\lambda_1 \sin\lambda_2) \\ & + A_3 E_3(\cos\lambda_3 + \cos\lambda_3 \cos\lambda_4 + \sin\lambda_3 \sin\lambda_4) \\ & + A_4 E_2(\sin\lambda_1 - \cos\lambda_2 \sin\lambda_1 + \cos\lambda_1 \sin\lambda_2) \\ & - A_5 E_3(\sin\lambda_3 - \cos\lambda_4 \sin\lambda_3 + \cos\lambda_3 \sin\lambda_4), \end{aligned} \tag{6.7}$$

where t is the time in μs, A_0 is the amplitude parameter in ADC which depends on the gain setting, t_p is the peaking time and all other parameters are obtained from an antialiasing filter simulation and are defined as

$$\begin{aligned} & A_1 = 4.31054 A_0, \quad A_2 = 2.6202 A_0, \\ & A_3 = 0.464924 A_0, \quad A_4 = 0.762456 A_0, \quad A_5 = 0.327684 A_0, \\ & E_1 = e^{\frac{-2.94809t}{t_p}}, \quad E_2 = e^{\frac{-2.82833t}{t_p}}, \quad E_1 = e^{\frac{-2.40318t}{t_p}}, \\ & \lambda_1 = 1.19361\frac{t}{t_p}, \quad \lambda_2 = 2.38722\frac{t}{t_p}, \\ & \lambda_3 = 2.5928\frac{t}{t_p}, \quad \lambda_4 = 5.18561\frac{t}{t_p}. \end{aligned} \tag{6.8}$$

Figure 6.3 shows the electronics response functions from equation 6.7 in time, with a gain of 4.7mV/fC and multiple different peaking time values for MicroBooNE [161, 164].

Figure 6.3 shows how the gain setting defines the peak conversion between electron charge (in fC) and waveform voltage (in mV), along with the peaking time affects the width of the distribution, getting wider for increasing peaking time. For SBND, the nominal gain and peaking time values of 14 mV/fC and 2.2 μs respectively were calculated from a data-driven method, utilising a Digital-to-Analogue Converter (DAC) pulser. The pulser injects ten different values of charge into the front-end electronics system, finding the waveform peaks and extracting the average response function for these waveforms. Then, equation 6.7 is fitted to the waveform, calculating the peak amplitude (in ADC) and peaking time (in μs). The nominal gain value is then calculated by finding the gradient of the ADC amplitude against DAC value graph. The Nominal shaping time is extracted as the weighted average of all DAC waveform peaking times, which resulted in nominal gain values of 14 mV/fC and 2.2 μs respectively for SBND.

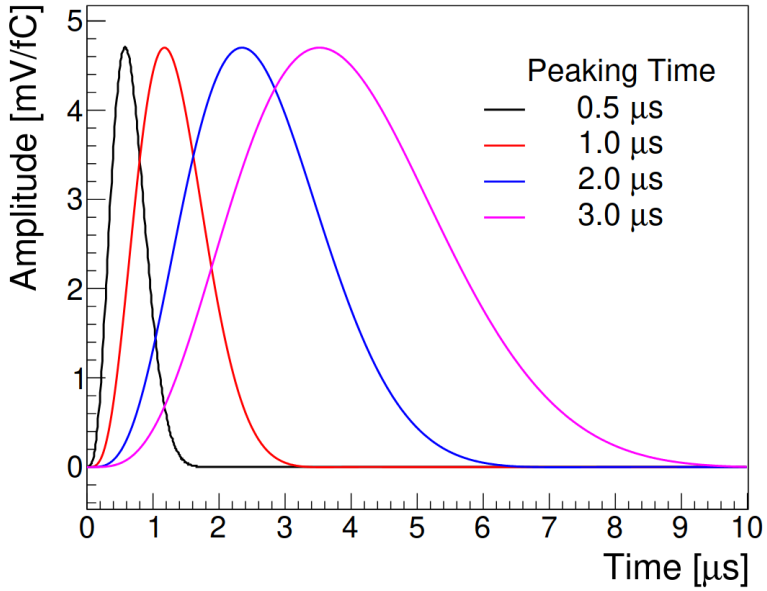

Figure 6.3: MicroBooNE pre-amplifier electronics response functions for a gain setting of 4.7 mV/fC and peaking times of 0.5 μs, 1.0 μs, 2.0 μs and 3.0 μs [161].

6.1.3 Field Response Function Modelling

As stated previously in section 6.1.1, the field response is the smearing of TPC waveforms due to current inductions on APA wires due to the electric field of nearby drifting ionisation electrons. Ramo's theorem describes the magnitude of the current induced on APA wires [165], where for a drifting charge q with velocity vector $\overrightarrow{v_q}$ in a weighted electric field $\overrightarrow{E_w}$, the current i induced on a nearby wire is

$$i = -q\overrightarrow{E_w} \cdot \overrightarrow{v_q}, \tag{6.9}$$

where $\overrightarrow{E_w}$ is the component of the externally applied electric field in the direction of $\overrightarrow{v_q}$, and only depends on the electrode geometry. $\overrightarrow{E_w}$ can be computed by removing the drifting charge, placing the targeted electrode at unit potential, and setting all other conductors to ground. $\overrightarrow{v_q}$ is a function of the external electric field, which is in turn dependent on the electrode geometry, as well as the applied drift voltage, wire bias voltage and liquid argon temperature. In the case of a point charge q_m drifting between electrodes, at the point where it is on an infinitesimal electrode with charge Q_I induced by q_m and potential V_I, Green's reciprocity theorem [166] gives

$$q_m \cdot V_m = Q_I \cdot V_I, \tag{6.10}$$

where V_m is the potential at the position of q_m induced by the sensing electrode potential V_I. Differentiating equation 6.10 with respect to time gives the current induced on the sensing electrode by q_m as

$$i = \frac{dQ_I}{dt} = q_m \cdot \vec{\nabla} V_w \cdot \frac{d\vec{r}}{dt}. \tag{6.11}$$

The weighting potential V_w is a dimensionless quantity defined as $V_w = V_m/V_I$. Using the fact that $\vec{\nabla} V_w = -\vec{E_w}$ and $\frac{d\vec{r}}{dt} = \vec{v_q}$, equation 6.11 is equivalent to equation 6.9. The total charge induced on a single APA wire from the electric field of a drifting charge q_m is given by the integral of the induced current

$$\int i dt = q_m \cdot (V_w^{end} - V_w^{start}), \tag{6.12}$$

which is proportional to the value of V_w at the start and end of the drift path [161]. This is the mathematical groundworks for field response function modelling in SBND, where field response functions are calculated using the Garfield software [154], and the Wire-Cell package uses these field response functions to model TPC waveforms on APA wires [155].

In the SBND simulation, field response functions take the form of an array of current values induced on APA wires, for all three wire planes, at 0.3 mm segments of the electron drift path, the same as one tenth the distance between each APA wire. The electric field strength across the TPC and bias voltages applied to each wire are also used to calculate the induced currents. The first step in calculating field response functions is to compute the possible electron drift paths for ionisation electrons drifting perpendicularly towards the wire plane, as 0.3 mm increments in the transverse direction. Figure 6.4 shows the calculated electron drift paths for MicroBooNE TPC readout wires.

Each electron path shown in Figure 6.4 starts 10 cm from the collection wire plane in the negative drift direction. After all possible electron paths are calculated, the next step is to calculate the weighting potentials for every wire at each point on all electron paths presented in Figure 6.4. Figure 6.5 shows the phase space of weighting potential values for each electron path in the MicroBooNE TPC.

Finally, the induced current for a given electron path and corresponding weighting potential is calculated using equation 6.9, including contributions from ±10 wires about the closest wire to the electron, repeating the calculations for increments of 0.3 mm in the transverse direction to the electron path every 0.1 µs. These field response calculations are approximations of the true case, and neglect detector effects such as diffusion, TPC edge effects or SCE which would result in additional function smearing. Wire-Cell is used to sum these field response functions together in time, outputting the total field response

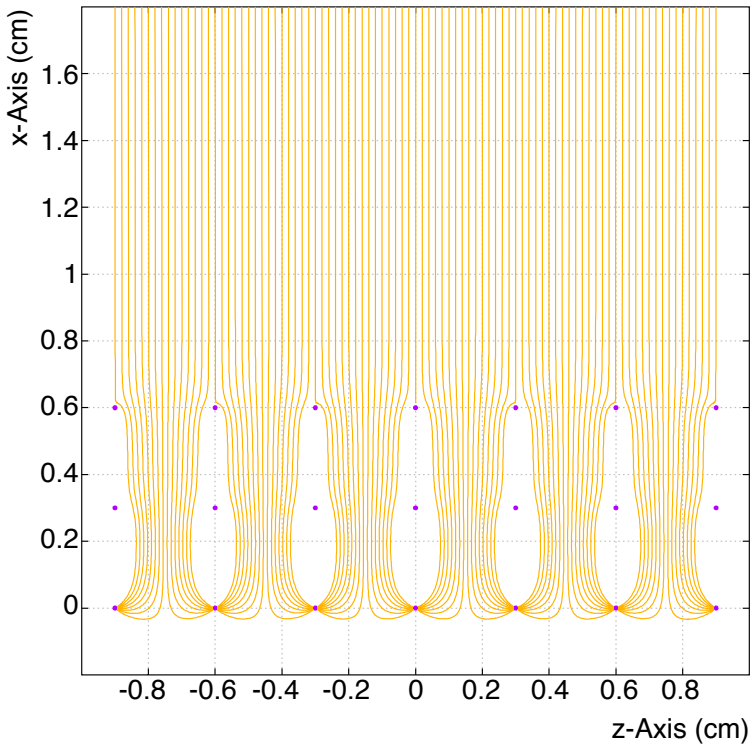

Figure 6.4: Ionisation electron drift paths in the MicroBooNE TPC subject to a 273 V/cm electric field. The first induction, second induction and collection plane wires are voltage-biased at -110 V, 0 V and 230 V and are projected +60°, -60° and 0° with respect to the normal of the page respectively. The x-axis is in the electric field direction and the z-axis is in the beam direction [161]. Electron paths are calculated in 0.3 mm segments using the 2D Garfield software [154].

function due to a single ionisation electron for each wire plane. Figure 6.6 shows the total field response function for each MicroBooNE APA wire plane represented as a waveform, plotting the current induced by a single electron over time.

The distinctive bipolar waveform shape exhibited by the induction plane wire field response in Figure 6.6 is due to a negative current induced on wires resulting in an initially positive voltage waveform, until the ionisation electron drifts past the wires, decreasing the weighting potential until it changes sign, leading to a negative voltage waveform. Collection plane wires always show a positive unipolar induced field response due to the weighting potential always increasing as the electron approaches, until it sharply drops to zero as the electron terminates on the wire. Signals on induction plane wires are generally smaller in amplitude than collection plane wires due to the negative voltage bias applied to the first induction plane, diverting the electrons from the area of maximum weighting potential, which is the closest point to the wire.

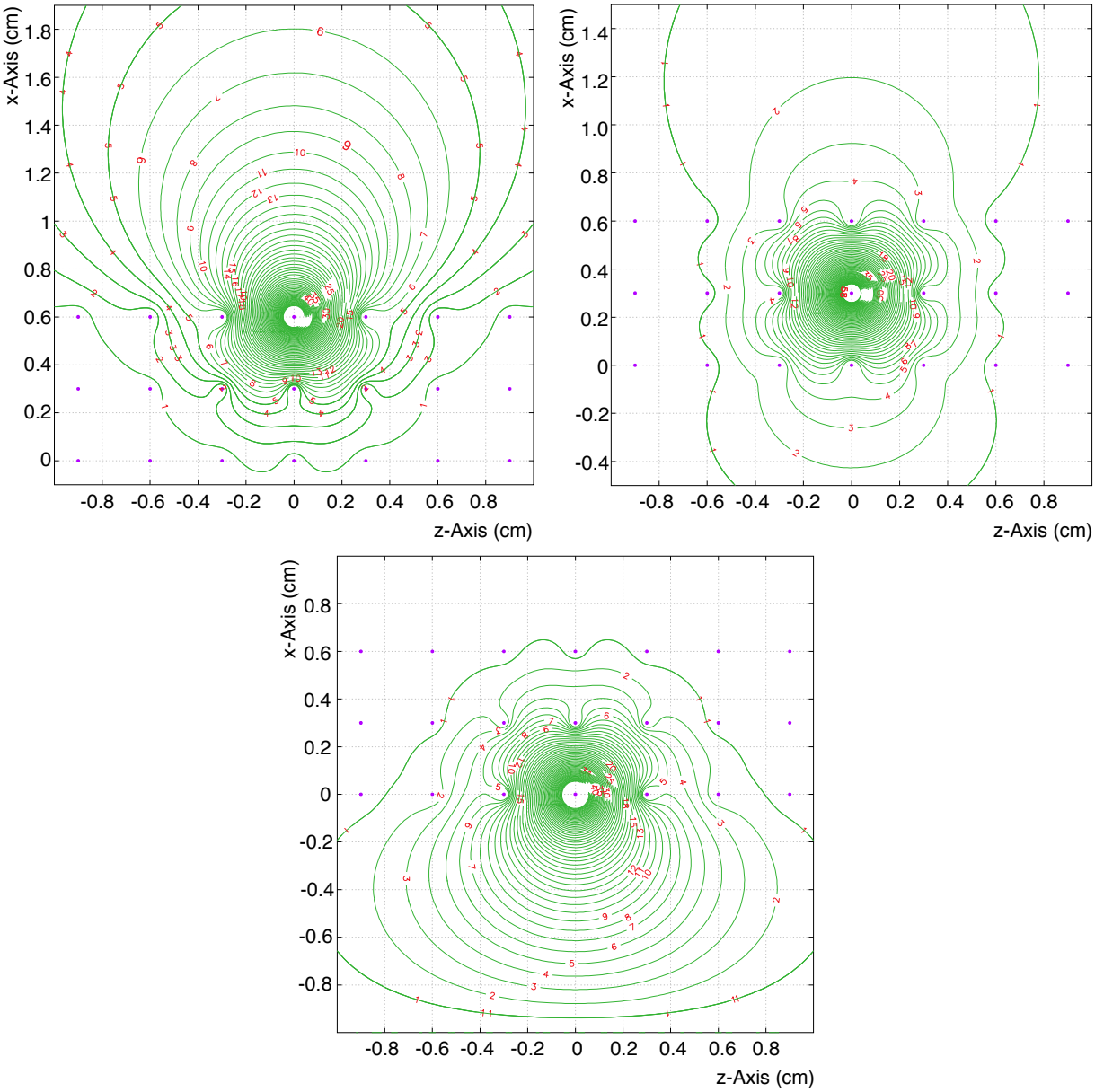

Figure 6.5: Weighting potential field values for a single wire in the first induction (top left), second induction (top right) and collection (bottom) wire planes for the MicroBooNE TPC, with an electric field strength of 273 V/cm. The x-axis is in the electric field direction and the z-axis is in the beam direction. Weighting potential is dimensionless and is relative to the electric potential on the target wire, indicated as percentages on equipotential lines [161]. Weighting potential values are calculated using the 2D Garfield software [154].

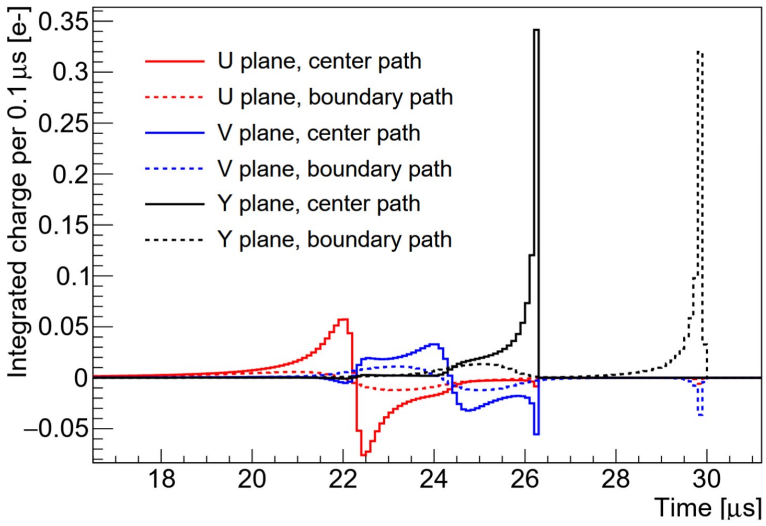

Figure 6.6: Total current induced over time from various paths of a single drifting ionisation electron for the closest wire on the first induction (U), second induction (V) and collection (Y) planes, each biased at -110 V, 0 V and 230 V respectively. Responses are also calculated for 1.5 mm boundaries between adjacent wires [161].

As well as calculating field response functions for different electron paths using Garfield, the magnitude and time profile of the field response on APA wires also varies with the angle of neutrino interaction induced charged particle tracks projected into the x–z plane with respect to the z-axis, called the track pitch angle θ_{xz}. x is the electron drift direction and z is the beam direction, meaning $\theta_{xz} = 0$ corresponds to tracks parallel to the APA and $\theta_{xz} = 90°$ perpendicular to the APA. The total wire response function is calculated by convolving the electronics and field response functions using equation 6.1, substituting R for the electronics response and S for the field response functions.

To accurately convolve both functions, the field response needs to be averaged over all possible electron drift paths using the Wire-Cell package. Since the electronics response only affects the waveform after being outputted by the TPC readout process, the same function is convolved with all three wire plane field response functions. Figure 6.7 shows the total wire response as a convolution of the field and electronics response functions for a single electron inducing a current on all three wire planes in the MicroBooNE TPC.

The total wire response function in Figure 6.7 shows clear signal smearing for all three wire planes as a result of ASIC amplification and ADC digitisation processes of the readout electronics chain. Convolving the collection plane field response with the electronics response, as well as including induced current contributions from many electron paths, results in smearing the sharp drop from peak to zero voltage observed in Figure 6.6 to a more gradual decrease to zero voltage, as observed in Figure 6.7. Understanding the effects

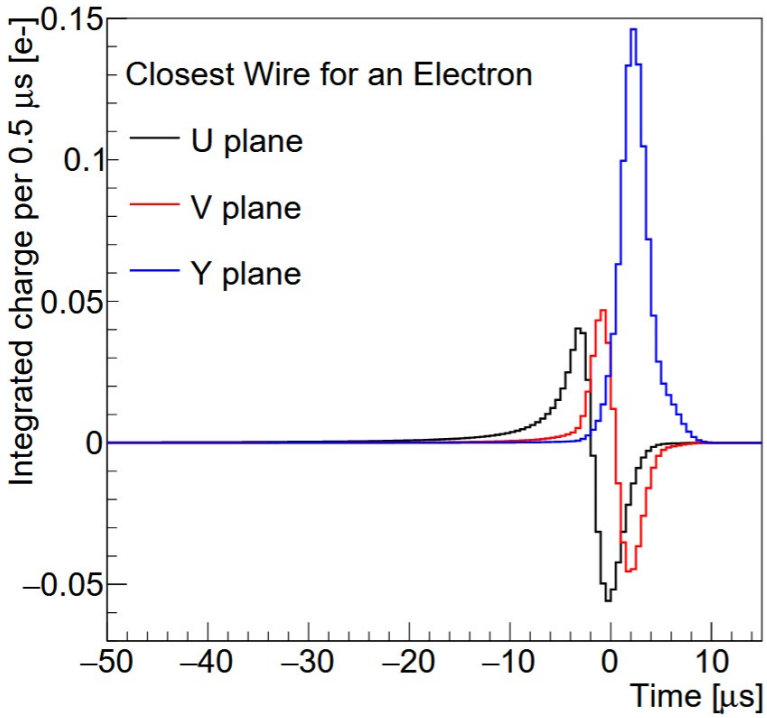

Figure 6.7: MicroBooNE total wire response function on the closest wire to a single ionisation electron for the first induction, second induction and collection planes (labelled U, V and Y respectively). Calculated by convolving the field response, averaged over all electron drift paths and computed by Garfield [154], with the electronics response function from equation 6.7 using a gain of 14 mV/fC and a peaking time of 2 µs [161].

of signal broadening when including contributions from different electron paths, adjacent wires and changing track pitch angle is integral to modelling the field response correctly.

6.2 Reconstructed Monte Carlo Waveforms

Other LArTPC experiments such as MicroBooNE [164], ICARUS [163] and ProtoDUNE-SP [167] validated the field response by comparing 2D field response functions simulated using Garfield to the deconvolved TPC readout waveforms as seen in data. However, at the time this work was undertaken, SBND was not yet collecting physics data, so a method for validating the field response using MC samples produced by the SBND simulation was developed, adapted from a similar methodology which was applied to ICARUS [163]. This involves comparing reconstructed TPC waveforms from a large sample of MC events, modelled by the SBND simulation, with a theoretical prediction for what the expected TPC waveform should look like using calculated field and electronics response functions.

6.2.1 Validation Methodology and Event Selection

Generating the MC event samples for TPC waveform reconstruction starts with simulating more than 100,000 cosmic-ray muon events using CORSIKA [152], selecting tracks that cross the SBND cathode and either anode plane. Anode-cathode crossing muons allow for better determination of the interaction time t_0, and therefore drift coordinate x, as well as including a wide range of track angles in the dataset. Ionisation electrons produced from track segments 2–5 cm in the longitudinal direction from the APA are then selected to reconstruct the output TPC waveforms. Track segments closer than 2 cm lead to biases in signal shape estimation on the unshielded first induction plane, and further than 5 cm causes significant waveform shape broadening due to diffusion [163]. TPC waveforms for each track are then reconstructed by averaging the signals from ± 5 wires about the central wire with the highest ADC amplitude. Then, all track waveforms are coherently added across the widest angle range possible, repeated for each wire plane, resulting in an average reconstructed TPC waveform for induction and collection plane wires.

This waveform is then compared with a theoretical prediction as to what the average waveform should look like assuming the input field response functions calculated using Garfield are nominally applicable to SBND. This theoretical prediction takes the form of a total wire response function for a single readout wire, similar to Figure 6.7, which is a convolution of the total 2D field response function and parametrised electronics response function in equation 6.7. Wire-Cell is used to compute the total 2D field response function by summing all single electron field response functions over all electron paths and pitch angles, including contributions from ± 10 adjacent readout wires. Average reconstructed MC waveforms sum over ± 5 adjacent readout wires instead to be less computationally intensive, whilst not losing sufficient signal contributions from wires outside this range.

Due to the misalignment of muon signals as a result of detector noise, additional smearing of the waveform with a dependency on muon pitch angle θ_{xz} will occur. The angular acceptance of anode-cathode crossing tracks in the SBND TPC with respect to the wire plane is approximately $26° \leq \theta_{xz} \leq 80°$. The minimum requirement for a track to be anode-cathode crossing in SBND is $\theta_{xz}^{min} \approx \tan^{-1}(2\text{ m}/5\text{ m}) \approx 22°$, but data observations showed that tracks with $\theta_{xz} < 26°$ exhibit complications in averaging signals due to inductions close to the edge of the APAs, as well as the fact that tracks with $\theta_{xz} < 26°$ lose more energy over the longer charged particle path length. Tracks with $\theta_{xz} > 80°$ make signal alignment in time more difficult, especially with the complex nature of bipolar signals in the induction planes. To account for the dependence of signal broadening on θ_{xz}, each response function from all the wire planes are convolved with a Gaussian with width

$\sigma(\theta_{xz}) = \sqrt{a^2 + b^2 \tan^2 \theta_{xz}}$, where a and b are parameters unique to each wire plane [163].

Ideally, the reconstructed MC waveform should line up with the theoretical prediction, and any disagreements will be due to inaccurate field response functions calculated using Garfield or Wire-Cell suboptimally modelling these functions into a TPC waveform in the SBND simulation. If waveform deviations are dependent on pitch angle, it is typically the Garfield field response function calculations that need correcting, otherwise if the differences are independent of pitch angle then the Wire-Cell code used within the SBND simulation needs modification. The goal of this validation procedure is to identify discrepancies in the waveforms and identify whether these are due to the Garfield or Wire-Cell simulations; both of which can be tweaked until the waveforms maximally align.

Both the SBND simulation and theoretical prediction calculation use the same set of field response functions as inputs to their respective waveform modelling processes. Altering these functions leads to trivial differences in the calculated total wire response, but leads to non-standard deviations in the shape of the reconstructed MC waveform. This is due to the disparity in the simplicity of calculating the theoretical prediction compared to running the field response functions through complex signal processing algorithms present in the SBND simulation. Theoretically, there is an optimal set of field response functions that most accurately describe current inductions on SBND readout wires from ionisation electrons, resulting in the average reconstructed MC waveform maximally aligning with the theoretical prediction. These optimal field response functions would typically be determined through comparisons with data waveforms. However, in the absence of SBND data, this methodology is sufficient in identifying whether the input field response functions or Wire-Cell simulation need correcting if the two waveforms do not maximally align.

6.2.2 Monte Carlo Event Sample Production

High statistics MC event samples of anode-cathode crossing cosmic-ray muons are produced using the SBND simulation. The particle generator file used a single particle gun to create ten muons (PDG code 13) at $t = 0$ s with 0.8 GeV/c average momentum, five of which have their muon tracks originating from the east side APA and the other five produced from the west side APA, with $\theta_{xz} = 45° \pm 45°$ measured from their respective APAs. y and z coordinates of the tracks are uniformly distributed across the detector, with $\theta_{yz} = 45° \pm 45°$, to avoid biases in track position and angular distribution. Figure 6.8 shows an event display depicting these MC cosmic-ray muon tracks.

For the purposes of this study, deviations in ionisation electron paths due to SCE are neglected. TPC waveform simulation begins with GEANT4 [153] modelling charged particle

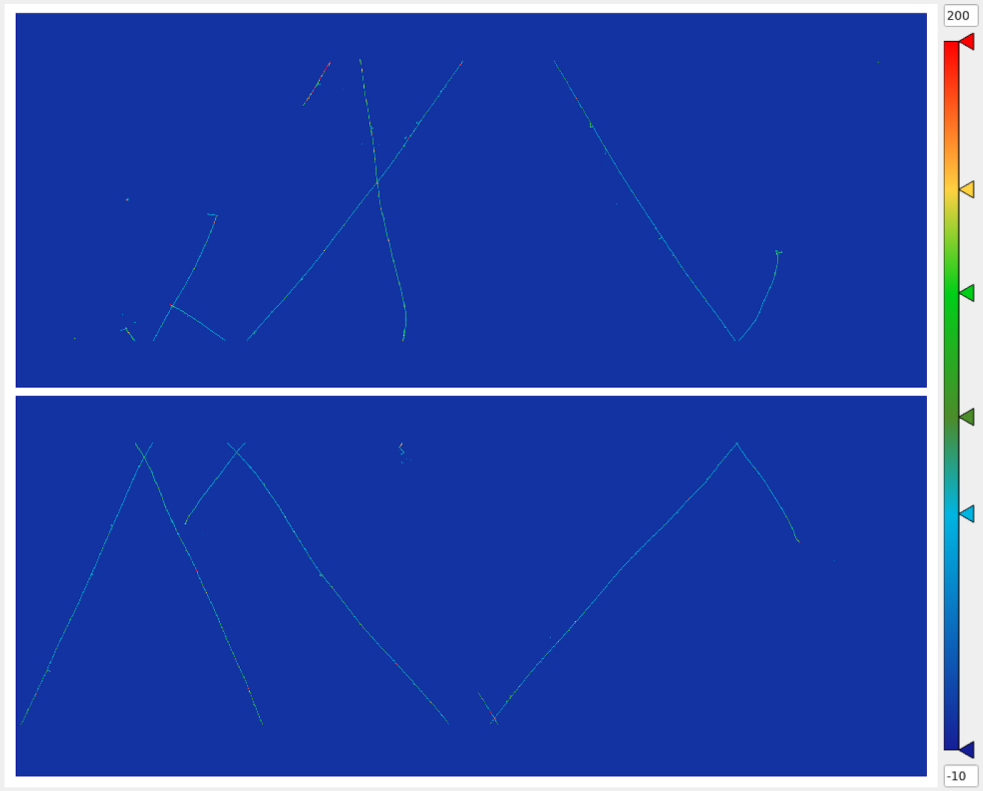

Figure 6.8: Event display with ten MC cosmic-ray muons tracks within the SBND cryostat. The x (drift), y (vertical) and z (beam) directions are pointed down, towards the reader and to the right of the plot respectively, giving a top-down view of SBND with the east TPC on the top and west TPC on the bottom. The colour axis on the right shows the range of energies of each track element in ADCs.

interactions with argon atoms releasing ionisation electrons, simulating signal inductions on APA wires, as well as accounting for waveform smearing and shaping due to diffusion and SCE. Next, Wire-Cell takes the field response functions from Garfield, calculates the total average 2D field response function for each wire, and convolves them with the parametrised electronics function in equation 6.7. This total wire response function is then convolved with the ionisation signal - also simulated using GEANT4 - to create the RawDigit data product, containing ADC over time functions, including response contributions from ± 5 wires adjacent to the central wire. Baseline noise is then coherently added to each wire channel, before shaping the waveforms through simulation of the ADC digitisation process, both resulting in slight signal broadening for all wire planes.

Each ADC waveform takes the form of an ADC against time function for each wire channel, discretised into in time ticks $t_s = 0.5$ µs. In the SBND simulation, the full drift time is 1.3 ms (2,600 t_s), with additional readout periods 0.2 ms (400 t_s) before

and after this drift window, giving a total time profile of 1.7 ms, or 3,400 time ticks, for each TPC waveform. In the standard SBND simulation workflow, RawDigit data products were dropped due to the high amount of storage required to produce waveforms for all wire channels from thousands of ionisation electrons per event. However, since waveform information is required for the field response validation study, a dedicated workflow was developed to keep the RawDigit data products, propagating them through LArSoft to output simulated signal waveforms on APA wires for each reconstructed track.

At the end of the LArSoft workflow, the RawDigit data products are fed into a program that skims across the length of each charged particle track, extracting information at each segment of the track. This results in a ROOT file containing the x, y and z coordinates and direction the track is heading in at each time tick t_s, as well as calorimetric information such as dE/dx and residual range. They also contain wire signal information associated with each track, including the wire numbers that each track induced a signal on for each wire plane, and the associated ADC over time waveform for each wire, contained within the RawDigit data product used for the field response validation study.

6.2.3 Average Monte Carlo Waveforms on SBND TPC Wires

After a sample of 200,000 MC anode-cathode crossing cosmic-ray muons were simulated using the aforementioned workflow, the next step in the validation methodology is to plot the average reconstructed TPC waveform for induction and collection plane wires. A program was developed in C++ for ICARUS for this purpose, which has been adapted for SBND's differing geometry, physics parameters and selection criteria. The main parameters governing the track selection criteria for this field response validation study are the ADC thresholds for each wire plane and the NonLinearity (NL) factor governing how straight a track is. ADC thresholds cut tracks that have negative/positive peaks above/below the chosen ADC threshold for induction/collection planes wires, so optimising this parameter is essential in distinguishing between signal and background noise.

A threshold value of ∓ 6 ADC for induction/collection plane wires was chosen based on visually scanning through many individual ADC waveforms from the 200,000 MC event sample, though a complete study on understanding the waveform amplitudes will be undertaken in the future to determine the optimal ADC threshold values for each wire plane. NL is a parameter governing how straight a track is, with an ideally straight track having a NL value of zero, increasing with greater deviations due to scattering off of argon atoms and production of delta rays. Based on understanding the NL distribution of each MC dataset, a NL threshold value of 4 was chosen, though a full study on this parameter for

SBND will be undertaken such that sufficiently straight tracks are selected.

The average reconstructed waveform program runs through the output ROOT file from the LArSoft workflow, scanning through each event and extracting the spatial, temporal and wire calorimetry information of each track, repeated for all three wire planes. Selection criteria are implemented such that only contributions to the waveform from track segments 2–5 cm from the anode are included, combining waveforms induced on both APAs. Then, the full range of wire numbers exhibiting signal inductions are calculated, as well as the track angles θ_{xz} and θ_{yz} based on the wire geometry and electron drift velocity, which is $v_e = 0.1571$ cm/µs for the electric field strength of 500 V/cm used in SBND.

Next, the program finds the wire with the minimum/maximum ADC value for the induction/collection plane(s), lining up the negative/positive peaks of waveforms ±5 wires around the central peak wire and coherently adding them, saving the waveform ±100 µs about the negative/positive peak. Finally, every averaged waveform for each track with angles $20° < \theta_{xz} < 80°$ is added coherently, resulting in a total average reconstructed waveform for each wire plane. The ROOT file containing the waveform information from the 200,000 MC cosmic-ray muon sample was inputted into the average waveform program, averaging 7,622 first induction plane, 7,638 second induction plane and 5,600 collection plane waveforms passing the selection criteria, producing the plots in Figure 6.9.

ADC baseline subtraction of the plots in Figure 6.9 was chosen such that the right-hand side of the first induction plane waveform at $t = 100$ µs corresponds to zero ADC, called right-hand baseline mode. This is so the gradual increase in induced current for $t < 0$ s from long-range ionisation electrons is observed. The second induction and collection plane wires show left-hand baseline mode where zero ADC corresponds to t =-100 µs, since these planes are shielded from long-range induction by the first induction plane. Induction plane waveforms exhibit the expected bipolar shape, with a larger negative peak for the first induction plane with respect to the more symmetrical second induction plane waveform, where the collection plane is showing the expected unipolar waveform shape.

An erroneous wide uplift in signal is observed to be centred around t = -40 µs for the plane 0 waveform, which could be due to overestimations in the waveform contributions from long-range ionisation electron induction. Additionally, there are small bipolar artefacts at approximately t = 20 µs for plane 0 and t = -70 µs for plane 1, which represent individual track induction waveforms, suggesting they are a result of signals from different wires being misaligned in the averaging process. Understanding the angular breakdown of the waveforms is essential in fully characterising and calibrating the response signals, as different track angles result in varying degrees of waveform broadening and smearing.

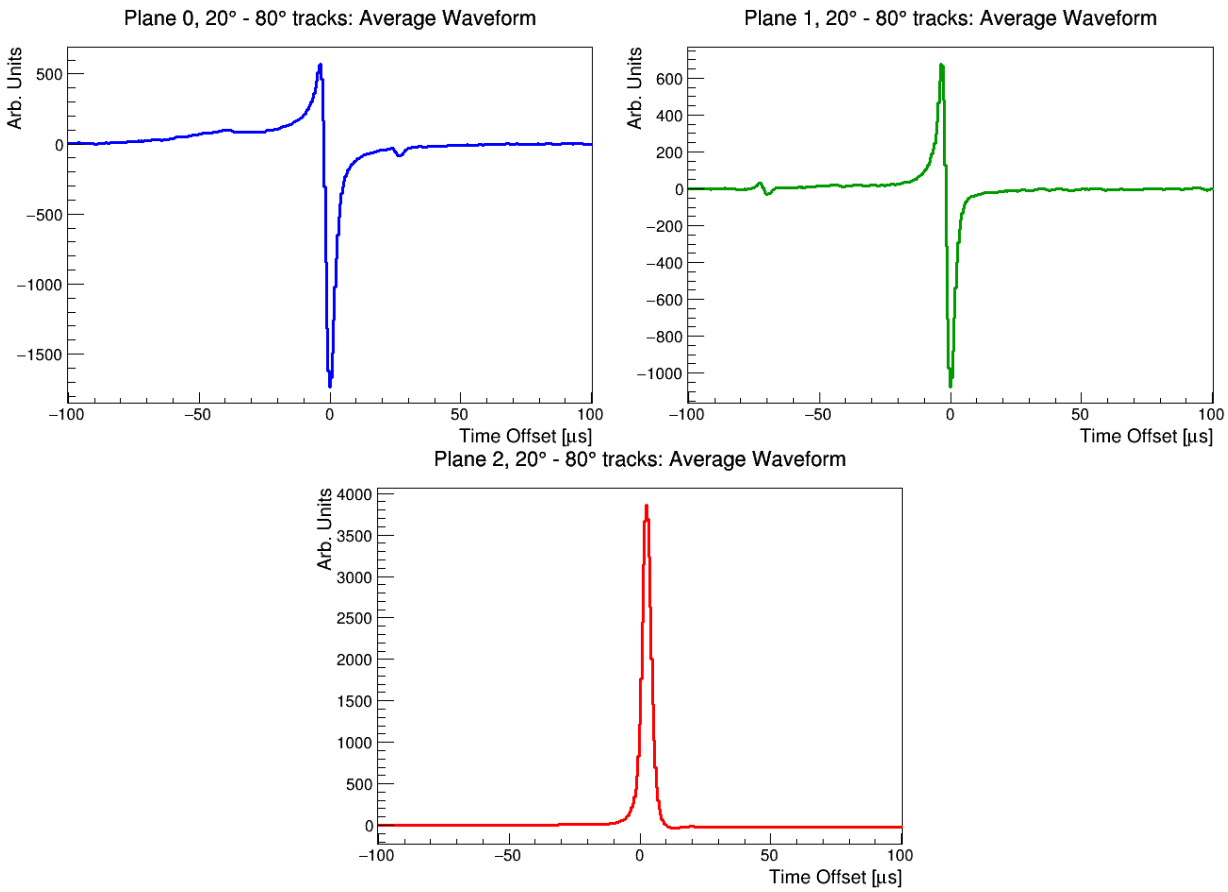

Figure 6.9: Reconstructed MC waveforms on SBND TPC readout wires for the first induction (top left), second induction (top right) and the collection (bottom) planes, averaged over 200,000 simulated anode-cathode crossing muon tracks within an angle range of $20° \leq \theta_{xz} \leq 80°$. Track segments 2–5 cm from the APA were selected, exceeding amplitudes of 6 ADC and including contributions of ±5 wires adjacent to the central wire.

Figure 6.10 shows the averaged reconstructed MC waveform for each wire plane, broken down into $\Delta\theta_{xz} = 10°$ angle segments in the range $20° < \theta_{xz} < 80°$.

As expected, the waveform plots in Figure 6.10 show large signal fluctuations for high ($\theta_{xz} > 70°$) and low ($\theta_{xz} < 30°$) track pitch angles in all wire planes. Tracks with high θ_{xz} exhibit difficulties lining up signals in time from wires adjacent to the central wire, due to them running almost perpendicular to the APA with such a small range of wires for ionisation electrons to induce signals on. Combined with the fact that perpendicular tracks emit electrons in roughly the same direction as the track itself, parallel to the drift direction x, making the process of lining up signals in time extremely difficult as electrons build up around the APA, which is particularly challenging when it comes to modelling the complex nature of bipolar induction plane waveforms.

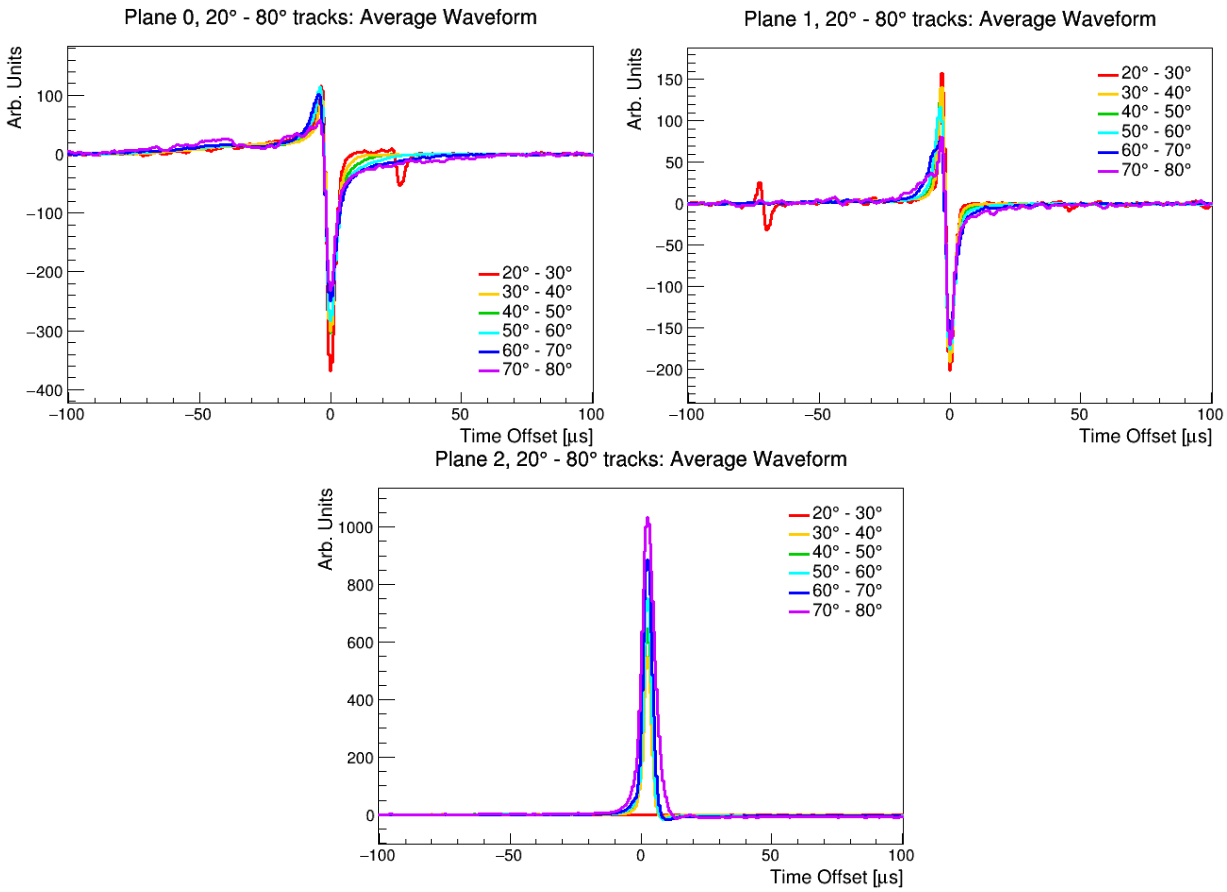

Figure 6.10: Total reconstructed MC waveforms on SBND TPC readout wires for the first induction plane (top left), second induction plane (top right) and the collection plane (bottom), broken down by $\Delta\theta_{xz} = 10°$ segments in the range $20° \leq \theta_{xz} \leq 80°$. Waveform plotting and selection criteria are the same as in Figure 6.9.

Conversely, tracks with lower θ_{xz} values are less likely to be selected due to their longer path length, running almost parallel to the APA, meaning they terminate too fast in the LAr medium for ionisation electrons to induce sufficient signals on readout wires. Additionally, the anode-cathode crossing selection criteria means that no tracks have $\theta_{xz} < 26°$, so very few tracks with $\theta_{xz} < 30°$ are present in the data. This leads to artefacts such as the anomalous oscillations at $t = 20$ µs for plane 0 and $t =$ -70 µs for plane 2 which are only present for $20° < \theta_{xz} < 30°$, representing misaligned signals from individual tracks.

Additionally, low statistics at $20° < \theta_{xz} < 30°$ leads to zero tracks passing the ADC threshold for the collection plane in Figure 6.10 in this angle range. This further supports the need for a full study on tuning the ADC thresholds for each wire plane, as they could be different for each wire plane, despite electronic noise affecting each wire plane equally. But for now, tracks with angles in the range of $30° < \theta_{xz} < 70°$ are sufficient for this study.

To better understand the difference in ADC amplitude for varying θ_{xz}, the time axis for the plots in Figure 6.10 is narrowed to -25 µs $< t <$ 25 µs, shown in Figure 6.11.

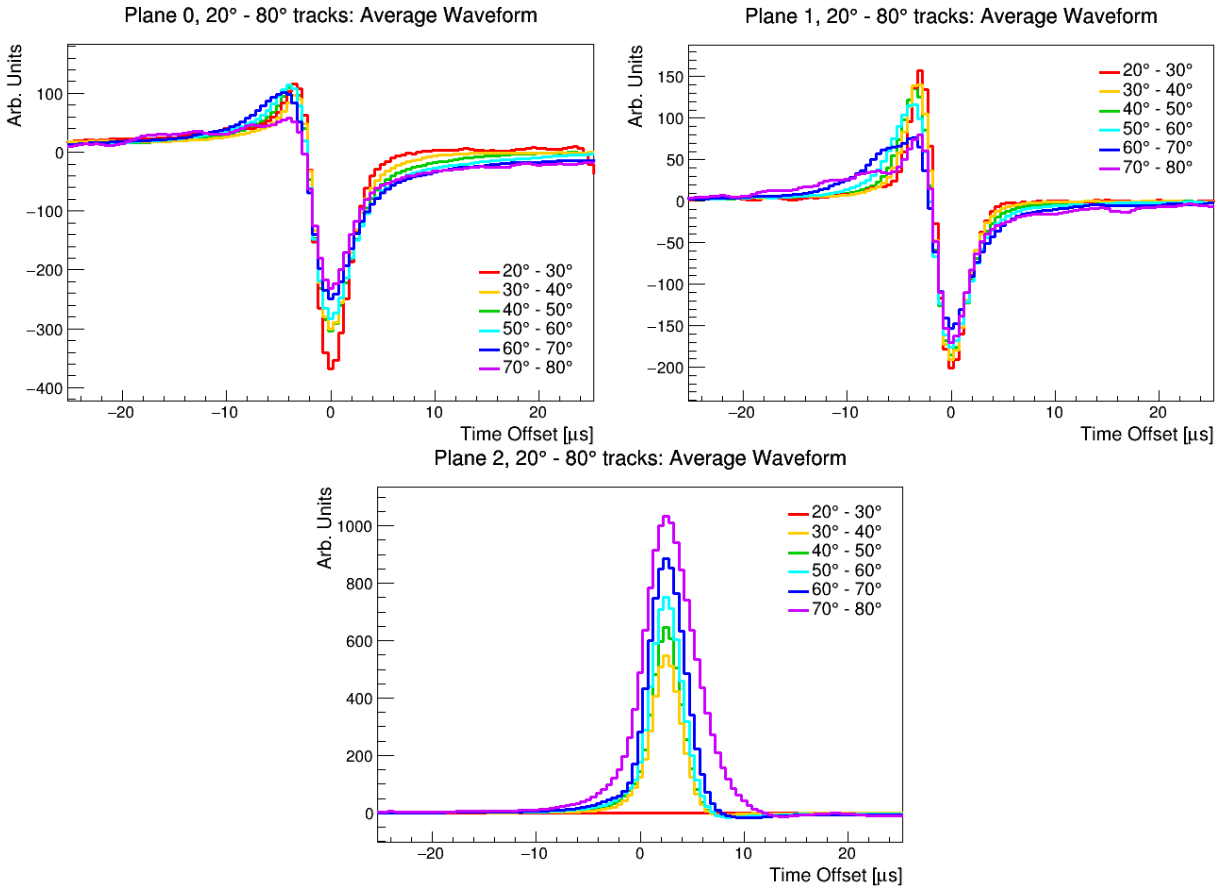

Figure 6.11: Total reconstructed MC waveforms on SBND TPC readout wires for the first induction plane (top left), second induction plane (top right) and the collection plane (bottom), broken down by $\Delta\theta_{xz} = 10°$ segments in the range $20° \leq \theta_{xz} \leq 80°$, with a narrower time axis range than Figure 6.10 of -25 µs $\leq t \leq$ 25 µs.

The narrower time axis in Figure 6.11 allows for better scrutinisation of how the signal peaks, timing width and fluctuations in waveform shape differ with respect to varying θ_{xz}. Plane 0 shows a more pronounced initial peak at around $t =$ -5 µs for track angles of $20° < \theta_{xz} < 60°$, with dips observed in higher θ_{xz}, especially with $\theta_{xz} > 70°$. The characteristic negative induction peak at $t = 0$ µs is most pronounced at $20° < \theta_{xz} < 30°$, reducing in amplitude as θ_{xz} increases. Tracks with lower θ_{xz} induce a greater positive and negative induction peak due to the simpler time profile of ionisation electrons spread across wire planes. This is because tracks with lower θ_{xz} are close to being parallel to the APA, making it easier to line up and coherently add waveforms when averaging over ±5 wires around the central wire, at the cost of making it more difficult to align waveforms in time.

This same trend can be seen in the positive and negative peaks of the plane 1 waveform, where tracks in the angle ranges of $\theta_{xz} = 20°$–$30°$ result in the greatest positive and negative induction peaks, decreasing in amplitude with increasing θ_{xz}. The collection plane waveform, despite selecting zero tracks with $\theta_{xz} < 30°$, exhibits a larger ADC amplitude and greater signal width with increasing θ_{xz}, which is most likely due to more charge being collected over a narrower wire range for tracks close to being perpendicular to the APA.

6.3 Response Function Modelling on SBND TPC Wires

Previously outlined in Section 6.1.3, SBND uses a 2D Garfield simulation [154] to model the induced current on readout wires from ionisation electrons over 0.3 mm path segments every 0.1 µs, including contributions from ±10 wires about the wire closest to the path, for all three wire planes. These calculations are then repeated altering the track pitch angles by $\delta\theta_{xz} = 2°$ from $\theta_{xz} = 20°$ to 80°. The plots in Figure 6.12 show the induced field response on SBND TPC readout wires from a single ionisation electron, averaged over every electron path segment and pitch angle, then averaged over all wires for each wire plane separately.

The first induction plane field response in Figure 6.12 gives the expected bipolar shape, with a slow increase in induced current to a positive peak, decreasing to a sharp negative peak and gradually trailing off to zero current. Approximately symmetrical positive and negative peaks are observed in the second induction plane field response. The collection plane gives its distinctive unipolar peak, with small fluctuations about its peak, then a long tail that trails off to zero current as time increases. The plots in Figure 6.12 show the total induced field response from a single ionisation electron over all possible paths, but it is also important to understand how the induced current varies with respect to the chosen electron path, in the transverse direction from the closest wire. The variance of the average field response with respect to transverse electron paths from -1.5 mm to 1.5 mm in 0.3 mm segments are presented in Figure 6.13 for each wire plane.

Figure 6.13 shows that electron paths closest to the central wire exhibit the largest induced currents for the induction planes. Induced currents on collection plane wires get lower and more time delayed the greater the electron path deviates from the path closest to the central wire. The minor negative peak observed in the right-hand side of the second induction plane occurs as electrons terminate on collection plane wires. The dependence of the field response to the electron path deviation from the central wire results in a non-trivial dependence on θ_{xz} due to the intrinsic relationship between θ_{xz} and the distribution of emitted ionisation electrons from the track. There is also an additional dependence on

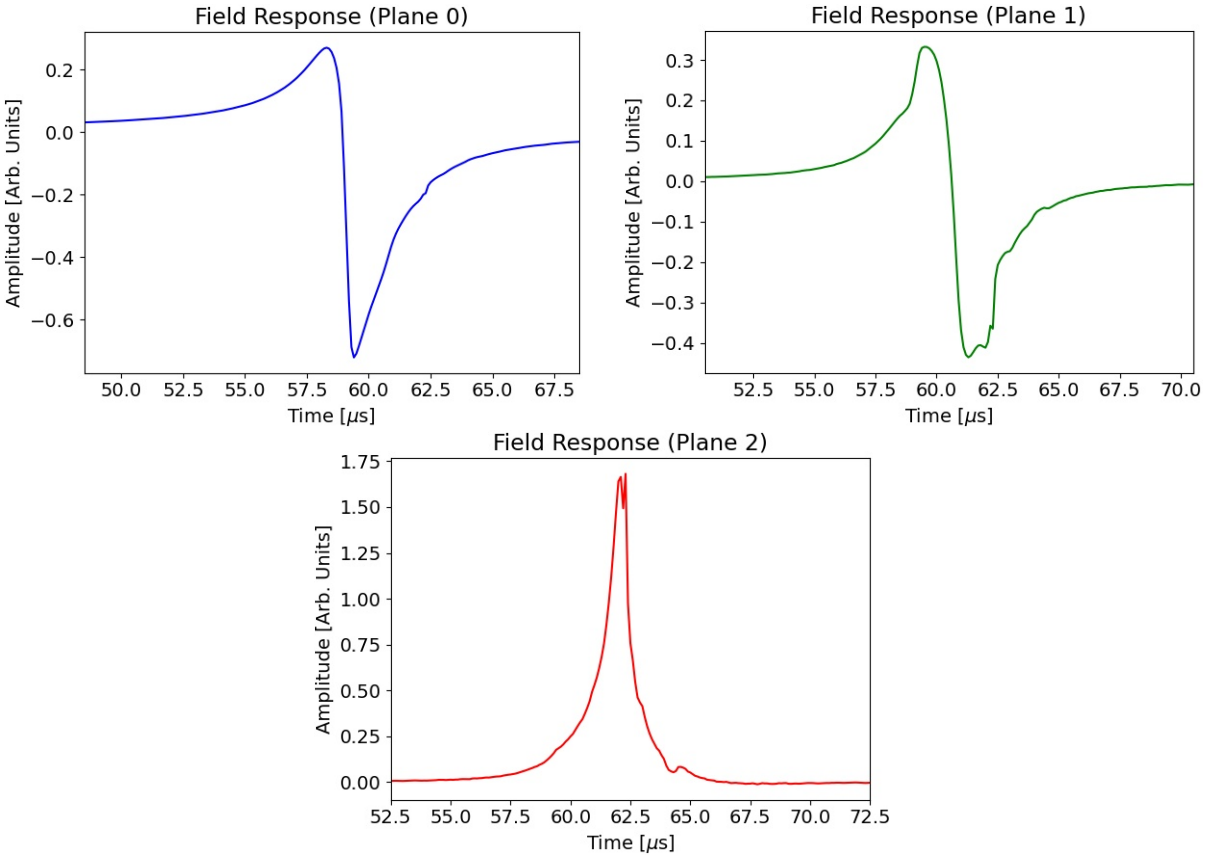

Figure 6.12: Induced current over time on SBND TPC readout wires for the first induction (top left), second induction (top right) and collection (bottom) wire planes. Currents are averaged over all electron paths, pitch angles and all wires in each wire plane. Field response functions are modelled using a 2D Garfield simulation [154].

the field response from a single ionisation electron on the pitch angle of the electron itself due to induced current past the wire plane and long-range induction, but this is accounted for by the 2D Wire-Cell simulation by using the true path of each ionisation electron.

The Wire-Cell package has the ability to interpolate induced currents on wires from electron paths at 0.03 mm increments, between the 0.3 mm path segments. To better understand the relationship between induced field response on TPC readout wires and θ_{xz}, plots of the field response for three chosen $\delta\theta_{xz} = 2°$ segments were produced for each wire plane, summing the contributions from all electron paths from -1.5 mm to 1.5 mm at 0.03 mm segments, which are shown in Figure 6.14.

The plots in Figure 6.14 exemplify the effect of signal broadening due to higher θ_{xz} as ionisation electrons build up about a central wire and become incoherent in time. There are also greater fluctuations in the induced current for higher θ_{xz}, as well as the overall amplitude for each wire plane being smaller; an artefact of summing over all the ionisation

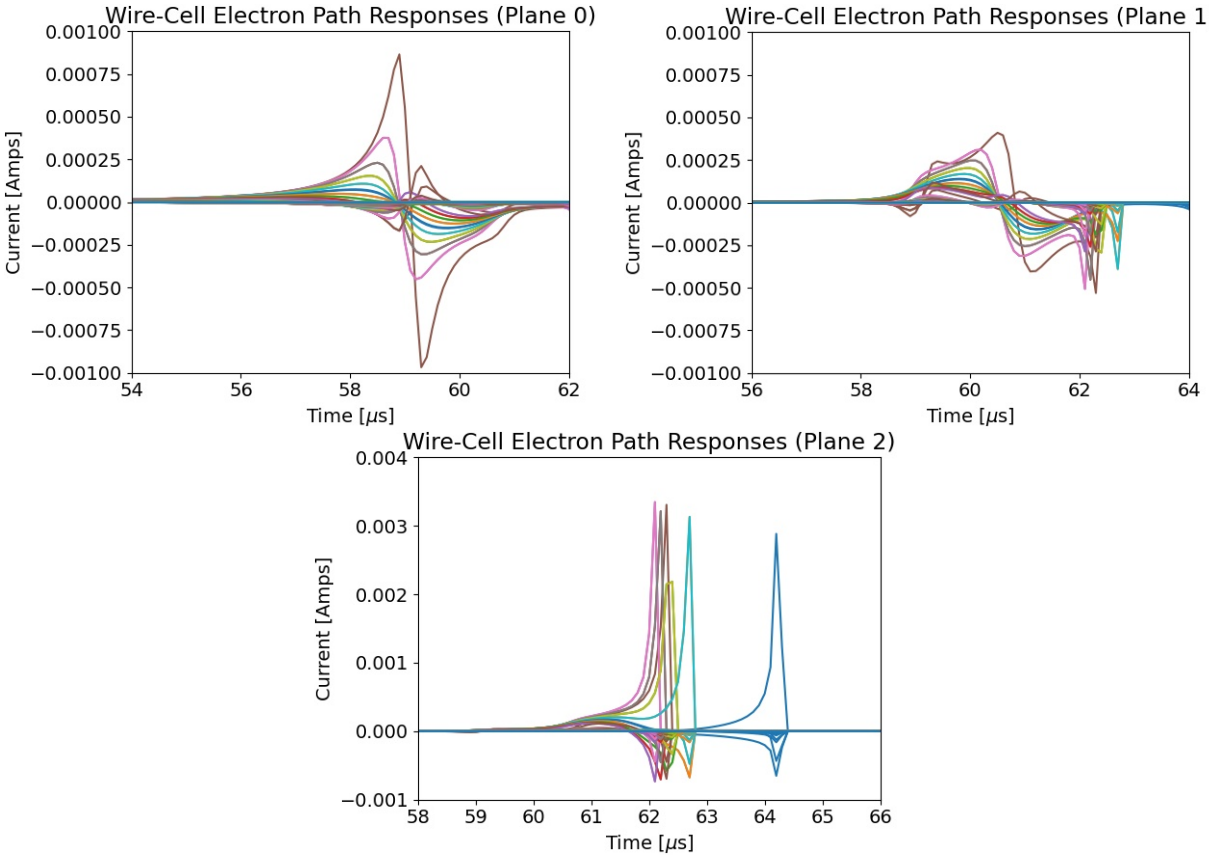

Figure 6.13: Induced current over time on SBND TPC readout wires with respect to electron path for the first induction (top left), second induction (top right) and collection (bottom) wire planes. Electron path deviation is measured in the transverse direction, parallel to the APA, at 0.3 mm segments, spanning -1.5 mm to 1.5 mm about the closest wire. Field response functions are modelled using a 2D Garfield simulation [154].

electron paths. This is apparent in the electron path plots in Figure 6.13, showing the various peaks and oscillations which in full field response functions when summed, which is the signal that the SBND TPC readout wires output.

Higher θ_{xz} gives rise to the long tail observed to the right of the collection plane peak in Figure 6.12. This is also a result of summing over every θ_{xz} segment, additionally broadening the waveform where the induced current would otherwise sharply drop to zero for each electron path, such as in Figure 6.13. Due to the intrinsic dependence of induced field response and θ_{xz}, the field response model must be validated at these $\delta\theta_{xz} = 2°$ segments. But before that, these calculated field response functions need to be convolved with the electronics response to obtain the total wire response on SBND TPC wires.

As previously described in Section 6.1.2, the electronics response is purely an artefact of the signal amplification process from the ASIC chips inside each FEMB in the SBND

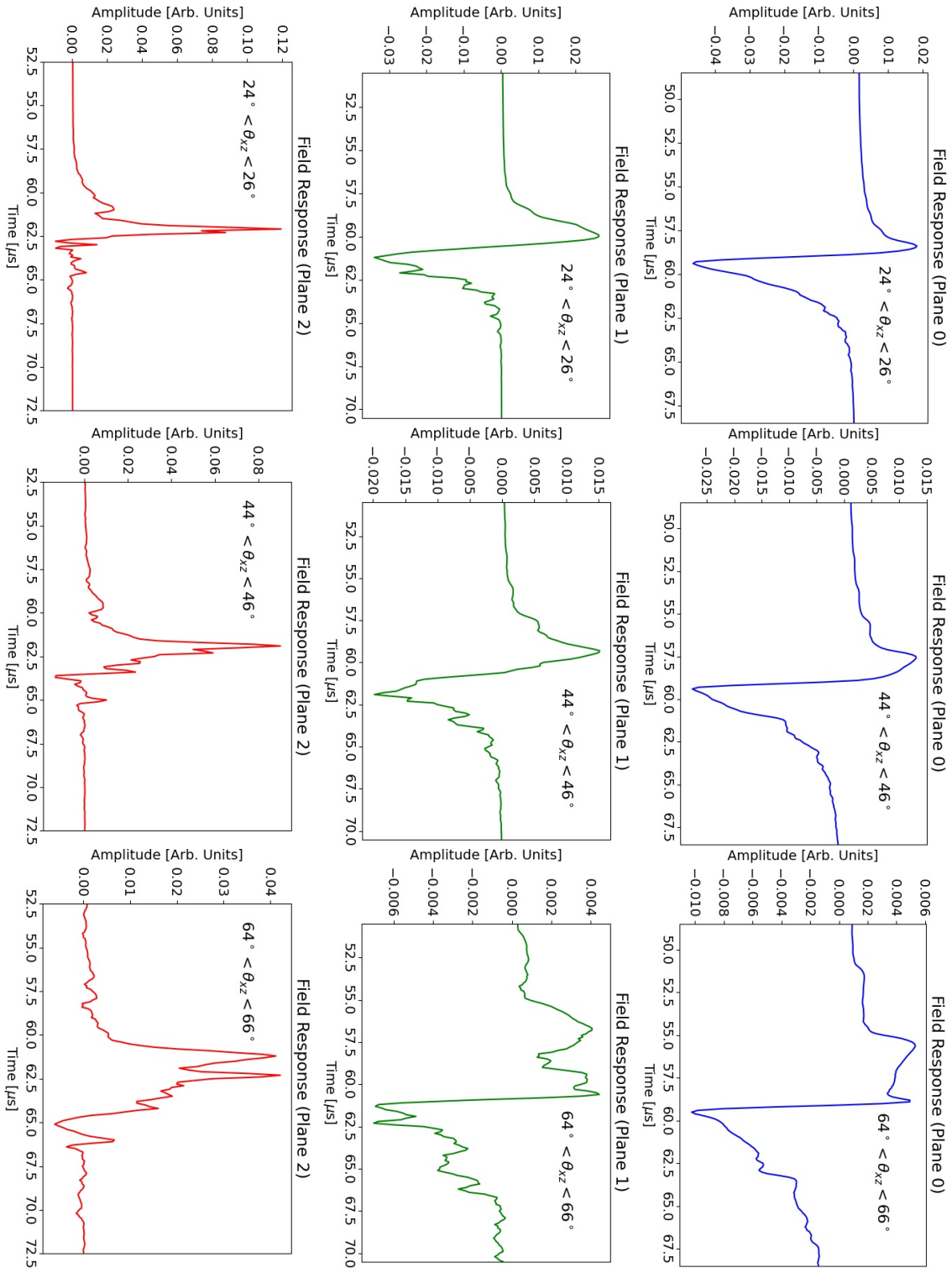

Figure 6.14: Induced current on first induction (right), second induction (middle) and collection (left) plane wires for θ_{xz} = 24°–26° (top), 44°–46° (middle), 64°–66° (bottom). Currents are averaged over 0.3 mm path segments from -1.5 mm to 1.5 mm about the central wire. Field response functions are modelled using a 2D Garfield simulation [154].

front-end electronics readout system. Given that this occurs after the TPC wire readout process, the same electronics response function affects all wire planes equally. Using the parametrised form of the electronics response in equation 6.7 with the parameters in equation 6.8, and using the gain of 14 mV/fC and peaking time of 2.2 µs, optimised for SBND, the electronics response function is plotted in Figure 6.15.

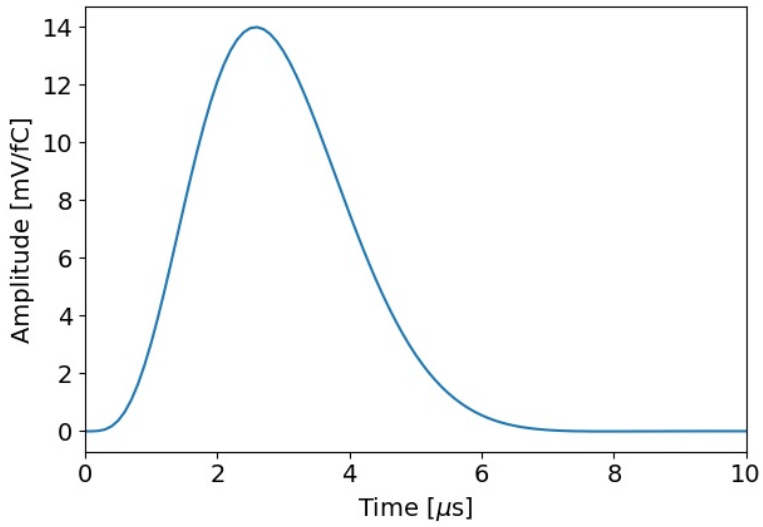

Figure 6.15: Electronics response function plotted from equation 6.7 using the parameters in equation 6.8, with a gain of 14 mV/fC and peaking time of 2.2 µs.

The electronics response plot in Figure 6.15 exhibits a peak at the chosen gain setting of 14 mV/fC, and with 5% deviation from the peak occurring at the selected peaking time of 2.2 µs. Given that Garfield calculates field response functions at 0.1 µs increments of drifting ionisation electrons, the granularity of time for the electronics response function in Figure 6.15 is also 0.1 µs, ranging from 0 to 100 ms.

The total wire response experienced by TPC waveforms outputted by each wire plane is calculated by convolving the total average field response function (represented in Figure 6.12) with the electronics response function (represented in Figure 6.15) using the 1D signal convolution technique in equation 6.1. This is performed by applying a forward Fourier transformation to both the electronics and field response functions, then multiplying both functions together and performing the inverse Fourier transform on the result. This is mathematically equivalent to equation 6.1, substituting R for the electronics response function and S for the field response function. These convolved field and electronics response plots are shown in Figure 6.16 for each wire plane.

The time axes for the total response plots in Figure 6.16 are offset such that $t = 0$ is defined by the positions of the negative peak for the first induction plane, the zero-amplitude

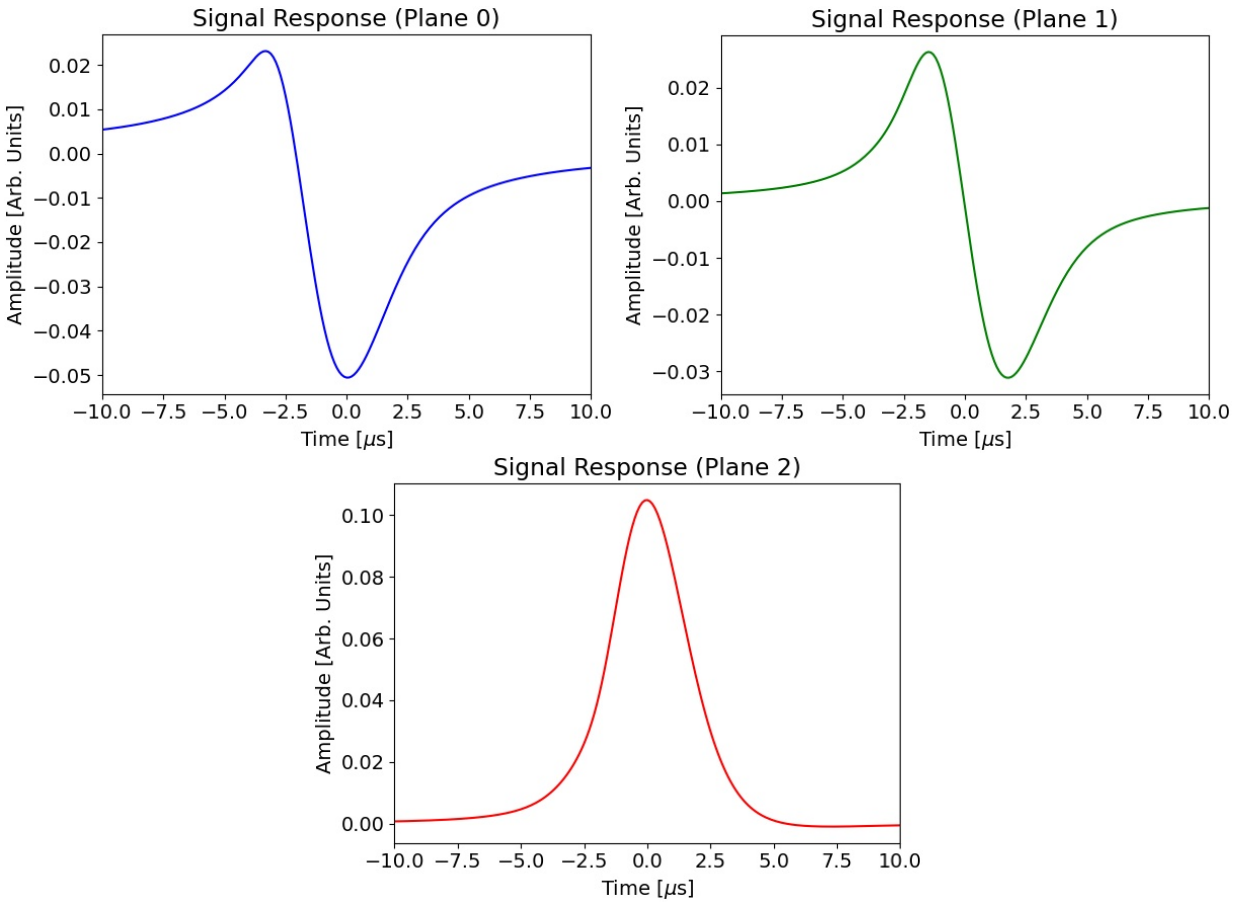

Figure 6.16: Convolved field and electronics response functions for the first induction (top left), second induction (top right) and collection (bottom) planes. Field response functions are modelled using Garfield [154] and electronics response from equation 6.7 using the parameters in equation 6.8, a gain of 14 mV/fC and a peaking time of 2.2 μs.

turning point for the second induction plane and the positive peak for the collection plane. All plots show the expected levels of waveform smoothing and broadening as a consequence of the signal amplification process. Convolution with the electronics response also results in an asymmetrical dip in the right-hand side of the collection plane waveform. To understand how the total wire response varies with θ_{xz}, the field response functions have been averaged over track pitch angle segments of $\Delta\theta_{xz} = 20°$ from 20° to 80°, for each wire plane, convolved with the electronics response to obtain the plots in Figure 6.17.

Variations in the angular distribution of total wire response plots in Figure 6.17 follow the same relationship between field response shape and θ_{xz} as demonstrated by the plots in Figure 6.14, only with additional broadening and smoothing effects due to convolution with the electronics response; analogous to ASIC signal amplification in the front-end readout electronics chain. Further signal smoothing occurs when averaging all the $\delta\theta_{xz} = 2°$ field

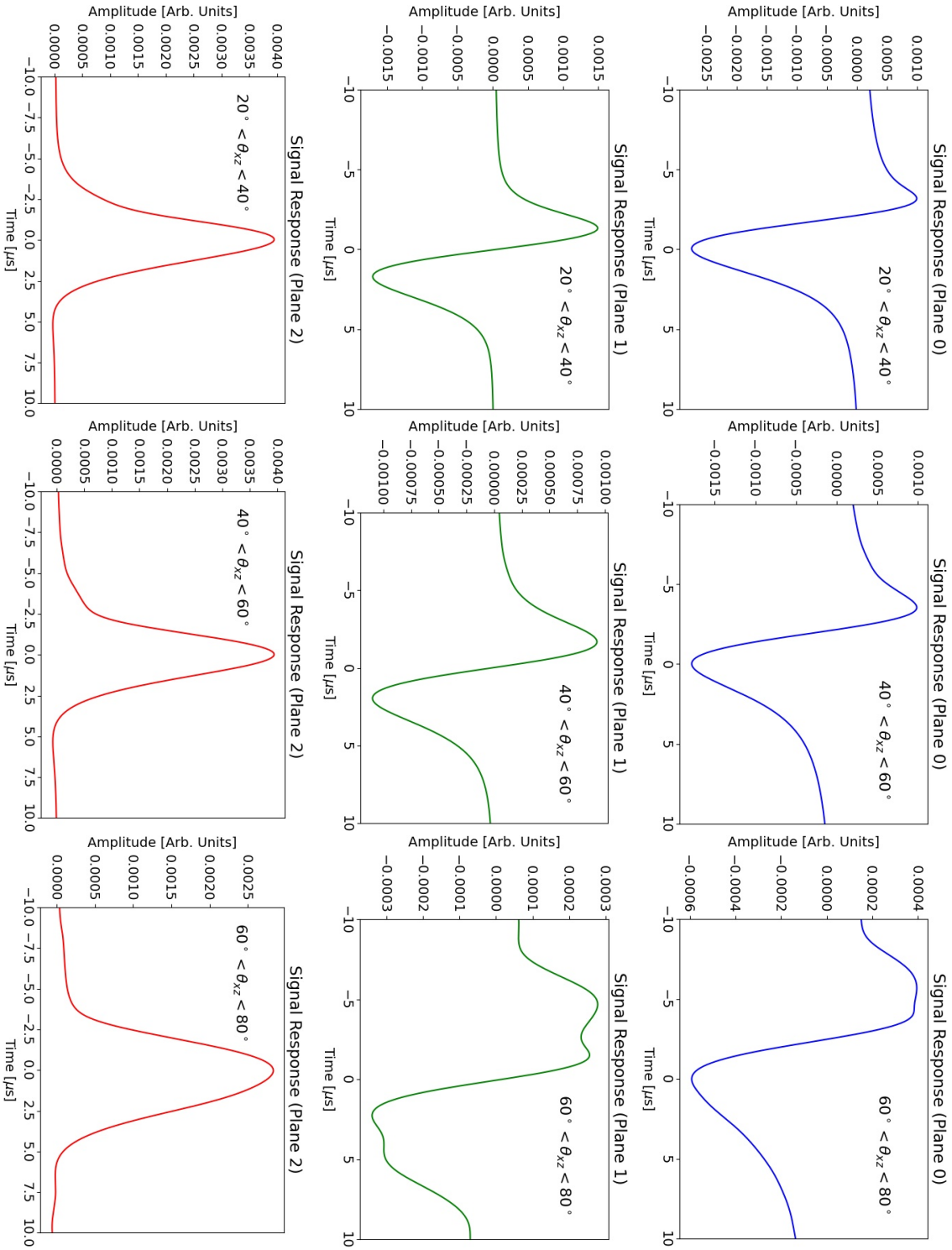

Figure 6.17: Convolved field and electronics response functions for the first induction (right), second induction (middle) and collection (left) planes, averaged over $\theta_{xz} = 20°$–$40°$ (top), 40°–60° (middle), 60°–80° (bottom). Field response functions are modelled using Garfield [154] and the electronics response is modelled from equation 6.7 using the parameters in equation 6.8 with a gain of 14 mV/fC and peaking time of 2.2 μs.

response functions into the $\Delta\theta_{xz} = 20°$ angle groups. This is most apparent in the multiple induced current peaks observed on the left-hand side of both induction plane plots for high θ_{xz}, and the right-hand leaning long tail observed in the collection plane. These double peak features are due to ionisation electrons building up near the anode when tracks are close to being perpendicular to the APA, resulting in a narrower time profile of ionisation electrons inducing currents in readout wires, overlapping in a very complex manner.

6.4 Field Response Validation Results with Monte Carlo Event Samples

Previously outlined in Section 6.2.1, the method by which the field response is validated in SBND before the experiment outputs TPC waveform data is to compare the average reconstructed waveform on readout wires from MC samples with the expected total wire response for different track pitch angles θ_{xz}. Additionally, the total wire response function is convolved with a Gaussian to account for signal misalignment from charged particle tracks with higher θ_{xz}. Any discrepancies between the reconstructed MC waveform and the total wire response convolved with the Gaussian should therefore be due to either the field response functions calculated by Garfield being suboptimal for the SBND simulation or the TPC waveform modelling procedure performed by Wire-Cell being inaccurate.

Induction plane plots have a minimum θ_{xz} of 26°, rising to 30° for the collection plane due to no tracks being selected below these values. In order to compare the overall shape of the waveforms, the total wire response, its convolution with the Gaussian and the reconstructed MC waveforms are all normalised such that the negative peak of the first induction plane signal is at $t = 0$ and are all equal to -1 arbitrary units. This is the same for the second induction plane except $t = 0$ is set to the zero-amplitude turning point of the bipolar signal, allowing for better scrutinisation of the initial positive peak. Collection plane waveforms are normalised such that the peak of the unipolar signal is at $t = 0$ and set to 1 arbitrary unit. Figure 6.18 shows the total wire response function, and the total wire response convolved with the Gaussian, normalised and overlaid with the average reconstructed MC waveform of six chosen pitch angle segments of $\delta\theta_{xz} = 2°$, for the first induction plane.

The first induction plane waveform comparison plots in Figure 6.18 show overall agreement from the negative peak to the right-hand side of the waveforms for the $\theta_{xz} = 25°$–$65°$ angle range, but large disparities start to appear for high θ_{xz}. This is most likely due to the difficulties of accurately applying the appropriate amount of waveform smearing for the highly complex induced current fluctuations at high θ_{xz}, which may require correcting

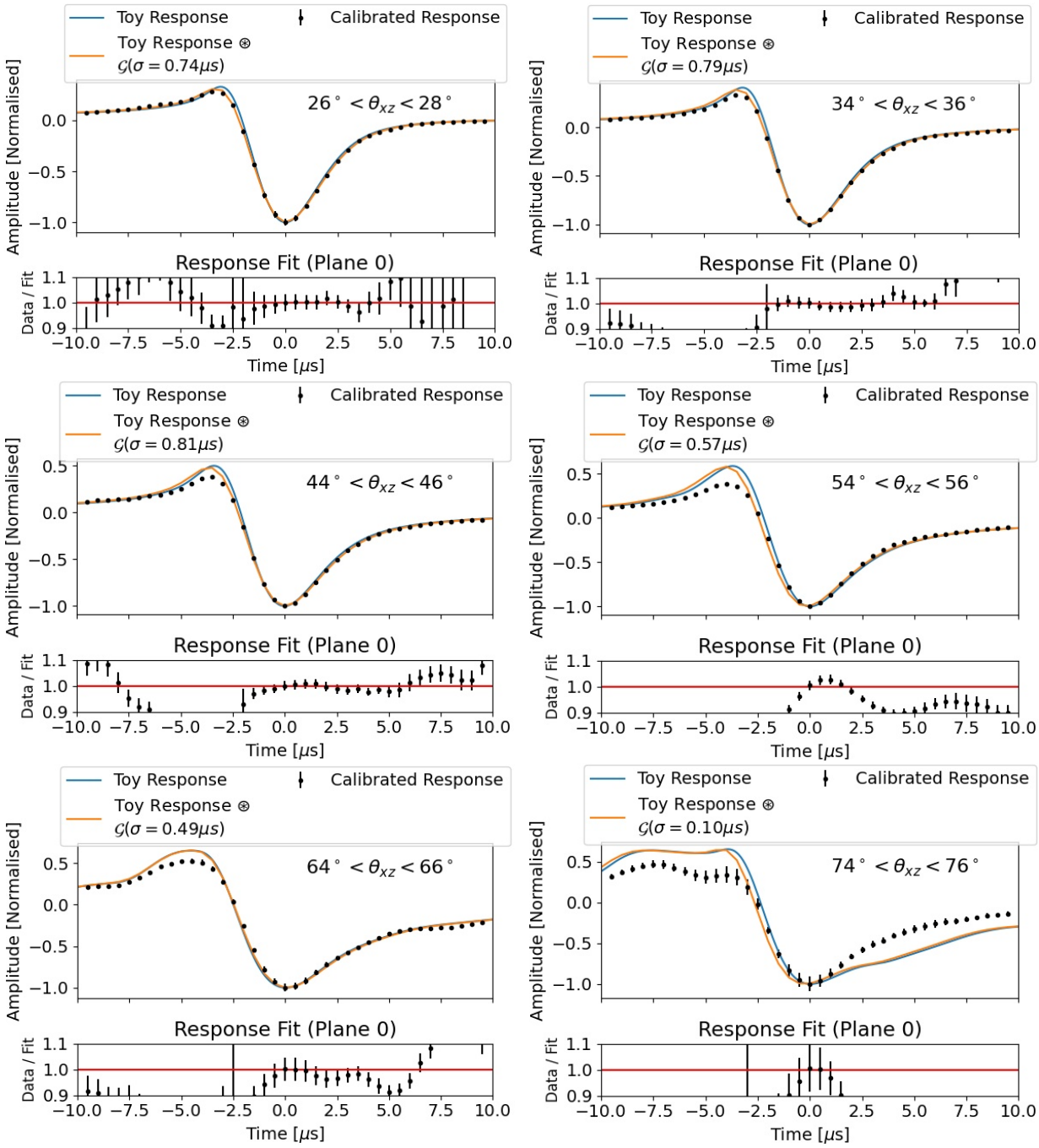

Figure 6.18: Comparisons of the average reconstructed MC waveform (calibrated response), the convolved field and electronics response functions (toy response) and the toy response convolved with a Gaussian (toy response $\circledast$ $\mathcal{G}$) on the first induction wire plane of the SBND APAs. Six $\delta\theta_{xz} = 2^\circ$ segments of the track pitch angle were chosen between 26° and 80°. Error bars on the calibrated response are calculated based on the standard error in the statistics of chosen tracks for that angle segment.

the 2D Garfield simulation to remedy these disparities. One consistent difference between the total wire response and the reconstructed MC waveforms at all track pitch angles is the amplitude of the first induction plane positive peak. This amplitude is dependent on the magnitude of the initially negative current induced on readout wires, where the MC reconstructed waveforms consistently exhibit a lower induced current compared to the 2D Garfield prediction. The cause of this deficit could be due to the detector response to charge, such as a lower electron lifetime or unoptimised wire voltage bias for the first induction plane in the SBND simulation, which is not accounted for in the Wire-Cell simulation. Figure 6.19 presents the waveform comparison plots for the second induction plane.

Figure 6.19 shows the reconstructed MC waveform lining up with the total wire response convolved with the Gaussian in the median angle ranges of $\theta_{xz} = 25°$–$60°$, similar to the first induction plane plots in Figure 6.18. However, much greater deviations start to appear for $\theta_{xz} > 60°$. This is also due to difficulties calculating field response functions for high θ_{xz} due to the complex bipolar nature of induction plane field response functions. However, the deficit in the positive peak for the second induction plane is most likely due to inaccuracies in how the SBND simulation accounts for wire plane transparency.

Wire plane transparency is the measure of how many ionisation electrons unintentionally terminate on induction plane wires instead of the collection plane. Observing a deficit in the positive peak of the MC waveform on second induction plane wires compared to the total wire response is indicative of the SBND simulation inaccurately modelling wire plane transparency. The primary tuneable parameter affecting wire plane transparency is the wire bias voltage which, at the time of producing this MC dataset, was still being optimised for SBND. As such, this study will be repeated after the nominal wire bias voltage settings for each wire plane have been implemented into the SBND simulation. Finally, Figure 6.20 shows the comparison plots for the collection plane.

The collection plane plots in Figure 6.20 show much better agreement than both induction plane plots in Figures 6.18 and 6.19, particularly for $\theta_{xz} < 70°$. This is primarily due to the ease of calculating unipolar field response functions for collection plane wires compared to the complex bipolar nature of positive and negative currents induced on induction plane wires. As such, these large disparities only seem to appear for $\theta_{xz} > 70°$ with collection plane waveforms, compared to the induction plane waveforms deviating greatly at $\theta_{xz} > 60°$. Despite this, the conclusion remains the same in correcting the method in which Garfield calculates field response functions at high θ_{xz}.

Disparities in the left and right-hand long tails of the collection plane waveforms could be due to an incorrect electronics response model when applied to the SBND simulation.

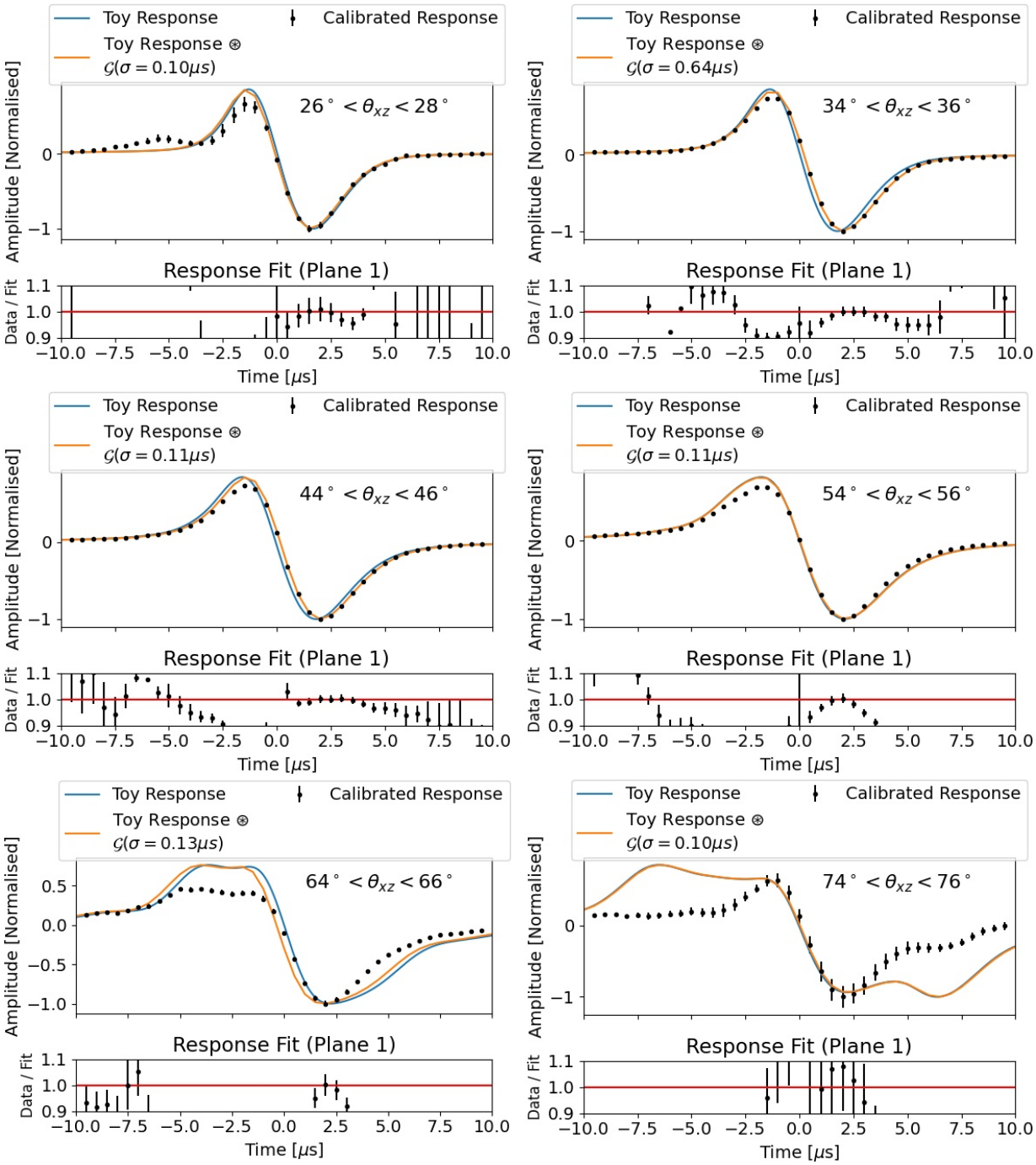

Figure 6.19: Comparisons of the average reconstructed MC waveform (calibrated response), the convolved field and electronics response functions (toy response) and toy response convolved with a Gaussian (toy response $\circledast$ $\mathcal{G}$) for the second induction wire plane of the SBND APAs. Six $\delta\theta_{xz} = 2^\circ$ segments were chosen between 26° and 80°. Error bars on the calibrated response are calculated based on the standard error in the statistics of chosen tracks for that angle segment.

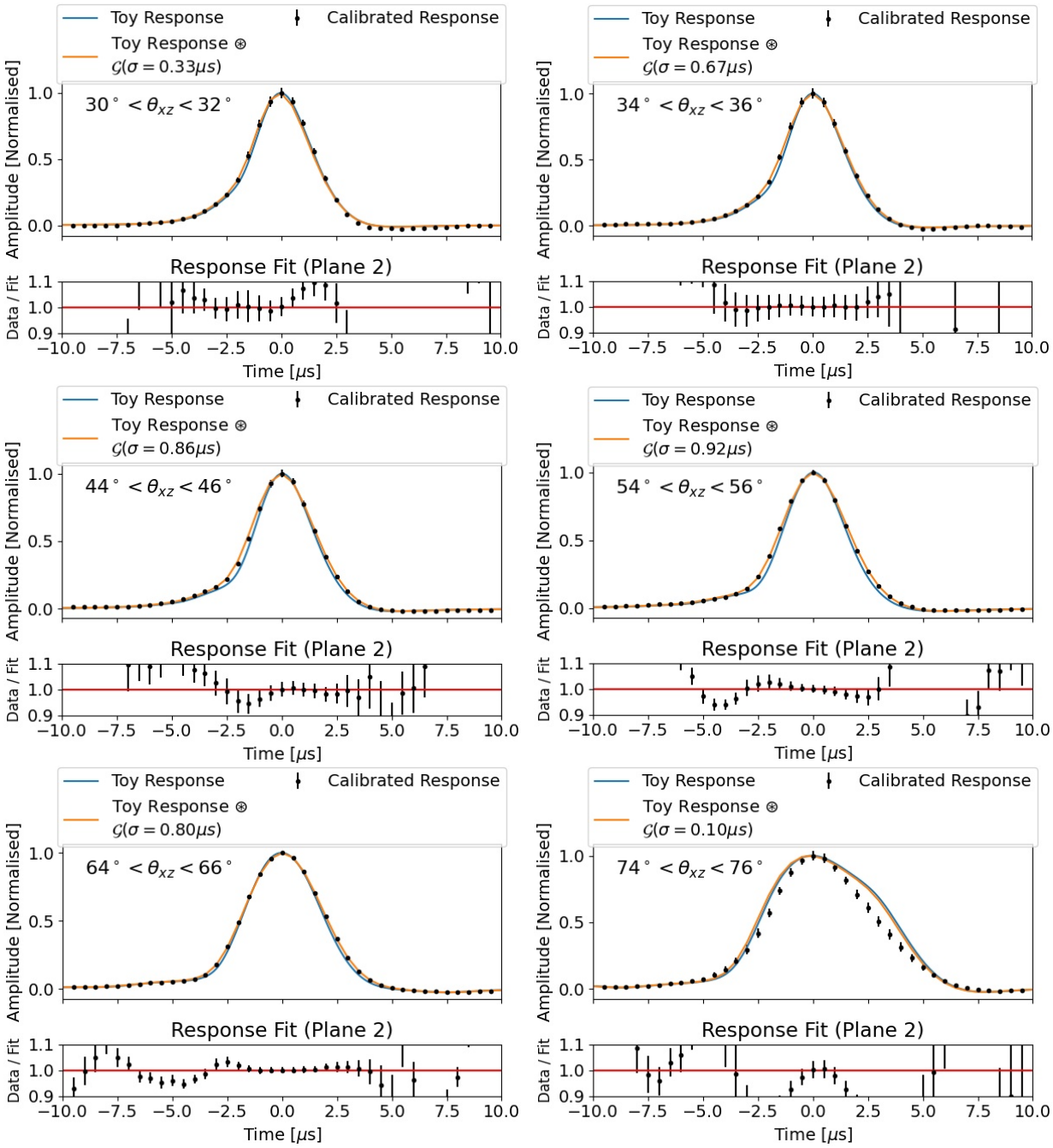

Figure 6.20: Comparisons of the average reconstructed MC waveform (calibrated response), the convolved field and electronics response functions (toy response) and the toy response convolved with a Gaussian (toy response $\circledast$ $\mathcal{G}$) on the collection wire plane of the SBND APAs. Six $\delta\theta_{xz} = 2^\circ$ segments of the track pitch angle were chosen between 30° and 80°. Error bars on the calibrated response are calculated based on the standard error in the statistics of chosen tracks for that angle segment.

Before SBND started collecting physics data, the electronics response was calibrated using simulated MC event samples. A fully accurate electronics response model can only be obtained after comparisons with SBND data. Other causes for these disparities could be due to inaccurate ADC threshold and NL parameters for the reconstructed MC waveform, contaminating the dataset with noise or track deviations due to delta ray emissions.

6.5 Conclusions

Validating field response modelling algorithms in the SBND simulation is paramount in accurately deconvolving ionisation electron signals from the measured waveform outputted by TPC readout wires. Comparisons of the average reconstructed MC waveform on all three APA wire planes with the expected total wire response shape, convolved with a smeared Gaussian, showed overall agreement. However, large disparities in waveform shape were apparent for tracks reconstructed at high pitch angles: $\theta_{xz} > 60°$ for induction plane waveforms and $\theta_{xz} > 70°$ for collection plane waveforms. The dependence this deviation has on track pitch angle is a clear indication that Garfield calculates field response functions inaccurately for high θ_{xz}, warranting modification of field response functions at these angles.

Reconstructed MC waveforms outputted by both induction planes showed a deficit in the positive peak compared to the Gaussian-convolved total wire response function, suggesting that the SBND simulation underestimates induced current on readout wires, possibly due to unoptimised electron lifetime models or wire bias voltages. The second induction plane deficit could also be indicative of an inaccurate wire plane transparency model used in the SBND simulation. The long tail observed in the right-hand side of the collection plane reconstructed MC waveforms, compared to the flatter Gaussian-convolved total wire response shape, implies that the electronics response is also not correctly modelled within the SBND simulation, and will require an optimisation study using SBND data to remedy. Other disparities are due to unoptimised ADC thresholds and NL parameters used in the reconstructed MC waveform selection criteria, which were initially chosen by hand-scanning event displays, and will require a full study with SBND data to optimise.

Since November 2024, SBND has been almost continually collecting physics data, outputting swathes of TPC waveforms to use for field response validation. The workflow for processing SBND data in order to extract waveform information from TPC readout wires and implement the field response validation methodology, as well as validation results and MC comparisons with data waveforms, are presented in Chapter 7.

Chapter 7

Field Response Validation Using SBND Data

Validating the field response in SBND consists of three main tasks. The first is to establish a methodology identifying disparities in the expected total wire response shape and TPC waveforms reconstructed from MC samples. The second consists of finding differences in the expected total wire response shape to TPC waveforms reconstructed from SBND data. The third ensures that the reconstructed MC waveforms align with SBND data waveforms. Completion of the first task is outlined in Chapter 6, whereas this chapter presents the work done undertaking the second and third tasks using the first batch of SBND data.

Section 7.1 presents the average reconstructed waveforms on TPC wires using SBND data, applying the same plotting procedure as the MC waveforms in Section 6.2.3. Comparisons of the expected total wire response shape to reconstructed SBND data waveforms are shown in Section 7.2. Section 7.3 contains the MC vs SBND data waveform comparison plots, finalising the work on validating the field response in SBND. General conclusions on the field response validation study are outlined in Section 7.4.

7.1 Reconstructed SBND Data Waveforms

Descriptions of how SBND software decodes raw TPC data, and details on the workflow developed to reconstruct waveforms outputted by APA wires, are in Section 4.4.4. This section presents the average waveforms outputted by induction and collection wire planes using early SBND data runs. Also presented are waveform comparisons reconstructing tracks with different pitch angles θ_{xz}, tracks contained in either the east or west TPC, and from SBND data runs altering the bias voltages of APA wires.

7.1.1 Average Data Waveforms on SBND TPC Wires

To extract waveform information from SBND TPC data a TPC decoder module is run on raw data files for a chosen number of SBND data runs, followed by applying the LArSoft reconstruction stages on the output. These are similar to the LArSoft reconstruction workflow used to extract waveform information from MC samples, described in Section 6.2.2, but with dedicated programs run on data. The same field response validation methodology and event selection criteria used with MC samples, described in Section 6.2.1, is applied to SBND data: selecting anode-cathode crossing cosmic-ray muon tracks with no bias in angular distribution, reconstructing the average waveform induced by ionisation electrons released from track segments 2–5 cm from the APA. From November 2024, SBND collected near-constant cosmic-ray muon data, producing runs with the exact criteria for the field response validation study selection process.

A single two-hour data run containing 25,000 total cosmic-ray muon events was chosen for this study, tagging muons using the north, south, east, west, top-high and bottom CRTs (before the top-low CRT installation was completed). TPC waveform data from this run was inputted into the average waveform analysis procedure, averaging signals from ±5 wires about the central wire, selecting tracks in the angle range of $20° < \theta_{xz} < 80°$. An amplitude cut of 6 ADC was also implemented to mitigate background noise, resulting in 1,138 plane 0, 1,076 plane 1 and 866 plane 2 selected waveforms. The average reconstructed SBND data waveforms for each wire plane are presented in Figure 7.1.

The average SBND data waveforms in Figure 7.1 exhibit the expected bipolar induction plane and unipolar collection plane waveform shapes. Minor fluctuations are observed in the induction plane plots about the central bipolar regions, which could be due to the relatively low statistics in the sample. Though around 1,000 selected waveforms for each wire plane is sufficient for a first field response validation study with SBND data, more statistics will be needed in the future to find finer differences in the total wire response and reconstructed data waveforms. Another factor which could be causing the fluctuating signal shape is the SBND trigger configurations set within the DAQ system, which were being optimised by the time of this data run, so some noise may be present in the waveforms which would otherwise be cut after passing the ADC threshold criteria. A minor bump at around $t = 10$ μs is observed in the collection plane plot, which is an indication that the electronics response model in the SBND simulation is different to what is observed in data. As such, work has been done to optimise electronics response modelling in SBND software.

Fully validating the field response functions requires an understanding of how signal shape varies with respect to the track pitch angle θ_{xz}, measured in the horizontal plane as

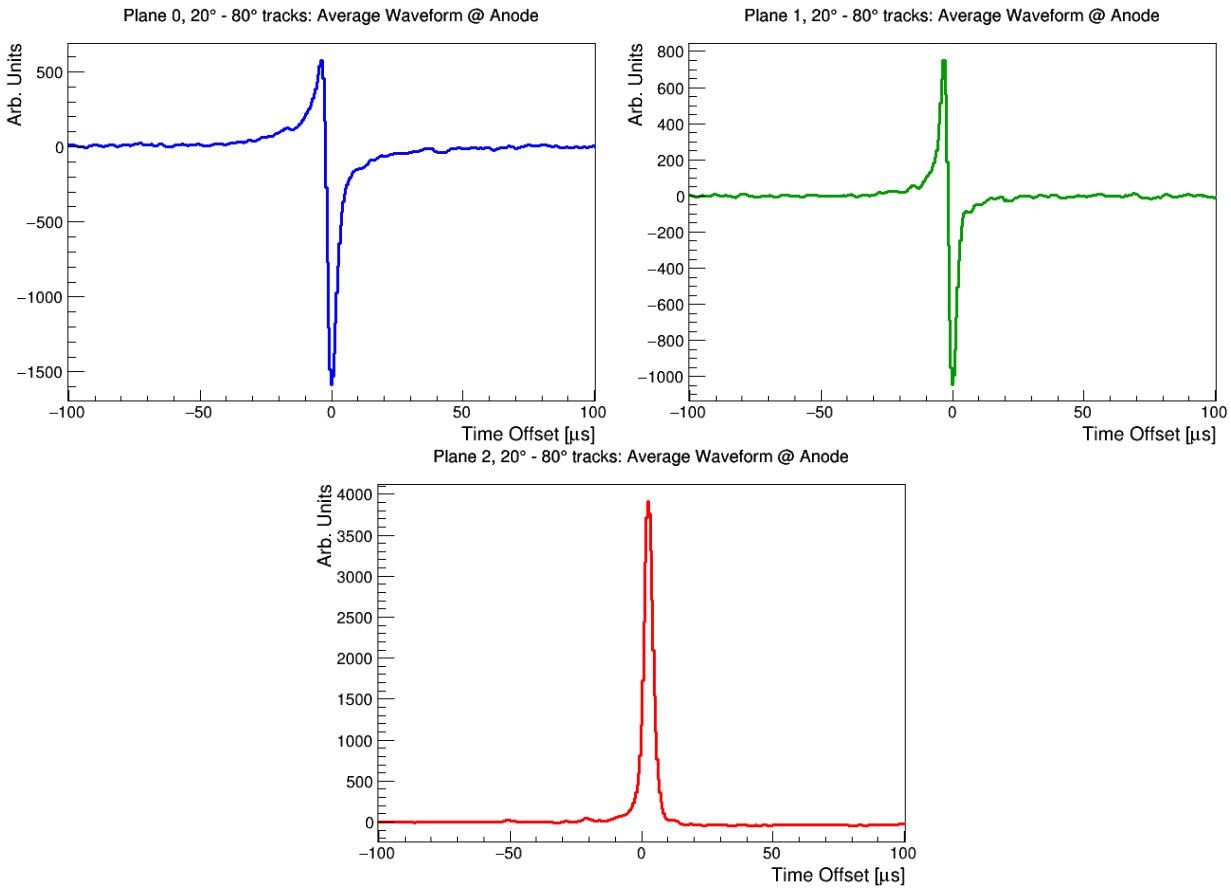

Figure 7.1: Average reconstructed waveforms on SBND TPC readout wires for the first induction (top left), second induction (top right) and the collection (bottom) planes using anode-cathode crossing cosmic-ray muon data.

the angle between the APA and track. This is the main angle that signal shape varies with due to changes in the distribution and rate of ionisation electron signal induction on APA wires. Plots of the average waveform outputted by TPC wires broken down into track pitch angle segments of $\Delta\theta_{xz} = 10°$ from 20° to 80°, are presented in Figure 7.2.

The plots in Figure 7.2 show a similar relationship between signal shape and θ_{xz} to the average waveforms from MC samples in Figure 6.11. These similarities include the greater positive/negative induction and collection plane peaks for higher θ_{xz}, as well as large signal fluctuations and subdued amplitudes for $\theta_{xz} > 70°$. Tracks with higher θ_{xz} are close to being perpendicular to the wire plane, meaning ionisation electrons drift almost parallel to the track. This results in electrons building up close to the APA, making it difficult to line up and average the waveforms in time, which is particularly apparent for bipolar induction plane signals, resulting in waveform fluctuations and subdued amplitudes present in the induction plane plots in Figure 7.2.

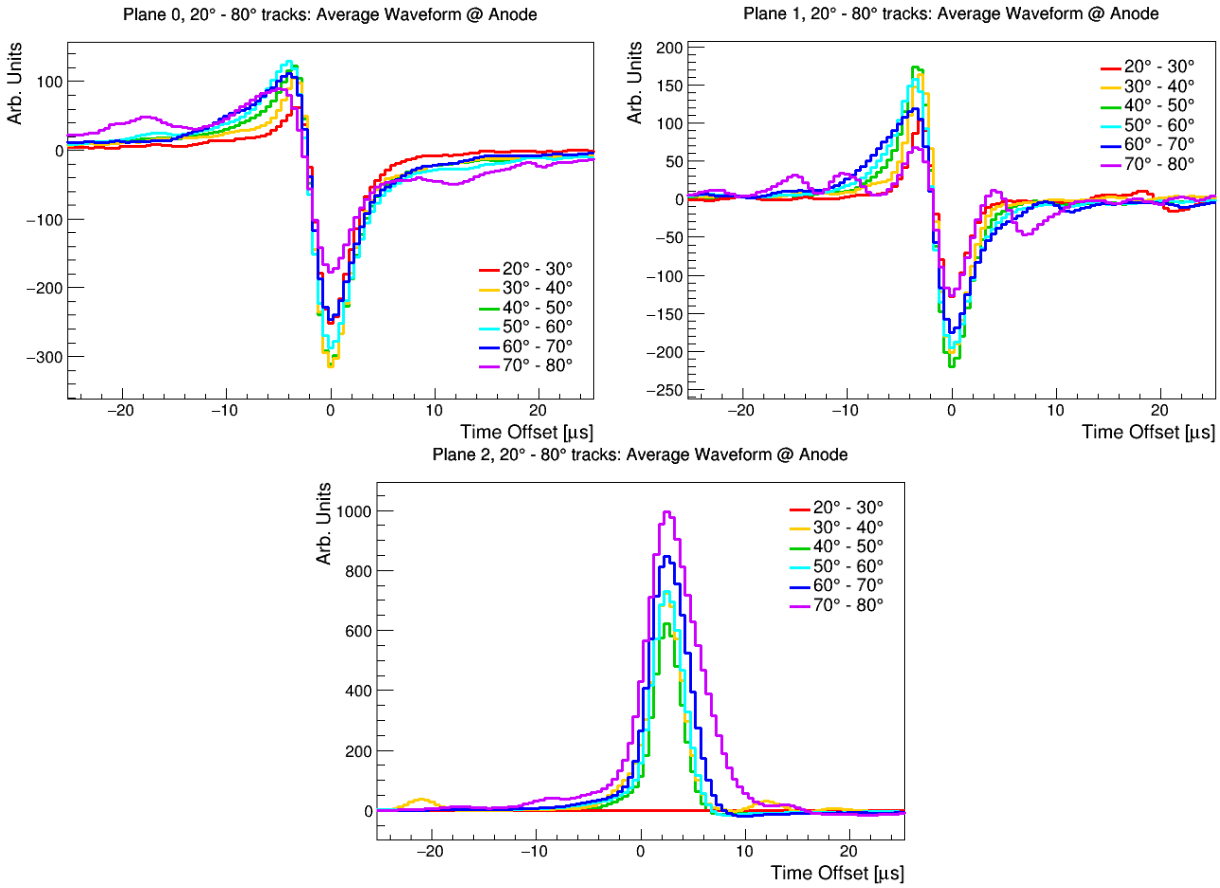

Figure 7.2: Average reconstructed waveform on SBND TPC readout wires for the first induction (top left), second induction (top right) and collection (bottom) planes using anode-cathode crossing cosmic-ray muon data. Waveforms are averaged in track pitch angle segments of $\Delta\theta_{xz} = 10°$ in the range $20° < \theta_{xz} < 80°$.

Tracks with $\theta_{xz} < 30°$ show much lower signal amplitudes in the positive/negative induction planes in the data waveforms, which is unlike the reconstructed MC waveforms in Figure 6.11 where tracks with $\theta_{xz} < 30°$ have the largest positive/negative induction plane extremities, though both exhibit zero selected collection plane tracks at this angle range. This is a result of low statistics in the data waveforms at low θ_{xz}, where selecting tracks for the field response validation study with lower θ_{xz} will always result in lower statistics with respect to higher θ_{xz} due to the tracks being less likely to meet anode-cathode crossing selection criteria. This is due to the minimum theoretical value of the pitch angle for anode-cathode crossing tracks being $\theta_{xz}^{min} \approx 22°$. In data, it is observed that $\theta_{xz}^{min} \approx 26°$ since anode-cathode crossing tracks with $\theta_{xz} < 26$ exhibit complications in reconstructing waveforms as the induced wires are too close to the edge of the APA.

Despite these quirks in reconstructing signal waveforms at extreme values of θ_{xz}, the

waveforms in Figure 7.2 from tracks with median angles of $30° < \theta_{xz} < 70°$ show the typical relationship between signal shape and θ_{xz}. Induction plane plots show high positive/negative peak amplitudes at its highest/lowest point for tracks with $30° < \theta_{xz} < 60°$, getting lower/higher with increasing θ_{xz}. This angle range exhibits optimal signal shape due to having a high enough θ_{xz} such that plenty of the tracks are anode-cathode crossing, yet low enough to avoid ionisation electron build-up near the APA. The second induction plane waveform shows a lower overall induced signal in data than MC which could be evidence of lower wire plane transparency. Investigations into the relationship between signal shape and wire voltage bias is outlined in Section 7.1.3, with comparisons between the total average MC and data waveforms being described in Section 7.3.

7.1.2 Comparison Between East and West TPCs

One feature of the average waveform analysis program is the ability to reconstruct waveforms induced on either the east or west APA in their respective TPCs. Cathode-crossing muon tracks span both TPC volumes in SBND, resulting in both APAs experiencing signal inductions from ionisation electrons drifting in opposite directions from the central cathode. This has no repercussions on track reconstruction, as SBND can still match the timing information from wires between both APAs back to the initial track, with the aid of cosmic-ray tagging and photon timing information using the CRTs and PDS respectively.

Likewise for the field response validation study, where only track segments 2–5 cm from either APA are considered in modelling the output waveform, it is not important which APA the ionisation signal is extracted from. However, investigating differences in waveform shape between the two APAs is important in identifying any potential errors in the SBND DAQ when collecting TPC data, anomalies in the SBND reconstruction chain, or if there are any shorted or noisy wires in a given wire plane.

During the reconstruction stage of the LArSoft workflow, each reconstructed track is discretised into segments with spatial coordinates at each time step $t_s = 0.5$ μs, including a parameter indicating which TPC that given track segment is in. The code decides which TPC the entire track is in based on the TPC the track has the most segments in, or equivalently, which TPC the track spends more time traversing. Table 7.1 shows the number of waveforms selected by the average waveform analysis code for the two-hour data run, and which TPC the tracks associated with each waveform predominantly resides in.

Ideally, track selection distribution between TPCs should be uniform due to both SBND TPCs being identical in geometry and efficacy in detecting and reconstructing charged particle tracks. Statistically, a 1% variance from 50% in one TPC selecting more/fewer

Table 7.1: Number of waveforms selected by the average waveform analysis code applied to the two-hour data run. Waveforms are broken down based on wire plane and which TPC the track associated with the waveform spent the most time traversing, with percentages indicating the track selection yield of that given TPC.

Wire Plane	East TPC	West TPC	Both TPCs
Plane 0	606 (53.3%)	532 (46.7%)	1138
Plane 1	566 (52.6%)	510 (47.4%)	1076
Plane 2	398 (46.0%)	468 (54.0%)	866
All Planes	1570 (51.0%)	1510 (49.0%)	3080

tracks than the other is expected, which is seen overall for SBND data tracks in Table 7.1. However, discriminating track selection with respect to wire plane shows the induction planes disproportionately favouring east TPC tracks to an approximately 3% margin, and the west TPC showing 4% more tracks inducing signals on the collection plane than the east. Table 7.2 shows the distribution in track selection on the 200,000 cosmic-ray muon MC samples produced by the SBND simulation, outlined in Section 6.2.2.

Table 7.2: Number of waveforms selected by the average waveform analysis code applied to the 200,000 cosmic-ray muon MC event sample. Waveforms are broken down based on wire plane and which TPC the track associated with the waveform spent the most time traversing, with percentages indicating the track selection yield of that given TPC.

Wire Plane	East TPC	West TPC	Both TPCs
Plane 0	3802 (49.9%)	3820 (50.1%)	7622
Plane 1	3728 (48.8%)	3910 (51.2%)	7638
Plane 2	2766 (49.4%)	2834 (50.6%)	5600
All Planes	10296 (49.4%)	10564 (50.6%)	20860

As expected, Table 7.2 shows a $\lesssim 1\%$ difference in waveform selection from tracks in either TPC. Every wire plane shows $\lesssim 1\%$ deviation from equal selection between TPCs, showing a very slight preference in the west TPC compared to the east, which could be down to a statistical anomaly or an effect of the SBND geometry. The greater disparity in the SBND data waveforms from tracks in either TPC indicates that there is bias towards one TPC over another in the SBND readout electronics chain or the DAQ system. Though a full study would need to be conducted on this, as this data run was taken whilst the detector was still being calibrated, so it is likely that this TPC non-uniformity issue is no longer apparent in the experiment. To compare how the waveform shape varies with respect

to which APA the track induces signals on, plots of the average waveform from tracks in the east and west TPCs in Table 7.1 are shown for each wire plane in Figure 7.3.

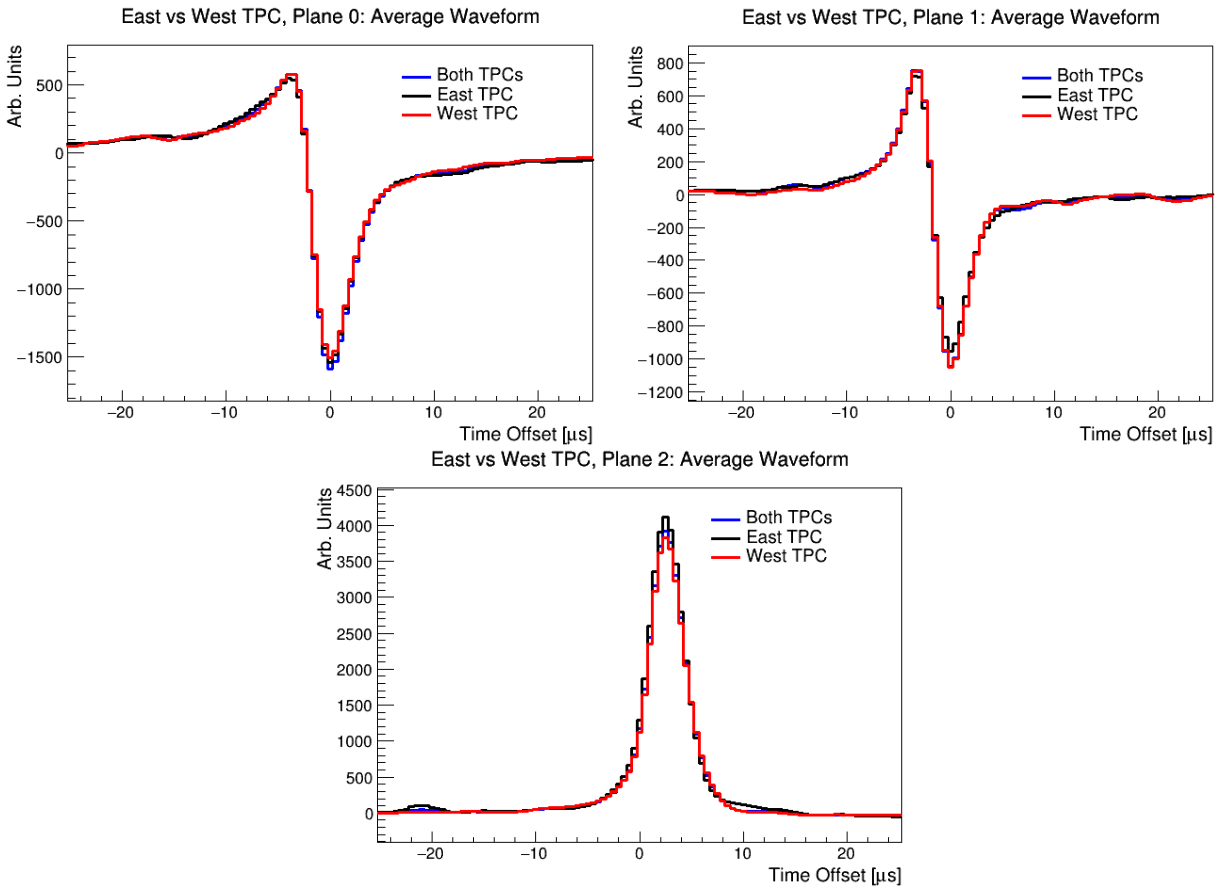

Figure 7.3: Average reconstructed waveforms on SBND TPC readout wires for the first induction (top left), second induction (top right) and the collection (bottom) planes using anode-cathode crossing cosmic-ray muon data from SBND, broken down based on which TPC the track spends the most time in.

No major distinctions between TPCs in regions outside the induction/collection plane peaks are observed in all wire planes in Figure 7.3. However, the west TPC exhibits a larger positive peak with respect to the east TPC for both induction plane plots, with a smaller/larger negative peak for the first/second induction plane. This could be due to the east TPC containing more tracks than the west TPC, broadening the waveform enough such that the initial positive peak is subdued, which is shown by the leading left-hand edge of both waveforms having a higher signal for east TPC tracks. The right-hand edge of the second induction plane plot also shows that the east TPC waveform is slightly broader, leading to the negative peak being more subdued with respect to the west TPC, which could be a result of differing wire transparency in the east TPC.

The collection plane waveform shows a larger peak and broader width for the east TPC with respect to the west, indicating that east APA wires experience larger signal inductions from ionisation electrons than the west, despite fewer tracks being selected in the east. This difference in waveform shape could be due to the parameters governing signal readout efficacy such as wire bias voltage, pre-amplification gain, or various trigger settings being uncalibrated for either APA. Verifying whether these disparities are due to detector effects in SBND involves comparing the SBND data waveforms in Figure 7.3 with the waveforms broken down by TPC from the MC samples, which is displayed in Figure 7.4.

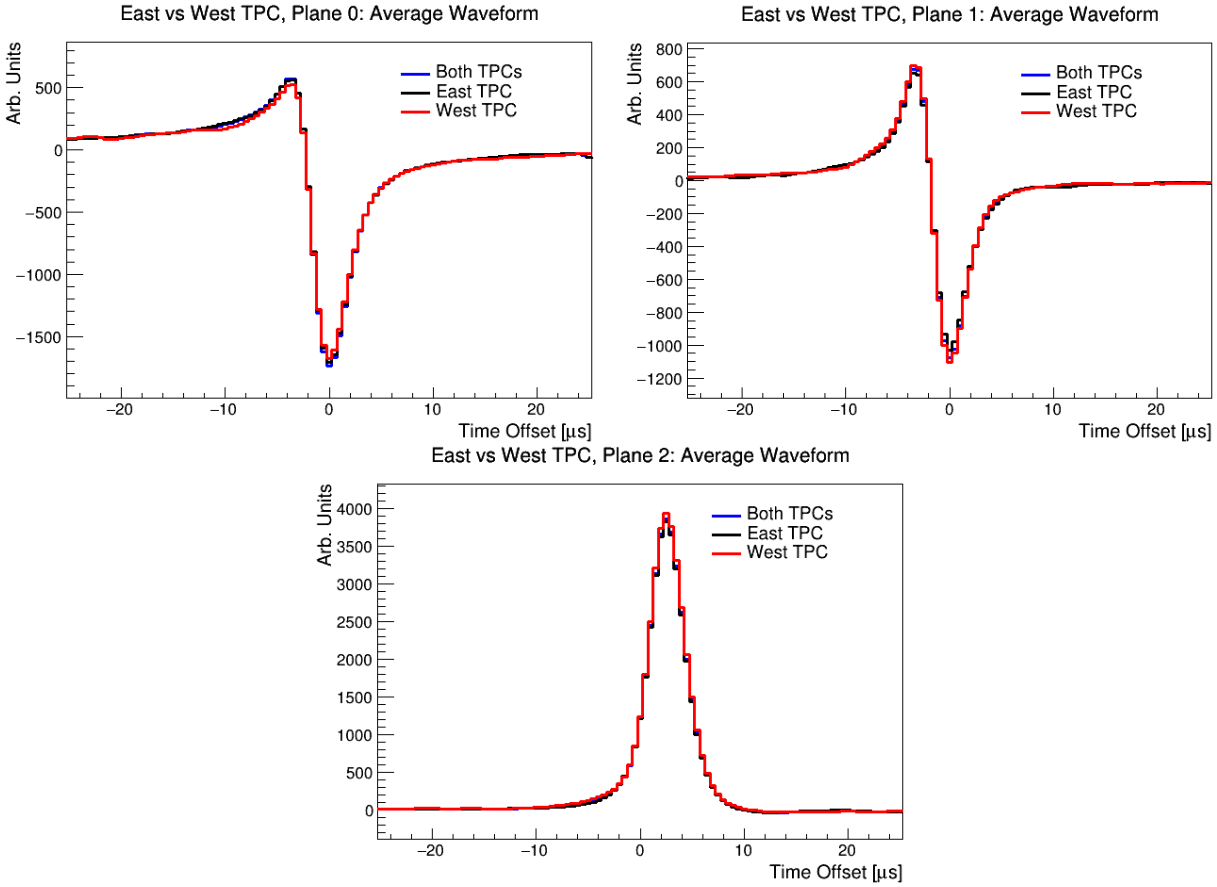

Figure 7.4: Average reconstructed waveform on SBND TPC readout wires for the first induction (top left), second induction (top right) and the collection (bottom) planes using anode-cathode crossing cosmic-ray muon MC event samples produced by the SBND simulation, broken down based on which TPC the track spends the most time in.

Despite the average waveforms from MC samples in Figure 7.4 also showing disparities in signal shape about the induction and collection plane peaks, they are less apparent than the SBND data plots in Figure 7.3. Though the MC waveforms have a more uniform track selection distribution between TPCs with respect to the data waveforms, the MC waveforms

still exhibit the same lesser negative peak on the first induction plane for west TPC tracks and greater negative peak on the second induction plane for east TPC tracks. This implies that the disparity in waveform shape between TPCs for the SBND data waveforms is due to how the SBND detector setup is encoded into the SBND software that models data waveforms. The same cannot be said for the larger collection plane peak in west TPC tracks, which shows the opposite case to the data waveforms, with a larger peak in east TPC tracks. This suggests that the SBND APA setup encoded into the SBND software is different from the physical detector, and must be amended through a full calibration study.

Since the two-hour SBND data run used in this section was taken quite soon after SBND started collecting cosmic-ray data with the TPC, CRT and PDS, any inaccuracies in how the SBND software models the physical detector could be because the detector was still being commissioned and calibrated at the time of data collection. One aspect of this calibration which has been talked about in previous sections is the optimisation of the wire bias voltage setting for each wire plane. The first induction plane should be biased around -200 V and the collection plane approximately +400 V. The second induction plane stays at zero bias voltage to maintain an electric field between itself and wire planes 0 and 2 for maximum signal induction on plane 0 and charge collection on plane 2.

7.1.3 Comparison With Different Wire Bias Voltages

Changing the bias voltage applied to each readout wire plane affects their transparency, leading to changes in the number of electrons passing through the induction planes and terminating on collection plane wires. Ideally, both induction planes should be 100% transparent to ionisation electrons, inducing a signal on wires as they drift past, with the collection plane being 0% transparent as all electrons should terminate on their wires. Any deficit in transparency observed in the induction planes is called intransparency, the magnitude of which is dependent on the electric field between wire planes. The strength of this electric field is defined by the applied bias voltages, with non-uniformities arising due to wires moving or oscillating slightly in the cold liquid argon. If the electric field between wire planes is not optimised, then ionisation electrons can terminate on the first or second induction planes, leading to deficits in calorimetric information from the initial neutrino interaction as charge is lost from not terminating on collection plane wires.

Due to the fact that the wires are sealed within the cryostat, the only method of ensuring minimum induction plane intransparency is to optimise the wire bias voltage applied to the first induction plane and collection plane wires. One way of achieving this is to observe variations in average waveform shape from SBND data runs with different bias

voltage settings for wire planes 0 and 2. Induction plane intransparency causes deformations in the waveform shape, boosting the positive peaks and diminishing the negative peaks on induction plane wires, and decreasing the collection plane waveform amplitude due to unintended termination of ionisation electrons on induction plane wires. Induction plane intransparency also causes variations in the field response induced on each wire plane as the distribution of induced currents on readout wires changes with wire position. Any observed induction plane intransparency could indicate that the spacing between induction plane wires is smaller than the nominal of 3 mm, possibly decreasing to a pitch of 2.5 mm.

As such, between October and November 2024, SBND collected TPC data using multiple different wire bias voltages, altering the first induction plane bias voltage from the nominal of -210 V to -220 V and -180 V; and the collection plane bias voltage from nominally 420 V to 460 V. Each wire bias voltage run is between 1 and 3 hours long, and when the bias voltage applied to one is altered the other wire planes are operating with nominal bias voltages. Table 7.3 shows the number of waveforms selected from altered wire bias voltage data runs after passing them through the average waveform analysis program.

Table 7.3: Number of waveforms selected by the average waveform analysis code applied to the SBND data runs altering the plane 0 wire bias voltage from the nominal of -210 V to -220 V and -180 V; and plane 2 from nominally 420 V to 460 V.

Wire Plane	Nominal	Plane 0: -220 V	Plane 0: -180 V	Plane 2: 460 V
Plane 0	1404	482	526	986
Plane 1	1264	670	670	1104
Plane 2	1074	316	320	604
All Planes	3742	1468	1516	2694

When comparing average reconstructed waveforms between different data runs of SBND, it is important to normalise the waveforms, which involves lining up the negative peaks of induction plane waveforms and unifying the integral of the collection plane. This is so that comparisons can be made in the relative defamations and signal broadening between waveforms as a result of physical processes such as changing track pitch angle and differences in wire response induction. Figure 7.5 shows the average reconstructed waveforms from SBND TPC data for the nominal and altered first induction plane wire biases, outlined in Table 7.3, overlaid with the aforementioned normalisation procedure.

The average waveform plots in Figure 7.5 show that altering the bias voltage of the first induction plane results in large waveform shape disparities for the first induction and collection plane plots. The first induction plane waveform shows similar shape for

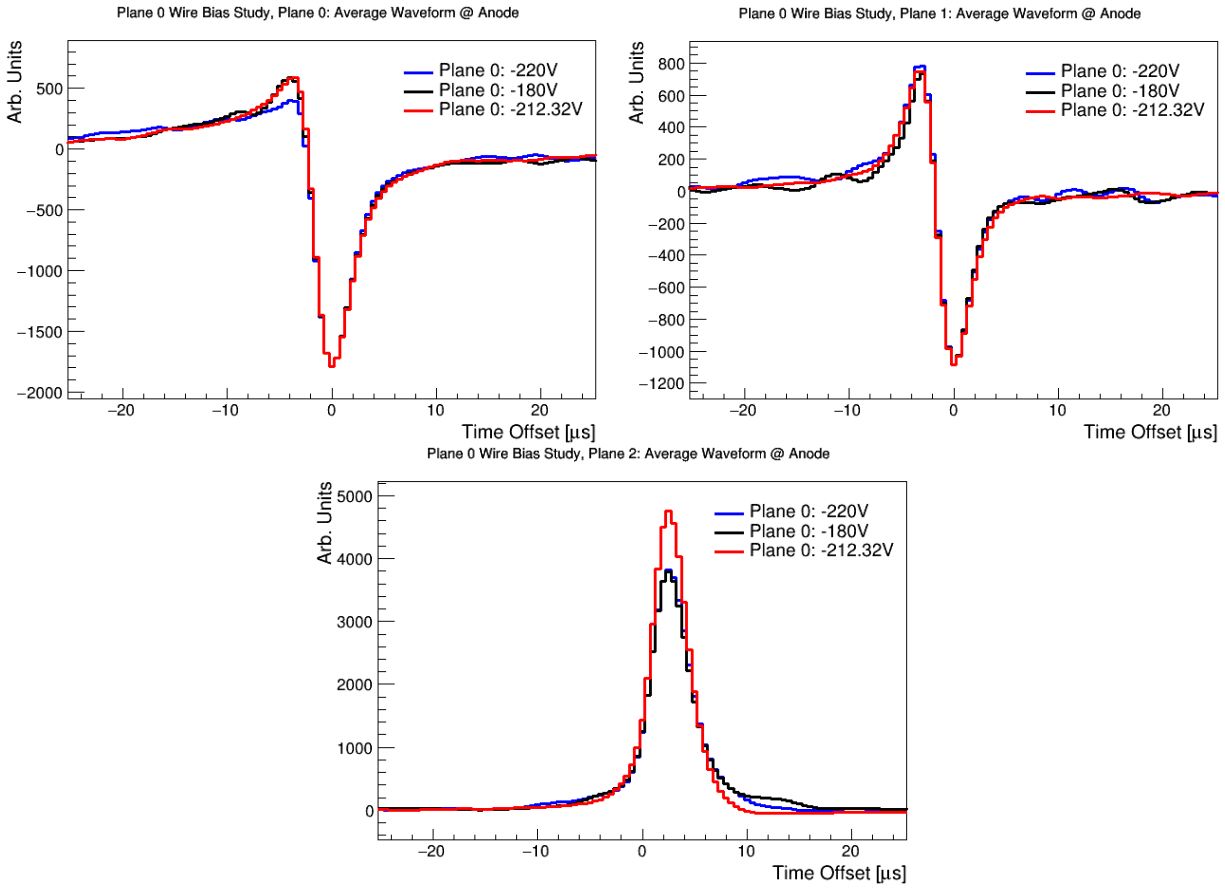

Figure 7.5: Average reconstructed waveform on SBND TPC readout wires for the first induction (top left), second induction (top right) and collection (bottom) planes using anode-cathode crossing cosmic-ray muon data. Wire bias voltage for first induction plane wires was altered from the nominal value of -210 V, to -220 V and -180 V.

wire biases of -210 V and -180 V, with a deficit in positive peak for -220 V, though the second induction plane waveform shows a slightly greater positive peak for -220 V. This greater initial positive peak for the -180 V and -210 V waveforms implies that electrons are terminating on the first induction plane. This would result in a deficit in collection plane waveform amplitude, which is observed for the -180 V waveform in Figure 7.5. Therefore, the -180 V bias voltage setting is too low (i.e. too close to 0 V) for the first induction plane.

Theoretically, decreasing the bias voltage on first induction plane wires below the nominal results in more charge terminating on collection plane wires, as electrons experience a greater coulomb force away from first induction plane wires. This makes the -220 V collection plane waveform in Figure 7.5 an anomaly, since it exhibits a wider waveform than the nominal wire bias setting, indicating fewer ionisation electrons are being collected on these wires. This could be an indication of different trigger settings when reading out TPC

signals for the -220 V run with respect to the other data runs, changing the angular cut of cosmic-ray muon tracks. The plots in Figure 7.5 suggest an optimal bias voltage value of -210 V for first induction plane wires.

Changing the bias voltage applied to first induction plane wires has a greater effect on the amount of charge terminating on collection plane wires than altering the collection plane bias voltage. However, if intransparency is already observed on either induction plane wires, then increasing the collection plane bias voltage can mitigate this affect by attracting more charge to terminate on collection plane wires. Decreasing the collection plane bias voltage below nominal would undoubtedly result in less charge being collected in the collection plane, which is undesirable for SBND, hence why there is no altered bias voltage run below the nominal. Figure 7.6 shows the average reconstructed waveforms from SBND data runs using collection plane bias voltage settings of the nominal 420 V and altered 460 V.

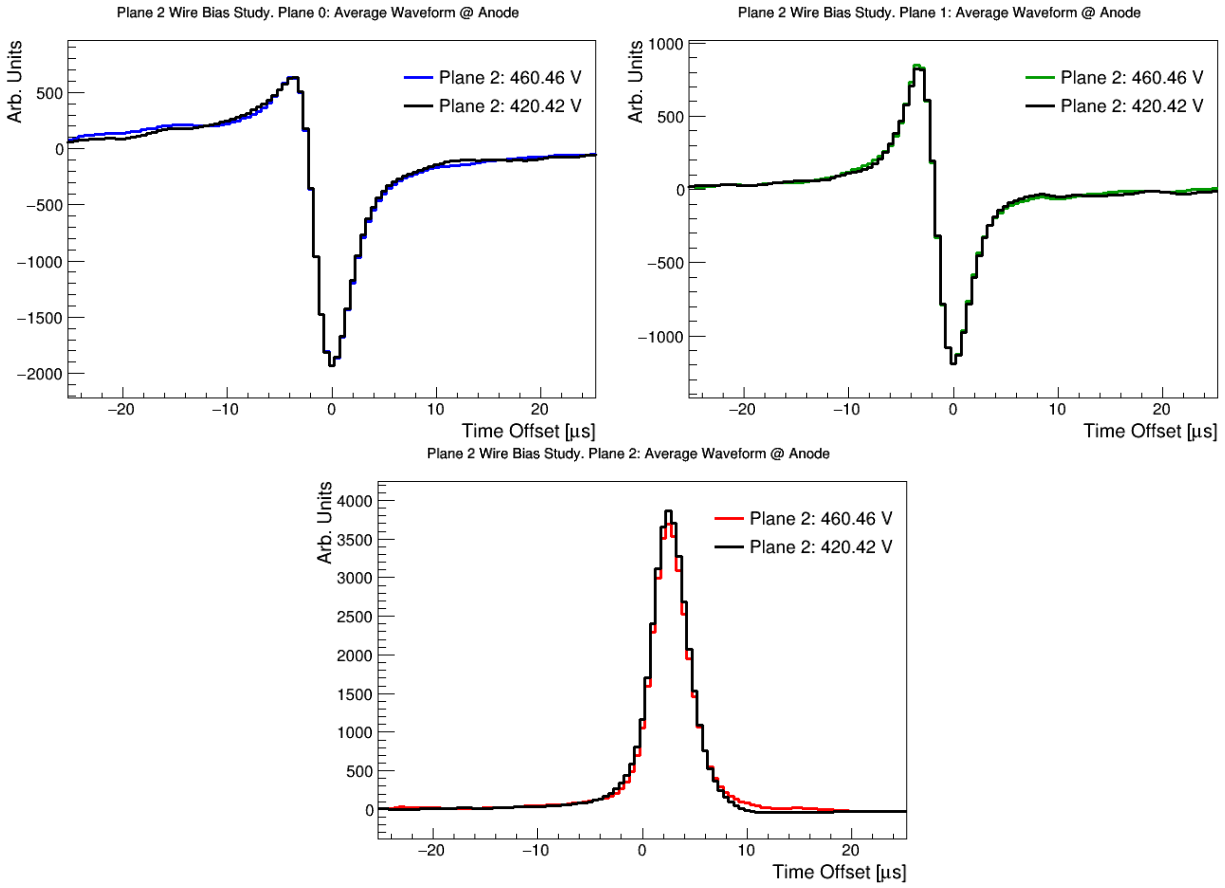

Figure 7.6: Average reconstructed waveform on SBND TPC readout wires for the first induction (top left), second induction (top right) and collection (bottom) planes using anode-cathode crossing cosmic-ray muon data. Wire bias voltage for collection plane wires was altered from the nominal value of 420 V to 460 V.

The plots in Figure 7.6 show little change in overall waveform shape for the first and second induction planes when altering the collection plane bias voltage, which is expected since the electric field between the induction planes would be unaffected by changing the collection plane bias voltage. However, the collection plane waveform shows that increasing the bias voltage results in a narrower peak with a slightly higher right-hand tail. Narrower collection plane peaks indicate higher ionisation electron collection yield, since other signal broadening factors such as signal response and diffusion are mitigated by the larger ionisation signal. As such, the plots in Figure 7.6 indicate the need for a higher than nominal bias voltage applied to collection plane wires.

A full study on optimising the bias voltage for the first induction and collection planes on SBND has been carried out as of the time of writing. This was done not only by looking at the change in waveform shape for different bias voltage runs of SBND, but also by tracking the variation in charge collection across different positions in the APAs for all three wire planes, observing any deficits in induced signals and collected charge on readout wires. The results of that study aligned with the results from this section in that there was evidence of intransparency in the second induction wire plane. Furthermore, it was found that the collection plane wire bias voltage needed to be increased to 600 V to mitigate this intransparency, and the first induction plane wire bias voltage stayed at the nominal setting of -210 V. This wire bias voltage setup minimises ionisation electrons terminating on induction plane wires and maximises charge collection yield on collection plane wires, as well as optimising detector uniformity.

7.2 Field Response Validation Results with SBND Data

Validating the field response using MC event samples in Chapter 6 entailed ensuring that the Garfield and Wire-Cell programs calculated field response functions and modelled these functions onto TPC readout wires correctly in the SBND simulation, respectively. Field response validation using SBND data verifies that SBND software deconvolves the ionisation signal from the total wire response in TPC data correctly, which requires an accurate model of the field response to deconvolve. This still achieves the goal of checking that Garfield and Wire-Cell are being run correctly in SBND software, but through deconvolution of SBND data waveforms rather than convolution with MC waveforms.

Ionisation signals in data can only be accurately deconvolved from the total wire response if the total field response functions modelled by Garfield and Wire-Cell matches with the physical detector response seen in data. As such, the average reconstructed SBND

data waveforms have been inputted into the same field response validation analysis program used in Section 6.4, with the same calculated field response functions and waveform modelling on APA wires to avoid any biases in the methodology. The only difference is the magnitude of smearing applied to the average reconstructed waveform on data with respect to MC to account for differences in the angular distribution of tracks in MC and data. The field response validation results for the first induction plane plots in six chosen $\delta\theta_{xz} = 2°$ angle segments from 26° to 80° using SBND data are presented in Figure 7.7.

The field response validation plots for the first induction plane in Figure 7.7 show similar disparities with the total wire response and angular distribution to the MC validation results in Figure 6.18. Namely, the data waveform seems to line up with the total wire response for tracks with $\theta_{xz} < 40°$, before disparities in the positive peak appear for increasing θ_{xz}, which becomes very apparent for $\theta_{xz} > 60°$. This deficit in the positive induction peak is less apparent than observed in the MC simulation, supporting the conclusions drawn from the MC validation results that the SBND simulation underestimates the electron lifetime or effects of diffusion on waveform shape. These physical parameters implemented into SBND software have since been calibrated to match SBND data.

Deficits in the positive induction peak, particularly for high θ_{xz}, as well large divergences in the data waveform and total wire response convolved with the Gaussian are also seen in Figure 7.7. These corroborate the field response validation results from MC samples suggesting that the field response function modelled using the 2D Garfield simulation at high track angles need to be modified. The field response validation plots for the second induction plane using SBND data are displayed in Figure 7.8.

The SBND data waveforms and total wire responses in Figure 7.8 show strong alignment for $\theta_{xz} < 40°$, then start to diverge for higher θ_{xz}, leading to disparities in the right-hand side of the waveforms for $\theta_{xz} > 60°$. The relatively large error bars present in data waveforms on both induction planes from tracks with higher θ_{xz}, in Figures 7.7 and 7.8, are due to lack of statistics. Zero waveforms from tracks with $\theta_{xz} > 72°$ on the second induction plane passed the selection criteria. This is apparent in the waveform angle breakdown plot for the second induction plane in Figure 7.2, showing a very subdued, fluctuating signal shape.

This deficit in track selection for high θ_{xz} on the second induction plane is most likely due to the fact that SBND was still being calibrated and commissioned for its TPC readout at the time this data was collected. The second induction plane is affected worse than the other two wire planes due the fact that it exhibits the most complex bipolar response waveform, making field response functions more complicated to model through 2D Garfield simulations. Second induction plane waveforms also suffer the greatest variation in wave-

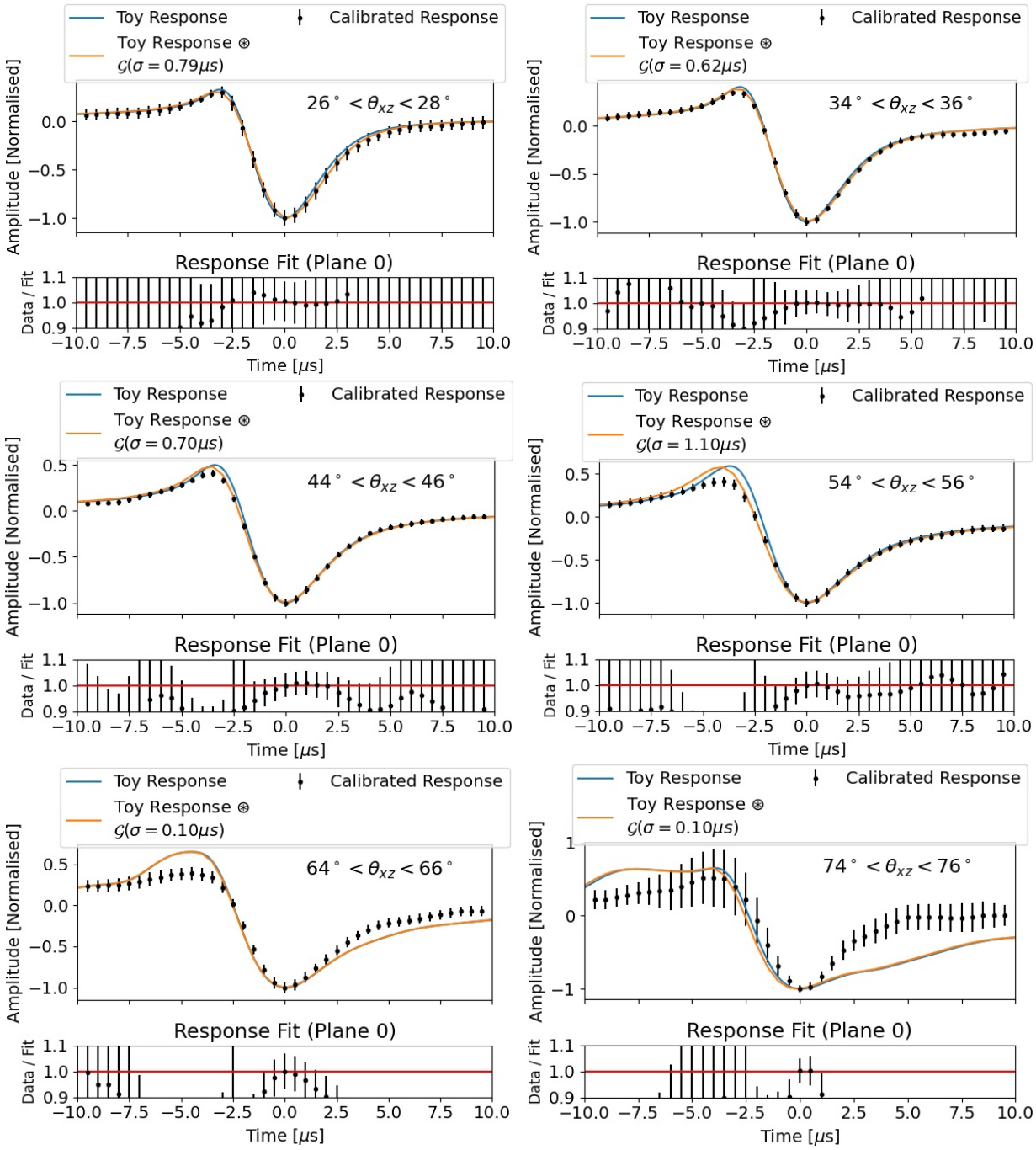

Figure 7.7: Comparisons of the average reconstructed waveform from first induction plane wires using a two-hour SBND data run (calibrated response), the convolved field and electronics response (toy response) and toy response convolved with a Gaussian (toy response $\circledast$ $\mathcal{G}$) for six chosen $\delta\theta_{xz} = 2^\circ$ segments between 26° and 80°. Error bars on the calibrated response are calculated based on the standard error in the statistics of tracks.

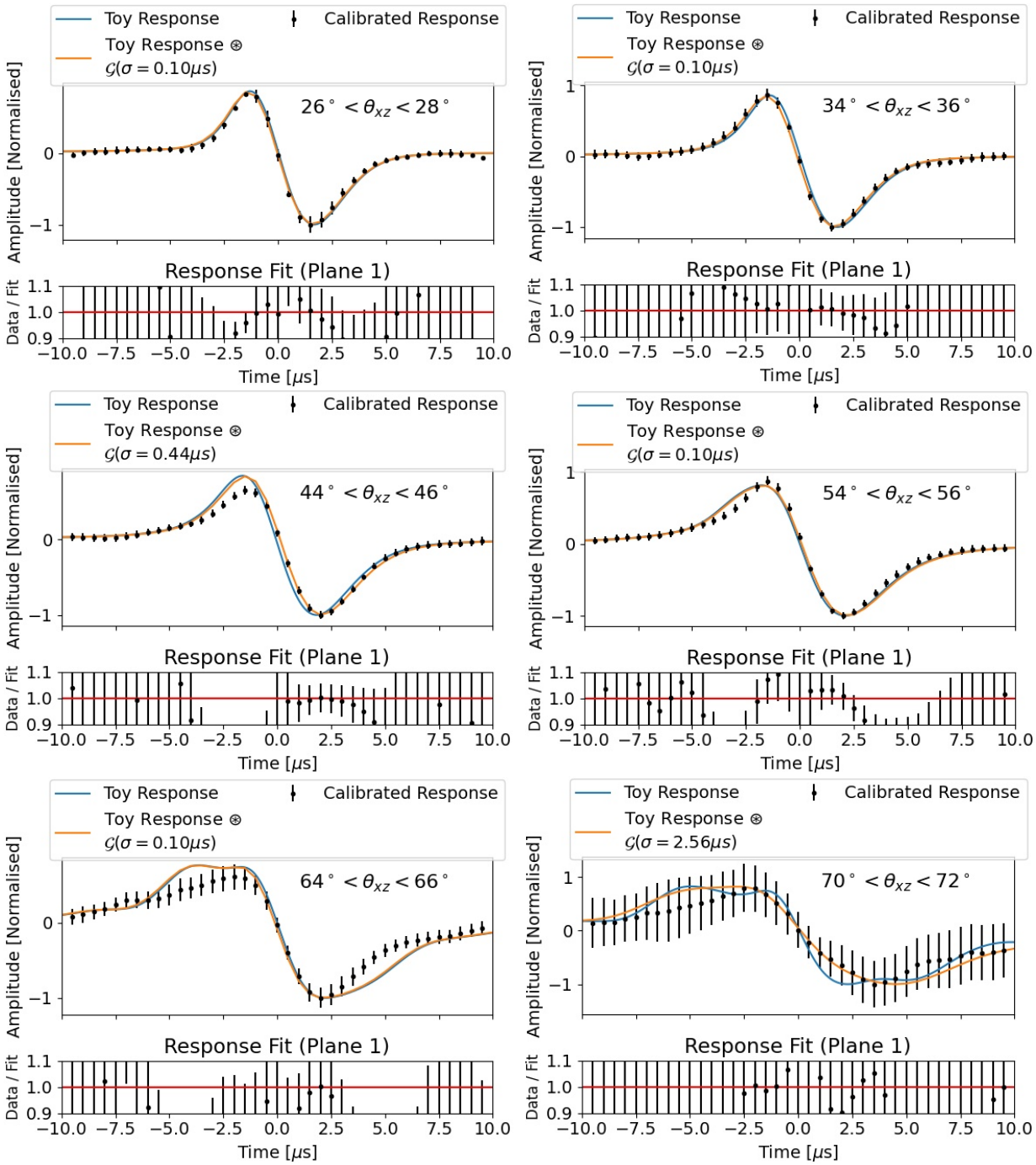

Figure 7.8: Comparisons of the average reconstructed waveform on second induction plane wires using a two-hour SBND data run (calibrated response), the convolved field and electronics response (toy response) and toy response convolved with a Gaussian (toy response $\circledast$ $\mathcal{G}$) for six chosen $\Delta\theta_{xz} = 2^\circ$ segments between 26° and 80°. Error bars on the calibrated response are calculated based on the standard error in the statistics of tracks.

form shape due to wire bias voltage alterations, which was still being calibrated for SBND at the time of data collection. Figure 7.9 presents the field response validation plots for the collection plane using SBND data.

The plots in Figure 7.9 also exhibit few selected tracks at $\theta_{xz} < 40°$, with the SBND data waveform and total wire response diverging for higher θ_{xz}. More tracks with high θ_{xz} have been selected for the collection plane waveform compared to the few observed in the induction planes for $\theta_{xz} > 70°$, supporting the conclusion from the waveform angle plots in Figure 7.2 that tracks close to perpendicular to the APA induce a lower amplitude signal on induction plane wires and a larger amplitude signal on collection plane wires. Figure 7.9 also shows good alignment with the total wire response convolved with the Gaussian and the SBND data waveform in the angle range of $40° < \theta_{xz} < 70°$. This supports the conclusions from the field response validation results using MC samples in Section 6.4, where the field response function calculations by the 2D Garfield simulation need to be corrected for high track pitch angles. This disparity could also suggest that SBND software is not reconstructing TPC waveforms correctly compared to SBND data, which will be confirmed by looking at the MC versus SBND data waveform plots.

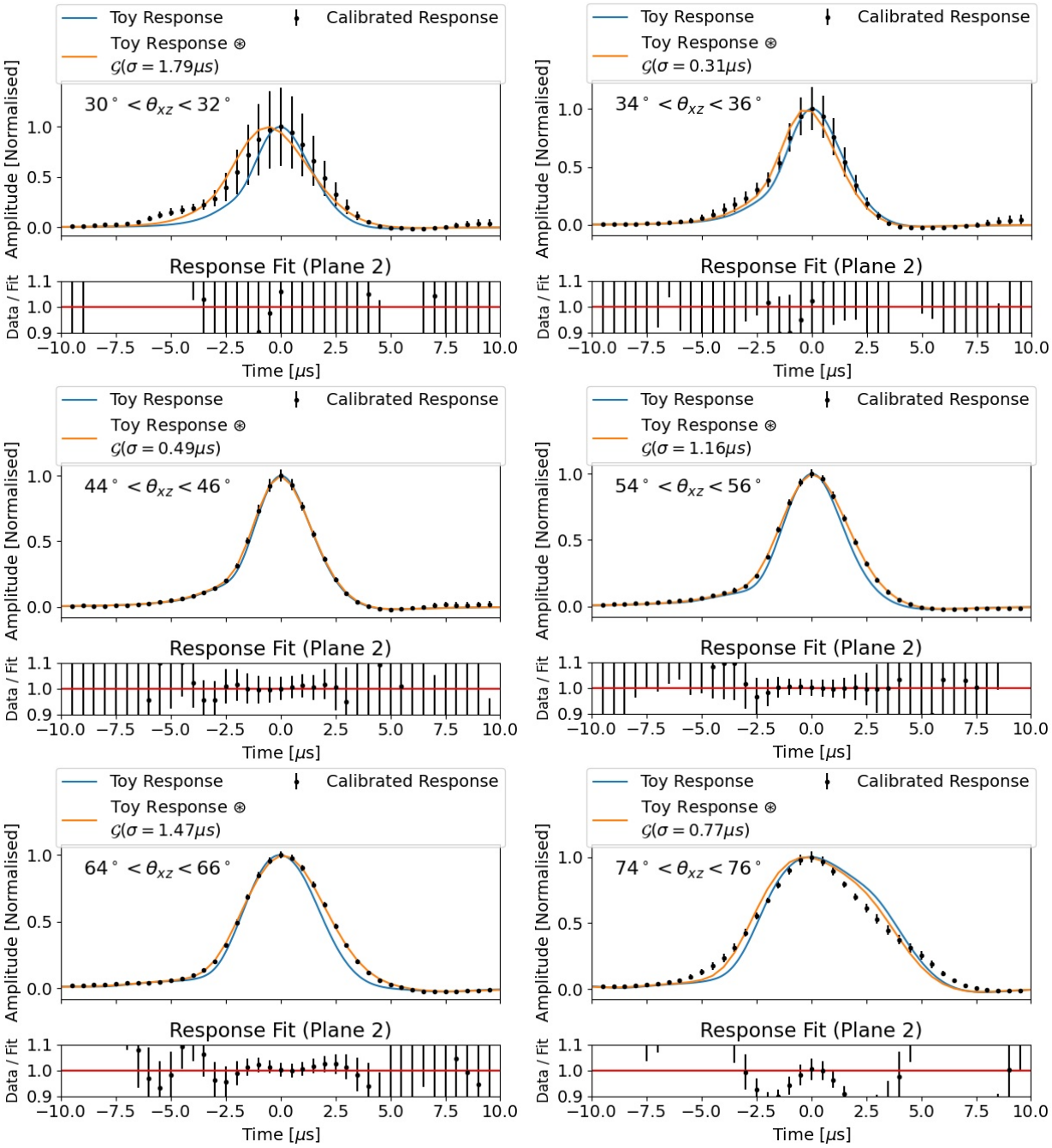

Figure 7.9: Comparisons of the average reconstructed waveform on collection plane wires using a two-hour SBND data run (calibrated response), the convolved field and electronics response (toy response) and toy response convolved with a Gaussian (toy response $\circledast$ $\mathcal{G}$) for six chosen $\Delta\theta_{xz} = 2^\circ$ segments between 26° and 80°. Error bars on the calibrated response are calculated based on the standard error in the statistics of tracks.

7.3 SBND Data vs Monte Carlo Waveforms

Comparing the average reconstructed waveforms from both MC event samples and SBND data to the calculated total wire response waveforms was undertaken in order to ensure that Garfield calculated the field response functions correctly, and that Wire-Cell modelled these functions to produce total wire response convolved waveforms on TPC readout wires accurately. These are the first steps in fully validating the field response modelling in SBND, with the last step involving measuring any differences in the waveforms reconstructed using MC event samples and SBND data. This is a more direct way of validating the field response, as it avoids biases in event generation, since the MC event samples and SBND data use the same average waveform analysis program. The first comparison between average MC and data waveforms is shown in Figure 7.10 for all three wire planes, where waveforms are normalised by lining up the negative induction plane peaks and unifying the integrals of the collection plane distributions.

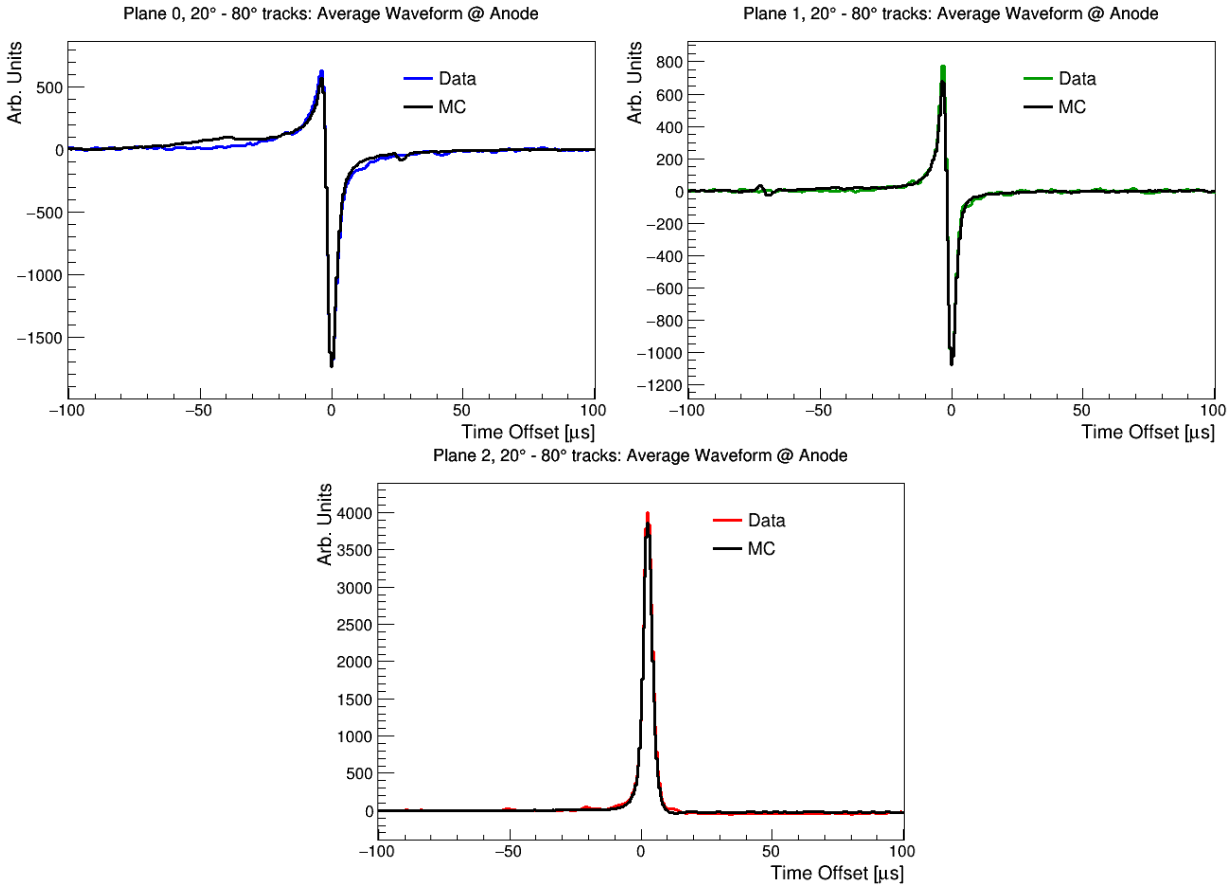

Figure 7.10: Average reconstructed waveforms on SBND TPC readout wires for the first induction (top left), second induction (top right) and the collection (bottom) planes using anode-cathode crossing cosmic-ray muons from MC event samples and SBND data.

The plots in Figure 7.10 show overall alignment between MC and data for all wire planes, which is a substantial result for an early data run of SBND, where typically there are great divergences in MC and data for other LArTPC experiments such as ICARUS [163] and MicroBooNE [164]. Small fluctuations in the data waveforms are present in all wire planes on either side of the central peak structures, which is due to the SBND dataset containing 500–1,000 selected anode-cathode crossing tracks compared to the 5,500–8,000 tracks present in the MC event sample.

An anomalous uplift in the first induction plane MC waveform around -60 μs $< t <$ -20 μs compared to data is observed in Figure 7.10. This could be a result of the noise model in the SBND simulation, used to subtract the coherent noise from individual wire channels, being inaccurate to what is observed in SBND data. As such, the field response study will need to be recreated once the noise model is updated in the SBND simulation from data-driven calibration studies. Figure 7.11 presents the MC versus data waveform plots in Figure 7.10, but with a narrowed time axis of -25 μs $< t <$ 25 μs.

The narrowed MC versus data waveform plots in Figure 7.11 show minor discrepancies in the regions close to the central peak areas, which is most apparent for the right-hand side of all wire plane plots. These minor discrepancies will also be due to a noise model that needs to be calibrated with SBND data, as well as minor signal broadening effects due to an unoptimised NL parameter. Overall, the data waveforms seem to exhibit slight signal broadening with respect to the MC, which could be due to how the electron lifetime, diffusion and SCE models integrated in the SBND simulation differ from what is seen in data. At the time of writing, work has been done to optimise these models by matching them with SBND data, so the field response validation methodology will be re-run with more recent datasets, so any minor discrepancies in waveform shape will be undoubtedly down to field response function calculation by Garfield.

The peaked regions of the plots in Figure 7.11 show that the MC waveforms exhibit deficits in positive peaks for the induction plane waveforms, which is an indication of differences in how the wire bias voltage settings are integrated in the SBND simulation compared to what appears in SBND data. The SBND data run representing these waveforms had nominal bias voltage settings of -210 V for plane 0 and 420 V for plane 2. Section 7.1.3 concluded that intransparency was observed in the second induction plane in SBND data due to more ionisation electrons terminating on induction plane wires and fewer on collection plane wires, resulting in a greater positive induction plane peak and broader collection plane signal. This further suggests that the SBND simulation is underestimating the amount of wire plane intransparency observed by the induction planes.

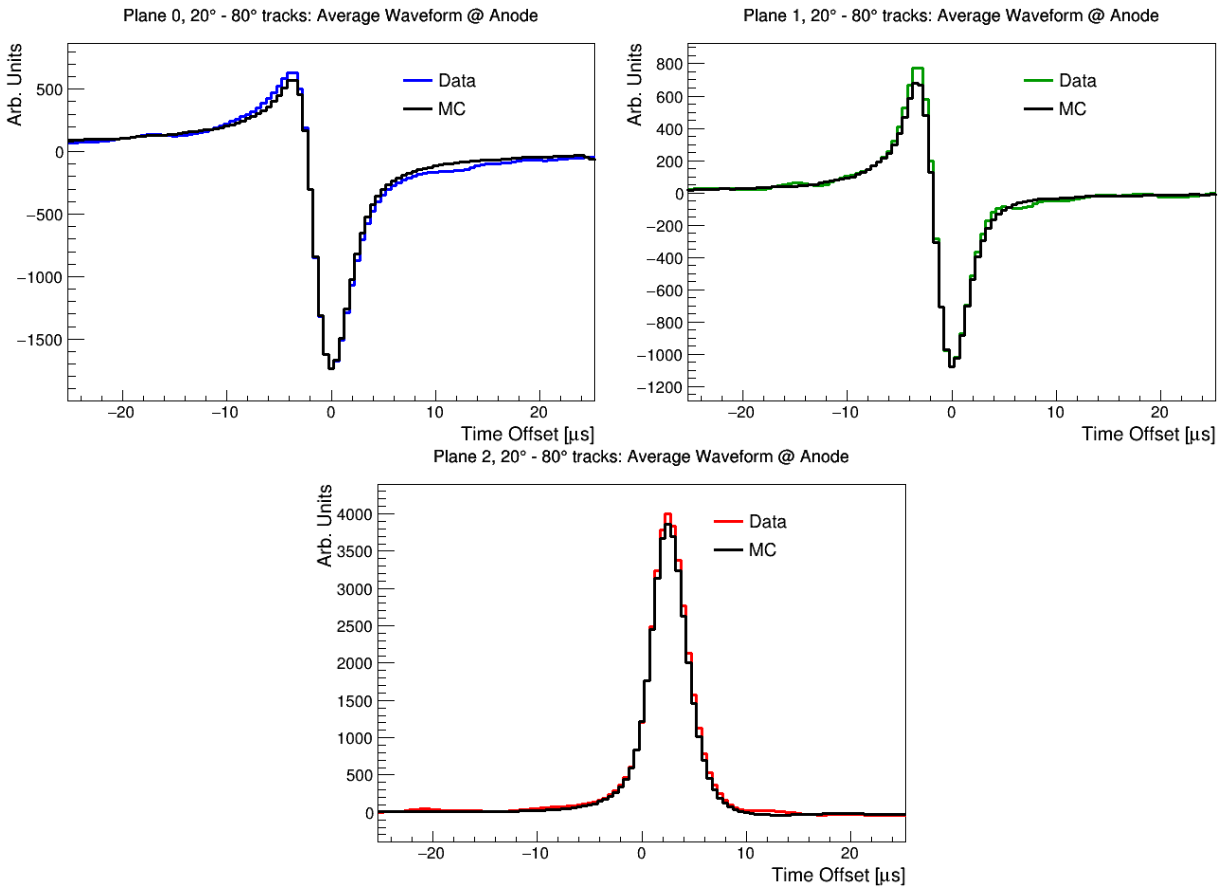

Figure 7.11: Average reconstructed waveforms on SBND TPC readout wires for the first induction (top left), second induction (top right) and the collection (bottom) planes using anode-cathode crossing cosmic-ray muons from MC event samples and SBND data, with a narrowed time axis of -25 µs $< t <$ 25 µs.

At the time of writing, the bias voltage settings have since been optimised in SBND to be -210 V for plane 0 and 600 V for plane 2, which should result in the MC and data waveforms lining up better. Additionally, slight signal broadening observed in the right-hand section of the collection plane data waveform implies an inaccurate electronics response model implemented into the SBND simulation. A long-timescale negative component to the right-hand side of the collection plane waveform is a result of signal convolution with the electronics response function, which is observed in data and is not present in MC, further supporting the need to optimise the electronics response modelling in SBND. Though, as of writing this chapter, this task has been completed, so the field response validation methodology will be repeated with this updated electronics response.

After ensuring that the electronics response model is correct, bias voltages are optimised for each wire plane, and ADC/NL thresholds in the average waveform script have been

tuned, any differences in the MC and data waveforms should either be down to how field response functions are calculated using the 2D Garfield simulation, or how total wire responses are modelled through Wire-Cell. Disparities can also arise in waveform shape due to the angular phase space of cosmic-ray muon tracks differing in MC and data. As such, it is important to look at the angular breakdown of the average MC and data waveforms with respect to θ_{xz}. The average waveforms on all wire planes have been plotted using MC event samples and SBND data, selecting tracks with θ_{xz} ranging from 20° to 80° in segments of $\Delta\theta_{xz} = 10°$. Results for the first induction plane are presented in Figure 7.12.

The first induction plane MC versus SBND data waveform plots in Figure 7.12 confirm that there are large variations in signal shape with respect to θ_{xz}, particularly at $\theta_{xz} < 40°$ and $\theta_{xz} > 60°$. Tracks with $\theta_{xz} < 40°$ in MC have greater front-end signal amplitudes, with the data waveforms exhibiting a greater amount of signal broadening on its right-hand side. The positive induction peaks line up very well for tracks with $30° < \theta_{xz} < 50°$, but for $\theta_{xz} < 30°$ the MC waveform has a higher positive induction peak than in data, and at $\theta_{xz} > 50°$ the data waveform is shown to have a higher positive peak. This motivates the need for the field response modelling in the SBND simulation to be corrected for tracks with higher θ_{xz}, so MC waveforms can better match data. The angular breakdown of MC versus data waveforms on the second induction plane are shown in Figure 7.13.

The relationship between θ_{xz} and second induction plane waveform shape in Figure 7.13 also shows a relatively larger positive peak in data than in MC. This is also direct evidence of intransparency on second induction plane wires, where the bias voltage settings in the SBND simulation are different from what is observed in data. Therefore, integrating the optimal bias voltage setting of 600 V for collection plane wires will mitigate this intransparency effect and show a greater alignment of the MC and data waveforms.

Second induction plane waveforms corresponding to tracks with $\theta_{xz} > 70°$ in Figure 7.13 exhibit great signal fluctuations in data compared to MC. This could be due complexities in lining up second induction plane waveforms in time for SBND data compared to MC. At the time of data collection, the CRT data reconstruction chain had not yet fully interfaced with the TPC readout chain, particularly in the realm of matching the timing information of tagged muon events. So even though the CRTs were able to match the spatial position of muons with respect to tracks traversing the TPC, inaccuracies arose when lining up the timing of waveforms induced on TPC readout wires. This is not the case for the SBND simulation generating MC event samples, and has only been apparent in SBND data when reconstructing tracks close to perpendicular to the APA (i.e. high θ_{xz}) on second induction plane wires, where signal shapes are the most complex.

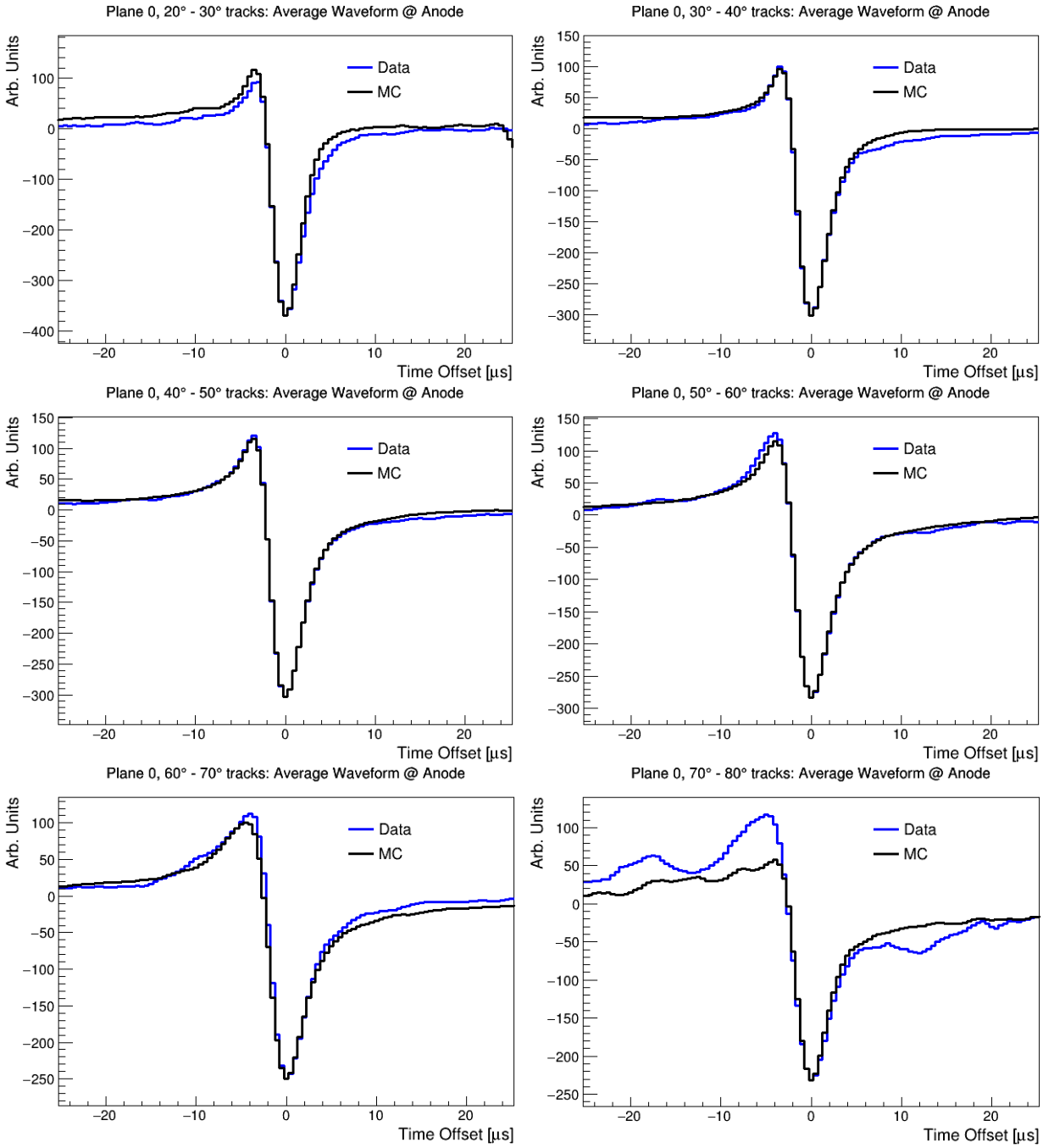

Figure 7.12: Average reconstructed waveforms on SBND TPC first induction plane wires for anode-cathode crossing cosmic-ray muons from MC event samples and SBND data. Plots are broken down with respect to track pitch angle θ_{xz} in segments of $\Delta\theta_{xz} = 10°$ from 20° to 80°. Full ±100 µs plots are presented in Figure B.1 in Appendix B.

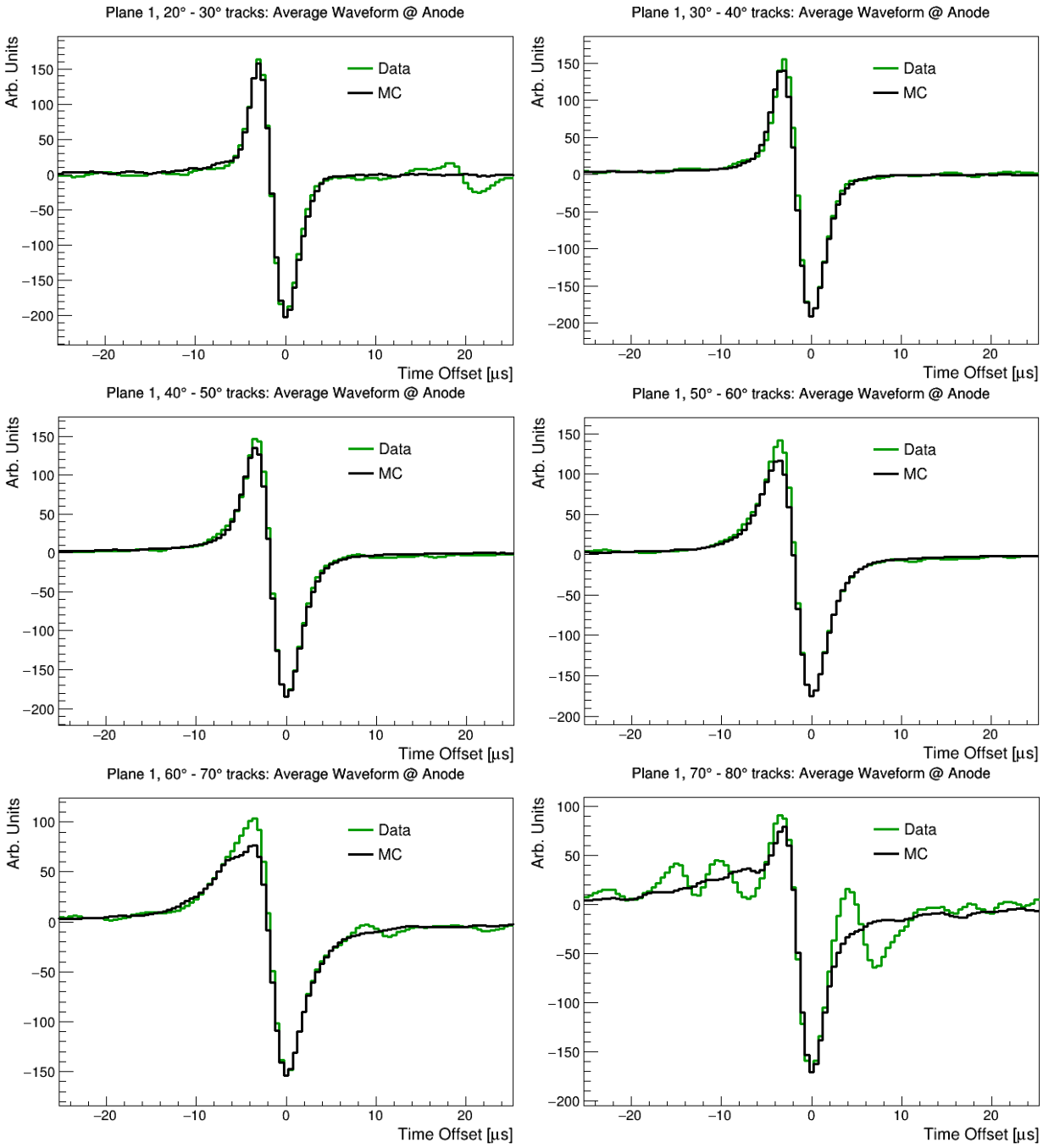

Figure 7.13: Average reconstructed waveforms on SBND TPC second induction plane wires for anode-cathode crossing cosmic-ray muons from MC event samples and SBND data. Plots are broken down with respect to track pitch angle θ_{xz} in segments of $\Delta\theta_{xz} = 10°$ from 20° to 80°. Full ±100 µs are presented in Figure B.2 in Appendix B.

Since the completion of this work, the CRT t_0 has been fully integrated into the SBND DAQ system using SBND data and matched with MC samples produced from the SBND simulation, so this would not be an issue with current SBND data runs. Finally, Figure 7.14 shows the angular breakdown of MC versus data waveforms for the collection plane.

The overall signal shape for collection plane waveforms in Figure 7.14 are much more varied and seemingly less dependent on θ_{xz} than what is observed for the induction plane waveforms in Figures 7.12 and 7.13. Both the MC and data waveforms failed to select any tracks with $\theta_{xz} < 30°$, which suggests that the ADC thresholds for the collection plane need to be optimised, since there were plenty of selected tracks with $\theta_{xz} < 30°$ for the induction planes. Despite this, the data waveforms seem to be consistently wider than the MC waveforms. The data waveforms show a negative component to the right of the peak for all θ_{xz} that is not observed in MC, further suggesting that this disparity is due to the electronics response not being accurately modelled in the SBND simulation, since this anomaly is independent of θ_{xz}. Calibration of the electronics response modelling in SBND has since been completed and verified with SBND data, so this disparity should no longer be present in current SBND data runs or newer versions of the SBND simulation.

Overall, SBND TPC waveforms exhibit good agreement for a first comparison of MC and data, more than what was first observed by ICARUS [163] due to SBND having a greater signal-to-noise ratio and ICARUS experiencing larger intransparency issues in the second induction plane as to what has been observed in SBND data. However, these results can be improved by optimising the ADC and NL thresholds in the track selection process of the average waveform analysis program, minimising the overall smearing due to noise and anomalous bumps in the right-hand side of the plots. Once this study is repeated with these optimisations, any differences in the MC and data waveforms will be driven solely by how the field response functions are calculated by Garfield and/or how these functions are used to model total wire responses on SBND TPC readout wires by Wire-Cell.

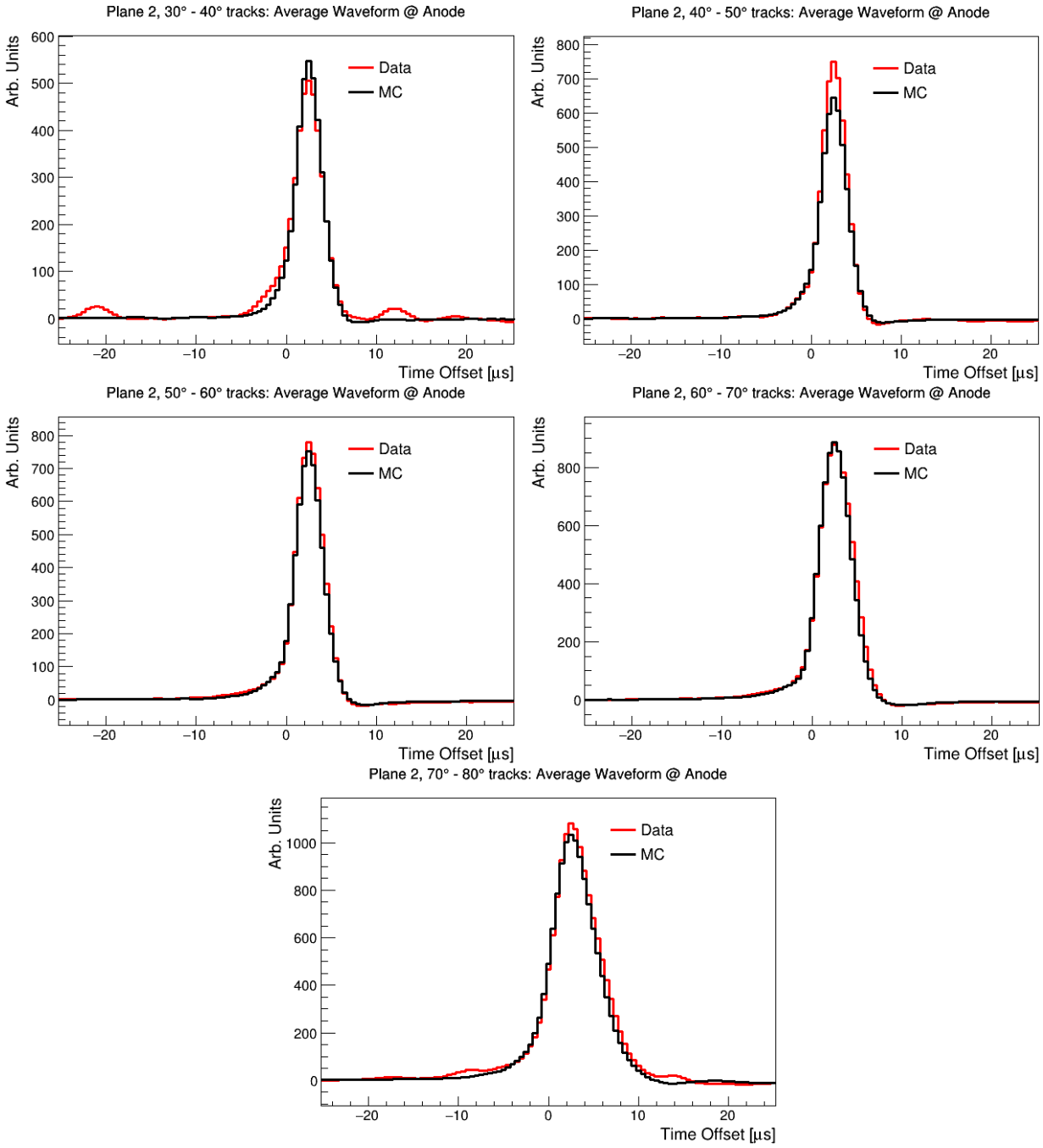

Figure 7.14: Average reconstructed waveforms on SBND TPC collection plane wires for anode-cathode crossing cosmic-ray muons from MC event samples and SBND data. Plots are broken down with respect to track pitch angle θ_{xz} in segments of $\Delta\theta_{xz} = 10°$ from 20° to 80°. Full ±100 µs plots are presented in Figure B.3 in Appendix B.

7.4 Conclusions

The work presented in this chapter and Chapter 6 represents a fully developed and executed methodology to test and validate the field response simulation in SBND, consisting of three main tasks. Chapter 6 contained work done on the first task, which involved comparing the average waveform on TPC readout wires, reconstructed from MC event samples, with the expected total wire response, which is a convolution of the electronics response and the field response functions, calculated using Garfield [154] and modelled on APA wires through Wire-Cell [155]. This chapter contained work done executing the latter two tasks: comparing the average waveform on TPC readout wires from SBND data runs with the same total wire response function; and a MC versus data study scrutinising disparities in the average reconstructed waveform from MC event samples and SBND TPC data.

The SBND data waveforms and total wire response functions showed overall agreement, with deficits in the positive induction peak observed for higher θ_{xz}, suggesting inaccurate field response functions for tracks with high θ_{xz}. Comparisons of SBND data waveforms with different wire bias voltages showed that the optimal bias voltage for the first induction plane is the nominal of -210 V. However, evidence of wire plane intransparency was observed for the second induction plane, motivating the need for a higher collection plane bias voltage than the nominal of 420 V to mitigate this effect, which has since been chosen to be 600 V. MC and SBND data waveform comparisons showed broader data waveforms than MC, which could be due to unoptimised ADC and NL threshold parameters, or an inaccurate noise model used in the SBND simulation. Slight signal broadening was also observed on the right-hand side of the collection plane waveforms, with an additional negative component observed in data that was not present in MC, suggesting that the electronics response is not modelled accurately in the SBND simulation.

At the time of writing, the wire bias voltages have since been optimised for SBND and integrated into the SBND simulation, and the electronics response has been fully calibrated and optimised using SBND data. The results presented in this chapter and Chapter 6 have led to this field response validation study being repeated by SBND collaborators using more recent SBND data runs, where none of the aforementioned inaccuracies are present, fully completing the field response validation procedure using SBND data. The results of this repeated study will be presented in an upcoming paper containing SBND calibration work.

Chapter 8

LArTPC Test Stand Commissioning at the University of Sheffield

LArTPC technology typically utilises several planes of wires to read out ionisation charges. This is particularly suitable for detectors with active LAr masses of $\mathcal{O}(100)$ tons such as ICARUS, MicroBooNE and SBND, where long wires can cover a wide area of the detector readout plane. However, wire planes have been known to exhibit ambiguities in event reconstruction, as well as pile-up of ionisation charges from multiple tracks occurring near the anode, particularly for tracks co-planar to the readout plane [102]. To address these issues with projective wire planes, development of an alternative charge readout mechanism has taken place over the last decade involving an array of pixels to collect ionisation electrons. One such testing ground for the development and optimisation of pixelated charge readouts for use in future LArTPCs is STEEL at the University of Sheffield.

This chapter contains work done commissioning each STEEL detector subsystem, ensuring the readout mechanisms are calibrated and optimised for long data collection runs. An experimental overview of the STEEL detector and its subsystems are detailed in Section 8.1. Section 8.2 contains work done testing the LAr purification system, calibrating the bias voltage of each subsystem and optimising the readout window for coincidence events, as well as characterising the timing of pixel signals when interfacing with other subsystems. Lastly, Section 8.3 contains general conclusions to the STEEL commissioning tasks.

8.1 STEEL: Sheffield TEst stand Experiment with Liquid argon

The University of Bern [168], and other studies [103, 169], have proven the viability of pixelated charge readout systems for use in future LArTPCs by showing that full 3D tracking of particles is possible with pixelated charge readout systems, as well as eliminating the ambiguities in track reconstruction intrinsic to wire plane readouts. The main goal of STEEL is to build on these studies by optimising the hit-finding and track reconstruction capabilities of pixelated charge readout systems, providing the groundwork for its use in large-scale LArTPC experiments such as the GAr component to the DUNE ND [104]. STEEL utilises a detector based on a design first conceived by BNL [170], adapted for use with a pixelated charge readout, pictured in Figure 8.1.

The main detector components of STEEL are a cylindrical stainless steel argon containment vessel called a dewar, four external CRTs, an internal PMT and a cylindrical LArTPC field cage, as well as a purification system circulating GAr and condensing it back to LAr using LN. Outlined in this section are details of the setup of these subsystems.

8.1.1 LAr Containment Vessel

Pictured in Figure 8.2, the STEEL detector consists of a cylindrical stainless steel dewar (60 cm height, 24 cm diameter) built to contain 27.6 L of LAr (22.1 L with LArTPC and readout equipment inside), with vacuum-sealed and double-walled edges to thermally isolate the LAr from the outside. LAr fills the dewar through an inlet at the bottom using a vacuum flange, kept thermally insulated through five steel baffles held 2 cm apart at the top of the dewar, supported by three threaded steel rods supporting the readout mechanisms inside the dewar. Internal LAr pressures are ideally maintained below 20 Pounds per Square Inch (PSI), though the dewar can withstand up to 30 PSI where pressure relief valves open up, gradually releasing argon in case the pressure exceeds this value.

A key feature of STEEL is the argon purification system, shown above the dewar in Figure 8.3, which filters out ENI such as H_2O and O_2 from the argon. Due to the dewar not being completely thermally isolated from the outside, the top layer of LAr in the dewar gradually boils off into a thin layer of GAr, passing through a vacuum-jacketed tube into the purification system, which is a 33 cm length, 5 cm diameter stainless steel cylinder. The first 11 cm of this tube contains 1 kg of 13X molecular sieve mesh beads, which have a critical diameter such that water molecules are absorbed whilst GAr atoms pass freely.

The last 22 cm of the purification tube contains 3 kg of Gettermax133 catalyst tablets

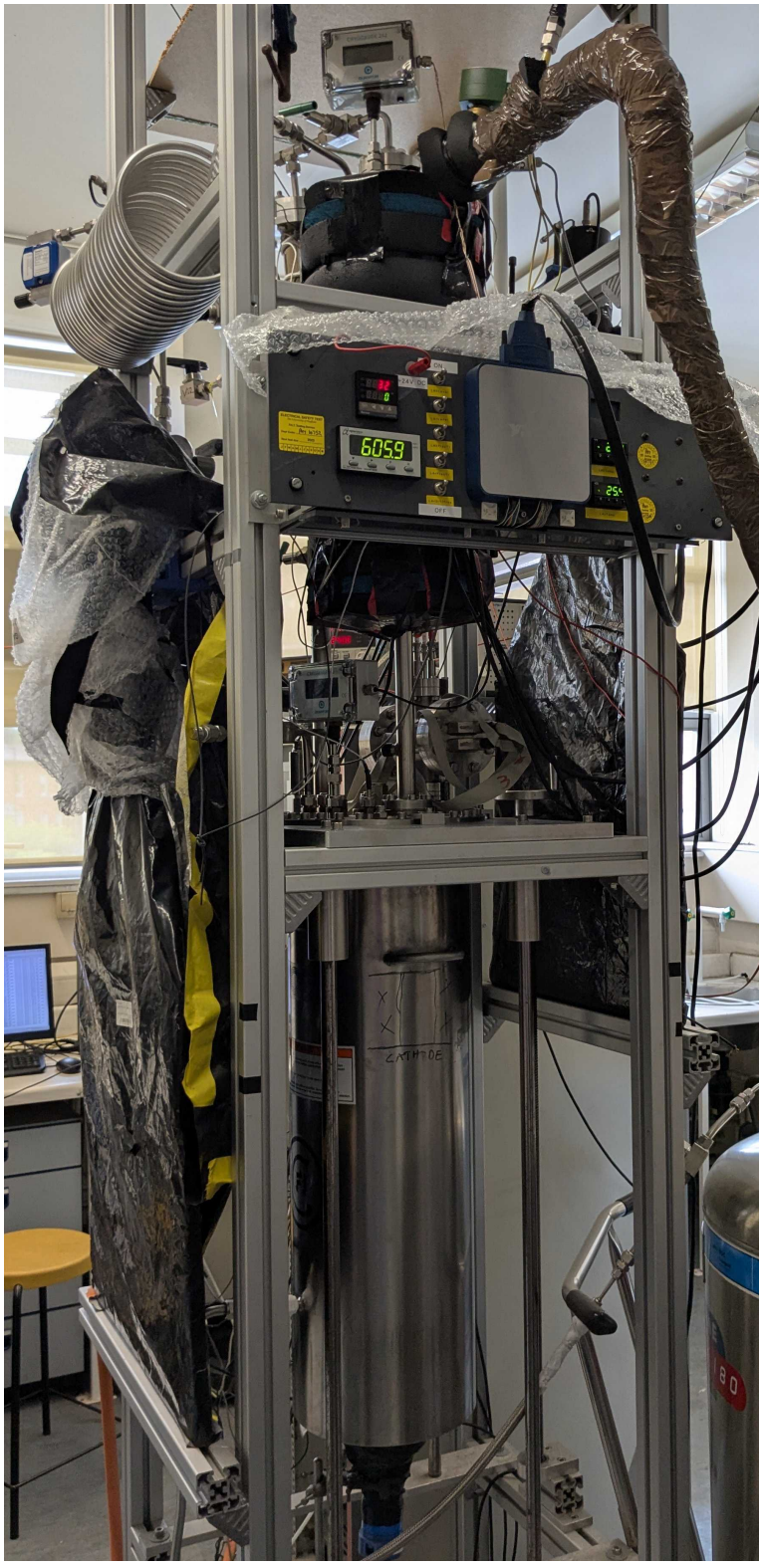

Figure 8.1: Picture of the STEEL experiment.

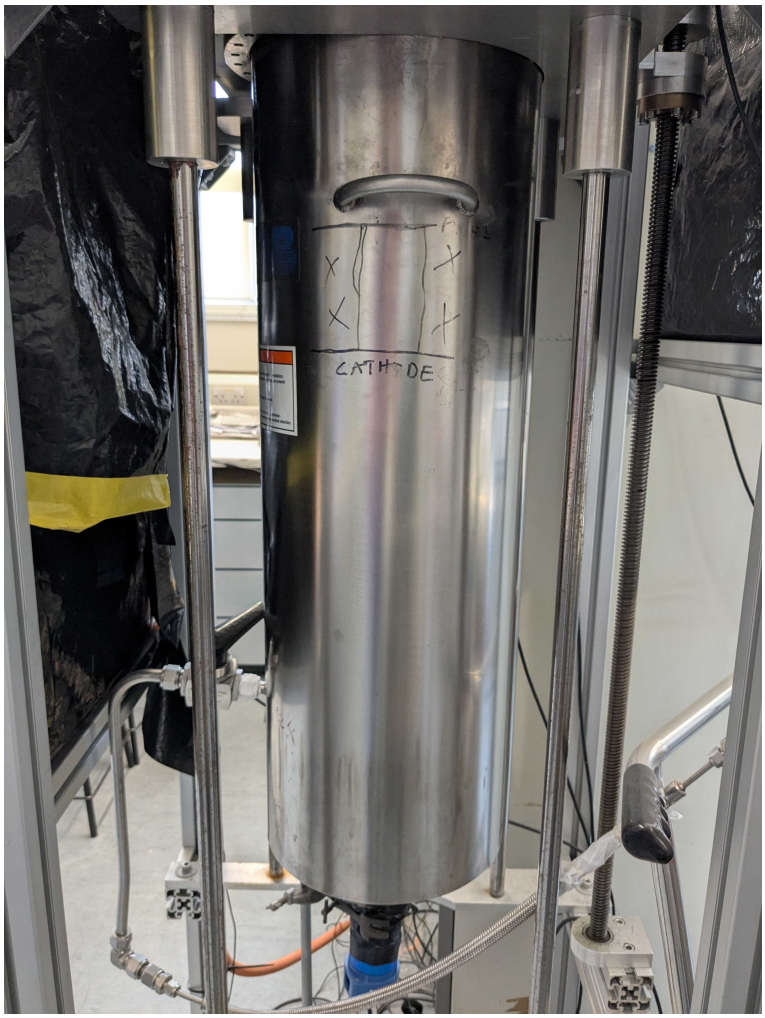

Figure 8.2: Picture of the STEEL dewar containing the LArTPC, indicated by the black drawing on the face of the dewar. It is a stainless steel cylinder 60 cm in height and 24 cm in diameter capable of containing 27.6 L of argon.

consisting of copper, zinc and aluminium which chemically absorb oxygen molecules through oxidation [171]. Eventually, the mesh beads become saturated with H_2O, and the catalyst tablets reach full oxidation. This is when the filtration systems need to be regenerated, which involves heating the purification cylinder with electrical heating tape to vaporise H_2O from the beads. Then, high purity GAr doped with 2% hydrogen gas is circulated through the system to attach to the O_2 oxidised in the catalyst tablets, producing H_2O, which then gets absorbed by the molecular sieves.

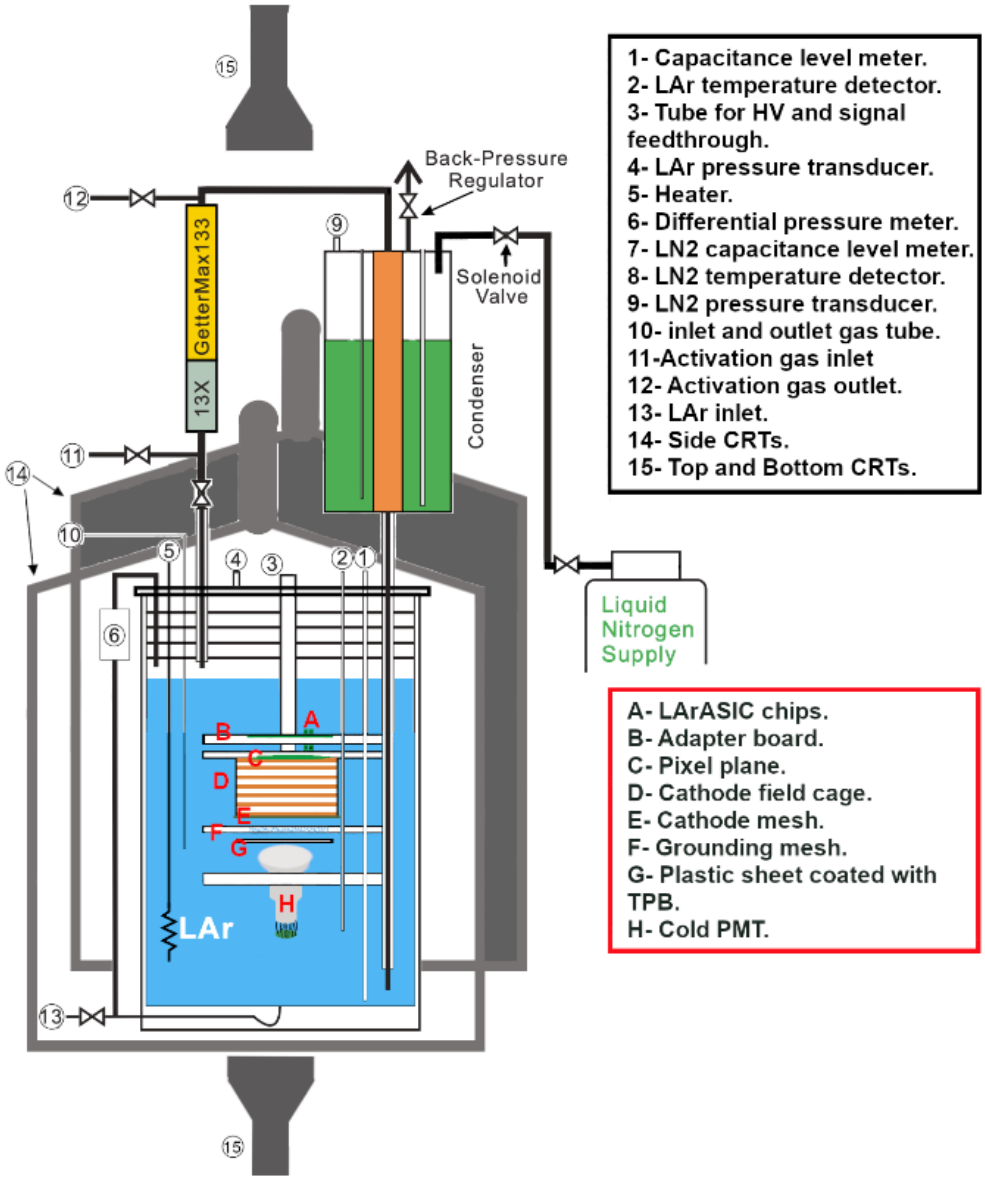

Figure 8.3: Schematic outlining the components and subsystems of STEEL, including the dewar, LArTPC, CRTs and purification/circulation system (sourced from [172]).

Once the GAr exits the purification cylinder, it passes through the condenser system,

which is a 47 cm length, 15 cm diameter stainless steel coaxial cylinder. LN at 78 K fills the outer cylinder, cooling the GAr in the inner cylinder through conduction, with the aid of copper wool, below its boiling point of 87 K, condensing into LAr and flowing back into the bottom of the dewar. LN pressure is stabilised through a back-pressure regulator, indirectly keeping the temperature and pressure of LAr in the dewar near-constant.

LN fills the condenser system continually until it reaches 90% capacity, where a pressure-relief valve connected to a flange opens up to release boiled-off LN until the condenser capacity drops to 30%, commencing filling again. This automated system keeps the condenser pressure from exceeding 60 PSI, though ambient LN pressures in the condenser typically fall between 30 PSI and 40 PSI. Argon purity, liquid level, temperatures and pressures are monitored live through various appliances which will be expanded upon in Section 8.1.4.

8.1.2 LArTPC and Pixelated Readout Plane

Within the dewar is the LArTPC, pictured in Figure 8.4, consisting of a cylindrical field cage, 10 cm in height and diameter, with the cathode on the bottom and anode on the top.

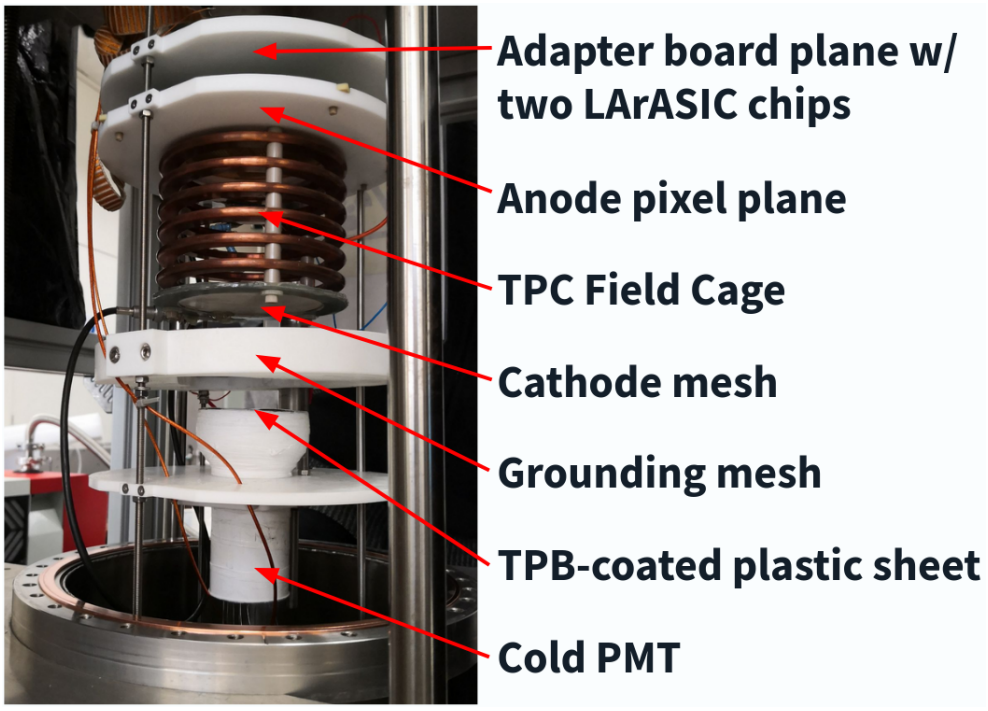

Figure 8.4: STEEL LArTPC with labelled components.

The field cage is constructed of six 6.35 mm thick copper rings linked by a 56 MΩ resistor to contain the electric field. It holds 0.79 L of active LAr volume, with the cathode negatively voltage biased by a CAEN V6521 [173] resulting in a downward electric field of

adjustable field strength up to 600 V/cm, drifting ionisation electrons upwards towards the anode. The cathode consists of a wire mesh, making it transparent to scintillation light such that the PMT situated below the cathode can collect sufficient photons for timing and triggering purposes. A grounding mesh is placed between the cathode and PMT to prevent electrical discharges from the electric field interfering with the PMT.

Ionisation charge signals are read out by the anode pixel plane, composed of a 10 cm × 10 cm eight-layered Printed Circuit Board (PCB) with 1008 total pixels. These pixels are divided into 28 squares, each containing 36 pixels aligned into a 6×6 square, with each pixel separated by 2.54 mm. The anode pixel plane used in STEEL, designed by the University of Bern [168], is depicted in Figure 8.5 alongside its position on the LArTPC.

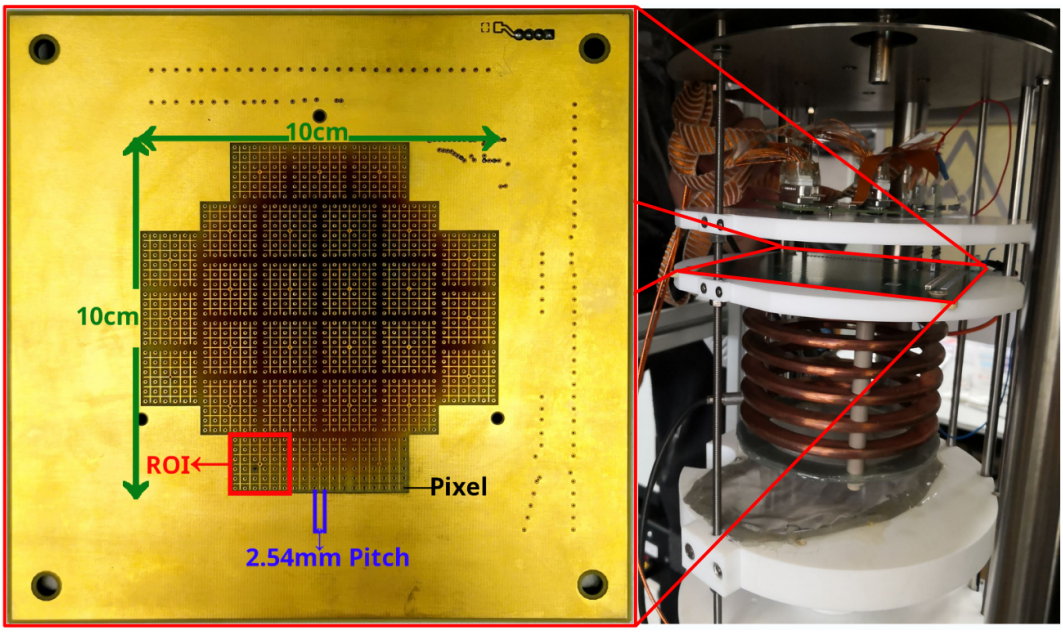

Figure 8.5: STEEL pixelated anode readout plane (pictured left), designed by the University of Bern [168], alongside its relative position in the STEEL LArTPC (pictured right).

Each square of 6×6 pixels is surrounded by a 1.67 cm x 1.67 cm voltage-biased induction grid called a Region Of Interest (ROI). ROIs are made from 152.4 µm wide copper traces, with the voltage bias supplied from the applied electric field. Drifting ionisation electrons induce signals on the ROIs, which focus charges towards the 900 µm-wide pixels inside that ROI, where they are collected. ROIs and pixels act analogously to induction and collection plane wires respectively. Raw pixel signals are passed through an adapter board with two ASIC chips, utilising LArASIC7 to pre-amplify and shape these raw charges into processed signals [174]. The shaping time and gain setting for these ASIC chips are 2 µs and 25 mV/fC respectively, set manually using an Arduino nano [175].

With 1008 total pixels collecting charge and 28 ROIs inducing signals, one would expect 1036 individual readout channels (one per pixel and ROI), requiring large amount of computational power and overwhelming any DAQ system collecting pixel data for STEEL. For this reason, the LArASIC7 firmware utilises multiplexing, allowing for each pixel in the same relative position of every 6×6 square of pixels to share a readout channel, decreasing the number of pixel readout channels from 1008 to 36, giving 64 total readout channels: 36 pixels and 28 ROIs. As such, the method for determining which exact pixel collected the ionisation charges in a given hit is to match the ROI waveform in time with the hit pixel waveform, as their signal inductions correspond to the same ionisation charge(s).

Processed pixel signals are then passed through a CAEN V1740 [144], acting as the pixel DAQ system, creating events with defined signal waveforms and timestamps. The only limitations present with LArASIC7 multiplexing is when multiple simultaneous pixel hits line up with one or more ROI induction pulse(s), making it difficult to determine which pixel hit is in which ROI. However, this rarely occurs as multiple separate hits would have to happen inside the narrow time window between the ROI induction signal and pixel collection peak. As well as this, ambiguous pixel hits corresponding to multiple ROI channels are flagged for post-DAQ processing, where they can be disentangled using higher level reconstruction tools developed for STEEL.

8.1.3 Subsystems and Supplementary Detectors

STEEL utilises four external CRTs and an internal 'cold' PMT, connected to a logic trigger system used to select cosmic-ray muon tracks fully traversing the active LArTPC volume. A schematic of the CRTs oriented around the dewar is shown in Figure 8.6.

The cold PMT is a Hamamatsu R11065 type PMT [176] designed to operate in cryogenic environments below ambient LAr temperatures of 87 K, hence the name 'cold PMT'. Operating at a nominal voltage of 1700 V applied by a CAEN V6521 power supply [173], it collects scintillation light released in muon-induced argon de-excitations, amplifying the photon energy to a measurable current. Argon de-excitation emits 128 nm photons in the VUV range; just below the UV thresholds that industrial PMTs are sensitive to. As such, the cold PMT is covered with a TPB coated plastic sheet which shifts the photon wavelength towards the UV range so they can be read out by the PMT.

Two of the CRTs are 50 cm x 50 cm x 2.5 cm plastic scintillator paddles coupled to electron tube 9954KB type PMTs [177] positioned vertically on the north and south side of the dewar, 65 cm horizontally apart. These are used in coincidence with the cold PMT to select cosmic-ray muons with angles less than 52° to the anode plane, since tracks with

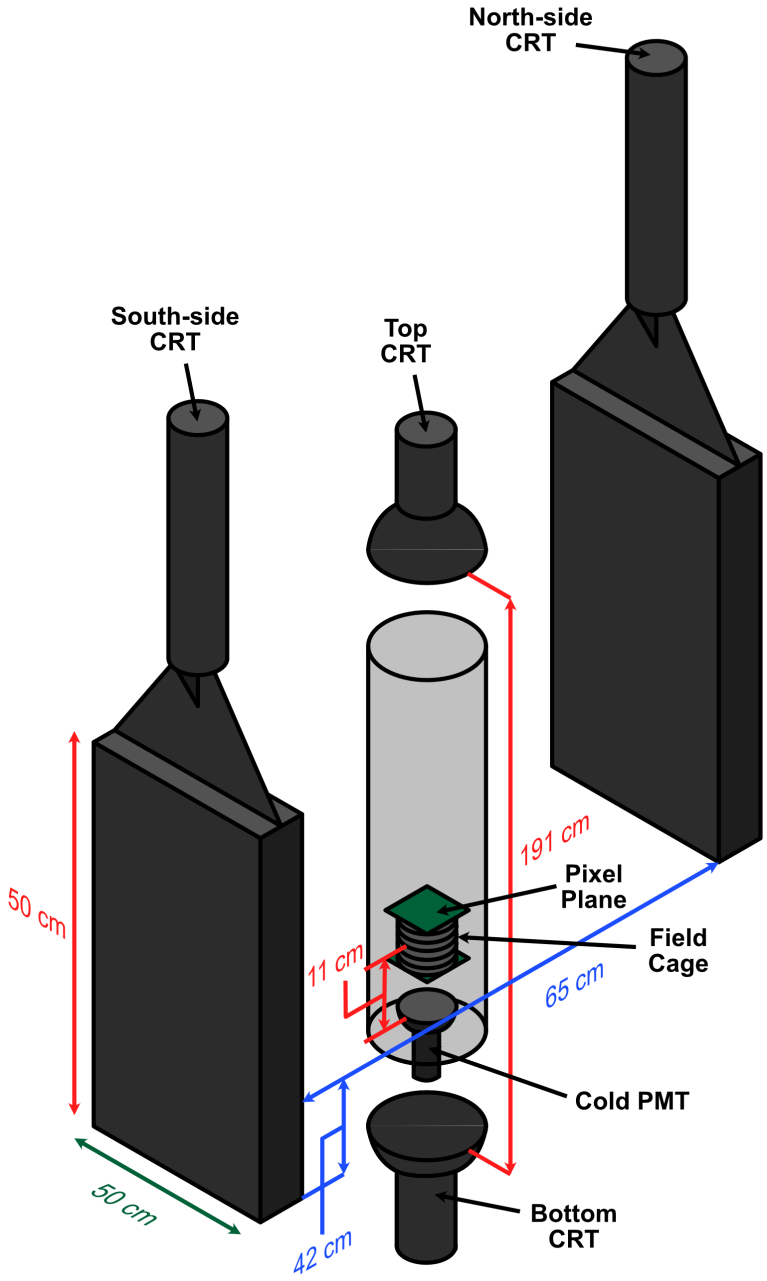

Figure 8.6: Schematic showing the relative position of the two side CRTs, top and bottom CRTs around the STEEL dewar with respect to the cold PMT and internal LArTPC.

greater angles have drift times larger than the 2 μs shaping time of the LArASIC amplifier. This can cause saturation, where a large amount of ionisation charges build up on ASIC capacitors, making it more difficult to read out raw signals and process waveforms in time.

The other two CRTs used are smaller 10 cm x 10 cm x 5 cm scintillator paddles, coupled to EMI 9791KB type PMTs [178], placed above and below the dewar 191 cm apart such that they vertically overlap with the anode plane. They trigger on near-vertical cosmic-ray muons, ensuring ionisation charges are deposited on the anode pixel plane and sufficient scintillation light is received by the cold PMT, regardless of argon purity. These were used during commissioning to test the signal output capabilities of the pixels and cold PMT, as well as to optimise the trigger window, which is expanded upon in Section 8.2.2.

All CAEN units, including high voltage supplies, logic discriminator units and DAQ hardware components are mounted on a server rack behind the dewar, pictured in Figure 8.7. The four CRTs and cold PMT are coupled together through a CAEN N417 discriminator [179], which creates a logic trigger window for implementing coincidences between the CRTs and cold PMT signals. All these subsystems are cabled together through the Keysight U5309A DAQ unit [180], which reads out a signal if either the two side CRTs or two top/bottom CRTs register a hit within a set trigger window of the cold PMT. This also interfaces with the CAEN V1740 pixel DAQ, opening the pixel readout window when the Keysight DAQ detects a fully reconstructed muon track passing through the LArTPC.

8.1.4 Operations and Data-collecting

Before STEEL can continuously collect cosmic-ray muon data, a specific procedure must be undertaken to ensure that all components and subsystems of the detector are fully operational and the dewar is in ideal condition. The dewar is filled completely with GAr and the condenser cylinder is filled with LN, recirculating GAr through the purification and condenser system such that the LAr:GAr ratio is maintained at 90:10 minimum and the ENI density is kept below 1 part per million (ppm). Additionally, LAr ambient temperatures and pressures need to be maintained below 87 K and 23 PSI (8 PSI above air pressure) respectively, as well as the temperature of LN in the condenser system staying below 86 K.

Live tracking of thermal parameters such as LAr/LN temperatures, pressures and argon liquid level are displayed on a LabVIEW program written on a National Instruments (NI) hardware computer [181], along with showing the voltages and currents of all detector components and subsystems. An NI PXI-6229 slow DAQ live monitor system [182] is also displayed above the STEEL detector as shown in Figure 8.8.

Argon and nitrogen temperatures are measured by PT100 Resistive Temperature De-

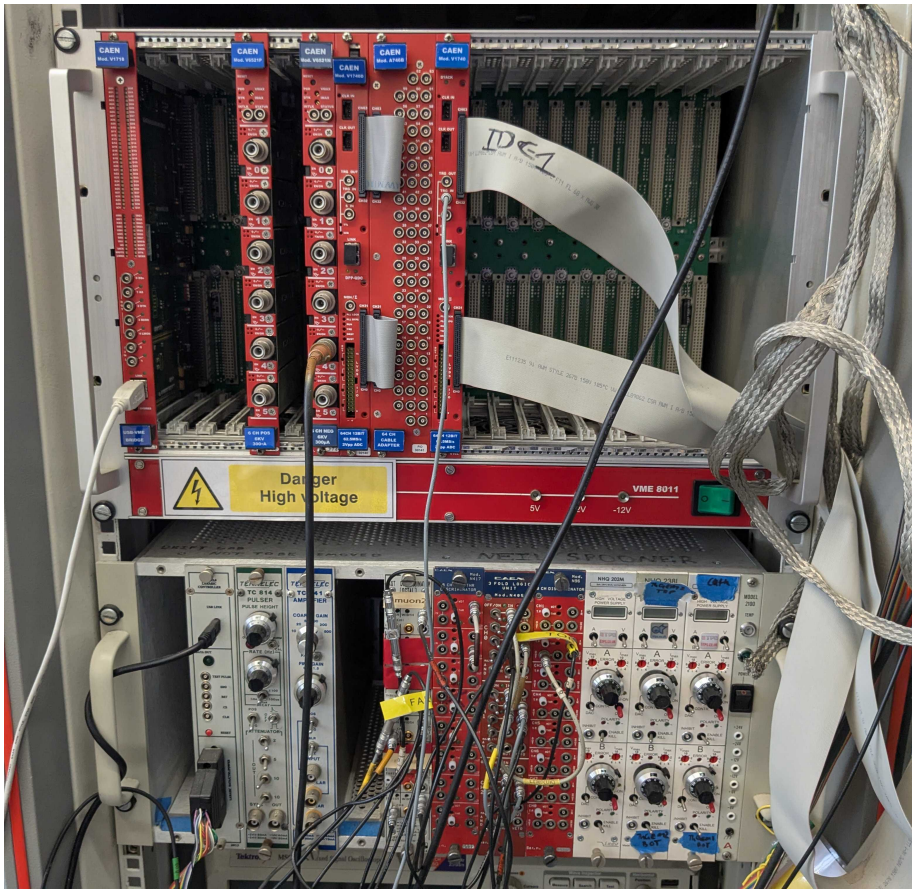

Figure 8.7: STEEL server rack showing the CAEN V1740 pixel DAQ processor, CAEN N417 logic discriminator unit and CAEN V6521 voltage supply units.

tector (RTD) devices [183], whereas pressures are measured using Omega PX209 series pressure transducers [184]. Argon liquid level is monitored by using these pressure transducers placed at the top and bottom of the dewar and calculating the difference in pressure at these extremities. Nitrogen liquid level is tracked using a CryoGauge 242 Telemetry liquid level gauge [185], which measures the capacitance between two concentric cylinders. Differences in argon purity are tracked live using a Servomex DF-550E Oxygen Analyser [186], placing the sensors directly after the purification cylinder.

Running the experiment involves configuring the DAQ with parameters such as trigger ADC thresholds, baseline ADC, time offsets, which channels to read out signals from, number of events to take or time limit of a single run. The STEEL DAQ system has eight separate readout channels consisting of the pixel DAQ, pixel trigger, cold PMT, north and south side CRTs, top and bottom CRTs and the logic trigger. Online monitoring allows for live waveforms, integration spectra and event displays for each pixel and ROI channel through baseline calculations, average pulse heights and noise RMS. C++ headers were

Figure 8.8: Live tracking of thermal parameters such as LAr/LN temperatures and pressures, as well as the argon liquid level on a NI PXI-6229 slow DAQ live monitor system. Pictured displaying relevant parameters for a dewar filled with air.

written to store metadata such as event number and pulse amplitude timestamps in both global UNIX time and ns, as well as channel data including ADC baselines and waveforms.

Processed data events by the DAQ produces a data file, which is then decoded into a ROOT file. There are separate decoder modules for the pixel data and Keysight DAQ collecting data from the other subsystems, which were custom written by STEEL collaborators. The Keysight decoder finds the baseline of the readout channel by calculating the average ADC before the trigger event time and subtracts it from the resultant waveform. Then, the RMS is calculated based on the standard deviation of the Gaussian fit to the waveform, as well as calculating the ADC amplitude and pulse width. The integral between the peak ADC and stopping point (where ADC returns to baseline) is calculated and saved as the induced/collected charge, and the waveform outside the pulse width defines the ADC baseline and RMS for that readout channel. Conversely, the pixel DAQ decoder circumvents pulse finding and calculates the pedestal ADC by taking the mean of a Gaussian fit to the waveform, removing points 3σ away from the mean.

A noise analysis was undertaken by Ala Zglam on the STEEL pixel anode, where the average noise RMS of each readout channel was determined. This involved fitting a Gaussian to the peak ADC of each channel waveform, then fitting another Gaussian to entries 5σ outside the first Gaussian and taking the standard deviation of the second Gaussian as the noise RMS of that pixel/ROI channel. This noise RMS was then converted to number of electrons using the shaping time of the LArASIC7 pre-amplifiers:

$$N_{\mathrm{ADC}/e^-} = \frac{25\ \mathrm{mV}}{1\ \mathrm{fC}} \cdot \frac{4096\ \mathrm{ADC}}{2000\ \mathrm{mV}} \cdot \frac{1.602 \times 10^{-4}\ \mathrm{fC}}{1\ e^-} = 0.008202\ \mathrm{ADC}/e^-, \tag{8.1}$$

where $2^{12} = 4096$ ADC is the number of ADC counts from the DAQ and 2000 mV is the peak-to-peak of the 12-bit DAQ. The number of electrons inducing signals corresponding to one ADC unit is given by the inverse of equation 8.1, computed as $N_{e\_/\mathrm{ADC}} = 121.9\ e^-/\mathrm{ADC}$. An estimation for the average signal-to-noise ratio of the system can be determined by calculating the expected number of electrons deposited into each pixel from a MIP travelling parallel to the pixel plane. This is given by

$$N_{e^-/\mathrm{MIP}} = 1.7 \times 10^6\ \mathrm{eV/cm} \cdot 0.254\ \mathrm{cm} \cdot \frac{1\ e^-}{23.6\ \mathrm{eV}} \cdot 0.68 = 12441.69\ e^-, \tag{8.2}$$

where 1.7×10^6 eV/cm is the typical energy deposited by a MIP in LAr, 0.254 cm is the width of each pixel, 23.6 eV is the ionisation energy of an argon atom and 0.68 is the recombination factor. This noise study found that the average RMS with the dewar circulating LAr for ROIs and pixels are 1.54 ± 0.19 ADC ($187 \pm 23\ e^-$) and 1.55 ± 0.11 ADC ($189 \pm 13\ e^-$) respectively [172]. Approximate signal-to-noise ratios of the ROIs and pixels are around 65 when operating with the dewar circulating LAr.

After performing a FFT on the pixel and ROI waveforms, multiple noise sources were detected at high frequencies. As such, a low pass filter was developed to remove signals with peaks corresponding to frequencies higher than 400 kHz, or if the amplitude is lower than 10 ADC. As such, an event is read out by the pixel DAQ if the ROI or pixel waveform amplitude exceeds 10 ADC and is at least five times the RMS of the waveform [172].

8.2 Commissioning of STEEL Subsystems

After construction of the detector was completed, work was undertaken testing each of its components and subsystems, ensuring the particle detection, argon purification and DAQ systems were fully operational. This was in preparation for eventually filling the dewar with LAr to collect continuous low-noise data, as well as maintaining sufficiently high LAr purity levels in the dewar for the entirety of a long data run.

8.2.1 Subsystem Voltage Calibrations

An important task before operating any of the STEEL subsystems is to optimise their applied voltage. Namely, the cold PMT and PMTs attached to the four CRTs. A higher voltage applied to a PMT results in a greater amplified current during the photomultiplication process, making cosmic-ray muon hits easier to detect and with higher resolution. This procedure involves ramping up the applied voltage using the CAEN V6521 [173], measuring

the current, then calculating the resistance using $V = IR$ and ensuring it is kept constant without the voltage/current breaking down, dropping to zero. Live PMT waveforms are viewed through an oscilloscope to check overall functionality.

The optimal operating voltages of the PMTs attached to the side CRTs were found to be 2000 V, with 433 μA current for the north-side CRT and 395 μA for the south-side CRT, breaking down at 2300 V. The PMTs attached to the top and bottom CRTs operated nominally at 1600 V, with 440 μA current measured for the top and 437 μA for the bottom, both breaking down at 1850 V. The nominal operating voltage of the cold PMT was found to be -1500 V, with a current of 42 μA, breaking down at -1750 V.

In order to optimise the electric field strength within the field cage, the cathode HV was also ramped up to test its nominal operating voltage without breaking down. The Cathode HV was maintained at 2000 V, breaking down at 2300 V, operating at a current of 4.87 μA. These tests were undertaken with an empty dewar, where the cathode HV has the capability for higher operating voltages in LAr. Later tests found that the cathode HV was able to gradually ramp up from 2500 V to 3500 V by the end of a long data with the dewar filled with LAr. These applied voltage settings were maintained throughout the data runs and led to high quality PMT and CRT data without breaking down.

8.2.2 CRT and PMT Coincidence Signal Triggering

The next commissioning task involved setting the logic trigger window in the Keysight DAQ such that the cold PMT and four CRTs can read out signals from the same cosmic-ray muon event. The first step was determining the mean time difference between muon signals induced on opposing CRTs. This involved connecting the side CRTs to the CAEN N417 discriminator unit, outputting an event if opposing CRTs recorded a hit within a set time window. Then, timestamps of the events were recorded and subtracted from one another and plotted into a histogram to find the average time difference between signals from the side CRTs. After filling the dewar with room temperature GAr, 1,000 coincident side CRT muon events were collected, triggering off of the CRTs and cold PMT (which was not technically cold in this case due to the argon being filled with room temperature GAr). The histogram of time differences between side CRT muon hits is shown in Figure 8.9.

Time differences between muon hits triggered on opposing CRTs approximately follows a Gaussian distribution. As such, a Gaussian was fit to the histogram in Figure 8.9, giving an average time difference of (-27.34±3.97) ns between the side CRTs. The top and bottom CRTs were also tested with the Gaussian fit giving a mean time difference of (-0.61 ± 10.99) ns. These time difference values are far below the 2 μs shaping time of the LArASIC7

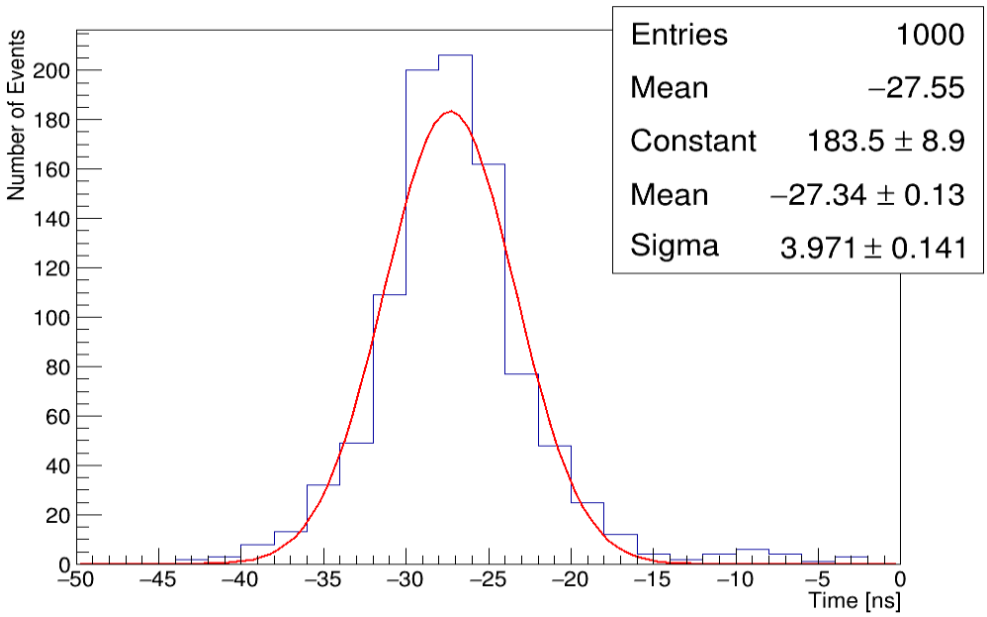

Figure 8.9: Time difference between side CRT hits from 1,000 cosmic-ray muon events with the STEEL dewar filled with room temperature GAr.

pixel readout and as such will not impact the quality of the pixel data, so these are deemed acceptable for triggering with the cold PMT.

Interfacing the CRTs with the cold PMT is achieved by connecting them both into the logic discriminator. Configuring the logic trigger time window involves lining up the waveforms of the CRTs and cold PMT for the same event in time and seeing the time difference between each signal peak. Figure 8.10 shows waveforms from a muon event inducing signals on the cold PMT and both side CRTs, and another muon event inducing signals on the top and bottom CRTs and the cold PMT.

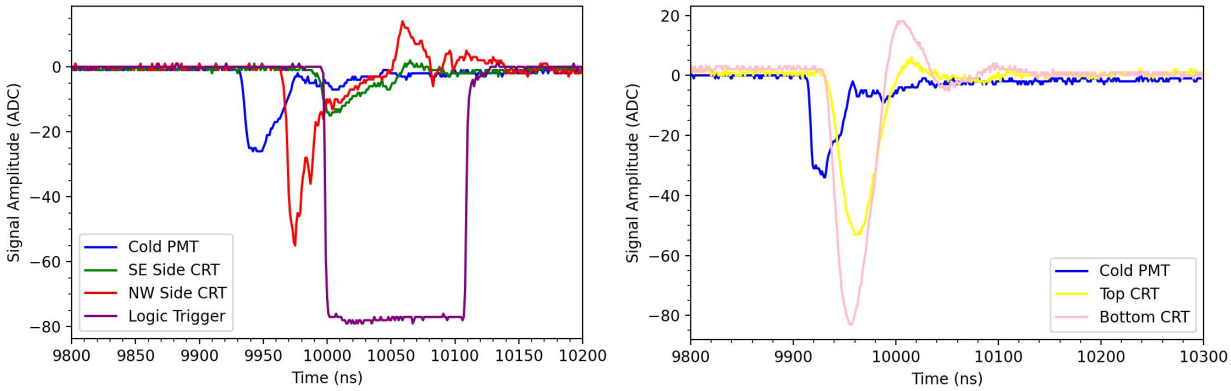

Figure 8.10: Two cosmic-ray muon events with one triggered in coincidence with the side CRTs and cold PMT (left) and the other triggering the top and bottom CRTs with the cold PMT (right). The logic trigger signal has a readout window set to 120 ns.

The muon event triggering on the side CRTs and cold PMT in Figure 8.10 exhibits a large PMT signal and a sufficiently wide logic trigger readout window of 120 ns. Only when two opposing CRTs and the cold PMT are hit does the logic readout window open, reading out signals for 20 μs (10 μs before and after the peak coincidence hit). Though the readout window for detecting coincidence hits between subsystems is only open for 120 ns. As long as each of the CRTs and cold PMT outputted a sufficiently large signal amplitude within the 120 ns readout window, the logic trigger window opens, and all data is read out.

Determining the threshold ADC signal amplitude value constituting a cold PMT hit over background noise was the next step of this commissioning task. Integrating the cold PMT into the logic trigger chain changes the frequency of muon events read out by the Keysight DAQ due to differences in the angular distribution of cosmic-ray muon tracks, since only a small fraction of muon tracks detected by both side CRTs fully traverse the field cage. Therefore, 9,000 cosmic-ray muon data events were collected triggering only on the side CRTs, but reading out cold PMT waveforms for each event in order to determine how many cosmic-ray muon tracks trigger on the cold PMT. The frequency of ADC amplitude values from cold PMT signals are presented in Figure 8.11.

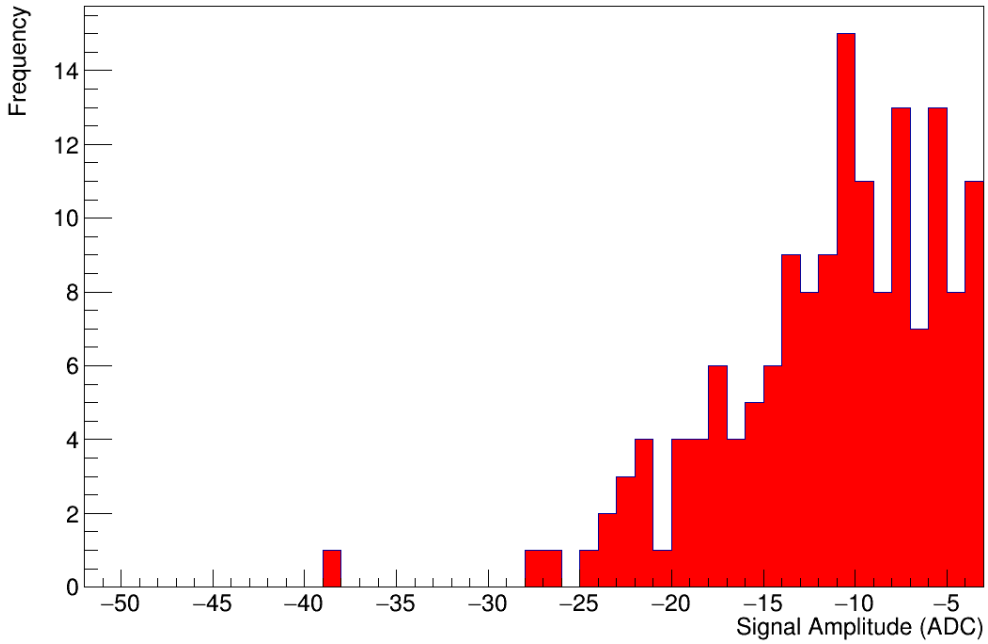

Figure 8.11: Frequency of PMT signal amplitude values fewer than or equal to -3 ADC, which contains 155 out of the 9,000 events in the dataset triggering only on the side CRTs.

Out of the 9,000 events in the dataset, only 155 exhibited a signal amplitude of -3 ADC or fewer (i.e. greater amplitude with negative polarity), giving the minimum ADC threshold constituting a cold PMT hit to be -3 ADC. This is consistent with the average

baseline noise of the PMT model being 2.5 ADC [176]. Despite the dewar being filled with GAr, this value is also applicable to when the dewar is filled with LAr, since scintillation light propagation is similar for GAr and LAr. The proportion of muon tracks traversing the field cage can be approximated to be ($155/9000 \approx$) 1.72%, or around one in every 58 events. This is of the same order of magnitude as the area overlaps of the field cage and one side CRT panel, which is around ($(10\text{ cm})^2/(50\text{ cm})^2 = 0.04 =$) 4%, or one in every 20 events, so the result is consistent with expectation. Therefore, it can be concluded that -3 ADC is a sensible minimum ADC threshold selection for the cold PMT.

8.2.3 LAr/LN Circulation Tests

After ensuring that each of the subsystems are operating nominally, testing how these systems operate when the dewar is filled with cryogenic LAr can commence, resulting from continuous circulation of GAr through the purification and condenser systems. Firstly, the dewar was gradually filled with GAr from a 40 L argon drum to around 82% capacity, cooling down to around 87 K with no LN in the condenser system. LAr pressure was constantly monitored during the filling process so it doesn't exceed 23 PSI, keeping the outlet valve open to alleviate pressure build-up.

Then, the outer coaxial cylinder of the condenser system was filled with LN from another 40 L nitrogen drum until it reached 90% capacity, dropping to 60% due to boil-off then automatically filling back up to 90% due to pressure-controlled valves (set to 30% in long data runs). It took approximately 7 minutes for the cylinder to fill from 60% to 90%, then another 35 minutes to naturally boil off from 90% back to 60% due to thermal contact with the circulating GAr. It is important to know the frequency of this cycle as it drives how often the 100 L nitrogen drum needs to be replaced during long data runs. The outer coaxial condenser cylinder is approximately 7.4 L in volume, taking around 42 minutes to empty and then fill 30% with LN from a 40 L drum suggests the drum will be depleted and need to be replaced in around 760 minutes, or 12 hours and 40 minutes. This is all while ensuring that the LN pressure does not exceed 60 PSI, stabilising at around 45 PSI.

When LN pressures stabilised, GAr continually circulated through the purification and condenser system until the argon liquid level reached 90% in the dewar and LAr pressure stabilised at around 20 PSI. All while data was taken from the top, bottom and side CRTs and the cold PMT to verify that a few coincidence events were being recorded every minute. After around 3 hours of circulation, the argon liquid level hit 95% and the LAr purity measured from the NI monitor was maintained at around 1 ppm, deeming the purification and condenser systems acceptable for use in long data collection runs. This eventually

led to a long data run being undertaken in the summer of 2023, lasting 22 days, amassing around 35,000 events with sufficiently high LAr purity maintained at approximately 1 ppm. More information on the physics analysis of this data is outlined in Chapter 9.

8.2.4 Pixel Signal Timing Calibrations

After integrating the CRTs and PMTs into the Keysight DAQ, this system can now be interfaced with the pixel DAQ through an additional logic trigger. The CAEN N417 discriminator is coded such that a pixel event is recorded through the CAEN V1740 when a coincidence signal is registered between two opposing CRTs and the cold PMT, recorded by the Keysight DAQ. However, unlike matching the CRT and PMT signals within the Keysight DAQ from the same muon track, matching Keysight DAQ events with pixel DAQ events corresponding to the same muon track incurs much greater time differences due to differing cable delays and data buffering that need to be understood and characterised.

This involved comparing the timestamps associated with the same muon event registered by the Keysight DAQ and pixel DAQ separately. Every event read out by the Keysight and pixel DAQ has two timestamps: a global UNIX timestamp of the second the event was registered since the UNIX Epoch on 1st January 1970 [187], and a nanosecond timestamp corresponding to the time of the signal peak after the global UNIX timestamp. Keysight DAQ event timestamps correspond to the time of the cold PMT peak signal. Keysight DAQ events always arrive before pixel DAQ events due to electron drift speeds in LAr towards the anode pixel plane being much slower than photon propagation towards the cold PMT, with pixel data being further delayed by the 2 μs shaping time of the LArASIC7 chips. In the 22-day data run, 36,264 pixel and 36,140 Keysight events were registered, giving an event rate of just over one muon track per minute. As such, the hard upper time limit for the same muon tracks being registered by the pixel and Keysight DAQs was set to 2 ms since it was extremely unlikely for two muon tracks to coincide within that time range, and for the signal delays between both DAQ systems to be any larger than 2 ms.

The overall difference in event number between the pixel and Keysight DAQs is a result of each readout mechanism having trigger and voltage settings that are optimised in isolation, and can cause some muon tracks that meet the pixel ADC threshold but not the CRT or cold PMT thresholds, and vice versa. However, for this study, there is a sufficient event number overlap between both DAQ systems to suggest that the subsystems are able to detect the same muon track. Every timestamp from the Keysight and pixel DAQ events in the 22-day data run were stored, and events with the same UNIX global second had the Keysight DAQ nanosecond timestamp subtracted from the pixel DAQ nanosecond

timestamp. Figure 8.12 shows the frequency of all time differences between Keysight and pixel DAQ events in bin widths of 10 μs.

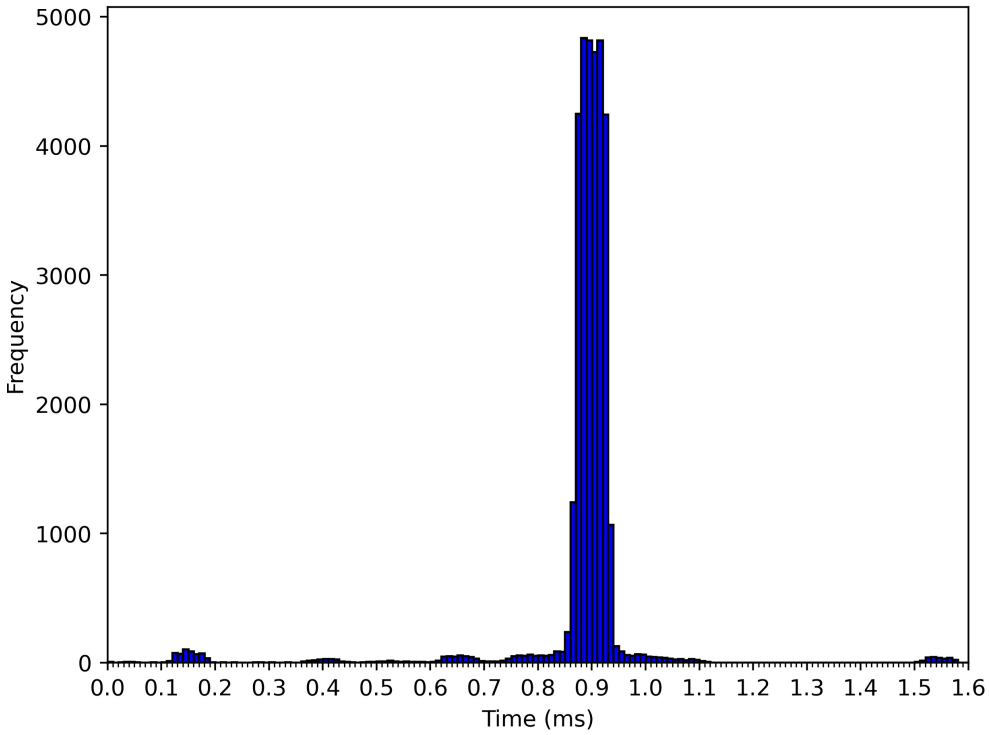

Figure 8.12: Difference between pixel and Keysight DAQ event timestamps for the same muon track. Bin widths are 10 μs with 33,120 overlapping events.

Figure 8.12 shows the most prolific time difference between Keysight DAQ and pixel DAQ events to be 0.9 ms. This peak has a standard deviation of 0.03 ms due to variations in time for differently angled muon tracks passing through the side CRTs and field cage. A total of 33,120 overlapping Keysight and pixel events fell within the 2 ms time window, giving a few thousand scattered events that exceed the 2 ms threshold, possibly due to residual particles inducing signals, unrelated to the muon track. Pixel events exhibiting a 0.9 ms time delay over Keysight DAQ events is most likely due to the greater signal processing time of the CAEN DAQ in building waveforms compared to the relatively simple Keysight DAQ. LArASIC7 preamplifier signals output 64 pixel and ROI readout channels compared to the six active channels in the Keysight DAQ. This delay is accounted and corrected for in data analysis when matching pixel events with CRT and cold PMT events.

For the majority of the 22-day data collecting run, the logic trigger was configured to read out data from the Keysight and pixel DAQs if a muon track was tagged by two of the opposing CRTs and the cold PMT. However, there were several sections of the run where the trigger settings were temporarily altered to investigate differences in data quality. One

such run used the Keysight DAQ to only trigger on the cold PMT, where another run used the internal LArASIC7 software to trigger only on the pixels. Timestamps for events triggered by the LArASIC7 pixel software in the Keysight and pixel DAQ were completely uncorrelated since the pixel DAQ only collects data if the Keysight DAQ is triggered, not vice versa. Figure 8.13 shows the frequency of time differences between pixel and Keysight DAQ events when triggering only on the cold PMT.

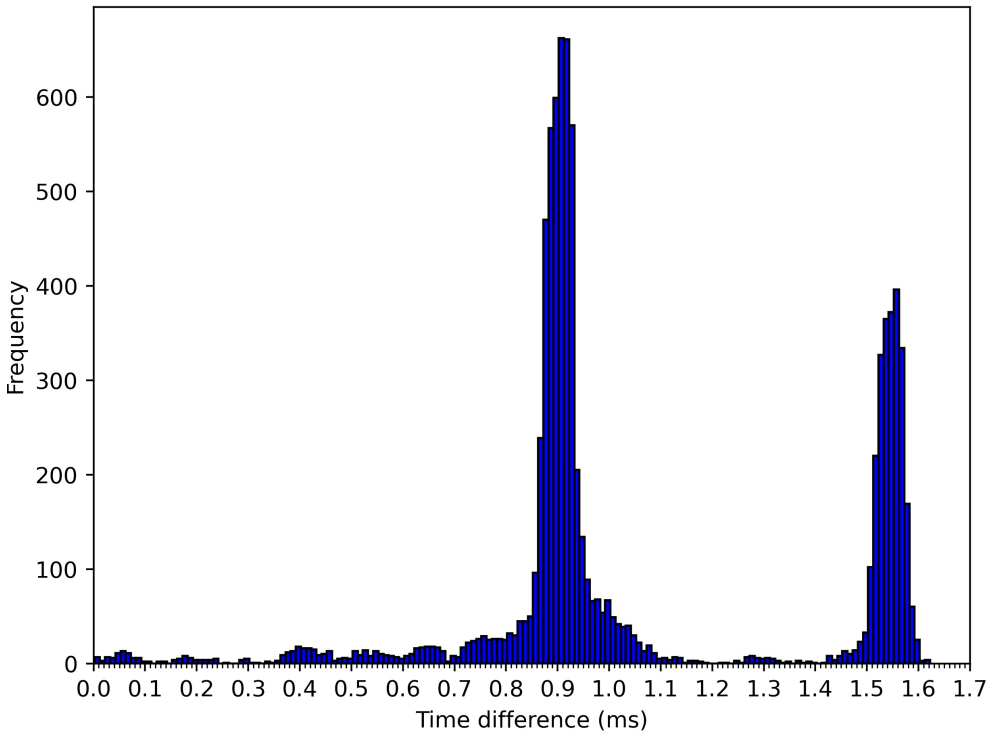

Figure 8.13: Difference between pixel and Keysight DAQ events timestamps for the same cold PMT triggered muon track. Bin widths are 10 µs with 8,339 overlapping events.

Figure 8.13 shows the expected 0.9 ms peak seen in Figure 8.12, with a slightly wider base due to lower statistics present in the cold PMT triggered dataset. The most prominent difference is the larger second peak between 1.5 ms and 1.6 ms., which explains the small cluster of time differences between 1.5 ms and 1.6 ms observed in Figure 8.12, suggesting it is an artefact of how the Keysight DAQ processes events triggered by the cold PMT. This will be accounted for in data analysis when using just cold PMT triggered muon events.

8.3 Conclusions

Presented in this chapter is the work done on commissioning tasks ensuring that each component and subsystem of STEEL is in optimal operating condition for a long data-

collection run. Finding the nominal applied voltage of each PMT attached to the four CRTs and the cold PMT was necessary to make sure muon hits are sufficiently amplified for current measurements. Calibrating the electric field strength within the field cage was achieved by stabilising the cathode HV to 2500–3500 V. The cold PMT and all four CRTs have a 120 ns logic window implemented across them to trigger on the same muon event in the Keysight DAQ. The Keysight DAQ is also interfaced with the pixel DAQ such that if a muon track is triggered by the Keysight DAQ, the pixel DAQ readout window is opened up to collect ionisation signals from said muon track, accounting for the (0.90 ± 0.03) ms time delay events processed by the pixel DAQ experience over the Keysight DAQ.

Successful LAr and LN circulation tests led to a 22-day data collection run of STEEL, amassing 36,264 pixel and 34,743 Keysight events with LAr purity levels measured to be consistently around 1 ppm. The first major data analysis task of STEEL, detailed in Chapter 9, involved measuring the ENI density over the course of the data run by measuring the triplet lifetime of scintillation pulses, compared with the same ENI density measurements calculated through determination of the electron lifetime from pixel data.

Chapter 9

Measurements of Electronegative Impurity Density in LAr at STEEL

Since the completion of the commissioning work on STEEL, and the success of the 22-day continuous data run of the experiment, work has been ongoing analysing the pixel, PMT and CRT data. This is all for the purposes of providing the groundworks for DUNE to implement a pixelated charge readout system in its GAr ND during Phase-II of running operations. Collaborators on STEEL have developed data analysis tools such as event displays showing pixel hits on the 2D pixel plane, or in 3D through electron drift time calculations, with full cosmic-ray muon track reconstruction capabilities.

This chapter presents work done tracking the purity of LAr in the STEEL dewar throughout the duration of the 22-day data run, ensuring that few ENI were present in the active LAr volume to minimise data loss. Section 9.1 outlines the theory behind estimating ENI density in LAr through measurements of the triplet lifetime of argon excimer decays and electron lifetime measurements. ENI density measurement results using cold PMT data from the Keysight DAQ are presented in Section 9.2. Section 9.3 shows the results for measuring electron lifetime using pixel data, leading to ENI density calculations. Finally, Section 9.4 contains general conclusions for the STEEL data analysis project.

9.1 Purity Tracking Through ENI Density Calculations

The quality of data outputted by LArTPC experiments is limited by the purity of the LAr, since ENI - such as O_2, N_2 or H_2O - present in the active LAr volume can absorb drifting ionisation electrons and scintillation photons before they can be read out by their respective detectors, quenching electron lifetime and scintillation light yield [92]. As such, LArTPCs

require sufficiently low ENI in LAr so the maximum possible number of ionisation electrons and scintillation photons can traverse the entire drift volume to have their respective signals read out at the edge of the field cage. Determining how many ionisation electrons or scintillation photons have been absorbed by ENI can lead to approximations of the ENI density in the LAr volume, the methodology of which is outlined in this section.

9.1.1 ENI Density Calculations Using Triplet Lifetime

When excited or ionised argon atoms reach an excimer state through equations 3.6 and 3.7 in Section 3.4, it exists in two singlet states, $^1\Sigma_u^+$ and $^1\Sigma_u^-$, and a triplet state, $^3\Sigma_u^+$. Parity conservation dictates that the $^1\Sigma_u^-$ state does not emit a photon, thus photon emission occurs through the ground state de-excitation transitions $^1\Sigma_u^+ \rightarrow {}^1\Sigma_g^+$, known as the fast component with time constant τ_1 in the nanosecond range; and $^3\Sigma_u^+ \rightarrow {}^1\Sigma_g^+$, known as the slow component with time constant τ_3 in the microsecond range [188]. De-excitation of the argon triplet excimer state by ENI occurs through the channel

$$\mathrm{Ar}_2^* \ + \ \mathrm{X}_2 \ \rightarrow \ 2\mathrm{Ar} \ + \ \mathrm{X}_2, \tag{9.1}$$

where Ar_2^* is the argon excimer state and X_2 is an ENI molecule (e.g. O_2, N_2 or H_2O). Ar_2^* excimers de-excite through equation 9.1 before they can emit photons, reducing scintillation light yield while ENI concentrations remain the same, resulting in a decreased effective τ_3 measurement. The measured value of τ_1 is mostly unaffected due to its rapid de-excitation. Therefore, determining the effective (measured) triplet lifetime τ_3' allows for an approximation of the ENI concentration in LAr. τ_3' can be ascertained by fitting a two component exponential excimer decay model, taking the form of a probability density function to the average scintillation pulse shape from a LArTPC data run, taking the form

$$f = Ae^{-\frac{t}{\tau_1'}} \ + \ Be^{-\frac{t}{\tau_3'}}. \tag{9.2}$$

From equation 9.2, A and B are constants and τ_1' and τ_3' are the measured fast (singlet) and slow (triplet) argon scintillation lifetimes respectively [189]. Literature reports that an additional intermediate time decay component τ_i might be required for the model to fit the scintillation pulse data, specifically for LAr singlet and triplet lifetime measurements [190], modifying equation 9.2 to the three component exponential decay model

$$f = Ae^{-\frac{t}{\tau_1'}} \ + \ Be^{-\frac{t}{\tau_3'}} + \ Ce^{-\frac{t}{\tau_i'}}, \tag{9.3}$$

where C is a constant. The rate at which scintillation light is quenched by ENI can be approximated as an exponential decrease in the density of argon excimer states present in LAr $[Ar_2^*]$ as a function of time t, following the equation

$$[Ar_2^*](t) = [Ar_2^*](t=0)e^{-k_X[X]t}, \tag{9.4}$$

where k_X is the quenching rate constant in ppm^{-1}, and [X] is the ENI density in ppm. The exponent in Equation 9.4 can be interpreted as an effective decrease in the measured triplet lifetime τ_3' from the theoretical maximum with zero impurities τ_3, related by

$$\frac{1}{\tau_3'} = \frac{1}{\tau_3} - k_X[X], \tag{9.5}$$

$$[X] = \frac{\tau_3 - \tau_3'}{\tau_3' k_X}. \tag{9.6}$$

k_X is a quantity unique to the impurity molecule in a substance, dependent on how rapidly the molecule de-excites excimers in the fluid, weakly dependent on the electric field strength of the TPC for fields $>$ 1 kV/cm (no dependence below this value) [120]. In the context of STEEL, the cathode voltage operated in the range of 2500–3500 V, with a TPC drift field length of 10 cm, giving an electric field of 0.25–0.35 kV/cm, so no change in k_X will be observed. STEEL is mostly concerned with oxygen contamination, which is reported by the WArP collaboration to have a quenching rate in LAr for electric fields $<$ 1 kV/cm of $k_{O_2} = (0.86 \pm 0.03)$ ppm^{-1} [191]. Measurements of the singlet and triplet decay constants with negligible ENI present in argon give their respective minimum values as $\tau_1 = (7.0 \pm 1.0)$ ns and $\tau_3 = (1.6 \pm 0.1)$ µs [159]. Literature also reports a measured value of the theorised intermediate lifetime to be $\tau_i = (50.3 \pm 6.4)$ ns [190].

9.1.2 ENI Density Calculations Using Electron Lifetime

Similarly to how scintillation light is absorbed by ENI in LAr, drifting ionisation electrons can also attach to ENI (X_2) through the process

$$e^- + X_2 \rightarrow X_2^{-*}, \tag{9.7}$$

where X_2^{-*} is the compound excited state of X_2. X_2^{-*} decays through one of three channels

$$X_2^{-*} \rightarrow X_2 + e^-, \tag{9.8}$$

$$X_2^{-*} \rightarrow X_2 + \gamma, \tag{9.9}$$

$$X_2^{-*} \rightarrow X^- + X. \tag{9.10}$$

Equation 9.8 describes auto-detachment, equation 9.9 shows a radiative decay to the ground state and equation 9.10 depicts dissociative fragmentation into stable negative and neutral atoms. For the types of ENI typically present in STEEL, de-excitation of X_2^{-*} typically occurs through equations 9.8 and equation 9.9 or a combination of the two. Assuming that the ionisation electron concentration is much smaller than the concentration of ENI (assumed to remain constant) where $[e] \ll [X_2]$, the rate at which the density of ionisation electrons are captured by ENI is given by

$$\frac{d[e]}{dt} = -k_e[X_2][e], \tag{9.11}$$

where k_e is the rate constant of electron attachment in LAr, which is weakly dependent on the electric field strength for $\epsilon > 1$ kV/cm [107]. Solving equation 9.11 for $[e]$ using the definition of electron lifetime τ_e gives

$$[e](t) = [e](t=0)e^{-k_e[X_2]t} = [e](t=0)e^{-\frac{t}{\tau_e}}, \tag{9.12}$$

$$\tau_e = \frac{1}{k_e[X]}, \tag{9.13}$$

which can be rearanged to give the ENI density in LAr with respect to measured τ_e as

$$[X_2] = \frac{1}{k_e\tau_e}. \tag{9.14}$$

For STEEL, the electron attachment rate for $X_2 = O_2$ in LAr has been calculated to be $k_e = 1.9$ ppm$^{-1}\mu$s^{-1} [192]. Determining τ_e at STEEL involves utilising a methodology adapted from the ICARUS T600 detector [92]. Both methodologies entail finding the relationship between the total measured charge ΔQ deposited on the anode plane and the calculated expected charge ΔQ_{exp} for each track, which are related by

$$\Delta Q = \Delta Q_{\text{exp}} e^{-\frac{t_d}{\tau_e}}, \tag{9.15}$$

where t_d is the drift time. So plotting $\Delta Q/\Delta Q_{\text{exp}}$ against drift distance d gives an exponential with τ_e determined as the inverse of the exponential decay constant of the fit multiplied by the electron drift speed v_e. Electron drift speed in STEEL was calculated based on a polynomial fit to known values of v_e (in cm/μs) with respect to a varying electric field

strength ϵ (in V/cm), following the equation determined by Ala Zglam [172]

$$v_e = 0.0154 + 5.09 \times 10^{-3}\epsilon - 3.95 \times 10^{-6}\epsilon^2. \tag{9.16}$$

Over the course of the 22-day data run of STEEL, the electric field strength gradually increased from 250 V/cm to 350 V/cm, resulting in an electron drift speed ranging from 0.104 cm/µs to 0.131 cm/µs. ΔQ_{exp} can be calculated using the relationship between the fractional energy loss of a MIP muon dE/dx and the number of electrons released from argon atoms per unit length dQ/dx, detailed in equation 3.1 in Section 3.4. Firstly, the muon track is reconstructed in 3D, finding the track length l, and assuming the number of electrons released is constant throughout length of the track, the total expected number of electrons collected by the anode readout plane (assuming no presence of ENI) is given by

$$\Delta Q_{\text{exp}} = \frac{R_B l}{W_{\text{LAr}}} \cdot \frac{dE}{dx}. \tag{9.17}$$

Using values of $W_{\text{LAr}} = (23.6 \pm 0.3)$ eV [108, 109], $dE/dx = 2.10$ MeV/cm, where $R_B = 0.619$–0.662 for an electric field strength range of $\epsilon = (0.25$–$0.35)$ kV/cm using the Birks recombination model, this gives the average number of electrons released by a MIP track per cm of track length to be in the range of $dQ/dx = (55,115$–$58,915)$ e^-/cm.

9.2 Results From Triplet Lifetime Measurements

Tracking ENI density in LAr over the 22-day data run of STEEL involved iteratively applying cold PMT data from 200 event decoded data files to the ENI density methodology outlined in Section 9.1.1. The analysis code extracts the cold PMT waveform from each event, calculates and subtracts the ADC baseline and saves the timestamp of the signal amplitude. All cold PMT waveforms are then aligned by the timestamp of their signal peak and averaged over the whole 200 event data file. This total average PMT waveform applied to a single 200 event Keysight DAQ data file is shown in Figure 9.1.

The total average waveform in Figure 9.1 is then inverted to be a positive peak in order to fit the two and three component exponential probability density functions in equations 9.2 and 9.3. Figure 9.2 shows the inverted average waveform with a log scale.

However, every cold PMT waveform was found to exhibit a consistent, low amplitude smaller pulse after the signal peak known as an afterpulse [193]. This was only visible when applying a log scale to the averaged waveform, such as between the 10400 ns and 10500 ns timestamps in Figure 9.2. Afterpulses are an intrinsic artefact of PMTs, and can either be

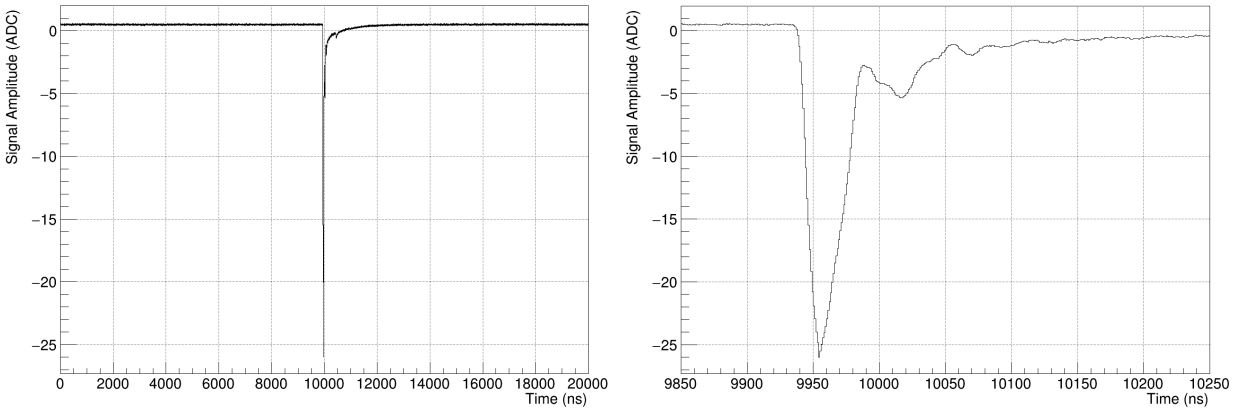

Figure 9.1: Average cold PMT waveform aligning 200 scintillation pulses by their peak timestamp and averaging their ADC value bin by bin. Plots show the full 20 μs readout window (left) and a narrower time axis about the average scintillation pulse (right).

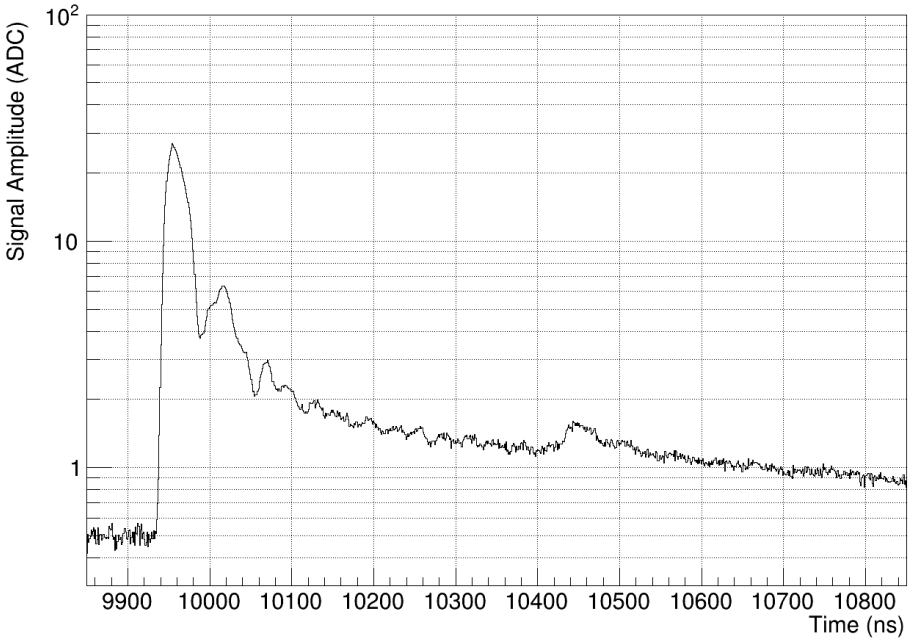

Figure 9.2: Average cold PMT waveform from Figure 9.1 inverted with a log scale.

short-delay pulses: occurring tens of nanoseconds after the signal peak, caused by electrons elastically scattering off of the first dynode; or long delay afterpulses which are due to the erroneous ionisation of residual argon atoms in the vicinity PMT [194].

Since these afterpulses are non-physical, affecting the goodness of exponential fits for triplet lifetime measurements, it is imperative to calibrate them out. A methodology was developed by the JUNO experiment [195] to do this, which was adapted by Hannah Burn for STEEL to remove these afterpulses in the average cold PMT waveforms, which is detailed in their Master's Dissertation [196]. After characterising and suppressing the afterpulse, the two and three component exponential probability density functions in equations 9.2 and 9.3 are fitted to the region of the inverted average scintillation pulse starting from the signal peak. This was applied to the inverted average waveform from Figure 9.2 representing one 200 event cold PMT data file, with the results of the fits shown in Figure 9.3.

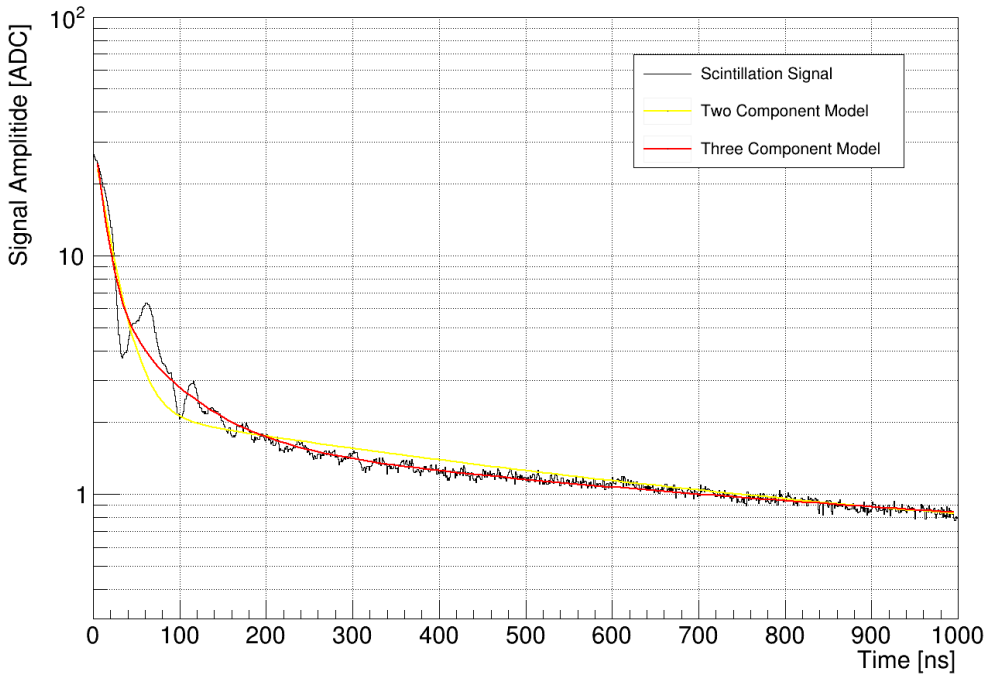

Figure 9.3: Inverted cold PMT waveform averaged over 200 events aligned by their signal peak, suppressing effects from PMT afterpulsing and with a log scale on the y-axis. The two and three component probability density functions in equations 9.2 and 9.3 respectively are fitted to the exponential decay to the right of the signal peak.

Figure 9.3 gives the best fit triplet lifetimes for the two and three component models to be $\tau'_{3,\text{two}} = (0.60 \pm 0.05)$ µs and $\tau'_{3,\text{three}} = (0.76 \pm 0.08)$ µs respectively. Substituting these values into the ENI density formula in equation 9.6 using $k_{\text{O}} = (0.86 \pm 0.03)$ ppm^{-1} [191] and $\tau_3 = (1.6 \pm 0.1)$ µs [159] gives the calculated ENI density to be $[\text{O}_2]_{\text{two}} = (1.95 \pm 0.34)$

ppm and $[O_2]_{\text{three}} = (1.27 \pm 0.30)$ ppm. Calculations of uncertainty propagation for the ENI density measurements are detailed in Appendix C.

Given that both the two and three component model fits give different triplet lifetime values, and therefore varying ENI density results, calculations of the chi-squared χ^2 divided by the number of Degrees Of Freedom (DOF) were applied to both models to determine which model fit the data better. χ^2 values for each graph are calculated using

$$\chi^2 = \sum_i \frac{(O_i - E_i)^2}{E_i}, \tag{9.18}$$

with the observed data O_i corresponding to the scintillation pulse and expected data E_i being the two or three component exponential decay model, summed over every time bin i for the entire fit. The number of DOF corresponds to the difference between the number of data points - equivalent to the number of bins in the scintillation pulse width - and the number of free parameters in the fit. The two component model in equation 9.2 has four free parameters (A, B, τ_1 and τ_3) and the three component model in equation 9.3 six free parameters (A, B, C, τ_1, τ_3 and τ_i), but since the number of data points typically ranges from 2000 to 6000 histogram bins, this difference in the number of DOF for each model is negligible. A lower χ^2/DOF value for each model means a better fit of the curve to the scintillation pulse, determining which model gives more reliable ENI density results.

For the 200 event sample in Figure 9.3, the two and three component χ^2/DOF values were calculated to be $\chi^2_{\text{two}}/\text{DOF} = 79.8/3314 = 0.0241$ and $\chi^2_{\text{three}}/\text{DOF} = 52.6/3312 = 0.0159$, making the three component model (with the intermediate component τ_i) a better fit to the scintillation pulse than the two component model. The three component exponential fit in equation 9.3 returns an intermediate lifetime value of $\tau_i = (68 \pm 15)$ ns, which is within 2σ of the measured value of $\tau_i = (50.3 \pm 6.4)$ ns reported by a 4-tonne DP demonstrator for ProtoDUNE [190]. However, this conclusion cannot be made until the χ^2/DOF values for two and three component models are compared over the whole dataset.

This process was repeated for every decoded Keysight DAQ file in the 22-day data run of STEEL. This consisted of 188 files of ∼200 events each, resulting in 36,140 cold PMT events triggering on itself and the top/bottom or side CRTs. In the final 12 hours of the 22-day data run, two six hour periods of data-collecting triggering only on the cold PMT and then pixel software were undertaken. This resulted in an additional 49 cold PMT triggered data files consisting of 10,600 events, and six data files triggering on the internal pixel LArASIC7 software containing 5,233 events (with each file containing around 1,000 events). Since the only requirement for measuring τ_3 is that sufficient scintillation light is

collected by the cold PMT, full track reconstruction is not required for this study and the alternatively triggered data runs can be used to measure τ_3 and determine ENI density.

Tracking the LAr purity over the course of the data run involved plotting the measured triplet lifetime and calculated ENI density values as a function of the time that each file started filling with data. With a total of 243 triplet lifetime and ENI density values, daily average triplet lifetime and ENI densities were calculated and plotted against time, shown in Figures 9.4 and 9.5 respectively. Furthermore, a summary table of the averaged results fitting the exponential models to the scintillation pulse are presented in Table 9.1.

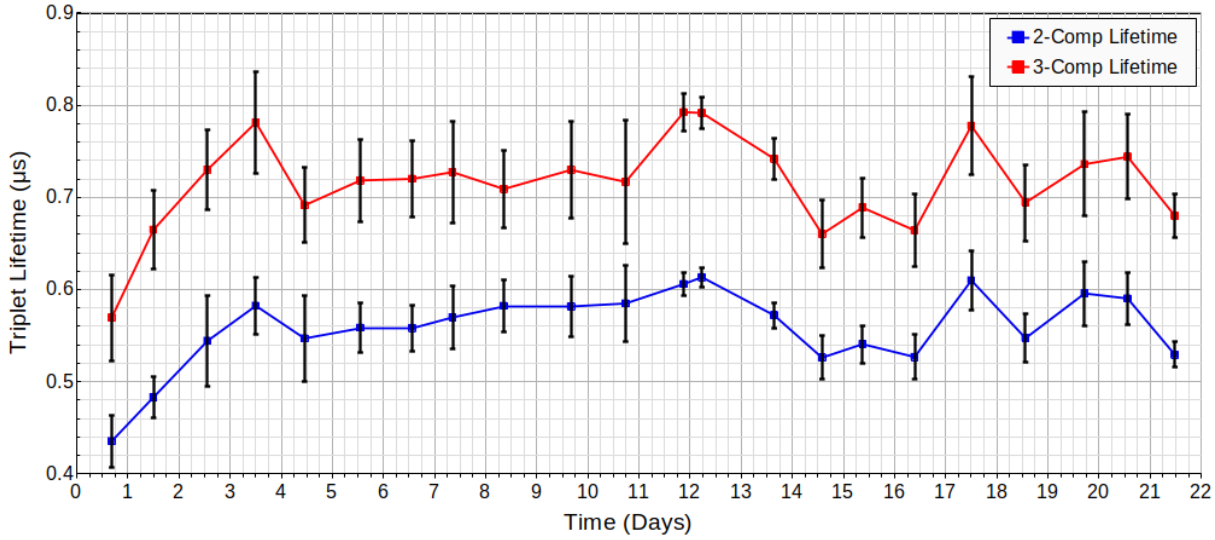

Figure 9.4: Daily average measured triplet lifetime τ_3' as a function of time since the start of the 22-day data run of STEEL. τ_3' was measured from fitting the two and three component exponential functions in equations 9.2 and 9.3 to averaged scintillation pulses from ∼200 events. The full unaveraged graph is in Figure D.1 in Appendix D.

Full unaveraged τ_3 and $[O_2]$ values over the 22-day data run are presented in Figures D.1 and D.2 respectively in Appendix D. The total average two-component triplet lifetime was determined to be $\tau_{3,\text{two}} = (0.556 \pm 0.006)$ µs, with the three component total average being $\tau_{3,\text{three}} = (0.715 \pm 0.009)$ µs. Substituting these values into equation 9.6 gives the calculated average oxygen impurity densities for the two and three component models as $[O_2]_{\text{two}} = (2.18 \pm 0.23)$ ppm and $[O_2]_{\text{three}} = (1.44 \pm 0.17)$ ppm. These results are similar to the total average two and three component ENI densities calculated from Figure 9.5, which are $[O_2]_{\text{two}} = (2.22 \pm 0.04)$ ppm and $[O_2]_{\text{three}} = (1.48 \pm 0.04)$ ppm respectively.

The singlet lifetime τ_1 was also measured for the two and three component model fitting, returning average values over the 22-day data run to be $\tau_{1,\text{two}} = (18.6 \pm 1.2)$ ns and $\tau_{1,\text{three}} = (12.4 \pm 0.8)$ ns respectively. These are much greater than the reported value in literature as

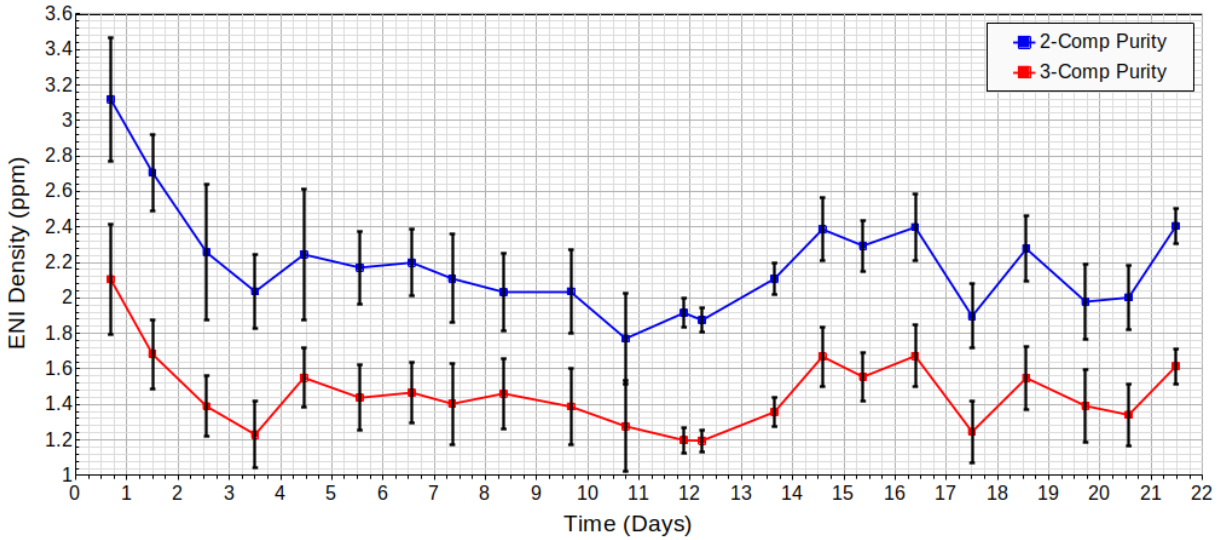

Figure 9.5: Daily average oxygen impurity density ($[O_2]$) as a function of time since the start of the 22-day data run of STEEL. $[O_2]$ was calculated from equation 9.6 using $k_O = (0.86 \pm 0.03)$ ppm^{-1} [191] and $\tau_3 = (1.6 \pm 0.1)$ µs [159]. Uncertainty propagations are detailed in Appendix C. The full unaveraged graph is in Figure D.2 in Appendix D.

Table 9.1: Total average excimer decay lifetime values τ_1, τ_3 and τ_i, oxygen impurity density $[O_2]$ and χ^2/DOF values for the two and three component exponentials in equations 9.2 and 9.3 fitted to 243 scintillation data files containing ~200 events each throughout the 22-day data run of STEEL. Uncertainties on the average χ^2/DOF values are the standard error of the statistical average of individual χ^2/DOF values.

	Two Component Model Fit	Three Component Model Fit
Singlet Lifetime, τ_1	(18.6 ± 1.2) ns	(12.4 ± 0.8) ns
Triplet Lifetime, τ_3	(0.556 ± 0.006) µs	(0.715 ± 0.009) µs
Intermediate Lifetime, τ_i	N/A	(69.6 ± 4.5) ns
Oxygen Impurity Density, $[O_2]$	(2.22 ± 0.04) ppm	(1.48 ± 0.04) ppm
χ^2/DOF of Fit	$(13.8 \pm 0.5) \times 10^{-3}$	$(9.98 \pm 0.31) \times 10^{-3}$

$\tau_1 = (7 \pm 1)$ ns [159], though the three component fit seems to be closer with a more precise fit. The intermediate lifetime τ_i was measured just from the three component fit, giving an average value across the entire run of $\tau_i = (69.6 \pm 4.5)$ ns. This value is also much higher than the value measured by the WArP collaboration of $\tau_i = (50.3 \pm 6.4)$ ns [190], though the presence of ENI in STEEL might have affected the individual τ_i measurements.

Determining whether the two or three component model results are most applicable to the data, the χ^2/DOF calculations for every exponential fit are compared. The average two component value was calculated to be $\chi^2_{\text{two}}/\text{DOF} = (13.8 \pm 0.5) \times 10^{-3}$, and the average three component value $\chi^2_{\text{three}}/\text{DOF} = (9.98 \pm 0.31) \times 10^{-3}$. Uncertainties were calculated to be the standard error of the statistical average of all individual χ^2/DOF values. Throughout the entire dataset, the three component model had a consistently lower χ^2/DOF value than the two component model, leading to the conclusion that the ENI results determined using the three component model are more applicable to the data than the two component model.

An average measured three component O_2 impurity density of (1.48 ± 0.04) ppm corresponds to an average expected electron lifetime - calculated using equation 9.14 with $k_e = 1.9$ ppm$^{-1}\mu$s^{-1} - of $\tau_e = (0.36 \pm 0.01)$ µs. This value will be compared with the electron lifetime measurements determined using pixel data, where ENI density is tracked as a function of time over the course of the 22-day data run of STEEL.

9.3 Results From Electron Lifetime Measurements

The ENI density determination procedure outlined in Section 9.1.2 was applied to every pixel file in the 22-day data run to track LAr purity. After running the noise filter on pixel files, data from all 28 ROI and 36 pixel channels are extracted for each event, containing ROI/pixel waveforms and channel IDs, ADC amplitudes and timestamps of the waveform peaks. Signal peaks are identified by finding the time of all local maxima and designating it a signal peak if the ADC amplitude exceeds five times the RMS of the waveform.

When a pixel channel outputs a signal waveform, one of the 28 pixels sharing the same relative position inside each 6×6 grid actually collected the ionisation charge(s) that produced said waveform. Given that each 6×6 grid is surrounded by an ROI inducing signals from ionisation electrons passing through them, the pixel associated with that waveform is determined by lining up the pixel waveform in time with all ROI waveforms, matching the hit pixel ID to a given ROI ID when their waveforms overlap.

Sometimes a pixel channel waveform lines up with more than one ROI due to LArASIC7 firmware misidentifications. In this case, a χ^2 value is calculated using equation 9.18 with

the signal region of the ROI waveform as the expected data E_i and the signal region of each pixel waveform as the observed data O_i. Number of DOF should be the same for each χ^2 calculation since the expected data (i.e. the ROI waveform) is the same for each pixel waveform. The pixel waveform with the lowest χ^2 value has its ID matched with the ROI ID for that event. Figure 9.6 shows matched pixel and ROI waveforms.

Figure 9.6: Pixel and ROI waveforms corresponding to the same ionisation electron signal on pixel 12 in ROI 14. Hits were matched by lining up the waveforms in time and finding the pixel waveform with the lowest χ^2 value compared to the ROI waveform.

The pixel and ROI waveforms in Figure 9.6 show the expected bipolar waveform shape, where the initially negative peak is due to long-range negative induction from ionisation electrons on the ROI and pixels, until the ionisation electron reaches the pixel anode plane at the zero-point of the waveform and is collected by the pixel, resulting in a positive peak. ROI and pixel waveform amplitudes vary due to the electron's vicinity to the ROI boundary as it crosses the anode, and amount of charge collected by the pixels respectively.

All pixels are assigned x and y coordinates in a 2D space based on the combination of pixel and ROI IDs on the anode pixel plane. This 2D space is then projected into 3D through calculation of the z-coordinate corresponding to drift distance from the anode. The z coordinate is determined from $d = v_e t_d$, where v_e is the electron drift velocity calculated from equation 9.16 and t_d is the electron drift time. t_d is measured as the difference between the peak times of the pixel and scintillation waveforms associated with that event.

The initial muon track is reconstructed by fitting a straight line to the hit pixels in the 3D space. This is done by projecting the pixel coordinates into a single array, then fitting a straight line to the data points, truncating it such that the track is entirely within the field cage: a 10 cm tall, 10 cm diameter cylinder. Then, the length of the line is measured as the theoretical track length l, which is used to calculate the expected number of electrons released from this track ΔQ_{exp} from equation 9.17.

Next, the actual charge collected by the pixels from the track ΔQ is calculated. Firstly, the area of each pixel waveform corresponding to an ionisation electron signal is identified, spanning the bipolar area around the positive and negative peak time. In Figure 9.6, the signal area of the pixel waveform spans approximately 14650 – 14680 ns. ΔQ is then calculated as the integral of the waveform spanning this region, using a positive value for the negative region. This is then converted to a total number of electrons deposited on the pixel by multiplying the integral by the number of electrons corresponding to one ADC value, $N_{e^-/\text{ADC}} = 121.9\ e^-/\text{ADC}$, calculated from equation 8.1 in Section 8.1.4. All ΔQ values for each pixel in the event is then added up, resulting in the total number of electrons received by the pixels from that reconstructed track.

Then, the ratio of the measured charge to expected charge $\Delta Q/\Delta Q_{\text{exp}}$ is calculated for each event, ensuring that there is never more measured charge than expected charge such that $0 < \Delta Q/\Delta Q_{\text{exp}} < 1$, if this is somehow not found to be the case, the data point is discarded. Plotting $\Delta Q/\Delta Q_{\text{exp}}$ against track length l should give an exponential decay akin to equation 9.15, so a single component exponential decay model is fitted to the distribution. From this, the electron lifetime is calculated as the inverse of the decay constant multiplied by v_e [92]. ENI density is then determined from equation 9.14 using $k_e = 1.9\ \text{ppm}^{-1}\mu\text{s}^{-1}$ [192]. Figure 9.7 shows the charge ratio against track length plot from a single 100 event pixel data file with fitted exponential decay.

The exponential fit in Figure 9.7 leads to a calculated electron lifetime value of $\tau_e = (0.55 \pm 0.09)\ \mu\text{s}$, corresponding to a measured oxygen impurity density of $[\text{O}_2]_e = (0.93 \pm 0.14)$ ppm for that pixel data file of 100 events. This methodology was repeated for every single pixel file in the 22-day data run, each containing around 100 events, to track the oxygen impurity density of STEEL over time. The pixel data consisted of 373 files triggering on the cold PMT and the top/bottom or side CRTs with 36,167 events in total; 333 files triggering only on the cold PMT, containing 37,441 events; and 102 files triggering only on the LArASIC7 pixel software for 10,200 events. Though the latter two trigger modes only applied to the last 12 hours of the run, they still resulted in a total of 808 pixel files containing 83,808 pixel events across the whole 22-day data run.

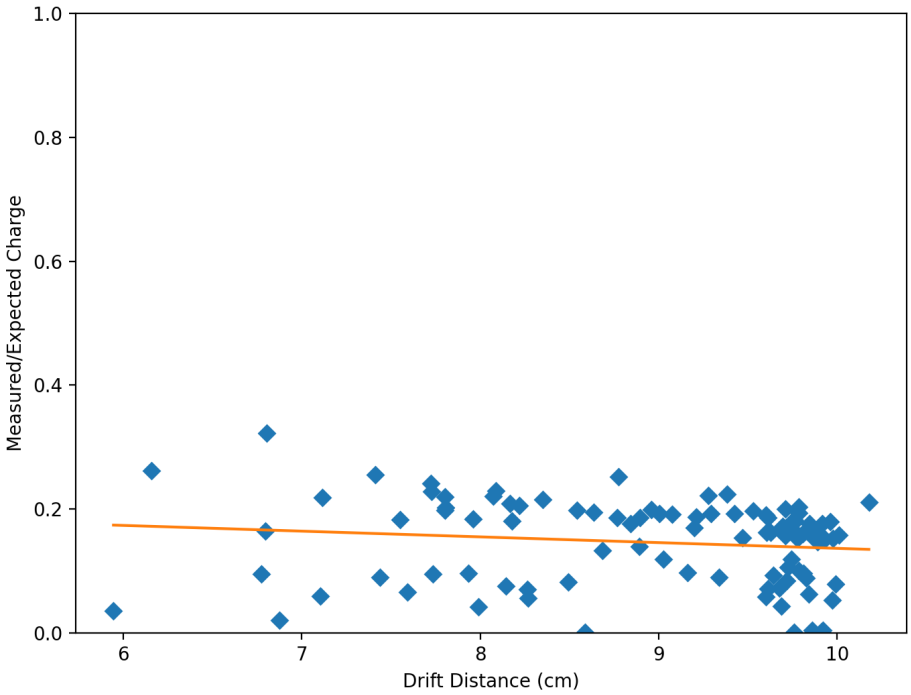

Figure 9.7: Ratio of the measured charge over the expected charge $\Delta Q/\Delta Q_{\text{exp}}$ collected by all pixels of a single reconstructed muon track for 100 pixel events, plotted against track length l. An exponential decay is fitted with the decay constant equal to $1/(\tau_e v_e)$.

However, many of the exponential fits to the charge ratio over track length plots returned anomalously high or low electron lifetime values, which was due to multiple factors. This was primarily due to difficulties fitting the exponential to charge ratio plots as the data points are widely scattered. Additionally, the peak finding algorithms sometimes misidentified pixel peaks, misattributing them to different ROI IDs, which was exacerbated by a number of noisy pixels particularly at the edge of the waveforms. Anomalous electron lifetime values were discarded, and these issues will be remedied for the next data run of STEEL. But for now, enough electron lifetime values were measured to produce plots of electron lifetime and oxygen impurity density over the course of the 22-day data run. Daily average τ_e and $[O_2]_e$ values are shown in Figures 9.8 and 9.9 respectively.

Full unaveraged τ_e and $[O_2]_e$ values over the 22-day data run are shown in Figures D.3 and D.4 in Appendix D. Figure 9.9 returns a total average oxygen impurity density of $[O_2]_e = (1.42 \pm 0.01)$ ppm, which is $< 2\sigma$ away from the average oxygen impurity density determined from the triplet lifetime measurements using scintillation pulse data: $[O_2]_\gamma = (1.48 \pm 0.04)$ ppm. Though the methodologies and datasets are entirely distinct, these two results are measuring the same physical quantity, so it owes to the success of STEEL that similar results are attained. However, Figure 9.8 gives a total average measured

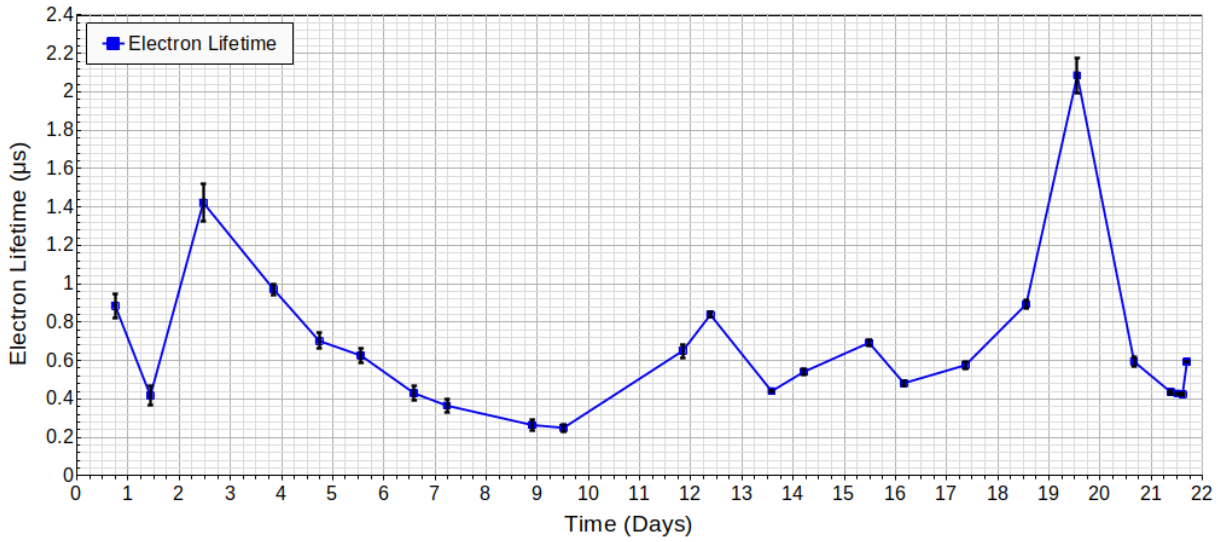

Figure 9.8: Daily average electron lifetime τ_e values as a function of time since the start of the 22-day data run of STEEL. τ_e was calculated from finding the exponential decay constant of the measured to expected charge ratio against track length from ∼100 pixel events each. The full unaveraged graph is in Figure D.3 in Appendix D.

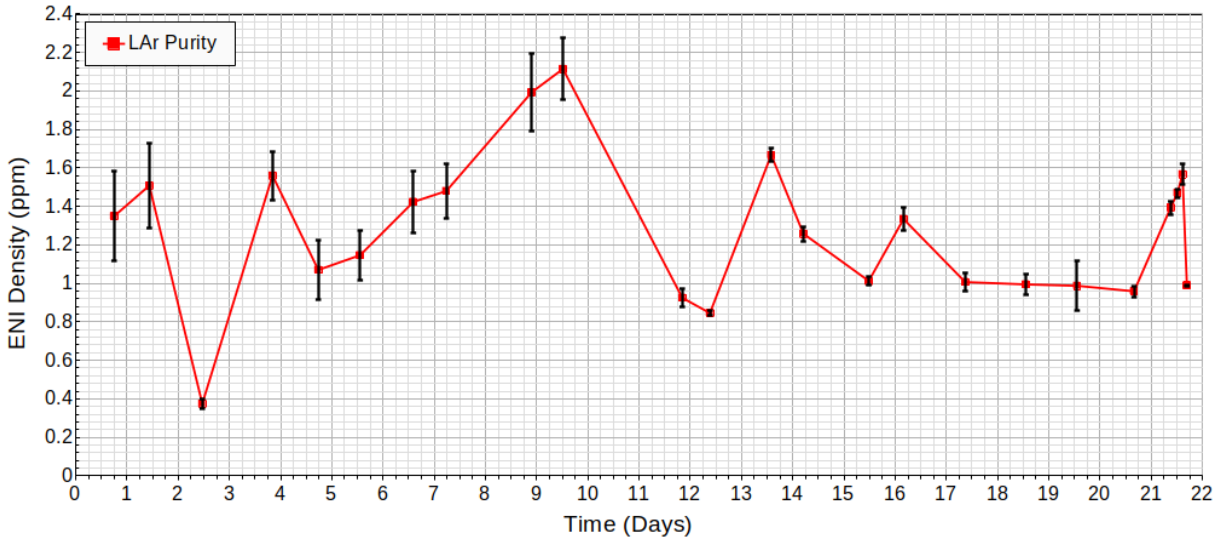

Figure 9.9: Daily average oxygen impurity density $[O_2]_e$ as a function of time since the start of the 22-day data run of STEEL. $[O_2]$ was calculated from equation 9.14 using $k_e = 1.9$ ppm^{-1}μs^{-1} [192]. The full unaveraged graph is in Figure D.4 in Appendix D.

electron lifetime value of $\tau_e = (0.491 \pm 0.003)$ µs, which differs greatly from the equivalent electron lifetime value $\tau_e = (0.36 \pm 0.01)$ µs calculated from the average triplet lifetime-determined $[O_2]_\gamma$ from cold PMT data in Section 9.1.1. This suggests that uncertainties for individual measurements are estimated incorrectly and need to be verified.

9.4 Conclusions

This concludes the first major data analysis task applied to STEEL data, determining the ENI density throughout the duration of the 22-day data run from measurements of the argon excimer triplet lifetime τ_3 using cold PMT data and electron lifetime τ_e using pixel data. Averaging τ_3 measurements and corresponding $[O_2]$ calculations from cold PMT data over the course of the 22-day data run returned $\tau_3 = (0.715 \pm 0.009)$ µs and $[O_2] = (1.48 \pm 0.04)$ ppm. Additionally, averages of the singlet and intermediate excimer decay lifetimes were calculated to be $\tau_1 = (12.4 \pm 0.8)$ ns and $\tau_i = (69.6 \pm 4.5)$ ns. A χ^2/DOF analysis of the two and three component exponential fits to scintillation pulses determined the three component model to fit the data better than the two component model.

Determination of τ_e and therefore $[O_2]$ using pixel data resulted in total average values of $\tau_e = (0.491 \pm 0.006)$ µs and $[O_2] = (1.42 \pm 0.01)$ ppm across the entire 22-day data run. The total average $[O_2]$ calculated using τ_3 measurements from cold PMT data was determined to be within 2σ of the same value calculated from τ_e measurements using pixel data. This marked the first data analysis task of STEEL a success, showing similar results using entirely different methodologies and datasets. Though improvements need to be made in estimating systematic uncertainties in the individual τ_e measurements for each data file.

Current and future work on STEEL involves optimising the hit-finding and track reconstruction algorithms, and taking an additional long data run for further data analysis. Eventually, the pixelated anode will be replaced with wire planes in order to directly compare track reconstruction capabilities of both charge readout mechanisms. This is all in efforts to provide the groundworks for DUNE ND-GAr using pixelated charge readout during Phase-II of its running operation.

Chapter 10

Conclusions

Presented in this thesis are major developments in calibrating the detector response of CRT events and TPC readout waveforms in SBND, and cosmic-ray muon events from pixelated charge readout in STEEL. These efforts are integral in optimising the neutrino reconstruction capabilities of SBND, and providing the groundworks for the use of a pixelated anode in future LArTPCs such as the DUNE ND, respectively. At the end of its first major data collection run in 2027, SBND will have amassed approximately 7 million ν_μ and 50 thousand ν_e events, the largest number of ν_μ and ν_e interactions of any accelerator neutrino detector in history. This allows SBND to perform the highest precision neutrino-argon cross-section measurements ever recorded, as well as search for rare particle interactions and decays. After SBND combines its BNB neutrino dataset with ICARUS, the SBN program will undertake a joint oscillation analysis, unequivocally determining whether previously measured neutrino oscillation anomalies are due to sterile neutrino mixing.

In pursuit of SBND optimising its particle reconstruction resolution, Chapter 5 detailed work done calibrating the timing precision of CRTs tracking muons passing through the detector. SBND requires ≤ 2 ns timing precision on all tagged muons, the same as neutrino interactions reconstructed in the TPC, in order to fully mitigate cosmic-ray backgrounds. A timing characterisation methodology was developed and applied to 18 FEBs attached to CRT modules before their installation on the north wall of SBND, with this methodology eventually being applied to all CRTs around SBND. Long data runs of CRTs in-situ on their A-frames were undertaken, plotting histograms of the timestamps corresponding to when T_0 and T_1 reset signals were received by each FEB, subtracting the respective reset windows to centre the distributions around zero seconds. Results showed that most of the CRTs exhibited T_0 timing drifts deviating up to 4 ns, which can be trivially subtracted from the data to achieve zero drift, and reasonable resolutions around 1–3 ns. However, T_1

timing drifts deviated around 20 ns and 40 ns on A-frames 1 and 2 respectively. Timing resolution for A-frame 1 FEBs fell within the acceptable range of 2 ns, but A-frame 2 FEBs exhibited up to 7 ns resolution, requiring repeated tests after CRTs are installed on the north wall, and in some cases FEB hardware corrections. At this point in time, all 146 CRTs have been installed around SBND and are continually outputting cosmic-ray muon data with timing resolutions of ≤ 2 ns for optimal cosmic-ray background removal.

Chapters 6 and 7 contained a completed three-step procedure verifying whether the SBND simulation correctly models the appropriate amount of TPC waveform smearing due to the field response. This was integral in ensuring that signals induced by ionisation electrons are accurately deconvolved from the total wire response, maximising charged particle reconstruction precision and neutrino flavour identification accuracy. The first step involved simulating 200,000 MC anode-cathode crossing cosmic-ray muons tracks, reconstructing the average TPC waveforms induced on all three wire planes. This was then compared with the expected total wire response modelled from field response functions calculated by Garfield, convolved with the parametrised electronics response and a Gaussian accounting for signal variations due to differently angled tracks. Step two repeated this methodology substituting MC event samples with SBND data, with Step three consisting of a MC versus data comparison of average reconstructed TPC waveform shape.

Comparisons between MC and data waveforms with the expected detector response both showed overall agreement, with disparities corresponding to tracks with $\theta_{xz} > 60°$ for the induction plane and $\theta_{xz} > 70°$ for the collection plane, suggesting that the Garfield field response function modelling algorithms need to be corrected for tracks with high θ_{xz}. Deficits in positive peaks of induction plane waveforms from MC events indicated that the SBND simulation exhibited unoptimised electron lifetime or wire transparency models. The latter conclusion was supported by comparing average waveforms from SBND data runs implementing different wire bias voltages in first induction and collection plane wires from nominal values of -210 V and 420 V respectively. This showed that intransparency was observed on induction plane wires, motivating the need for an increased collection plane bias voltage to mitigate this phenomenon, which has now been increased to 600 V in SBND.

Deficits in MC and data waveforms were also observed to the right of the collection plane peak, indicating that the electronics response was being incorrectly modelled in the SBND simulation. Overall, MC waveforms lined up well with data waveforms, with the former exhibiting slight broadening due to an unoptimised noise model in SBND software. Since the completion of this work, electronics response and noise model calibration and optimisation studies have been undertaken using SBND data. The field response validation

methodology has since been repeated, where the only disparities in MC and data waveform shape with respect to the expected total wire response were due to inaccuracies in the field response function modelling algorithms used by the 2D Garfield simulation, the results of which will be presented in an upcoming SBND calibration paper.

Technological advancement of an alternative charge readout mechanism to projective wire planes, an array of pixels, was undertaken through detector commissioning and data analysis of the University of Sheffield LAr test-stand, STEEL, in Chapters 8 and 9 respectively. Essential commissioning tasks included optimisation of subsystem operating voltage, LAr/LN circulation tests and trigger readout calibration for interfacing of CRT and cold PMT data with the pixel data. The completion of these tasks led to a 22-day continuous data run of STEEL, collecting pixel data with sufficiently low LAr impurity of around 1 ppm, measured through live data monitoring instruments.

The first physics analysis task of STEEL was to verify this LAr purity through ENI density calculations using scintillation triplet lifetime τ_3 measured from cold PMT data and electron lifetime τ_e determined from pixel data. Two and three component exponential decay models were fit to cold PMT waveforms, averaged over 200 events, where the singlet τ_1, triplet τ_3 and (for the three component model) intermediate τ_i lifetimes were extracted, calculating the oxygen impurity density $[O_2]_\gamma$ using τ_3. Total average results over the course of the 22-day data run gave $\tau_3 = (0.715 \pm 0.009)$ µs and $[O_2]_\gamma = (1.48 \pm 0.04)$ ppm, with $\tau_1 = (12.4 \pm 0.8)$ ns and $\tau_i = (69.6 \pm 4.5)$ ns, where a chi-squared analysis concluded that the three component model fit the data better than the two component model.

Determining τ_e using pixel data involved plotting the ratio of the total charge collected by pixels and the theoretical charge released from each track against track length, for 100 tracks per data file, fitting an exponential with τ_e related to the decay constant, then calculating $[O_2]_e$ using τ_e. Averaging measured τ_e and $[O_2]_e$ over the 22-day data run yielded $\tau_e = (0.491 \pm 0.006)$ µs and $[O_2]_e = (1.48 \pm 0.04)$ ppm. The fact that $[O_2]_\gamma$ and $[O_2]_e$ are so similar despite being calculated through distinct datasets and methodologies owes to the success of this analysis. The future of STEEL aims to improve hit-finding and track reconstruction code, validating them with another long data run. This is in service of STEEL's eventual goal of directly comparing track reconstruction capabilities between pixelated charge readout and wire planes used in most LArTPCs, as well as providing the software foundations for the Phase-II run of DUNE ND-GAr using pixels to read out charge.

Bibliography

[1] H. Becquerel, On the rays emitted by phosphorescence, Compt. Rend. Hebd. Seances Acad. Sci. **122**, 420 (1896).

[2] E. Rutherford, Radioactive Processes, Proceedings of the Physical Society of London **18**, 595 (1903).

[3] O. Hahn, L. Meitner, and O. von Baeyer, Uber die β-strahlen des aktivien niederschlags des thoriums, Physikalische Zeitschrift **12**, 273 (1911).

[4] J. Danysz, Sur les rayons β des radiums B, C, D, E, Le Radium **10**, 4 (1913).

[5] W. E. F. Pauli, Open letter to radioactive persons, Technical report, 1930.

[6] E. Fermi, Trends to a Theory of beta Radiation. (In Italian), Nuovo Cim. **11**, 1 (1934), [,535(1934)].

[7] F. Reines and C. L. Cowan, The neutrino, MacMillan & Company, 1956.

[8] E. J. Konopinski and H. M. Mahmoud, The Universal Fermi Interaction, Phys. Rev. **92**, 1045 (1953).

[9] M. L. Perl et al., Evidence for anomalous lepton production in e+- e- annihilation, Physical Review Letters **35**, 1489 (1975).

[10] G. Danby et al., Observation of High-Energy Neutrino Reactions and the Existence of Two Kinds of Neutrinos, Phys. Rev. Lett. **9**, 36 (1962).

[11] P. W. Higgs, Broken Symmetries and the Masses of Gauge Bosons, Phys. Rev. Lett. **13**, 508 (1964).

[12] V. Avati et al., Cosmic multi-muon events observed in the underground CERN-LEP tunnel with the ALEPH experiment, Astroparticle Physics **19**, 513 (2003).

[13] P. A. Aarnio et al., The DELPHI detector at LEP, Nucl. Instrum. Meth. A **303**, 233 (1991).

[14] O. Adriani et al., Results from the L3 experiment at LEP, Phys. Rep. **236**, 1 (1993).

[15] O. Collaboration et al., The OPAL detector at LEP, Nuclear Instruments and Methods in Physics Research Section A: Accelerators, Spectrometers, Detectors and Associated Equipment **305**, 275 (1991).

[16] P. Rowson, D. Su, and S. Willocq, Highlights of the SLD physics program at the SLAC linear collider, Annual Review of Nuclear and Particle Science **51**, 345 (2001).

[17] S. Schael et al., Precision electroweak measurements on the Z resonance, Phys. Rept. **427**, 257 (2006).

[18] K. Kodama et al., Observation of tau neutrino interactions, Phys. Lett. **B504**, 218 (2001).

[19] B. Pontecorvo, Mesonium and anti-mesonium, Sov. Phys. JETP **6**, 429 (1957), [Zh. Eksp. Teor. Fiz.33,549(1957)].

[20] Z. Maki, M. Nakagawa, and S. Sakata, Remarks on the Unified Model of Elementary Particles, Progress of Theoretical Physics **28**, 870 (1962).

[21] R. Davis, D. S. Harmer, and K. C. Hoffman, Search for Neutrinos from the Sun, Phys. Rev. Lett. **20**, 1205 (1968).

[22] J. N. Bahcall, N. A. Bahcall, and G. Shaviv, Present Status of the Theoretical Predictions for the ^{37}Cl Solar-Neutrino Experiment, Phys. Rev. Lett. **20**, 1209 (1968).

[23] V. Gribov and B. Pontecorvo, Neutrino astronomy and lepton charge, Physics Letters B **28**, 493 (1969).

[24] K. Hirata et al., Observation of a small atmospheric muon neutrino/electron neutrino ratio in Kamiokande, Physics Letters B **280**, 146 (1992).

[25] R. Becker-Szendy et al., Electron- and muon-neutrino content of the atmospheric flux, Physical review D: Particles and fields **46**, 3720 (1992).

[26] W. Allison et al., Measurement of the atmospheric neutrino flavour composition in Soudan 2, Physics Letters B **391**, 491 (1997).

[27] S. Fukuda et al., The Super-Kamiokande detector, Nuclear Instruments and Methods in Physics Research Section A: Accelerators, Spectrometers, Detectors and Associated Equipment **501**, 418 (2003).

[28] T. Kajita, Atmospheric neutrino results from Super-Kamiokande and Kamiokande — Evidence for muon neutrino oscillations, Nuclear Physics B - Proceedings Supplements **77**, 123 (1999).

[29] Y. Fukuda et al., Evidence for Oscillation of Atmospheric Neutrinos, Phys. Rev. Lett. **81**, 1562 (1998).

[30] A. Bellerive et al., The sudbury neutrino observatory, Nuclear Physics B **908**, 30 (2016).

[31] The Nobel Prize in Physics 2015.

[32] C. Giganti, S. Lavignac, and M. Zito, Neutrino oscillations: the rise of the PMNS paradigm, Prog. Part. Nucl. Phys. **98**, 1 (2018).

[33] I. Girardi, S. T. Petcov, and A. V. Titov, Predictions for the Majorana CP Violation Phases in the Neutrino Mixing Matrix and Neutrinoless Double Beta Decay, Nucl. Phys. **B911**, 754 (2016).

[34] B. Kayser, Neutrino Oscillation Physics, in *Proceedings, 2011 European School of High-Energy Physics (ESHEP 2011): Cheile Gradistei, Romania, September 7-20, 2011*, pages 107–117, 2014, [,1(2012)].

[35] J. Arafune, M. Koike, and J. Sato, CP Violation and Matter Effect in Long Baseline Neutrino Oscillation Experiments, 1997.

[36] C. S. Wu, E. Ambler, R. W. Hayward, D. D. Hoppes, and R. P. Hudson, Experimental Test of Parity Conservation in Beta Decay, Phys. Rev. **105**, 1413 (1957).

[37] J. H. Christenson, J. W. Cronin, V. L. Fitch, and R. Turlay, Evidence for the 2π Decay of the K_2^0 Meson, Phys. Rev. Lett. **13**, 138 (1964).

[38] R. Aaij et al., First Observation of CP Violation in the Decays of Bs0 Mesons, Physical Review Letters **110** (2013).

[39] R. Aaij et al., Observation of CP Violation in Charm Decays, Phys. Rev. Lett. **122**, 211803 (2019).

[40] Tanabashi, M. *et al.* (Particle Data Group), Review of Particle Physics, Phys. Rev. D **98**, 030001 (2018).

[41] H. Nunokawa, S. J. Parke, and J. W. F. Valle, CP Violation and Neutrino Oscillations, Prog. Part. Nucl. Phys. **60**, 338 (2008).

[42] Q. R. Ahmad et al., Measurement of the Rate of $\nu_e + d \rightarrow p + p + e^-$ Interactions Produced by ^8B Solar Neutrinos at the Sudbury Neutrino Observatory, Phys. Rev. Lett. **87**, 071301 (2001).

[43] K. Eguchi et al., First Results from KamLAND: Evidence for Reactor Antineutrino Disappearance, Phys. Rev. Lett. **90**, 021802 (2003).

[44] M. H. Ahn et al., Measurement of Neutrino Oscillation by the K2K Experiment, Phys. Rev. **D74**, 072003 (2006).

[45] K. Abe et al., Indication of Electron Neutrino Appearance from an Accelerator-produced Off-axis Muon Neutrino Beam, Phys. Rev. Lett. **107**, 041801 (2011).

[46] P. Adamson et al., Combined analysis of ν_μ disappearance and $\nu_\mu \rightarrow \nu_e$ appearance in MINOS using accelerator and atmospheric neutrinos, Phys. Rev. Lett. **112**, 191801 (2014).

[47] Y. Abe et al., Indication of Reactor $\bar{\nu}_e$ Disappearance in the Double Chooz Experiment, Phys. Rev. Lett. **108**, 131801 (2012).

[48] F. P. An et al., Observation of electron-antineutrino disappearance at Daya Bay, Phys. Rev. Lett. **108**, 171803 (2012).

[49] J. K. Ahn et al., Observation of Reactor Electron Antineutrino Disappearance in the RENO Experiment, Phys. Rev. Lett. **108**, 191802 (2012).

[50] P. Adamson et al., Electron neutrino and antineutrino appearance in the full MINOS data sample, Phys. Rev. Lett. **110**, 171801 (2013).

[51] X. Qian and P. Vogel, Neutrino mass hierarchy, Progress in Particle and Nuclear Physics **83**, 1–30 (2015).

[52] L. Stanco, The neutrino mass hierarchy from oscillation, in *Proceedings, Prospects in Neutrino Physics (NuPhys2017): London, UK, December 20-22, 2017*, pages 97–106, 2019, [,71(2019)].

[53] P. Adamson et al., Constraints on Oscillation Parameters from ν_e Appearance and ν_μ Disappearance in NOvA, Phys. Rev. Lett. **118**, 231801 (2017).

[54] P. F. de Salas, D. V. Forero, C. A. Ternes, M. Tortola, and J. W. F. Valle, Status of neutrino oscillations 2018: 3σ hint for normal mass ordering and improved CP sensitivity, Phys. Lett. **B782**, 633 (2018).

[55] Valencia-Globalfit, http://globalfit.astroparticles.es/, 2018.

[56] P. F. de Salas, S. Gariazzo, O. Mena, C. A. Ternes, and M. Tórtola, Neutrino Mass Ordering from Oscillations and Beyond: 2018 Status and Future Prospects, (2018).

[57] S. Gariazzo et al., Neutrino masses and their ordering: Global Data, Priors and Models, JCAP **1803**, 011 (2018).

[58] M. Goodman, The Deep Underground Neutrino Experiment, Advances in High Energy Physics **2015**, 1 (2015).

[59] B. Pontecorvo, Neutrino experiments and the problem of conservation of leptonic charge, Sov. Phys. JETP **26**, 165 (1968).

[60] C. Athanassopoulos et al., Evidence for $\overline{\nu}_\mu \to \overline{\nu}_e$ Oscillations from the LSND Experiment at the Los Alamos Meson Physics Facility, Phys. Rev. Lett. **77**, 3082 (1996).

[61] A. Aguilar-Arevalo et al., Evidence for neutrino oscillations from the observation of anti-neutrino(electron) appearance in a anti-neutrino(muon) beam, Phys. Rev. **D64**, 112007 (2001).

[62] A. A. Aguilar-Arevalo et al., Search for Electron Neutrino Appearance at the $\Delta m^2 \sim 1$ eV^2 Scale, Phys. Rev. Lett. **98**, 231801 (2007).

[63] M. Maltoni and T. Schwetz, Sterile neutrino oscillations after first MiniBooNE results, Phys. Rev. **D76**, 093005 (2007).

[64] A. A. Aguilar-Arevalo et al., Unexplained Excess of Electron-Like Events From a 1-GeV Neutrino Beam, Phys. Rev. Lett. **102**, 101802 (2009).

[65] A. A. Aguilar-Arevalo et al., A Combined $\nu_\mu \to \nu_e$ and $\bar{\nu}_\mu \to \bar{\nu}_e$ Oscillation Analysis of the MiniBooNE Excesses, 2012.

[66] A. Aguilar-Arevalo et al., Significant Excess of Electronlike Events in the MiniBooNE Short-Baseline Neutrino Experiment, Physical Review Letters **121** (2018).

[67] A. A. Aguilar-Arevalo et al., Updated MiniBooNE neutrino oscillation results with increased data and new background studies, Phys. Rev. D **103**, 052002 (2021).

[68] S. Gariazzo, C. Giunti, M. Laveder, Y. F. Li, and E. M. Zavanin, Light sterile neutrinos, Journal of Physics G: Nuclear and Particle Physics **43**, 033001 (2016).

[69] B. Dasgupta and J. Kopp, Sterile neutrinos, Physics Reports **928**, 1 (2021), Sterile neutrinos.

[70] B. Armbruster et al., Upper limits for neutrino oscillations muon-anti-neutrino —> electron-anti-neutrino from muon decay at rest, Phys. Rev. D **65**, 112001 (2002).

[71] N. Agafonova et al., Final results of the search for $\nu_\mu \to \nu_e$ oscillations with the OPERA detector in the CNGS beam, JHEP **06**, 151 (2018).

[72] J. Todd, R. Chen, and J. H. and, Search for muon neutrino disappearance due to sterile neutrino oscillations with the MINOS/MINOS+ experiment, Journal of Physics: Conference Series **888**, 012163 (2017).

[73] P. Adamson et al., Search for sterile neutrinos in MINOS and MINOS+ using a two-detector fit, Phys. Rev. Lett. **122**, 091803 (2019).

[74] R. Wendell et al., Atmospheric neutrino oscillation analysis with sub-leading effects in Super-Kamiokande I, II, and III, Phys. Rev. D **81**, 092004 (2010).

[75] M. G. Aartsen et al., Determining neutrino oscillation parameters from atmospheric muon neutrino disappearance with three years of IceCube DeepCore data, Phys. Rev. D **91**, 072004 (2015).

[76] M. Dentler et al., Updated Global Analysis of Neutrino Oscillations in the Presence of eV-Scale Sterile Neutrinos, JHEP **08**, 010 (2018).

[77] S. Ajimura et al., Technical Design Report (TDR): Searching for a Sterile Neutrino at J-PARC MLF (E56, JSNS2), (2017).

[78] M. A. Acero et al., Search for Active-Sterile Antineutrino Mixing Using Neutral-Current Interactions with the NOvA Experiment, Phys. Rev. Lett. **127**, 201801 (2021).

[79] K. Abe et al., Search for light sterile neutrinos with the T2K far detector Super-Kamiokande at a baseline of 295 km, Phys. Rev. D **99**, 071103 (2019).

[80] H. Almazán et al., Improved sterile neutrino constraints from the STEREO experiment with 179 days of reactor-on data, Phys. Rev. D **102**, 052002 (2020).

[81] I. Alekseev et al., Search for sterile neutrinos at the DANSS experiment, Phys. Lett. B **787**, 56 (2018).

[82] A. P. Serebrov et al., Search for sterile neutrinos in the neutrino-4 experiment, JETP Lett. **105**, 347 (2017).

[83] M. Andriamirado et al., Improved short-baseline neutrino oscillation search and energy spectrum measurement with the PROSPECT experiment at HFIR, Phys. Rev. D **103**, 032001 (2021).

[84] P. A. Machado, O. Palamara, and D. W. Schmitz, The Short-Baseline Neutrino Program at Fermilab, Annual Review of Nuclear and Particle Science **69**, 363 (2019).

[85] C. Rubbia, The liquid-argon time projection chamber: a new concept for neutrino detectors, Technical report, CERN, Geneva, 1977.

[86] M. Aleksa and C. Fabjan, Fundamental physics with noble liquid detectors, in *IEEE International Conference on Dielectric Liquids, 2005. ICDL 2005.*, pages 1–12, 2005.

[87] J. Asaadi, Liquid Argon Time Projection Chambers, 2017.

[88] K. Scholberg, Supernova Neutrino Detection in Water Cherenkov Detectors, in *Journal of Physics-Conference Series*, volume 309, page 012028, 2011.

[89] Y. Yamazaki et al., Accelerator Technical Design Report for High-Intensity Proton Accelerator Facility Project, J-PARC, KEK-Report 2002-13, JAERI-Tech **44** (2003).

[90] F. Cavanna, M. Kordosky, J. Raaf, and B. Rebel, LArIAT: Liquid Argon In A Testbeam, (2014).

[91] R. Acciarri et al., Construction of precision wire readout planes for the Short-Baseline Near Detector (SBND), Journal of Instrumentation **15**, P06033–P06033 (2020).

[92] S. Amoruso et al., Analysis of the liquid argon purity in the ICARUS T600 TPC, Nuclear Instruments and Methods in Physics Research Section A: Accelerators, Spectrometers, Detectors and Associated Equipment **516**, 68 (2004).

[93] M. Antonello et al., Operation and performance of the ICARUS-T600 cryogenic plant at Gran Sasso underground Laboratory, JINST **10**, P12004 (2015).

[94] P. Abratenko et al., ICARUS at the Fermilab Short-Baseline Neutrino program: initial operation, Eur. Phys. J. C **83**, 467 (2023).

[95] S. Amerio et al., Design, construction and tests of the ICARUS T600 detector, Nucl. Instrum. Meth. A **527**, 329 (2004).

[96] N. Canci, The ICARUS T600 Detector at LNGS Underground Laboratory, Physics Procedia **37**, 1257 (2012), Proceedings of the 2nd International Conference on Technology and Instrumentation in Particle Physics (TIPP 2011).

[97] L. Bagby et al., Overhaul and installation of the ICARUS-T600 liquid argon TPC electronics for the FNAL Short Baseline Neutrino program, Journal of Instrumentation **16**, P01037 (2021).

[98] R. Acciarri et al., Design and construction of the MicroBooNE detector, Journal of Instrumentation **12**, P02017 (2017).

[99] R. Acciarri et al., The Short-Baseline Near Detector at Fermilab: Input to the European Strategy for Particle Physics 2026 Update, (2025).

[100] R. Acciarri et al., First Observation of Low Energy Electron Neutrinos in a Liquid Argon Time Projection Chamber, Phys. Rev. D **95**, 072005 (2017).

[101] L. H. Whitehead, Status of single phase and dual phase DUNE prototype detectors at CERN, PoS **ICHEP2018**, 300. 4 p (2019).

[102] J. Asaadi et al., First Demonstration of a Pixelated Charge Readout for Single-Phase Liquid Argon Time Projection Chambers, Instruments **4** (2020).

[103] D. Dwyer et al., LArPix: demonstration of low-power 3D pixelated charge readout for liquid argon time projection chambers, Journal of Instrumentation **13**, P10007 (2018).

[104] A. A. Abud et al., Deep Underground Neutrino Experiment (DUNE) Near Detector Conceptual Design Report, Instruments **5** (2021).

[105] H. Bethe, Theory of the Passage of Fast Corpuscular Rays Through Matter, Annalen Phys. **5**, 325 (1930).

[106] R. M. Sternheimer, The Density Effect for the Ionization Loss in Various Materials, Phys. Rev. **88**, 851 (1952).

[107] R. Acciarri et al., A study of electron recombination using highly ionizing particles in the ArgoNeuT Liquid Argon TPC, Journal of Instrumentation **8**, P08005 (2013).

[108] M. Miyajima et al., Average energy expended per ion pair in liquid argon, Phys. Rev. A **9**, 1438 (1974).

[109] E. Shibamura et al., Drift velocities of electrons, saturation characteristics of ionization and W-values for conversion electrons in liquid argon, liquid argon-gas mixtures and liquid xenon, Nuclear Instruments and Methods **131**, 249 (1975).

[110] L. Onsager, Initial Recombination of Ions, Phys. Rev. **54**, 554 (1938).

[111] J. B. Birks, Scintillations from Organic Crystals: Specific Fluorescence and Relative Response to Different Radiations, Proceedings of the Physical Society. Section A **64**, 874 (1951).

[112] G. Jaffé, Zur theorie der ionisation in kolonnen, Annalen der Physik **347**, 303 (1913).

[113] J. Thomas and D. A. Imel, Recombination of electron-ion pairs in liquid argon and liquid xenon, Phys. Rev. A **36**, 614 (1987).

[114] R. Acciarri et al., A Proposal for a Three Detector Short-Baseline Neutrino Oscillation Program in the Fermilab Booster Neutrino Beam, (2015).

[115] Y. Li et al., Measurement of Longitudinal Electron Diffusion in Liquid Argon, Nucl. Instrum. Meth. A **816**, 160 (2016).

[116] N. Gee, M. A. Floriano, T. Wada, S. S.-S. Huang, and G. R. Freeman, Ion and electron mobilities in cryogenic liquids: Argon, nitrogen, methane, and ethane, Journal of applied physics **57**, 1097 (1985).

[117] P. Abratenko et al., Measurement of space charge effects in the MicroBooNE LArTPC using cosmic muons, JINST **15**, P12037 (2020).

[118] M. Antonello et al., Experimental observation of an extremely high electron lifetime with the ICARUS-T600 LAr-TPC, JINST **9**, P12006 (2014).

[119] V. Meddage, Electron Attenuation Measurement using Cosmic Ray Muons at the MicroBooNE LArTPC, in *Meeting of the APS Division of Particles and Fields*, 2017.

[120] E. Segreto, Properties of liquid argon scintillation light emission, Phys. Rev. D **103**, 043001 (2021).

[121] P. Cennini et al., Detection of scintillation light in coincidence with ionizing tracks in a liquid argon time projection chamber, Nuclear Instruments and Methods in Physics Research Section A: Accelerators, Spectrometers, Detectors and Associated Equipment **432**, 240 (1999).

[122] G. Seidel, R. Lanou, and W. Yao, Rayleigh scattering in rare-gas liquids, Nuclear Instruments and Methods in Physics Research Section A: Accelerators, Spectrometers, Detectors and Associated Equipment **489**, 189 (2002).

[123] D. Garcia-Gamez, P. Green, and A. M. Szelc, Predicting Transport Effects of Scintillation Light Signals in Large-Scale Liquid Argon Detectors, Eur. Phys. J. C **81**, 349 (2021).

[124] A. P. Furmanski and C. Hilgenberg, Neutrino energy estimation in neutral current interactions and prospects for sterile neutrino searches, Phys. Rev. D **103**, 112011 (2021).

[125] G. Cheng et al., Dual baseline search for muon antineutrino disappearance at $0.1\text{eV}^2 < \Delta m^2 < 100\text{eV}^2$, Phys. Rev. D **86**, 052009 (2012).

[126] M. G. Aartsen et al., Searching for eV-scale sterile neutrinos with eight years of atmospheric neutrinos at the IceCube Neutrino Telescope, Phys. Rev. D **102**, 052009 (2020).

[127] V. C. L. Nguyen, Towards a Search for Heavy Neutral Leptons Decaying into Neutral Pionsin the Short-Baseline Near Detector, Phd thesis, Department of Physics and Astronomy, The University of Sheffield, UK, 2024.

[128] B. Batell, J. Berger, and A. Ismail, Probing the Higgs portal at the Fermilab short-baseline neutrino experiments, Phys. Rev. D **100**, 115039 (2019).

[129] K. J. Kelly, S. Kumar, and Z. Liu, Heavy axion opportunities at the DUNE near detector, Phys. Rev. D **103**, 095002 (2021).

[130] J. Berger and G. Putnam, Sensitivity to kaon decays to ALPs at fixed target experiments, Phys. Rev. D **110**, 055035 (2024).

[131] P. deNiverville, C.-Y. Chen, M. Pospelov, and A. Ritz, Light dark matter in neutrino beams: Production modeling and scattering signatures at MiniBooNE, T2K, and SHiP, Phys. Rev. D **95**, 035006 (2017).

[132] L. Buonocore, C. Frugiuele, and P. deNiverville, Hunt for sub-GeV dark matter at neutrino facilities: A survey of past and present experiments, Phys. Rev. D **102**, 035006 (2020).

[133] B. Batell, J. Berger, L. Darmé, and C. Frugiuele, Inelastic dark matter at the Fermilab Short Baseline Neutrino Program, Phys. Rev. D **104**, 075026 (2021).

[134] A. A. Aguilar-Arevalo et al., Neutrino flux prediction at MiniBooNE, Phys. Rev. D **79**, 072002 (2009).

[135] T. H. C. M. Catanesi et al., Measurement of the production cross-section of positive pions in the collision of 8.9 GeV/c protons on beryllium, The European Physical Journal C **52**, 29 (2007).

[136] A. A. Aguilar-Arevalo et al., First measurement of the muon neutrino charged current quasielastic double differential cross section, Phys. Rev. D **81**, 092005 (2010).

[137] Y. Nagai, Addendum to the NA61/SHINE Proposal: A Low-Energy Beamline at the SPS H2, Technical report, CERN, Geneva, 2021.

[138] T. D. Collaboration et al., Design, construction and operation of the ProtoDUNE-SP Liquid Argon TPC, Journal of Instrumentation **17**, P01005 (2022).

[139] SBND Collaboration, Scintillation light in SBND: simulation, reconstruction, and expected performance of the photon detection system, Eur. Phys. J. C **84**, 1046 (2024).

[140] Photomultiplier tube R5912 | Hamamatsu Photonics, https://hep.hamamatsu.com/eu/en/products/R5912.html, Accessed: 31-08-2025.

[141] A. Machado et al., The X-ARAPUCA: an improvement of the ARAPUCA device, Journal of Instrumentation **13**, C04026 (2018).

[142] VX1730 / VX1730S - 16/8 Channel 14 bit 500 MS/s Digitizer - CAEN - Tools for Discovery, https://www.caen.it/products/vx1730/, Accessed: 31-08-2025.

[143] C. Brizzolari et al., Cryogenic front-end amplifier design for large SiPM arrays in the DUNE FD1-HD photon detection system, Journal of Instrumentation **17**, P11017 (2022).

[144] V1740 - 64 Channel 12 bit 62.5 MS/s Digitizer - CAEN - Tools for Discovery, https://www.caen.it/products/v1740/, Accessed: 09-07-2025.

[145] R. Acciarri et al., Cosmic Ray Background Removal With Deep Neural Networks in SBND, Frontiers in Artificial Intelligence **Volume 4 - 2021** (2021).

[146] R. Chytracek, J. McCormick, W. Pokorski, and G. Santin, Geometry description markup language for physics simulation and analysis applications, IEEE Transactions on Nuclear Science **53**, 2892 (2006).

[147] P. Moreira, J. Serrano, T. Wlostowski, P. Loschmidt, and G. Gaderer, White rabbit: Sub-nanosecond timing distribution over ethernet, in *2009 International Symposium on Precision Clock Synchronization for Measurement, Control and Communication*, pages 1–5, 2009.

[148] E. Snider and G. Petrillo, LArSoft: toolkit for simulation, reconstruction and analysis of liquid argon TPC neutrino detectors, Journal of Physics: Conference Series **898**, 042057 (2017).

[149] C. Green et al., The art framework, Journal of Physics. Conference Series **396** (2012).

[150] R. Brun and F. Rademakers, ROOT — An object oriented data analysis framework, Nucl. Instrum. Meth. A **389**, 81 (1997).

[151] C. Andreopoulos et al., The GENIE Neutrino Monte Carlo Generator, Nucl. Instrum. Meth. A **614**, 87 (2010).

[152] D. Heck, J. Knapp, J. N. Capdevielle, G. Schatz, and T. Thouw, CORSIKA: A Monte Carlo code to simulate extensive air showers, (1998).

[153] S. Agostinelli et al., GEANT4: A simulation toolkit, Nucl. Instrum. Meth. **A506**, 250 (2003).

[154] R. Veenhof, Garfield, recent developments, Nuclear Instruments and Methods in Physics Research Section A: Accelerators, Spectrometers, Detectors and Associated Equipment **419**, 726 (1998).

[155] X. Qian, C. Zhang, B. Viren, and M. Diwan, Three-dimensional imaging for large LArTPCs, Journal of Instrumentation **13**, P05032 (2018).

[156] J. S. Marshall and M. A. Thomson, The Pandora software development kit for pattern recognition, The European Physical Journal C **75** (2015).

[157] T. Doke, K. Masuda, and E. Shibamura, Estimation of absolute photon yields in liquid argon and xenon for relativistic (1 MeV) electrons, Nuclear Instruments and Methods in Physics Research Section A: Accelerators, Spectrometers, Detectors and Associated Equipment **291**, 617 (1990).

[158] T. Doke et al., Absolute Scintillation Yields in Liquid Argon and Xenon for Various Particles, Japanese Journal of Applied Physics **41**, 1538 (2002).

[159] A. Hitachi et al., Effect of ionization density on the time dependence of luminescence from liquid argon and xenon, Phys. Rev. B **27**, 5279 (1983).

[160] D. L. Igor Kreslo, Martin Auger, SBND Cosmic Ray Tracker Design and Performance Technical Note, (2019).

[161] C. Adams et al., Ionization electron signal processing in single phase LArTPCs. Part I. Algorithm Description and quantitative evaluation with MicroBooNE simulation, Journal of Instrumentation **13**, P07006 (2018).

[162] R. Acciarri et al., Noise Characterization and Filtering in the MicroBooNE Liquid Argon TPC, Journal of Instrumentation **12**, P08003 (2017).

[163] P. Abratenko et al., Calibration and simulation of ionization signal and electronics noise in the ICARUS liquid argon time projection chamber, Journal of Instrumentation **20**, P01032 (2025).

[164] C. Adams et al., Ionization electron signal processing in single phase LArTPCs. Part II. Data/simulation comparison and performance in MicroBooNE, Journal of Instrumentation **13**, P07007 (2018).

[165] S. Ramo, Currents Induced by Electron Motion, Proceedings of the IRE **27**, 584 (1939).

[166] G. Green, An Essay on the Application of mathematical Analysis to the theories of Electricity and Magnetism., Journal für die reine und angewandte Mathematik **44**, 356 (1852).

[167] B. Abi et al., First results on ProtoDUNE-SP liquid argon time projection chamber performance from a beam test at the CERN Neutrino Platform, Journal of Instrumentation **15**, P12004 (2020).

[168] J. Asaadi et al., First Demonstration of a Pixelated Charge Readout for Single-Phase Liquid Argon Time Projection Chambers, 2018.

[169] C. Adams et al., Enhancing neutrino event reconstruction with pixel-based 3D readout for liquid argon time projection chambers, Journal of Instrumentation **15**, P04009 (2020).

[170] Y. Li et al., A 20-liter test stand with gas purification for liquid argon research, Journal of Instrumentation **11**, T06001 (2016).

[171] GetterMax 133: Copper Catalysts For Oxygen Removal, https://www.research-catalysts.com/cu-cats-for-O2, Accessed: 09-07-2025.

[172] A. Zglam, Selection and Reconstruction of Muon Neutrino and Muon Antineutrio Pi-Zero Production Interactions on Argon with the Short-Baseline Near Detector, Phd thesis, Department of Physics and Astronomy, The University of Sheffield, UK, 2023.

[173] V6521 - 6 Channel 6 kV/300 microamp VME HV Power Supply Module - CAEN - Tools for Discovery, https://www.caen.it/products/v6521/, Accessed: 09-07-2025.

[174] G. De Geronimo et al., Front-end ASIC for a liquid argon TPC, in *IEEE Nuclear Science Symposium and Medical Imaging Conference*, pages 1658–1666, 2010.

[175] Nano | Arduino Documentation, https://docs.arduino.cc/hardware/nano/, Accessed: 09-07-2025.

[176] Photomultiplier tube R11065-20 | Hamamatsu Photonics, https://hep.hamamatsu.com/eu/en/products/R11065-20.html, Accessed: 09-07-2025.

[177] 9954B Series - 51 mm Photomultiplier - ET Enterprises Ltd, https://et-enterprises.com/products/photomultipliers/product/p9954b-series, Accessed: 09-07-2025.

[178] EMI Photomultiplier Tubes 1970, https://frank.pocnet.net/other/EMI/EMI_Photomultiplier_Tubes_1970.pdf, Accessed: 09-07-2025.

[179] N417 - 8 Channel Low Threshold Discriminator - CAEN - Tools for Discovery, https://www.caen.it/download/?filter=N417, Accessed: 09-07-2025.

[180] U5309A PCIe High-Speed Digitizer - Startup Guide, https://www.keysight.com/us/en/assets/9018-04026/quick-start-guides/9018-04026.pdf, Accessed: 09-07-2025.

[181] LabVIEW User Manual - NI, https://www.ni.com/docs/en-US/bundle/labview/page/user-manual-welcome.html, Accessed: 09-07-2025.

[182] NI PXI-6229 Supported Properties - NI, https://www.ni.com/docs/en-US/bundle/ni-daqmx-c-api-ref/page/cdaqmxsupp/pxi-6229.html, Accessed: 09-07-2025.

[183] PT-100 Series Platinum Resistance Sensors - Omega Engineering, https://assets.omega.com/manuals/M3567.pdf, Accessed: 09-07-2025.

[184] Solid State Pressure Transducer - Omega Engineering, https://assets.omega.com/manuals/M3567.pdf, Accessed: 09-07-2025.

[185] CryoGauge 242 Telemetry Liquid Level Gauge - Wessington Cryogenics, https://ess.wessingtoncryogenics.com/cryo-parts/level-gauges-alarms/cryogauge-242-telemetry-liquid-level-gauge/, Accessed: 09-07-2025.

[186] Servomex DF-550E Oxygen Analyzer Operator Manual, https://www.servomex.com/wp-content/uploads/2023/01/Manual-DF550E-RevD-v20.11-100611.pdf, Accessed: 09-07-2025.

[187] Unix Time Stamp - Epoch Converter, https://www.unixtimestamp.com/, Accessed: 09-07-2025.

[188] O. Barnabà et al., A comparison between scintillation light Analog and Digital Trigger for large volume Liquid Argon Time Projection Chambers, Journal of Instrumentation **15**, C04024 (2020).

[189] R. Acciarri et al., Effects of Nitrogen contamination in liquid Argon, Journal of Instrumentation **5**, P06003 (2010).

[190] C. Lastoria, Analysis of the light production and propagation in the 4-tonne dual-phase demonstrator, Journal of Instrumentation **15**, C06029 (2020).

[191] R. Acciarri et al., Oxygen contamination in liquid Argon: Combined effects on ionization electron charge and scintillation light, JINST **5**, P05003 (2010).

[192] G. Bakale, U. Sowada, and W. F. Schmidt, Effect of an electric field on electron attachment to sulfur hexafluoride, nitrous oxide, and molecular oxygen in liquid argon and xenon, The Journal of Physical Chemistry **80**, 2556 (1976).

[193] G. Lamaze, J. Whittaker, R. Schrack, and O. Wasson, After-pulse suppression for 8850 and 8854 photomultipliers, Nuclear Instruments and Methods **123**, 403 (1975).

[194] U. Akgun et al., Afterpulse timing and rate investigation of three different Hamamatsu Photomultiplier Tubes, Journal of Instrumentation **3** (2008).

[195] Q. Wu et al., Study of after-pulses in the 20-inch HQE-MCP-PMT for the JUNO experiment, Nuclear Instruments and Methods in Physics Research Section A: Accelerators, Spectrometers, Detectors and Associated Equipment **1003**, 165351 (2021).

[196] H. Burn, Testing New Pixelated Readout Technologies with the Sheffield Test Stand Experiment with Liquid Argon., Master's dissertation, Department of Physics and Astronomy, The University of Sheffield, UK, 2024.

Appendix A

Two Flavour Oscillation Probability Derivation

Deriving the two-flavour oscillation probability of observing a ν_e or ν_μ eigenstate involves first expressing ν_e and ν_μ in terms of the mass eigenstate wavefunctions, and vice versa. The two-neutrino paradigm assumes $\Delta m^2_{21} \ll \Delta m^2_{32}$ and $\theta_{13} \ll \frac{\pi}{2}$, where Δm^2_{ij} is the square mass difference of neutrino mass eigenstates, defined in equation 2.15. Assuming natural units ($c = \hbar = 1$) and vacuum oscillations (i.e. no matter effects), expanding the matrix equation in equation 2.9 gives weak neutrino eigenstate wavefunctions

$$|\nu_e\rangle = \cos(\theta)|\nu_1\rangle + \sin(\theta)|\nu_2\rangle, \tag{A.1}$$

$$|\nu_\mu\rangle = -\sin(\theta)|\nu_1\rangle + \cos(\theta)|\nu_2\rangle, \tag{A.2}$$

where the mass eigenstate wavefunctions $|\nu_1\rangle$ and $|\nu_2\rangle$ satisfy the time-dependent relativistic Schrödinger equation, with solutions in the lab frame of energy E_j and momentum p_j, at distance x from the origin x_0 for $x > x_0$ along the beamline, at time $t > t_0$ as

$$|\nu_1(x,t)\rangle = e^{-i(E_1 t - p_1 x)}|\nu_1(x_0,t_0)\rangle, \tag{A.3}$$

$$|\nu_2(x,t)\rangle = e^{-i(E_2 t - p_2 x)}|\nu_2(x_0,t_0)\rangle. \tag{A.4}$$

Substituting equations A.3 and A.4 into equations A.1 and A.2 give the expanded weak eigenstate wavefunctions

$$|\nu_e(x,t)\rangle = \cos(\theta)e^{-i\frac{m_1^2 x}{2E_1}}|\nu_1(x_0,t_0)\rangle + \sin(\theta)e^{-i\frac{m_2^2 x}{2E_2}}|\nu_2(x_0,t_0)\rangle, \tag{A.5}$$

$$|\nu_\mu(x,t)\rangle = -\sin(\theta)e^{-i\frac{m_1^2 x}{2E_1}}|\nu_1(x_0,t_0)\rangle + \cos(\theta)e^{-i\frac{m_2^2 x}{2E_2}}|\nu_2(x_0,t_0)\rangle. \tag{A.6}$$

Assuming a pure ν_μ beam at $x = x_0$ and $t = t_0$, this gives $|\nu_e(x_0,t_0)\rangle = 0$, $|\nu_\mu(x_0,t_0)\rangle = 1$, giving the mass wavefunctions as $|\nu_1(t_0,t_0)\rangle$ =-sin(θ) and $|\nu_2(t_0,t_0)\rangle = \cos(\theta)$. Substitute these conditions into equation A.5 and A.6 to get the eigenfunctions

$$|\nu_e(x,t)\rangle = \frac{1}{2}\sin(2\theta)\left(e^{-i\frac{m_2^2 x}{2E_2}} - e^{-i\frac{m_1^2 x}{2E_1}}\right) \tag{A.7}$$

$$|\nu_\mu(x,t)\rangle = \sin^2(\theta)e^{-i\frac{m_1^2 x}{2E_1}} + \cos^2(\theta)e^{-i\frac{m_2^2 x}{2E_2}}. \tag{A.8}$$

Using the approximation that neutrino mass states are relativistic such that $m_j \ll E_j$, giving $p_j \approx E_j$, and that their respective energies are approximately the same $E_1 \approx E_2 = E = p$, substituting equations A.8 and A.7 into equation 2.10 (using $\alpha = \mu$ and $\beta = e$) gives the ν_μ disappearance probability $P(\nu_e \to \nu_e)$ to be

$$P(\nu_\mu \to \nu_e) = \sin^2(2\theta)\sin^2\left(\frac{\Delta m_{12}^2 x}{4E}\right). \tag{A.9}$$

In the context of large-scale neutrino accelerator experiments, the units of these parameters are best expressed such that Δm^2 is measured in eV^2, E in GeV and x as the length of the baseline L in km. Converting from natural units back to physical units using $\hbar c = 197$ MeVfm, applying these assumptions to equation A.9, the form of ν_μ disappearance probability applied to two-detector neutrino oscillation experiments is

$$P(\nu_\mu \to \nu_e) = \sin^2(2\theta)\sin^2\left(1.27\frac{\Delta m_{12}^2[\text{eV}^2]L[\text{km}]}{E[\text{GeV}]}\right). \tag{A.10}$$

In the two-neutrino paradigm, the sum of ν_μ disappearance $P(\nu_\mu \to \nu_e)$ and appearance $P(\nu_\mu \to \nu_\mu)$ probabilities is unity, so the ν_μ appearance probability is given as

$$P(\nu_\mu \to \nu_\mu) = 1 - \sin^2(2\theta)\sin^2\left(1.27\frac{\Delta m_{21}^2[\text{eV}^2]L[\text{km}]}{E[\text{GeV}]}\right). \tag{A.11}$$

Appendix B

Full Monte Carlo vs SBND Data Waveforms

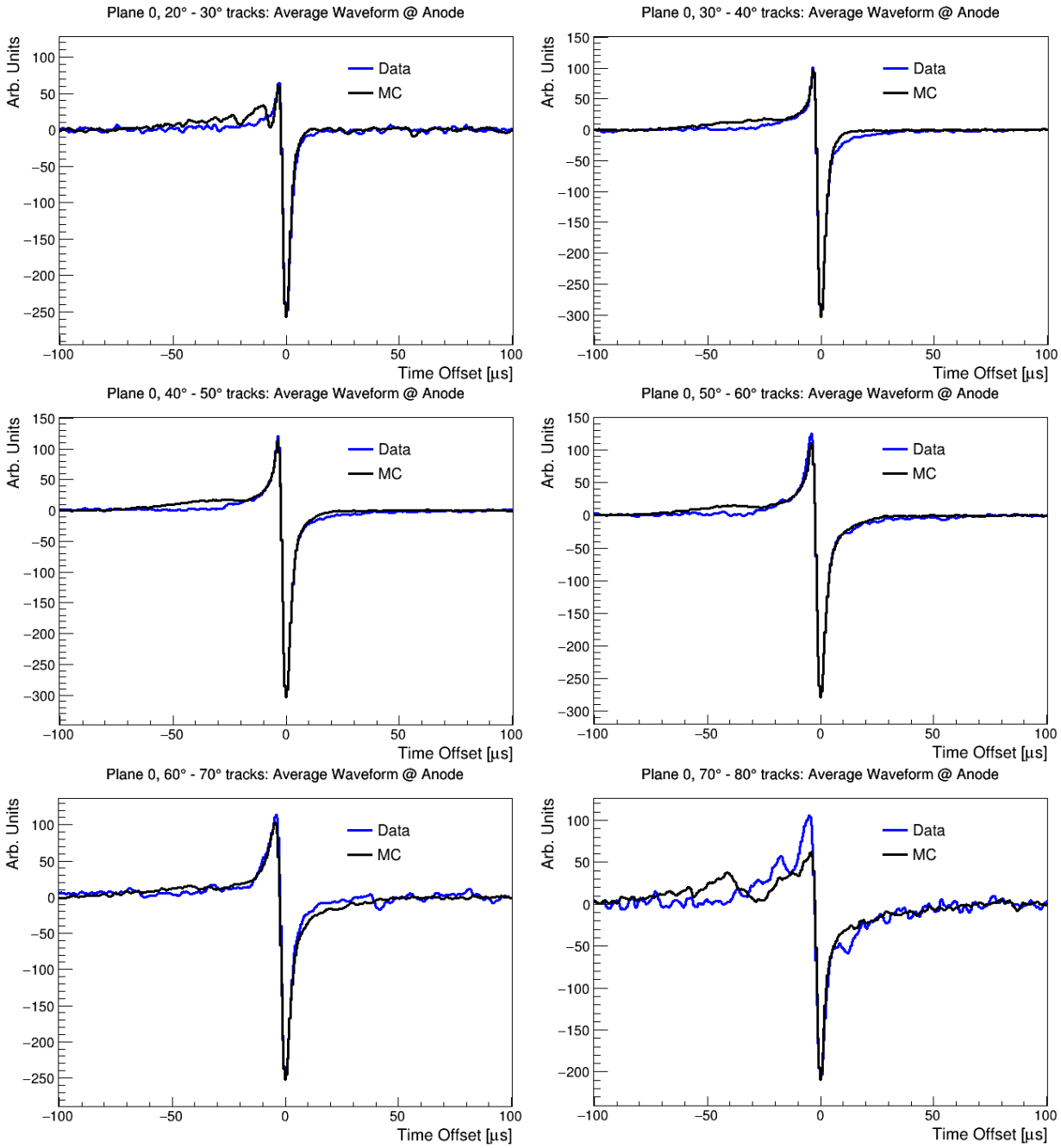

Figure B.1: Average reconstructed waveforms on SBND TPC first induction plane wires for simulated MC cosmic-ray muon event samples and a two-hour run of SBND collecting cosmic-ray muon data. Plots are broken down with respect to track pitch angle θ_{xz} in segments of $\Delta\theta_{xz} = 10°$ from 20° to 80°.

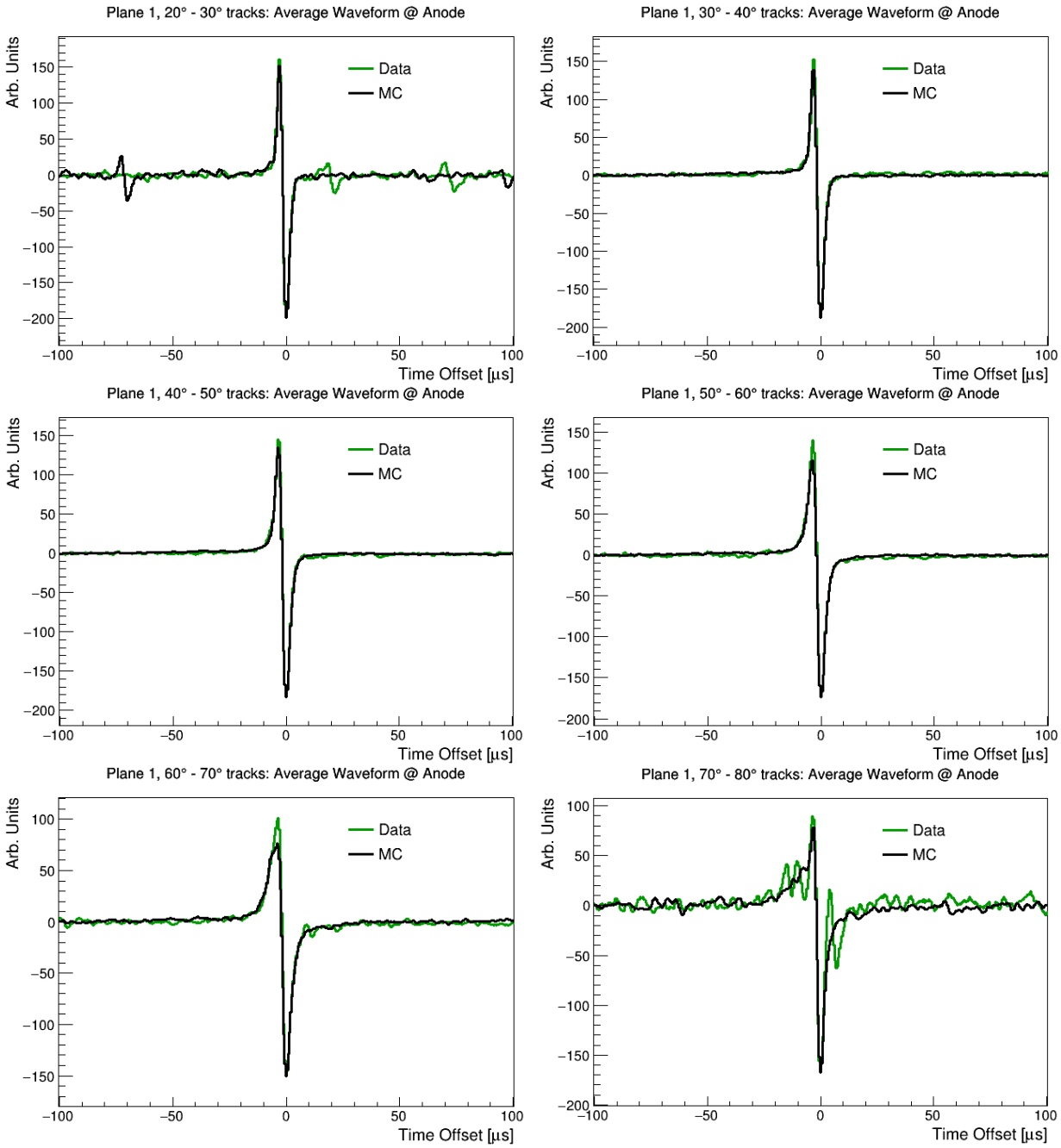

Figure B.2: Average reconstructed waveforms on SBND TPC second induction plane wires for simulated MC cosmic-ray muon event samples and a two-hour run of SBND collecting cosmic-ray muon data. Plots are broken down with respect to track pitch angle θ_{xz} in segments of $\Delta\theta_{xz} = 10°$ from 20° to 80°.

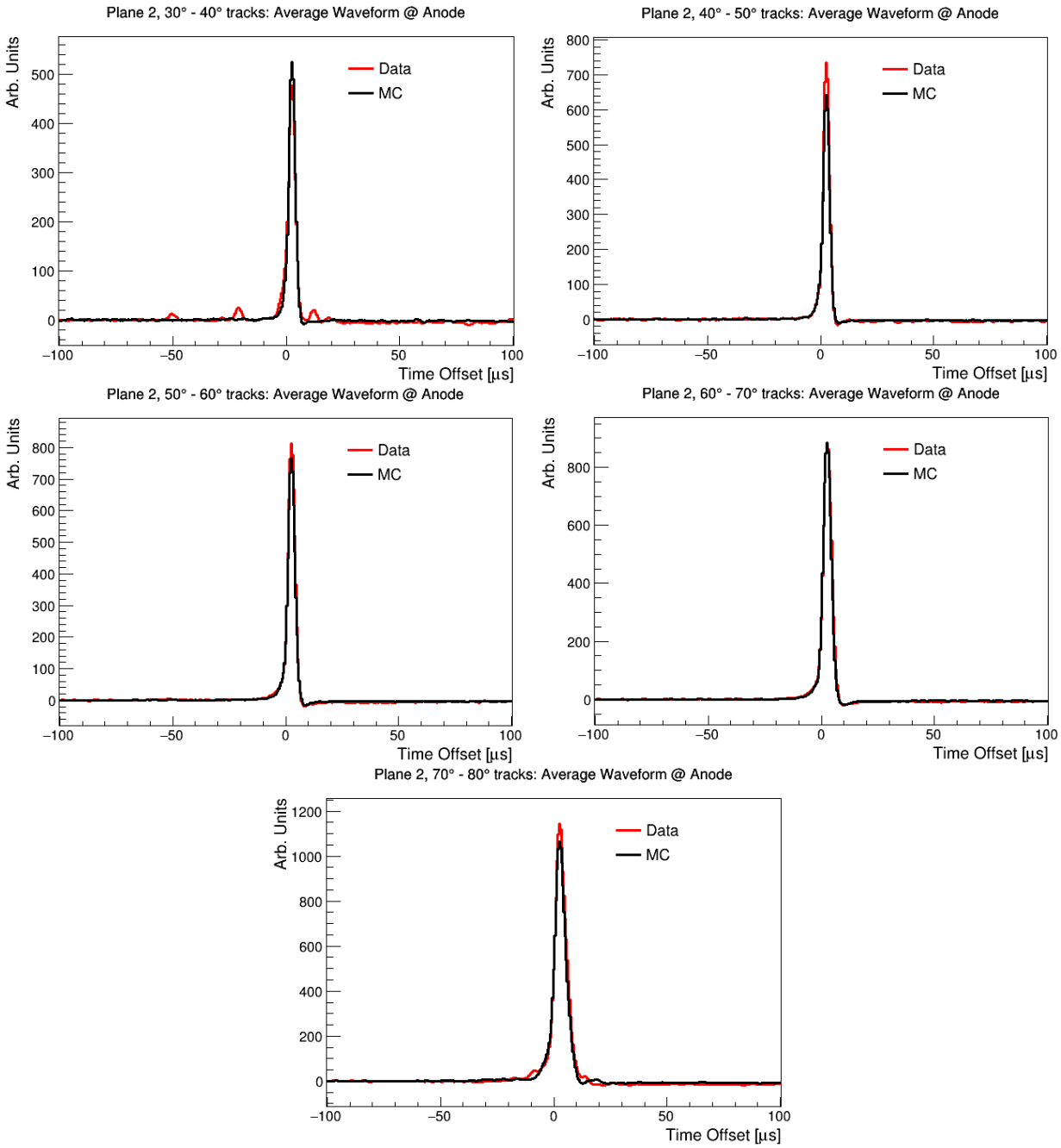

Figure B.3: Average reconstructed waveforms on SBND TPC second induction plane wires for simulated MC cosmic-ray muon event samples and a two-hour run of SBND collecting cosmic-ray muon data. Plots are broken down with respect to track pitch angle θ_{xz} in segments of $\Delta\theta_{xz} = 10°$ from 30° to 80°.

Appendix C

STEEL Uncertainty Propagation

The equation for calculating the ENI density within liquid argon is

$$[X] = \frac{\tau_3 - \tau_3'}{\tau_3' k_X}, \tag{C.1}$$

with quenching rate k_X, measured triplet decay constant τ_3' and theoretical maximum triplet decay constant for zero ENI τ_3. Differentiating equation C.1 with respect to the three independent parameters gives:

$$\Delta[X] = \sqrt{\left(\frac{d[X]}{dk_X}\Delta k_X\right)^2 + \left(\frac{d[X]}{d\tau_3}\Delta\tau_3\right)^2 + \left(\frac{d[X]}{d\tau_3'}\Delta\tau_3'\right)^2}. \tag{C.2}$$

By substituting equation C.1, these differentials can be computed as:

$$\frac{d[X]}{dk_X} = \frac{d}{dk_X}\left(\frac{\tau_3 - \tau_3'}{\tau_3' k_X}\right) = -\frac{\tau_3 - \tau_3'}{\tau_3' k_X^2} = -\frac{[X]}{k_X}, \tag{C.3}$$

$$\frac{d[X]}{d\tau_3} = \frac{d}{d\tau_3}\left(\frac{\tau_3}{\tau_3' k_X} - \frac{1}{k_X}\right) = \frac{1}{\tau_3' k_X}, \tag{C.4}$$

$$\frac{d[X]}{d\tau_3'} = \frac{d}{d\tau_3'}\left(\frac{\tau_3}{\tau_3' k_X} - \frac{1}{k_X}\right) = -\frac{\tau_3}{\tau_3'^2 k_X}. \tag{C.5}$$

Substituting equations C.3, C.4 and C.5 into equation C.2 and simplifying gives the final expression for the uncertainty in ENI density as

$$\Delta[X] = \frac{1}{k_X}\sqrt{\left([X]\Delta k_X\right)^2 + \left(\frac{\Delta\tau_3}{\tau_3'}\right)^2 + \left(\frac{\tau_3\Delta\tau_3'}{\tau_3'^2}\right)^2}. \tag{C.6}$$

Appendix D

STEEL Full Lifetime and ENI Density Plots

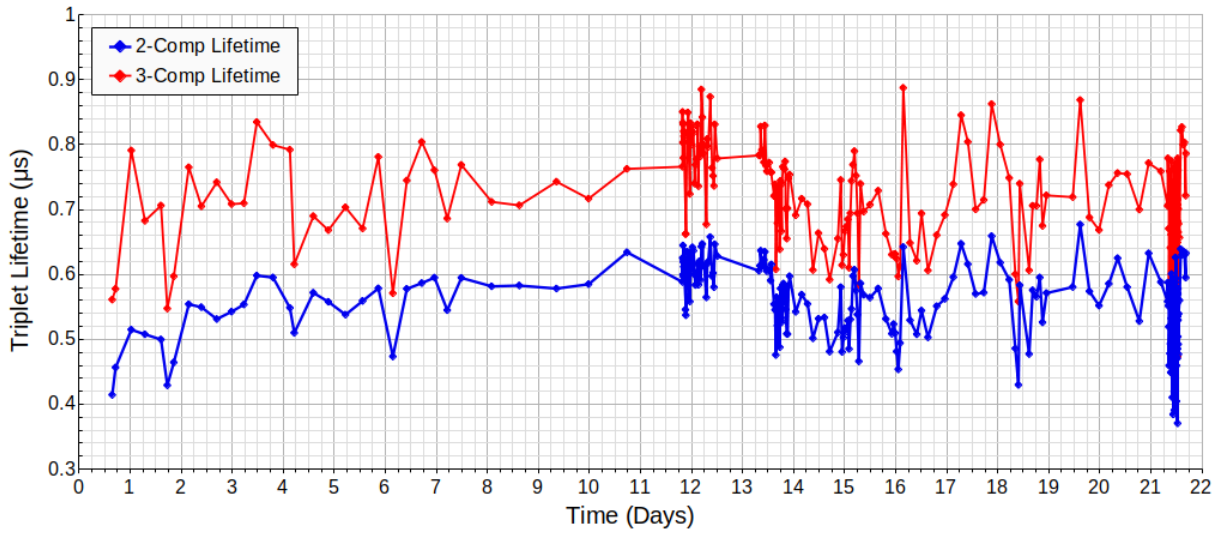

Figure D.1: Measured triplet lifetime τ_3 as a function of time since the start of the first day of the 22-day data run of STEEL for 243 Keysight DAQ data files. τ_3 was measured from fitting the two and three component exponential decay models in equations 9.2 and 9.3 to averaged scintillation pulses from ∼200 events.

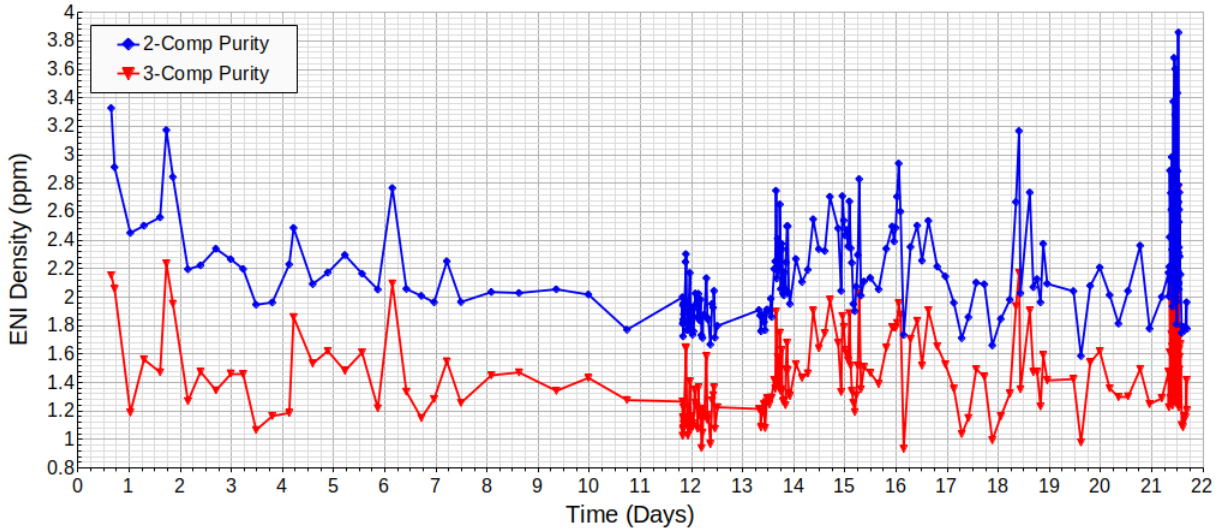

Figure D.2: Calculated Oxygen impurity density $[O_2]$ in LAr as a function of time since the start of the first day of the 22-day data run of STEEL for 243 Keysight DAQ data files. $[O_2]$ was calculated from equation 9.6 using a quenching rate of $k_O = (0.86 \pm 0.03)$ ppm^{-1} [191] and a maximum triplet lifetime value for zero ENI presence of $\tau_3 = (1.6 \pm 0.1)$ µs [159]. Uncertainty propagation calculations are detailed in Appendix C.

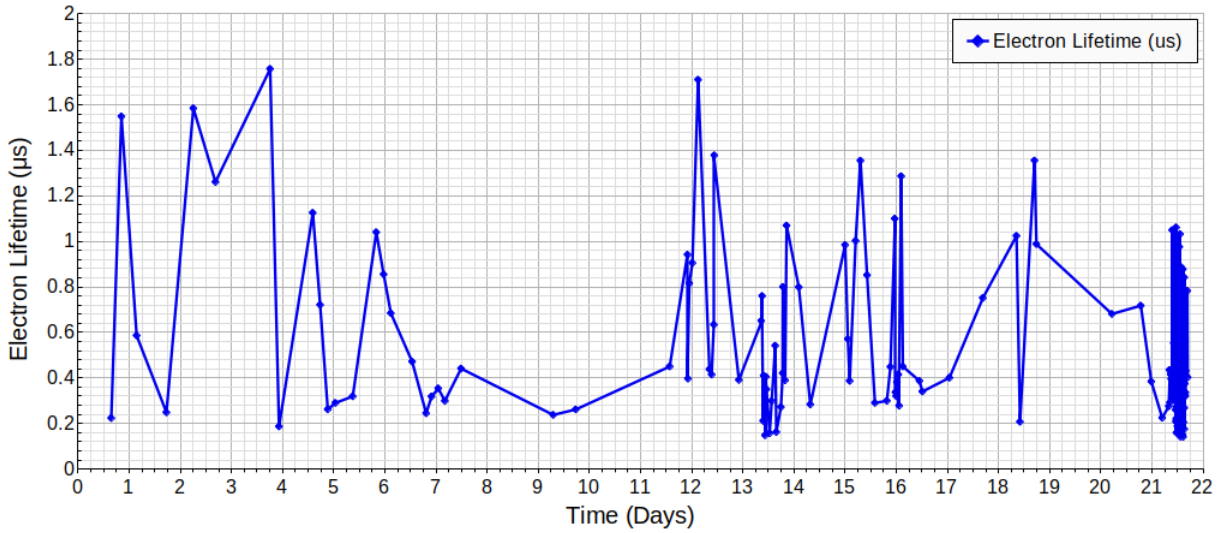

Figure D.3: Measured electron lifetime τ_e as a function of time t since the start of the first day of the 22-day data run of STEEL for 808 pixel data files. τ_e was calculated from finding the exponential decay constant of the measured to expected charge ratio against track length from ∼100 pixel events. Data points with poor exponential fits or with greater measured charge than expected charge were discarded.

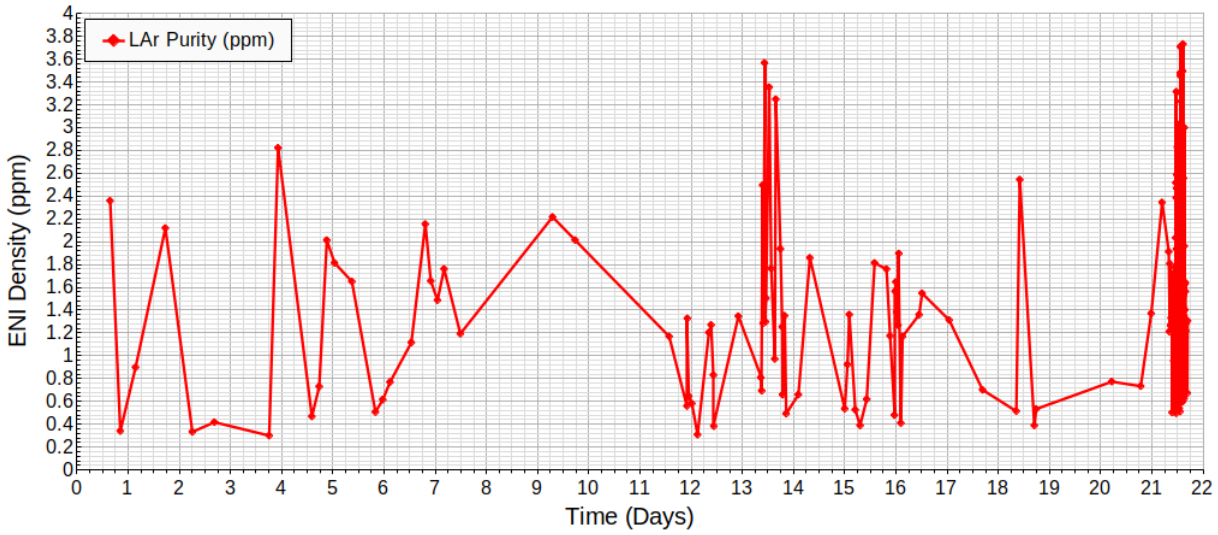

Figure D.4: Calculated oxygen impurity density $[O_2]$ in LAr as a function of time since the start of the first day of the 22-day data run of STEEL for 808 pixel data files. $[O_2]$ was calculated from equation 9.14 using $k_e = 1.9$ ppm$^{-1}\mu$s^{-1} [192].